

STRATEGIC IMMOBILISATION OF CATALYTIC METAL  
NANOPARTICLES IN METAL-ORGANIC FRAMEWORKS

Amanda Anderson

A Thesis Submitted for the Degree of PhD  
at the  
University of St Andrews



2017

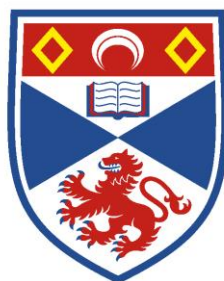
Full metadata for this item is available in  
St Andrews Research Repository  
at:  
<http://research-repository.st-andrews.ac.uk/>

Please use this identifier to cite or link to this item:  
<http://hdl.handle.net/10023/10816>

This item is protected by original copyright

# Strategic Immobilisation of Catalytic Metal Nanoparticles in Metal-Organic Frameworks

Amanda Anderson



University of  
St Andrews

This thesis is submitted in partial fulfilment for the degree of PhD  
at the University of St Andrews

April 2017





**3. Permission for publication:**

In submitting this thesis to the University of St Andrews I understand that I am giving permission for it to be made available for use in accordance with the regulations of the University Library for the time being in force, subject to any copyright vested in the work not being affected thereby. I also understand that the title and the abstract will be published, and that a copy of the work may be made and supplied to any bona fide library or research worker, that my thesis will be electronically accessible for personal or research use unless exempt by award of an embargo as requested below, and that the library has the right to migrate my thesis into new electronic forms as required to ensure continued access to the thesis. I have obtained any third-party copyright permissions that may be required in order to allow such access and migration, or have requested the appropriate embargo below.

The following is an agreed request by candidate and supervisor regarding the publication of this thesis:

**PRINTED COPY**

Embargo on all or part of print copy for a period of 1 year on the following ground(s):

- Publication would preclude future publication

**ELECTRONIC COPY**

Embargo on all or part of electronic copy for a period of 1 year on the following ground(s):

- Publication would preclude future publication

**ABSTRACT AND TITLE EMBARGOES**

- |  |     |
|--|-----|
| a) I agree to the title and abstract being published | YES |
| b) I require an embargo on abstract                  | NO  |
| c) I require an embargo on title                     | NO  |

Date

signature of candidate

signature of supervisor

signature of supervisor

# Acknowledgements

To begin, I would like to thank my supervisors Professor Paul Wright and Professor Chris Baddeley for their guidance and support over my PhD. I'm grateful for their encouragement, feedback, and advice throughout my time in St Andrews. I would like to also thank Professor Robert Tooze and Sasol for their discussions and funding. Additionally, I'd like to also thank the EPSRC and the University of St Andrews for funding.

I would like to thank Dr. Steve Francis and Dr. Federico Grillo for their help in surface science. Their time and effort towards training, teaching and discussing results with me on the STM, HREELS, XPS and everything else is greatly appreciated. A big thank you also goes out to Dr. Riho Seljamäe-Green for teaching me STM, and Christian Larrea for assistance in fixing and optimizing the HREELS and vacuum. I am thankful for the computational work completed by Dr. Herbert Früctl, and to Professor Neville Richardson for the use of his UHV equipment.

I thank Mrs. Sylvia Williamson for training and collection of N<sub>2</sub> adsorption data. Thanks to Mrs. Melanja Smith and Dr. Thomas Lebl for the wonderful NMR facilities. Thanks to Dr. Yuri Andreev for the training and technical support for the powder XRD. I'd like to thank Ross Blackley, who provided training and support on the electron microscopes. Also, thank you to Bobby, who has helped massively in fixing things when I break them.

I am grateful for the huge amount of support and scientific discussion from both the Wright and Baddeley group. A special thanks to Dr. Alex Greenaway for support, training and a great office atmosphere and Dr. Laura Mitchell for getting me up to speed on MOF catalysis. And a huge thanks to all the Wright group for the fun times in the lab and office and for all the delicious baked goods along the way. Also, an immeasurably large thanks to the Kamer group who let me borrow things constantly, maintained the dry solvent stills and provided access to the high-pressure system.

I'd like to give a huge thanks to the friends I have made during my time in St Andrews. These people have helped to get my mind off of the chemistry woes and also as people I could vent to. Thank you to Lorenz, Megan, Esther, Sherry, Paola, Luke, Franziska,

## Acknowledgements

---

Robert, Ciaran, Stefan, Amanda, Rana and everyone else for the lovely meals, games, and pub times. These are memories I will cherish forever.

I would also like to my family and friends who were supporting and encouraging me along the way – all the Skype times have made it feel like we aren't 4,700 miles apart.

And finally, Frank, I am so thankful we could have St. Andrews as an adventure together. I appreciate everything you do, from catalysis discussions to cooking dinners (lots of times simultaneously). Thank you for always giving scientific support and personal support. I can't wait to see what Eindhoven has in store for us next.

# Abstract

This thesis describes the synthesis, characterisation and catalytic testing of multifunctional immobilised metal nanoparticle in metal-organic framework (MOF) materials. Combining the activity of metal nanoparticles with the porosity and Lewis acidity of metal-organic frameworks provides a single catalytic material which can perform multi-step reactions.

Strategies to immobilise the metal nanoparticles within the metal-organic frameworks have been investigated. Immobilisation has been achieved by applying three different methodologies. First, deposition of metal nanoparticle precursors within mesoporous MOFs is discussed. Chapter 3 shows the effectivity of the double solvents deposition technique to achieve dispersed and small nanoparticles of around 2.7 nm. The best system combined Pd nanoparticles with MIL-101(Cr). This system was further investigated in tandem reductive amination catalysis, discussed in Chapter 4, to investigate the activity and selectivity provided by these multifunctional catalysts.

Another immobilisation technique was performed by coating Pd decorated SiO<sub>2</sub> spheres with a MOF layer. Using this technique, MOF was grown cyclically in solution, providing tuneable shell thicknesses of MOF on the metal nanoparticle decorated oxide spheres. While the homogeneity of the MOF shell needs more optimisation, it was determined that the surface charge on the spheres played an important role in the growth of MOF in the desired location.

Finally, the third immobilisation technique is the core-shell growth of MOF on colloidal metal nanoparticles. Polymer-capped metal nanoparticles with well-defined shapes were synthesised and characterised. From here, the optimisation of conditions for core-shell growth of UiO-66 and MIL-100(Sc) were investigated. Conditions which provided the desired core-shell morphology were found for both MOF types. These materials were then subsequently used in tandem reductive amination catalysis and a more straightforward styrene hydrogenation. It was shown that the metal nanoparticles remain active catalysts within either MOF shell and the MOF shell stabilises the metal nanoparticle and acts as a Lewis acid catalyst.

---

---

# Table of Contents

---

Declarations.....	i
Acknowledgements .....	iii
Abstract .....	v
Table of Contents .....	vii
Chapter 1 Introduction .....	1
1.1 Background .....	2
1.2 MOFs as Lewis Acidic Catalysts .....	3
1.2.1 HKUST-1 .....	4
1.2.2 UiO-66.....	5
1.2.3 MIL-100 and MIL-101 .....	7
1.3 Design Strategies for Metal Nanoparticles in MOFs .....	8
1.3.1 Top-down Design of Materials .....	9
1.3.2 Bottom-up Design of Materials .....	11
1.4 Nanoparticles in MOFs for Catalysis.....	15
1.4.1 Size Selectivity in MNP in MOF catalysis .....	16
1.4.2 Catalytic Enhancement in MNP in MOF Catalysis .....	16
1.4.3 Metal Nanoparticle in MOFs for Tandem Catalysis.....	17
1.5 Metal-Organic Coordination Networks .....	19
1.5.1 Model MOFs .....	19
1.5.2 Pressure Gap and Materials Gap <sup>3</sup> .....	20
1.6 Project Scope .....	21
1.7 References .....	22
Chapter 2 Characterisation Techniques .....	27

## Table of Contents

---

2.1 Introduction .....	28
2.2 Characterisation Techniques: Immobilised Nanoparticles in MOF .....	28
2.2.1 Powder X-ray Diffraction .....	28
2.2.2 Nitrogen Adsorption <sup>1-5</sup> .....	30
2.2.3 Transmission Electron Microscopy <sup>6-7</sup> .....	33
2.2.4 Scanning Electron Microscopy <sup>9</sup> .....	36
2.2.5 Energy Dispersive X-Ray Spectroscopy <sup>10</sup> .....	36
2.2.6 X-ray Photoelectron Spectroscopy <sup>12</sup> .....	38
2.2.7 Fourier Transform Infrared Spectroscopy <sup>14</sup> .....	40
2.2.8 Solution State Nuclear Magnetic Resonance Spectroscopy <sup>15</sup> .....	41
2.3 Characterisation Techniques: Metal Organic Coordination Networks .....	44
2.3.1 Reflection Absorption Infrared Spectroscopy <sup>18</sup> .....	44
2.3.2 High Resolution Electron Energy Loss Spectroscopy <sup>19</sup> .....	46
2.3.3 Scanning Tunneling Microscopy <sup>18, 22-23</sup> .....	48
2.4 References .....	51
Chapter 3 Metal Nanoparticle Deposition and Formation in MOF Supports: Synthesis and Characterisation of Multifunctional Materials .....	53
3.1 Introduction .....	54
3.2 Experimental .....	56
3.2.1 MOF Synthesis .....	56
3.2.2 Metal Nanoparticle Deposition .....	58
3.3 Metal Nanoparticle in MOF Catalyst Characterisation .....	59
3.3.1 Optimisation of MOF Synthesis .....	59
3.3.2 Optimisation of MNP Deposition .....	64
3.4 Conclusions and Outlook .....	79

---

3.5 References .....	81
Chapter 4 Multifunctional MOF and MNP/MOF Materials: The influence of the MOF Support on MNP Catalysis and Tandem MNP/MOF Catalysis.....	83
4.1 Introduction.....	84
4.2 Experimental.....	87
4.2.1 Reductive Amination Catalysis Testing.....	87
4.2.2 Citronellal to Menthol .....	91
4.2.3 Chloronitrobenzene to Chloroaniline.....	91
4.2.4 Autoclave Temperature Discrepancy .....	91
4.2.5 NMR Methods .....	92
4.3 Reductive Amination: Low Temperature (50 °C) Catalysis.....	94
4.3.1 Kinetics.....	96
4.3.2 Recyclability and Leaching Test .....	99
4.4 Reductive Amination: High Temperature (90 °C) Catalysis.....	103
4.4.1 Achieving Full Conversion and High Selectivity .....	104
4.4.2 Optimising Pd Loadings .....	105
4.4.3 Kinetics.....	105
4.4.4 Recyclability and Leaching Test .....	113
4.5 Catalyst Activity in Other Reactions .....	116
4.5.1 Citronellal to Menthol .....	116
4.5.2 Chloronitrobenzene to Chloroaniline.....	121
4.6 Catalysing and Stabilising with Polyoxometalates .....	125
4.6.1 Synthesis and Characterisation .....	126
4.6.2 Imine Formation Catalysis .....	132
4.6.3 Nanoparticle Deposition in MIL-101(Sc) .....	136

## Table of Contents

---

4.7 Conclusions and Outlook .....	138
4.8 References .....	141
Chapter 5 Bottom-Up Catalyst Synthesis: MOF Growth on Pd SiO <sub>2</sub> Spheres .....	143
5.1 Introduction .....	144
5.2 Experimental.....	145
5.2.1 Silica Sphere Synthesis and Functionalisation .....	146
5.2.2 Metal Nanoparticle Deposition .....	146
5.2.3 MOF Growth Methods .....	147
5.2.4 Catalysis .....	147
5.3 Silica Sphere Characterisation .....	148
5.4 Metal Nanoparticle Deposition .....	151
5.5 Multi-cycle MOF growth.....	153
5.6 Modifying Surface Charge .....	165
5.7 MIL-100(Fe) catalysis.....	166
5.8 Conclusion and Outlook .....	167
5.9 References .....	169
Chapter 6 Well-Defined Catalysts: Core-Shell Synthesis of MNP@MOF Materials.....	171
6.1 Introduction.....	172
6.2 Experimental.....	174
6.2.1 MNP shape synthesis.....	174
6.2.2 Optimised MNP@UiO-66 Synthesis .....	175
6.2.3 Optimised MNP@MIL-100(Sc) Synthesis .....	175
6.2.4 Catalysis conditions .....	176
6.3 MNP Shape and Characterisation.....	177

---

6.4 MOF Growth: Optimising Synthesis Concentrations to Achieve Core-Shell Materials.....	180
6.4.1 UiO-66.....	180
6.4.2 MIL-100(Sc).....	187
6.5 Catalysis .....	190
6.5.1 UiO-66.....	190
6.5.2 MIL-100(Sc).....	195
6.6 Conclusions and Outlook .....	196
6.7 References .....	200
Chapter 7 Metallosupramolecular Assembly by Dissociation of Metal Carbonyls on Au(111) .....	203
7.1 Introduction.....	204
7.2 Experimental.....	206
7.3 Results and Discussion.....	208
7.3.1 Scanning Tunnelling Microscopy .....	208
7.3.2 Reflection Absorption Infrared Spectroscopy .....	212
7.3.3 High Resolution Electron Energy Loss Spectroscopy.....	213
7.3.4 Density Functional Theory Calculations .....	218
7.4 Conclusions and Outlook .....	223
7.5 References .....	224
Chapter 8 Conclusions and Outlook .....	227
8.1 Conclusions.....	228
8.2 Outlook .....	230
Abbreviations.....	233

## Table of Contents

---

# Chapter 1

---

Introduction

## 1.1 Background

Catalysis is vital for the modern world, and is used in the production of approximately 90% of all chemicals and materials used today.<sup>1</sup> Its importance is intertwined with the drive towards new sustainable technologies and emerging novel synthetic methods. Because of this, research on developing efficient catalysts has been at the forefront of chemical and chemical engineering research for several decades. Three separate fields of catalysis can be distinguished: heterogeneous, homogeneous and enzymatic. Heterogeneous catalysis, where the reactant and catalyst are in different physical phases, is often achieved by flowing liquid or gas reactants over supported catalytically active metal particles or other solid catalysts. Heterogeneous catalysts benefit from the ability of being easily separated from the reactants and products due to their different phases, and can often work at higher temperatures and pressures than their homogeneous or enzymatic analogues. One downside of heterogeneous catalysts is their lack of selectivity in catalysis when compared to homogeneous counterparts due to different types of reactive sites on a heterogeneous catalyst.<sup>2</sup> Developing highly selective and active heterogeneous catalysts for industrially relevant catalytic reactions is an area of intense research.

Research in developing catalytic metal particles on supports focusses on the understanding of interactions during the formation of the material as well as the interactions between metal, support and reactants in subsequent catalytic reactions. The interaction between the support and metal particles plays a large role in the activity of the catalyst.<sup>3</sup> Maximising the surface area of a support allows for large quantities of catalytically active metal particles to be dispersed throughout the support and provides more interactions to occur within a relatively small mass. As the metal particle size gets smaller its surface area to volume ratio drastically increases, which gives the particle different structural and electronic properties when compared to the bulk material and enables a larger percentage of atoms within the particle to interact with reactants on the surface. For this reason, metal nanoparticle (MNP) research has flourished with respect to elucidating surface structures and interactions with their surroundings and using these interactions in useful applications.

Solid acid catalysts also play a large role in the chemical industry. Zeolites are among the most prominent class of solid acids used for petrochemical transformations.<sup>4</sup> Porous zeolitic materials can form highly acidic solid catalysts after ammonium ion exchange and pre-treatment, which can facilitate a wide variety of reactions such as alkylations, isomerisations and aminations.<sup>4</sup> However, zeolites suffer from limited pore sizes, where there is an approximately 1 nm limit which puts these materials in the microporous regime (pores less than 2 nm). Especially for liquid phase reactions this presents an issue due to mass transfer limitation during the catalysis. The reactions within these micropores can be limited by the diffusion of reactants towards the catalytic active site rather than the performance of the active site itself. Additionally, because zeolitic materials are aluminosilicates, their structures are limited by combination of these elements.

Metal organic frameworks are another class of emerging porous solid acid catalysts. They offer a wide variety of structures due to their near-limitless options of metal and organic linker units. By combining the activity of metal nanoparticles with the solid acid catalysts as supports, a multifunctional catalyst can be achieved. This introduction will discuss the field of MOFs as Lewis acid catalysts (section 1.2), metal nanoparticles within MOFs and their catalytic capabilities (section 1.4), design strategies to obtain these materials (section 1.3) and model MOFs on surfaces which can give insight on molecular interaction within the bulk materials (section 1.5). Section 1.6 outlines the scope of the subsequent thesis chapters.

## **1.2 MOFs as Lewis Acidic Catalysts**

Metal-organic frameworks, in contrast to zeolites, offer significant flexibility in structure and pore size. Metal-organic frameworks are materials where an organic linker, often, but not exclusively, containing carboxylate moieties, is bonded to metal or metal oxide nodes. The coordination of the metal to organic molecules creates crystalline materials with a vast variety in structure and function. Some of these combinations create MOFs in the mesoporous regime (2 to 50 nm pore size), which moves towards minimisation of mass transfer limitations. Additionally, some MOFs possess the ability to become solid acid catalysts by removal of weakly coordinated

ligands, such as water, solvent or acetic acid, from the metal nodes. However, MOFs suffer from a lack of thermal and chemical stability when compared to zeolites. Additionally, in some MOFs, removing coordinatively attached solvent from the pores causes pore collapse and leads to amorphous materials. Overall, zeolites and MOFs are not likely to compete as catalysts in reactions requiring harsh conditions where zeolites are more robust, but due to the tunability of MOFs in both chemical functionality and a structural sense there is potential for niche applications in catalysis with these materials.

### 1.2.1 HKUST-1

One of the first MOFs that was heavily investigated with respect to Lewis acid catalysis was HKUST-1.<sup>5</sup> This MOF, made from copper and trimesic acid, forms microporous square shaped cages of 9 Å and side pores of 5 Å, shown in Figure 1.1. Upon removal of a stoichiometric amount of water from the Cu paddlewheels, HKUST-1 becomes an active acid catalyst.

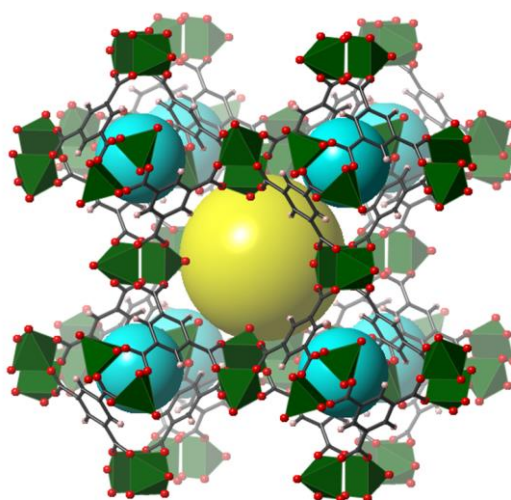


Figure 1.1 HKUST-1 consisting of Cu and trimesic acid (green: Cu, red: O, dark grey: C, light grey: H, yellow and cyan: pore voids).

HKUST-1 has been used as an acid catalyst in a variety of reactions, such as cyanosilylation of aldehydes and acetone<sup>6</sup>, isomerisation of  $\alpha$ -pinene oxide<sup>7</sup>, cyclisation of citronella<sup>7</sup>, Friedel-Crafts Michael addition<sup>8</sup> and imine formation<sup>8</sup>. HKUST-1 is now a commercially available material, Basolite™C300, and has been investigated for adsorption<sup>9</sup>, electrochemistry<sup>10</sup> and catalysis.

### 1.2.2 UiO-66

UiO-66 is a Zr-based MOF which offers high chemical and thermal stability. This MOF has a cubic structure consisting of  $[\text{Zr}_6\text{O}_4(\text{OH})_4]^{12+}$  nodes and terephthalic acid linkers, shown in Figure 1.2, with pores of around 6 Å (seen in yellow).<sup>11</sup> Because of the high connectivity of this MOF when fully coordinated with 12 terephthalic acid linkers per Zr metal centre, missing linkers can be tolerated within the structure while maintaining high stability. Modulation can be achieved by adding a monocarboxylic acid into the synthesis causing missing linker defects within the final structure. At full linker coordination the UiO-66 pore volume is approximately  $0.44 \text{ cm}^3 \text{ g}^{-1}$ , but can grow up to  $1.0 \text{ cm}^3 \text{ g}^{-1}$  upon tuning the concentration of missing linkers.<sup>12</sup> This modifies the gas adsorption properties of the material<sup>12</sup> as well as altering the catalytic capabilities of UiO-66<sup>13</sup>.

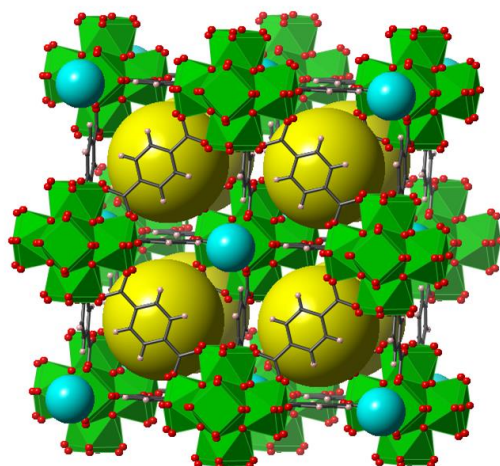


Figure 1.2 UiO-66 crystal structure. Green: Zr, red: O, dark grey: C, light grey: H, yellow and cyan: pore voids.

Vermoortele *et al.* showed a modular approach to increasing the catalytic activity of UiO-66 by partial substitution of the terephthalic acid linkers by trifluoroacetic acid (TFA).<sup>14</sup> They found that by adding amounts of TFA ranging between 1 to 20 equivalents the conversion for the cyclisation of citronellal increased from 34% with no modulation to 75% with 20 equivalents of trifluoroacetic acid. The catalysts in this study were also probed to determine when the TFA dissociates from the Zr cluster. It

was found that at 200°C they were still bound but when heated to 270-320°C, a clear loss of fluorine was observed, indicating the trifluoroacetic acid is removed from the metal site. Additionally, six monocarboxylic acids were tested as modulators to determine the influence each has on the catalytic activity. While trifluoroacetic acid had the largest positive effect, acetic acid gave the next most active catalyst. While Shearer *et al.*<sup>15</sup> suggested that there is a direct correlation between  $pK_a$  of acid and the modulation of UiO-66, it was determined that the  $pK_a$  of the monocarboxylate modulator does not necessarily increase the catalytic activity of the resultant MOF.

Shearer *et al.* studied the defect chemistry of UiO-66 by modulating defects with four different monocarboxylic acids; acetic acid, formic acid, difluoroacetic acid and trifluoroacetic acid.<sup>15</sup> These acids have  $pK_a$  values of 4.76, 3.77, 1.24 and 0.23, respectively. The trend of pore volume, and thus cluster defects, increased with decreasing  $pK_a$  of the modulator. It is stated that the more acidic modulator leads to more deprotonated modulator in the MOF synthesis. This in turn leads to an increased probability for the monocarboxylic acid to coordinate to the Zr metal node compared to the terephthalic acid, thus leading to more defects in the Zr cluster. Shearer *et al.* conclude that the stronger the acidic modulator the more defects will occur in the cluster, which in turn would lead to more acid sites within the final MOF. However, this conclusion is not necessarily correlated to the activity of the catalyst, as seen by Vermoortele *et al.*, who showed that acetic acid modulated UiO-66 performs better as a citronellal cyclisation catalyst than UiO-66 modulated with formic acid (45% conversion compared to 13% respectively).<sup>14</sup>

Another method for increasing the activity of UiO-66 is the use of functionalised terephthalic acid, as published in another account by Vermoortele *et al.*<sup>16</sup> UiO-66 materials were synthesised with one of eight different functionalised terephthalic acids. The MOF was used as a catalyst in the cyclisation of citronellal to isopulegols. It was found that the UiO-66 synthesised with nitro-terephthalic acid increased the activity 56 times. The paper suggests the interaction of the citronellal and the nitro group with respect to the MOF metal active site creates the optimal orientation of the citronellal to undergo cyclisation.

### 1.2.3 MIL-100 and MIL-101

MIL-100 and MIL-101 are both mesoporous MOFs with an MTN structure.<sup>17-18</sup> MIL-100 uses trimesic acid as a linker while MIL-101 contains a terephthalic acid linker. In both MIL-100 and MIL-101 the metal trimer ( $M_3O$ ,  $M = Cr, Sc, Fe, Al, V$ ) creates supertetrahedra with the linker molecules, which then form into small and large cages. These small and large cages orient to form the MTN structure. The difference in coordination of the metal to three carboxylates in trimesic acid compared to two in terephthalic acid leads to a difference in overall pore size. The metal trimer, supertetrahedron, small cage, large cage and overall structures of MIL-100 and MIL-101 are shown in Figure 1.3. MIL-100 has cages with diameters of 2.5 nm and 3.0 nm with hexagonal windows of 0.9 nm and pentagonal windows of 0.5 nm. MIL-101 has cages slightly larger at 2.9 nm and 3.4 nm with hexagonal windows of 1.6 nm and pentagonal windows of 1.2 nm. In both cases, the small cage consists of only pentagonal windows, while the large cage is made with both pentagonal and hexagonal windows.

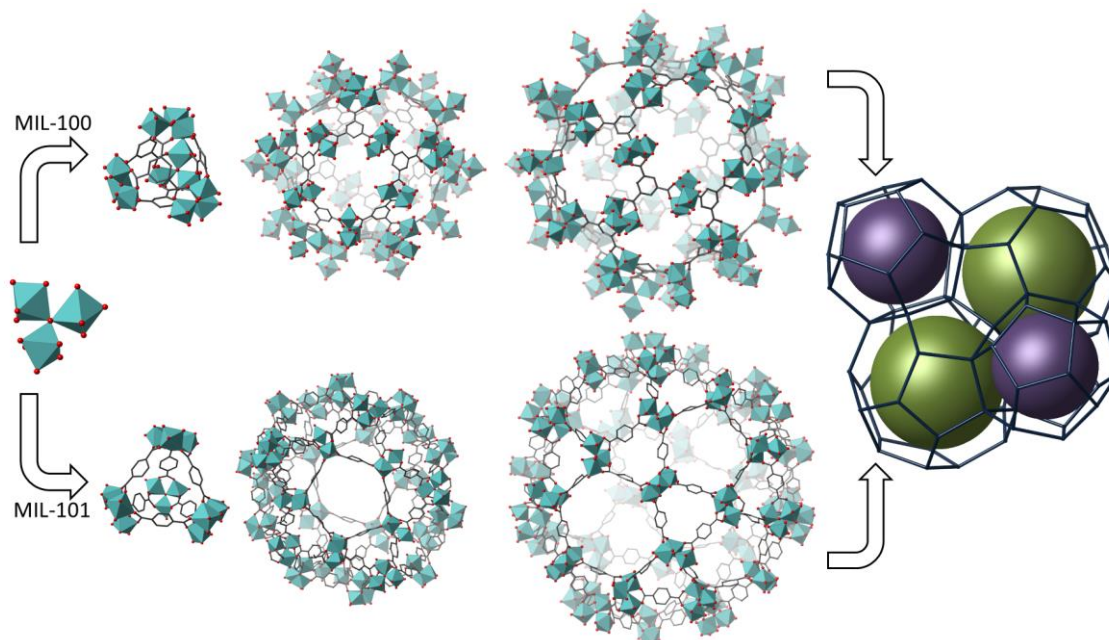


Figure 1.3 MIL-100 (top) formed with trimesic acid and MIL-101 (bottom) formed with terephthalic acid, both showing the corresponding (left to right) trimer, supertetrahedron, small cage, large cage and overall MTN structure. Blue: metal, dark grey: C, red: O.

Both MIL-100 and MIL-101 have been extensively used for their catalytic properties. Upon activation at around 150°C in vacuum, coordinated water leaves the metal nodes and both MOFs become active Lewis acid catalysts. MIL-100(Fe) has been used in Claisen-Schmidt condensation reactions in order to form chalcones<sup>19</sup> and MIL-100(Sc) has been used in a huge variety of C-C and C=N bond forming reactions<sup>8</sup>, demonstrating its impressive catalytic activity. MIL-101 has been investigated as a catalyst for intermolecular carbonyl-ene reactions and Friedel-Crafts Michael addition reactions.<sup>8</sup> Additionally, due to their large pores, metal nanoparticles and other guest molecules, such as polyoxometalates (POMs),<sup>20-23</sup> have been deposited within both MIL-100 and MIL-101 in order to alter the catalytic properties of the system.

### **1.3 Design Strategies for Metal Nanoparticles in MOFs**

Immobilization of metal nanoparticles within a MOF can be achieved by a variety of methods. Depositing MNPs within MOFs can afford stable and active catalysts. The MNP active sites remain readily accessible through the network of the porous MOF materials. Another benefit of immobilising MNPs is that it can prevent catalyst degradation through possible sintering or leaching mechanisms, which leads to a more stable catalytic material. For this reason, ideally the MNPs are dispersed within the MOF pores rather than on the surface, where the influence of the MOF support plays less of a role. To achieve these multicomponent materials, two major types of material design strategies have been investigated.

In terms of MNPs in MOFs, the top-down strategy involves depositing metal nanoparticle precursors within an already prepared MOF support. Subsequently, upon addition of a reducing agent, nanoparticles are formed. Bottom-up design starts with the synthesis of the nanoparticle first, thus allowing direct control over the nanoparticle size and morphology, then growing MOF around the MNP to form the multicomponent material. A diagram showing the two design strategies is depicted in Figure 1.4.

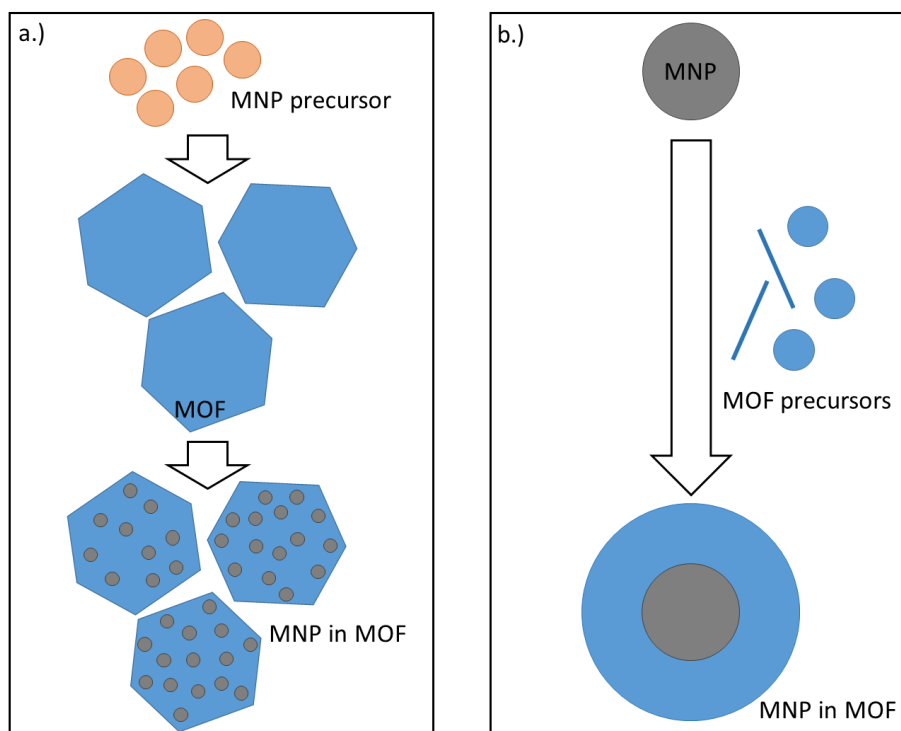


Figure 1.4 Two approaches to prepare MNP containing MOF materials. (a.) a top-down approach of depositing MNP precursors into the porous MOFs then reducing to form MNPs and (b.) a bottom-up approach of growing MOFs around MNPs.

### 1.3.1 Top-down Design of Materials

The top-down approach to MNP in MOFs starts with depositing nanoparticle precursors within the MOF pores. A number of deposition routes have been developed, from grinding or solution impregnation to incipient wetness methods, among others.<sup>24</sup>

Grinding metal nanoparticle precursors with MOF supports was the method Ishida *et al.* utilized to form Au MNP in MOF-5 ( $[(Zn_4O(BDC)_3)_n]$ , BDC= terephthalic acid).<sup>25</sup> In this method a volatile Au solid,  $Me_2Au(acac)$ , was used and it is claimed that by solid grinding of the MNP precursor and MOF, a smaller average nanoparticle size and narrower size distribution was achieved compared to chemical vapour deposition or solution impregnation. It was argued that the high uniformity of the material when using the solid grinding approach is due to the rapid diffusion of the vapour within the MOF support.

Solution impregnation of MNP precursors was accomplished by Zlotea *et al.* by stirring an aqueous  $H_2PdCl_4$  solution with the MIL-100(Al) support followed by reduction of the

metal salt with flowing H<sub>2</sub>/Ar to form nanoparticles.<sup>26</sup> In this work PdCl<sub>2</sub> was turned into a H<sub>2</sub>PdCl<sub>4</sub> solution by dissolving the metal salt in an aqueous HCl solution. This acidic solution caused some degradation in the crystallinity of the material, shown by slight peak broadening in the XRD. The MNP size calculated by the XRD peaks suggests that the Pd particles, on average, occupy two of the mesoporous cages indicating either that some structural integrity of the porous MOF support is affected, or that many of the MNPs are not within the pores.

Another solution impregnation study was carried out by El-Shall *et al.* with Pd, Cu and PdCu MNP in MIL-101(Cr) and compared with a similar incipient wetness deposition method to prepare MNPs.<sup>27</sup> When using the solution impregnation method, the metal loading was higher (as determined by ICP), but the MNPs were deposited on the surface of the MOF in addition to the desired deposition within the pores. This is undesirable for catalysis because mobile particles on the surface can easily undergo sintering and leaching during the catalytic experiments, which leads to deactivation of the catalyst.

Incipient wetness is similar to solution impregnation but uses the value of the pore volume of the support to determine accurately the required amount of metal salt solution. Incipient wetness uses capillary action within the porous support to allow the metal salt solution to enter the pores. In this deposition method, it is important to add metal salt solution in small portions at a time to allow the capillary action to occur. Incipient wetness is commonly used for deposition of MNPs in MOFs because it leads to better dispersion within the MOF structure and minimises the number of MNPs on the support surface.<sup>27</sup> Alterations to a traditional incipient wetness procedure have been accomplished with the double solvents method. In this method, originally published by Aijaz *et al.*<sup>28</sup>, MIL-101(Cr) is dried and subsequently suspended in a nonpolar solvent. The aqueous metal salt solution is slowly added to the system and enters the hydrophilic pores while the nonpolar solvent covers the surface. This has been shown to give small nanoparticles of AuNi,<sup>29</sup> Ag,<sup>30</sup> Pd,<sup>30</sup> and Pt.<sup>28</sup> This is the method of choice for the top-down preparation of MNPs in MOFs within this thesis, and will be discussed in greater detail in Chapter 3.

### 1.3.2 Bottom-up Design of Materials

Bottom-up design of MNP in MOFs can potentially allow for greater control over the nanoparticle position within the MOF, the nanoparticle size and the MOF shell growth and morphology. Because the nanoparticle is formed before the MOF is grown around it, harsher conditions can be used to prepare the MNP than in the top-down route. The conditions for MOF growth are delicate, as both the concentration and ratio of MOF precursors with respect to MNP are important in allowing the MNP to act as the MOF nucleation site. These core-shell materials can be advantageous because there is more control on the orientation of the MNP within the MOF. This ensures the MNP is immobilised and also can be beneficial for size-selective reactions in catalysis applications, depending on the MOF used as the shell of the hybrid particle.

Much of the literature concerning the design of core-shell MNP@MOF materials discusses microporous MOFs as size selectivity barriers to MNPs during catalysis. In a study by Zhang *et al.*, Pd nanoparticles were deposited on mesoporous silica spheres and then coated with ZIF-8 (Zn(2-MeIM), 2-MeIM= 2-methylimidazole).<sup>31</sup> After deposition and reduction of Pd(NH<sub>3</sub>)<sub>4</sub>Cl<sub>2</sub> on the mesoporous silica spheres but prior to MOF growth, the spheres were coated with polystyrenesulfonate (PSS). It was determined that the PSS coating was a critical step towards core-shell materials. They found that the Zn<sup>2+</sup> ions would adsorb onto the PSS coated SiO<sub>2</sub> which would allow MOF growth. If the PSS coating step was not performed, ZIF-8 was obtained as a fine powder instead of incorporated as a shell on the Pd/SiO<sub>2</sub>. This shows the important role the surface charge plays in growing MOF around relatively large objects. The catalytically active materials were tested in the reduction of 1-hexene as well as cyclohexene. It was determined that the rate of cyclohexene reduction was significantly slower, probably due to the diffusion limitations of the bulky molecule compared to 1-hexene through the 3.4 Å windows of ZIF-8.

Jiang *et al.* studied the influence of different parameters on the synthesis of Pd@ZIF-8 materials.<sup>32</sup> By systematically changing the ratios of Pd:Zn<sup>2+</sup> and 2-MeIM:Zn<sup>2+</sup> the material synthesis conditions could be optimized. It was determined that at molar Pd:Zn<sup>2+</sup> ratios larger than 0.012 the Pd nanoparticles started to appear on the surface

of the ZIF-8 crystals. Hence, the ratio has to be lower than this value when core-shell materials are desired. When examining the influence of the amount of linker with respect to the zinc metal node, it was found that 2-MeIm:Zn<sup>2+</sup> ratios of 1.5 and 1 formed the best core-shell materials. At higher ratios, it was determined that the growth rate of ZIF-8 is too high which led to small ZIF-8 crystals with Pd adsorbed on the surface rather than inside. By lowering this ratio, and slowing the growth of ZIF-8, the adsorption of nanoparticles into the MOF during formation could be ensured.

In a publication by Liao *et al.*, mesoporous MIL-100(Fe) was grown around Au NPs in a cyclic fashion.<sup>33</sup> Au MNPs were prepared by the reduction of chloroauric acid with sodium citrate to form particles of around 40 nm. The citrate was exchanged with PVP and dispersed in DMF. The shell growth of MIL-100(Fe) was performed by dispersing the colloid in an ultrasonic solution of FeCl<sub>3</sub>·6H<sub>2</sub>O in DMF for 10 minutes, followed by centrifuging and washing. Next, the colloid was dispersed in an ultrasonic solution of trimesic acid for 20 minutes. After another washing and centrifugation step, the first cycle of MIL-100(Fe) was completed. By repeating this growth cycle multiple times, the shell of MIL-100(Fe) gradually grows thicker. This versatile method to grow MIL-100(Fe) in a step-by-step fashion allows for control over the shell thickness which can influence the overall material properties. The thickness of the shell is directly correlated with the number of Lewis acid sites surrounding each MNP, which can alter the behaviour of the catalyst during reactions.

Na *et al.* reported a method to prepare Pt@UiO-66 catalysts which demonstrated unusual behaviour in methylcyclopentane catalysis.<sup>34</sup> Polyvinylpyrrolidone (PVP) capped 2 nm Pt MNP colloids were synthesised in a polyol synthesis procedure, using ethylene glycol serving as both solvent and reducing agent. The solvent was exchanged for DMF, which is the solvent needed for the next step of MOF growth. UiO-66 was then grown around the Pt MNPs leading to a small collection of MNPs in the centre of each highly crystalline UiO-66 crystal of approximately 150 nm. The MOF synthesis conditions were chosen such that the MNPs act as nucleation points and all UiO-66 crystals contained MNPs.

### 1.3.2.1 Colloidal Nanoparticles

The bottom-up design strategy offers a highly versatile approach and allows nanoparticle properties, such as morphology, functionality and size, to be precisely tailored prior to MOF growth. When using nanoparticle colloids, the stable solution of suspended MNPs can be used as nucleation sites for the successive MOF growth. The field of colloidal nanoparticle chemistry has advanced in the methodology used for controlling particle shape and size although the underlying mechanisms for shape-controlled MNP synthesis are often not well understood.<sup>35</sup>

The controlled shapes of nanoparticles can lead to interesting changes in catalytic properties because of the different crystal planes that are on the surface. A report by Song *et al.* discusses a method for shape control of Pt nanoparticles by silver ion doping.<sup>36</sup> By varying the Ag concentration between 1.1 mol%, 11 mol% and 32 mol% the Pt nanocrystals change from cubes to cuboctahedra to octahedral shapes while maintaining particle sizes of around 10 nm. The cube shape shows {100} crystal faces on all sides. The octahedral show {111} crystal faces on all sides, and the cuboctahedra has a mixture of the two faces (triangular as {100} and cubic faces {111}), seen in Figure 1.5. The Pt particles could be purified by repetitive washing steps, leaving no traces of Ag as determine by EDX, UV absorption and XRD.

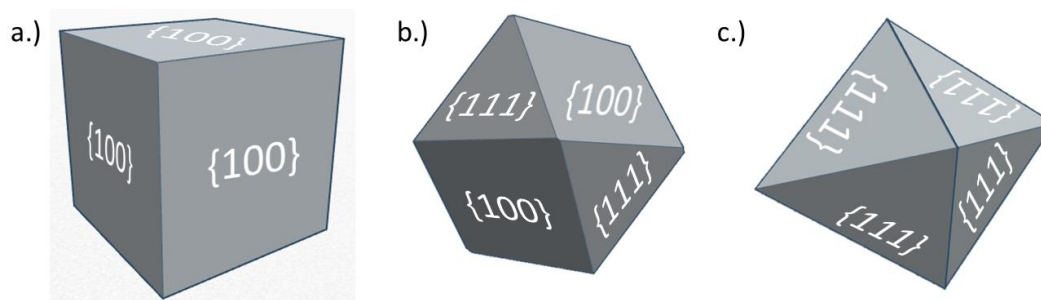


Figure 1.5 The Pt nanocrystal shapes of (a.) cube, (b.) cuboctahedra and (c.) octahedra.

Alayoglu *et al.* reported a procedure for the synthesis of Pt nanoparticle colloids which allows control over the shape and size of the particles and subsequently leads to changes in the selectivity in the hydrogenative conversion of methylcyclopentane, shown in Figure 1.6.<sup>37</sup> Four Pt MNP shapes (spheres, cubes, cuboctahedra and octahedra) were synthesised using a polyol method with controlled sizes around 6 nm.

After depositing the MNPs on mesoporous SiO<sub>2</sub> they were tested in a methylcyclopentane reaction seen in Figure 1.6. It was determined that the cuboctahedra and spheres exhibited the highest turnover frequency (TOF), which is likely attributed to the increased number of steps and edges within their structure. The MNPs demonstrated differences in selectivity as well. The Pt octahedra were most selective towards hexane formation while the cubes were most selective towards benzene formation. This shows that changing the crystal morphology of the MNP catalyst can have a huge influence on the outcome of catalytic reactions.

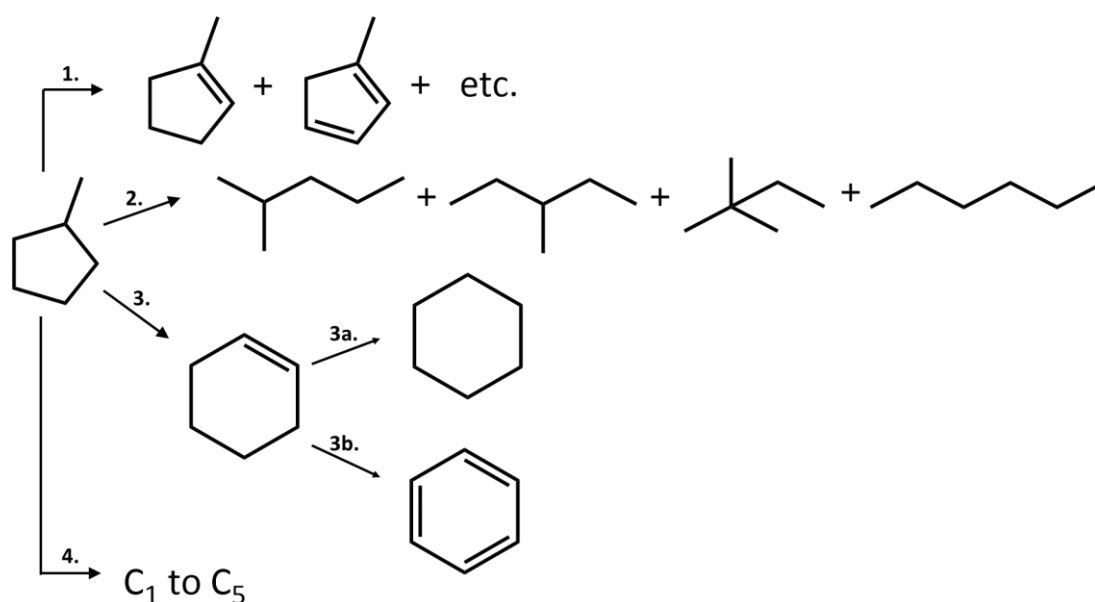


Figure 1.6 Reaction pathway for methylcyclopentane hydrogenative conversions.<sup>34</sup> (1.) dehydrogenation, (2.) ring opening and isomerisation, (3.) ring enlargement, (3a.) hydrogenation, (3b.) dehydrogenation, (4.) cracking.

### 1.3.2.2 Strategies for MOF growth

As previously shown, two methods are reported in recent literature for MOF growth in bottom-up synthesis of materials. Applying colloidal nanoparticles to a MOF synthesis procedure can afford core-shell materials. Alternatively, growing MOF in a layer-by-layer procedure can also produce core-shell materials. The ease of the colloidal MNP route is obvious, because the layer-by-layer method takes much more time to build up a substantial shell. However, the apparent control of the layer-by-layer method in terms of shell thickness is attractive when using MNPs in MOF synthesis.

## 1.4 Nanoparticles in MOFs for Catalysis

The MOF support can have three roles on the catalysis outcome. The MOF can either not participate as a catalyst, aid in changing the activity of the MNP, or act as a catalyst independently. Table 1.1 shows some of the recent literature which shows the three actions in which the MOF support has on the catalysis outcome.

Table 1.1 Summary of some of the recent literature combining MNPs and MOFs for catalytic applications.

MNP	MOF	MOF action	Reaction	Ref.
Pt/Al <sub>2</sub> O <sub>3</sub>	SIM-1	Size Selectivity	Hydrogenations	38
Pd	ZIF-L	Size Selectivity	Hydrogenations	39
Pt	UiO-66	Size Selectivity	Hydrogenations	40
Pt	ZIF-8	Size Selectivity	Hydrogenations	41
Pt	ZIF-8	Size Selectivity	Hydrogenations	42
Pd	ZIF-8	Size Selectivity	Hydrogenations	43
PdPt & RuPt	UiO-66	Size Selectivity	Hydrogenation of nitrobenzene	44
Pd	ZIF-8	Size Selectivity	Hydrogenations	31
Pd	MIL-101(Cr)	Enhancement	Hydrodeoxygenation of vanillin	45
Pd	MIL-101(Al)-NH <sub>2</sub>	Enhancement	Hydrogenation of 5-hydroxymethylfurfural	46
Pt	UiO-66	Enhancement	Methylcyclopentane reactions	34
AuPd	MIL-101(Cr)	Enhancement	Oxidation of aromatic hydrocarbons	47
Au	MIL-101(Cr)	Enhancement	Oxidation of alcohols	48
PdAg	MIL-101(Cr)	Tandem	Reductions and reductive aminations	30
Pd and Pt	MIL-101(Cr)	Tandem	Reductions and reductive aminations	49
Pd	MIL-101(Cr)	Tandem	Citronellal to menthol	50
Pd	MIL-101(Cr)	Tandem	Methylisobutyl ketone synthesis from acetone	51
Pd	UiO-66-NH <sub>2</sub>	Tandem	Oxidation and acetalization	52
Pd	IRMOF-3	Tandem	Knoevenagel condensation and hydrogenation	53

### 1.4.1 Size Selectivity in MNP in MOF catalysis

Size selection is a common approach in which a MOF, while not participating or altering the activity of the catalyst, does influence the catalytic outcome. Wang *et al.* published a procedure for the synthesis of hollow ZIF-8 nanospheres with Pd MNPs inside.<sup>54</sup> The procedure starts with depositing Pd MNPs on carboxylate-terminated polystyrene (CPS). The ZIF-8 is then grown around the Pd/CPS and subsequently the CPS is dissolved with DMF to finalise the nanoreactor synthesis. Next, the materials were tested in the hydrogenation of different sized molecules. It was found that the Pd MNPs were able to reduce 1-hexene because in this case the substrate was small enough to get through the pores of the ZIF-8 shell. However, the Pd was not able to reduce cis-cyclooctene, trans-stilbene or triphenylethylene because they were too large to transport through the ZIF-8 pores to interact with the Pd MNPs.

### 1.4.2 Catalytic Enhancement in MNP in MOF Catalysis

The influence of an acidic MOF support can assist MNPs by changing selectivity or activity. For instance, in a study by Ke *et al.*, core-shell Au NPs deposited on Fe<sub>3</sub>O<sub>4</sub> were covered in a shell of MIL-100(Fe) and tested in the reduction of 4-nitrophenol to 4-aminophenol.<sup>55</sup> These catalysts were synthesised by a cyclic MOF formation, similar to the methodology discussed earlier. It was found that with 5 cycles of MIL-100(Fe) growth, the catalyst was more active than just Au MNPs on Fe<sub>3</sub>O<sub>4</sub>. This indicates that the MOF and Au have a synergistic effect in 4-nitrophenol reduction. The MIL-100(Fe) does not play a role as an active site towards catalytic transformation but it is clear that the acidity of the MOF has an influence on the Au MNP catalysis. An additional benefit of this system was the Fe<sub>3</sub>O<sub>4</sub> within the system offered easy catalyst separation by magnetic filtration, thus allowing the catalyst to be easily recovered.

In a study by Na *et al.*, Pt@UiO-66 core-shell materials were prepared and used in methylcyclopentane hydrogenative conversions.<sup>34</sup> In this report UiO-66 was grown around 2 nm Pt nanoparticles, capped with PVP. The pathways for the hydrogenative conversion of methylcyclopentane are shown in Figure 1.6. When the Pt MNPs are deposited on UiO-66 rather than synthesised in a core-shell fashion, the methylcyclopentane is converted to ring-opening/isomerisation products as well as

products from dehydrogenation pathways. However, when UiO-66 is grown around the Pt MNPs the selectivity of products from ring enlargement conversions increases to 63.4%. It is claimed there are no acidic sites present on UiO-66 and instead two different theories accounting for the change of selectivity were suggested. One theory discussed was that the molecular vibration of the methylcyclopentane may be accelerated within the UiO-66 pores and as such could lower activation barriers towards the ring enlargement pathway. Alternatively, another theory discussed that the diffusion of H<sub>2</sub> into the MOF pores is fast compared to the methylcyclopentane and produces a nanoreactor-type system which changes the relative amount of H<sub>2</sub> around the Pt active sites, thus changing the selectivity of the catalysis.

### **1.4.3 Metal Nanoparticle in MOFs for Tandem Catalysis**

Metal nanoparticles in MOFs as multifunctional catalysts use the acid sites within a MOF as an active site for catalytic transformations as well as the MNP active sites. This enables tandem reactions to occur in one-pot, and sometimes under one single set of experimental conditions. In a study by Cirujano *et al.* Pd and Pt nanoparticles were deposited within MIL-101(Cr) and tandem catalysis was performed.<sup>49</sup> One of the main reactions probed was the synthesis of secondary arylamines by a three step process, shown in Figure 1.7. Starting initially with a nitro-substituted aromatic compound and a ketone or aldehyde, the Pt or Pd MNPs reduce the nitro group to an amine. In the next step the Lewis acidic MIL-101(Cr) catalyses the formation of an imine. Finally, the Pt or Pd MNP reduces the imine to form a secondary arylamine.

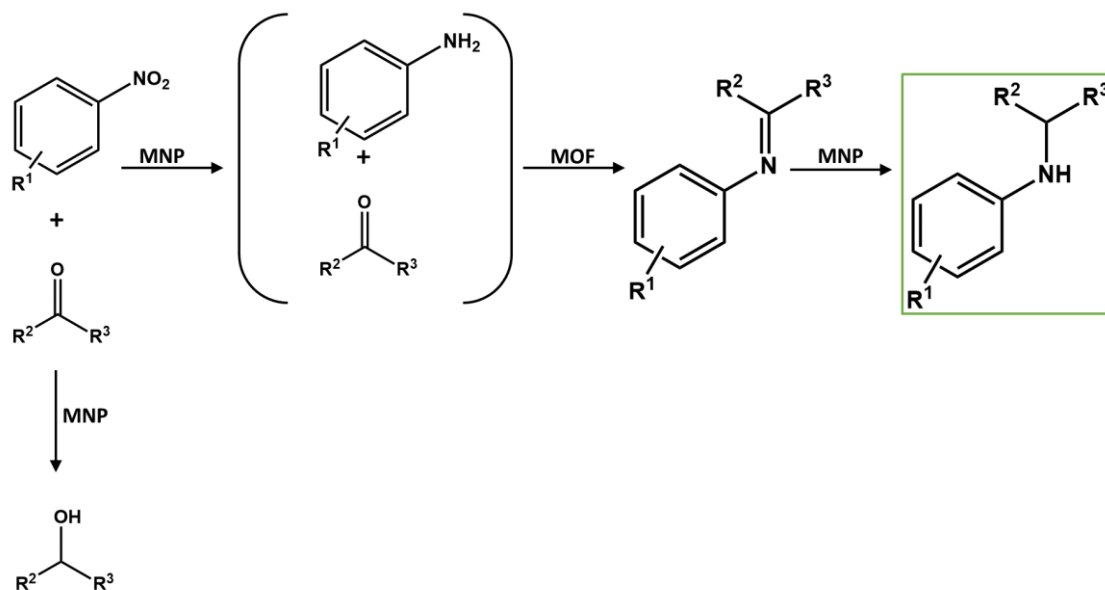


Figure 1.7 Secondary arylamine formation from nitro-aromatic group and a ketone or aldehyde. The MNP catalyses the nitro into an amino group, then the MOF site catalyses the imine formation, and the Pd or Pt catalyses the final imine reduction to form a secondary arylamine.

It was observed that the MNP containing MOF materials performed more selectively than traditional Pt or Pd on carbon or Al<sub>2</sub>O<sub>3</sub>. An alternative reaction pathway can take place in which the Pt or Pd reduces not only the nitro group to an amine but also reduces the C=O to an alcohol. This alternative pathway prevents the formation of the desired secondary arylamine.

Another study on tandem reactions was performed by Zhao *et al.* using a core-shell Pd@IRMOF-3 system.<sup>53</sup> IRMOF-3 is a Zn-BDC-NH<sub>2</sub> MOF, synthesised with Zn(NO<sub>3</sub>)<sub>2</sub> and 2-aminoterephthalic acid. The amine groups throughout the structure behave as a weakly basic amine which catalyses the first step of the tandem Knoevenagel condensation and the Pd MNPs catalyse the subsequent hydrogenation reactions, seen in Figure 1.8. The core-shell Pd@IRMOF-3 catalyst is able to achieve 100% conversion and 86% selectivity to the desired 2-(4-aminobenzylidene)-malonitrile. The side products of further hydrogenation of C=C bonds are minimised with the core-shell material (14% combined), but do appear in larger quantities for Pd deposited on IRMOF-3 (29% selectivity combined) and the Pd MNPs alone (32% selectivity combined). This indicates the morphology of the catalysts can play a large role in the

catalysis outcome, even if both active sites are identical as is the case in Pd@IRMOF-3 compared to Pd on IRMOF-3.

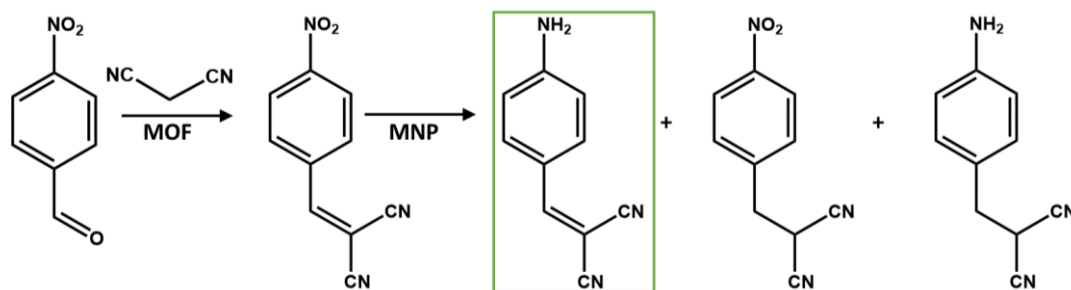


Figure 1.8 Knoevenagel condensation and subsequent hydrogenation tandem reaction. The condensation reaction is catalysed by the  $-NH_2$  of the IRMOF-3 shell and the subsequent hydrogenation is performed by the Pd MNPs core. The desired product is outlined in green.

## 1.5 Metal-Organic Coordination Networks

Metal-organic coordination networks (MOCNs) provide molecular control towards novel supramolecular arrays on surfaces. The rational design of depositing metals and organic molecules on surfaces allows for strategic design of pore size<sup>56</sup> and MOCN functionality<sup>57</sup>. Although not a prerequisite to MOCN formation, much of the field performs synthesis and observation experiments in ultra-high vacuum (UHV). This is mainly to preserve the cleanliness of the surface, thus allowing only the desired molecules to interact upon deposition. Additionally, UHV conditions are necessary for some characterisation techniques to allow electrons to travel without contaminant collision from sample to detector.

### 1.5.1 Model MOFs

Metal organic coordination networks can be viewed as similar systems to the three-dimensional MOFs. The synthesis of MOCNs by rational design has been shown, and although the surface formation of MOCNs is different from solution formation of MOFs, there are many similarities between the two systems.<sup>58</sup> In a study by Stepanow *et al.* carboxylate linkers were used in conjunction with Fe metal nodes to form nanoporous networks on Cu(100) which allowed for host-guest interactions.<sup>59</sup> Three linkers were used: terephthalic acid, trimellitic acid and *p*-terphenyldicarboxylic acid. In each case a MOCN was obtained. Upon formation of the Fe-carboxylate MOCN the

surface was dosed with C<sub>60</sub> (buckminsterfullerenes). In each case the C<sub>60</sub> molecule was adsorbed in the nanopore of the MOCN, and probed for the dominating host-guest interaction. In the case of the functionalised terephthalic acid (trimellitic acid) the C<sub>60</sub> was interacting most with the functionalised moiety. This shows similarities to MOFs when using functionalised linkers to add different qualities into the system, as in the case of linker functionalisation in MIL-101 for enhanced H<sub>2</sub> adsorption.<sup>60</sup>

In a publication by Decker *et al.* MOCNs were used to steer the growth of Co and Fe nanoclusters.<sup>61</sup> In this work, dicyanitrile-oligophenyl linkers, containing 3 to 5 phenyl rings, were used as the linker and Co atoms served as the metal node on Ag(111). Upon formation of the honeycomb network, Fe or Co atoms were dosed onto the surface. It was determined that depending on number of phenyl rings, the Fe or Co nanoclusters decorated the MOCN template in different locations. In all cases, the Fe or Co only interacted with the metal-organic framework, leaving the large hexagonal shaped pores empty. This shows control of guest molecules (metal nanoclusters) can be tuned by changing the properties of the MOCN such as linker length.

### 1.5.2 Pressure Gap and Materials Gap<sup>3</sup>

As previously mentioned, many of the MOCN or other surface science studies are performed under UHV conditions. This is a long-standing challenge within the field because the pressure between catalytically active systems operating at normal catalytic conditions and the performed UHV studies differs by several orders magnitude. It is difficult to determine if the adsorbate species observed in single crystal UHV studies elucidate the mechanisms of reactions performed with similar materials at high pressure catalysis conditions. However, finding trends in surface science and bridging the gap to real catalysis conditions has led to better performing and smarter design of catalysts.

Additionally, the discrepancy between studies on single crystal materials which give insight into mechanisms of bulk materials is known as the materials gap. The study of a relevant catalyst and its surface science analogue can elucidate many key aspects of the catalytic process, but the ideality of the system may not show all the nuances of the actual catalyst.

The combination of both surface science experiments with catalytic testing has proven to be a way to both understand the factors that play a role in catalytic selectivity and activity which leads to the development of better materials for catalysis.

## 1.6 Project Scope

Multifunctional materials can act as catalysts which can perform multiple steps in tandem. This can greatly reduce operating costs in multi-step synthesis procedures because the separation and purification intermediate steps can be eliminated. This thesis will focus on the strategic design of multifunctional catalysts consisting of metal nanoparticles within metal-organic frameworks and their applications in tandem one-pot catalysis. A probe reaction which combines the necessity for a Lewis acid catalyst (MOF) as well as a reductive catalyst (MNP) will be used to determine the bifunctionality of the prepared materials. The activity and stability in catalysis for each catalyst preparation route will be examined for progress and optimisation towards a better multifunctional catalyst. The thesis is divided into five chapters of research topics on different aspects of developing multifunctional catalysts:

- Chapter 3 will focus on the top-down approach of depositing metal salts into porous MOFs and the formation of the nanoparticles upon reduction.
- Chapter 4 will discuss the applications of these materials in multi-step catalysis. The optimisation of the reaction will be discussed, as well as strategies to enhance stability and activity of these catalysts.
- Chapter 5 will concentrate on the first bottom-up approach of growing MOFs on silica spheres and the difficulties of surface charge and synthetic procedures of these materials.
- Chapter 6 will discuss another strategic bottom-up approach of growing MOFs on colloidal metal nanoparticles.
- Chapter 7 will focus on growing monolayer MOFs on single crystal metal surfaces. This model approach gives insight at the molecular level which is otherwise hard to achieve with bulk materials.

## 1.7 References

1. Bowker, M., *The Basis and Applications of Heterogeneous Catalysis*. 1998.
2. Augustine, R. L., *Heterogeneous Catalysis for the Synthetic Chemist*. Marcel Dekker, Inc.: 1996.
3. Park, J. Y.; Somorjai, G. A., *Current Trends of Surface Science and Catalysis: Bridging Materials and Pressure Gaps in Surface Science and Heterogeneous Catalysis*. Springer: 2014; Vol. 1.
4. Tanabe, K.; Hölderich, W. F., Industrial Application of Solid Acid-Base Catalysts. *Appl. Catal., A* **1999**, *181*, 399-434.
5. Chui, S. S.-Y.; Lo, S. M.-F.; Charmant, J. P. H.; Orpen, A. G.; Williams, I. D., A Chemically Functionalizable nanoporous Material  $[\text{Cu}_3(\text{TMA})_2(\text{H}_2\text{O})_3]_n$ . *Science* **1999**, *283*, 1148-1150.
6. Schlichte, K.; Kratzke, T.; Kaskel, S., Improved Synthesis, Thermal Stability and Catalytic Properties of the Metal-Organic Framework Compound  $\text{Cu}_3(\text{BTC})_2$  improved Synthesis, Thermal Stability and Catalytic Properties of the Metal-Organic Framework Compound  $\text{Cu}_3(\text{BTC})_2$  *Micropor. Mesopor. Mater.* **2004**, *73*, 81-88.
7. Alaerts, L.; Séguin, E.; Poelman, H.; Thibault-Starzyk, F.; Jacobs, P. A.; de Vos, D. E., Probing the Lewis Acidity and Catalytic Activity of the Metal-Organic Framework  $[\text{Cu}_3(\text{Btc})_2]$  (BTC=Benzen-1,3,5-Tricarboxylate) Probing the Lewis Acidity and Catalytic Activity of the Metal-Organic Framework  $[\text{Cu}_3(\text{Btc})_2]$  (BTC=Benzen-1,3,5-Tricarboxylate). *Chem. Eur. J.* **2006**, *12*, 7353-7363.
8. Mitchell, L.; Gonzalez-Santiago, B.; Mowat, J. P. S.; Gunn, M. E.; Williamson, P.; Acerbi, N.; Clarke, M. L.; Wright, P. A., Remarkable Lewis Acid Catalytic Performance of the Scandium Trimesate Metal Organic Framework MIL-100(Sc) for C–C and C=N Bond-Forming Reactions. *Catal. Sci. Tech.* **2013**, *3*, 606-617.
9. Bordiga, S.; Regli, L.; Bonino, F.; Groppo, E.; Lamberti, C.; Xiao, B.; Wheatley, P. S.; R.E., M.; Zecchina, A., Adsorption Properties of HKUST-1 toward Hydrogen and Other Small Molecules Monitored by IR. *Phys. Chem. Chem. Phys.* **2007**, *9*, 2676-2685.
10. Hendon, C. H.; Walsh, A., Chemical Principles Underpinning the Performance of the Metal-Organic Framework HKUST-1. *Chem. Sci.* **2015**, *6*, 3674-3683.
11. Cavka, J. H.; Jakobsen, S.; Olsbye, U.; Guillou, N.; Lamberti, C.; Bordiga, S.; Lillerud, K. P., A New Zirconium Inorganic Building Brick Forming Metal Organic Frameworks with Exceptional Stability *J. Am. Chem. Soc.* **2008**, *130*, 13850-13851.
12. Wu, H.; Chua, Y. S.; Krungleviciute, V.; Tyagi, M.; Chen, P.; Yildirim, T.; Zhou, W., Unusual and Highly Tunable Missing-Linker Defects in Zirconium Metal-Organic Framework UiO-66 and Their Important Effects on Gas Adsorption. *J. Am. Chem. Soc.* **2013**, *135*, 10525-10532.
13. Ling, S.; Slater, B., Dynamic Acidity in Defective UiO-66. *Chem. Sci.* **2016**, *7*, 4706-4712.
14. Vermoortele, F.; Bueken, B.; Le Bars, G.; Van de Voorde, B.; Vandichel, M.; Houthoofd, K.; Vimont, A.; Daturi, M.; Waroquier, M.; Van Speybroeck, V.; Kirschhock, C.; De Vos, D. E., Synthesis Modulation as a Tool to Increase the Catalytic Activity of Metal–Organic Frameworks: The Unique Case of UiO-66(Zr). *J. Am. Chem. Soc.* **2013**, *135*, 11465-11468.

15. Shearer, G. C.; Chavan, S.; Bordiga, S.; Svelle, S.; Olsbye, U.; Lillerud, K. P., Defect Engineering: Tuning the Porosity and Composition of the Metal-Organic Framework UiO-66 via Modulated Synthesis. *Chem. Mater.* **2016**, *28*, 3749-3761.
16. Vermoortele, F.; Vandichel, M.; van de Voorde, B.; Ameloot, R.; Waroquier, M.; van Speybroeck, V.; De Vos, D. E., Electronic Effects of Linker Substitution on Lewis Acid Catalysis with Metal-Organic Frameworks. *Angewandte Chemie* **2012**, *51*, 4887-4890.
17. Férey, G.; Mellot-Draznieks, C.; Serre, C.; Millange, F.; Dutour, J.; Surblé, S.; Margiolaki, I., A Chromium Terephthalate-Based Solid with Unusually Large Pore Volumes and Surface Area. *Science* **2005**, *309*, 2040-2042.
18. Férey, G.; Mellot-Draznieks, C.; Serre, C.; Millange, F., Crystallized Frameworks with Giant Pores: Are There Limits to the Possible? *Acc. Chem. Res.* **2005**, *38*, 217-225.
19. Dhakshinamoorthy, A.; Alvaro, M.; Garcia, H., Claisen-Schmidt Condensation Catalyzed by Metal-Organic Frameworks. *Adv. Synth. Catal.* **2010**, *352*, 711-717.
20. Bromberg, L.; Diao, Y.; Wu, H.; Speakman, S. A.; Hatton, T. A., Chromium(III) Terephthalate Metal Organic Framework (MIL-101): HF-Free Synthesis, Structure, Polyoxometalate Composites, and Catalytic Properties. *Chem. Mater.* **2012**, *24*, 1664-1675.
21. Canoni, R.; Roch-Marchal, C.; Sécheresse, F.; Horcajada, P.; Serre, C.; Hardi-Dan, M.; Férey, G.; Grenèche, J.-M.; Lefebvre, F.; Chang, J.-S.; Hwang, Y.-K.; Lebedev, O.; Turner, S.; Van Tendeloo, G., Stable Polyoxometalate Insertion within the Mesoporous Metal Organic Framework MIL-100(Fe). *J. Mater. Chem.* **2011**, *21*, 1226.
22. Juan-Alcañiz, J.; Ramos-Fernandez, E. V.; Lafont, U.; Gascon, J.; Kapteijn, F., Building MOF Bottles around Phosphotungstic Acid Ships: One-Pot Synthesis of Bi-Functional Polyoxometalate-MIL-101 Catalysts. *J. Catal.* **2010**, *269*, 229-241.
23. Salomon, W.; Yazigi, F. J.; Roch-Marchal, C.; Mialane, P.; Horcajada, P.; Serre, C.; Haouas, M.; Taulelle, F.; Dolbecq, A., Immobilization of Co-Containing Polyoxometalates in MIL-101(Cr): Structural Integrity Versus Chemical Transformation. *Dalton Trans.* **2014**, *43*, 12698-12705.
24. Meilikhov, M.; Yusenko, K.; Esken, D.; Turner, S.; van Tendeloo, G.; Fischer, R. A., Metals@MOFs - Loading MOFs with Metal Nanoparticles for Hybrid Functions. *Eur. J. Inorg. Chem.* **2010**, *2010*, 3701-3714.
25. Ishida, T.; Nagaoka, M.; Akita, T.; Haruta, M., Deposition of Gold Clusters on Porous Coordination Polymers by Solid Grinding and Their Catalytic Activity in Aerobic Oxidation of Alcohols. *Chem. Eur. J.* **2008**, *14*, 8456-8460.
26. Zlotea, C.; Campesi, R.; Cuevas, F.; Leroy, E.; Dibandjo, P.; Volkringer, C.; Loiseau, T.; Férey, G.; Latroche, M., Pd Nanoparticles Embedded into a Metal-Organic Framework: Synthesis, Structural Characteristics, and Hydrogen Sorption Properties. *J. Am. Chem. Soc.* **2010**, *132*, 2991-2997.
27. El-Shall, M. S.; Abdelsayed, V.; Khder, A. E. R. S.; Hassan, H. M. A.; El-Kaderi, H. M.; Reich, T. E., Metallic and Bimetallic Nanocatalysts Incorporated into Highly Porous Coordination Polymer MIL-101. *J. Mater. Chem.* **2009**, *19*, 7625-7631.
28. Aijaz, A.; Karkamkar, A.; Choi, Y. J.; Tsumori, N.; Ronnebro, E.; Autrey, T.; Shioyama, H.; Xu, Q., Immobilizing Highly Catalytically Active Pt Nanoparticles inside

the Pores of Metal-Organic Framework: A Double Solvents Approach. *J. Am. Chem. Soc.* **2012**, *134*, 13926-9.

29. Zhu, Q. L.; Li, J.; Xu, Q., Immobilizing Metal Nanoparticles to Metal-Organic Frameworks with Size and Location Control for Optimizing Catalytic Performance. *J. Am. Chem. Soc.* **2013**, *135*, 10210-10213.

30. Chen, Y.-Z.; Zhou, Y.-X.; Wang, H.; Lu, J.; Uchida, T.; Xu, Q.; Yu, S.-H.; Jiang, H.-L., Multifunctional PdAg@MIL-101 for One-Pot Cascade Reactions: Combination of Host-Guest Cooperation and Bimetallic Synergy in Catalysis. *ACS Catal.* **2015**, *5*, 2062-2069.

31. Zhang, T.; Li, B.; Zhang, X.; Qiu, J.; Han, W.; Yeung, K. L., Pd Nanoparticles Immobilized in a Microporous/Mesoporous Composite ZIF-8/MSS: A Multifunctional Catalyst for the Hydrogenation of Alkenes. *Micropor. Mesopor. Mater.* **2014**, *197*, 324-330.

32. Jiang, H.; Yan, Q.; Chen, R.; Xing, W., Synthesis of Pd@ZIF-8 via an Assembly Method: Influence of the Molar Ratios of Pd/Zn<sup>2+</sup> and 2-Methylimidazole/Zn<sup>2+</sup>. *Micropor. Mesopor. Mater.* **2016**, *225*, 33-40.

33. Liao, J.; Wang, D.; Liu, A.; Hu, Y.; Li, G., Controlled Stepwise-Synthesis of Core-Shell Au@MIL-100(Fe) Nanoparticles for Sensitive Surface-Enhanced Raman Scattering Detection. *Analyst* **2015**, *140*, 8165-8171.

34. Na, K.; Choi, K. M.; Yaghi, O. M.; Somorjai, G. A., Metal Nanocrystals Embedded in Single Nanocrystals of MOFs Give Unusual Selectivity as Heterogeneous Catalysts. *Nano Lett.* **2014**, *14*, 5979-5983.

35. Tao, A. R.; Habas, S.; Yang, P., Shape Control of Colloidal Metal Nanocrystals. *Small* **2008**, *4*, 310-325.

36. Song, H.; Kim, F.; Connor, S.; Somorjai, G. A.; Yang, P., Pt Nanocrystals: Shape Control and Langmuir-Blodgett Monolayer Formation. *J. Phys. Chem. B* **2005**, *109*, 188-193.

37. Alayoglu, S.; Aliaga, C.; Sprung, C.; Somorjai, G. A., Size and Shape Dependence on Pt Nanoparticles for the Methylcyclopentane/Hydrogen Ring Opening/Ring Enlargement Reaction. *Catal. Lett.* **2011**, *141*, 914-924.

38. Aguado, S.; El-Jamal, S.; Meunier, F.; Canivet, J.; Farrusseng, D., A Pt/Al<sub>2</sub>O<sub>3</sub>-Supported Metal-Organic Framework Film as the Size-Selective Core-Shell Hydrogenation Catalyst. *Chem. Commun.* **2016**, *52*, 7161-7163.

39. Xue, S.; Jiang, H.; Zhong, Z.; Low, Z.-X.; Chen, R.; Xing, W., Palladium Nanoparticles Supported on a Two-Dimensional Layered Zeolitic Imidazolate Framework-L as an Efficient Size-Selective Catalyst. *Micropor. Mesopor. Mater.* **2016**, *221*, 220-227.

40. Zhang, W.; Lu, G.; Cui, C.; Liu, Y.; Li, S.; Yan, W.; Xing, C.; Chi, Y. R.; Yang, Y.; Huo, F., A Family of Metal-Organic Frameworks Exhibiting Size-Selective Catalysis with Encapsulated Noble-Metal Nanoparticles. *Adv. Mater.* **2014**, *26*, 4056-4060.

41. Zhang, W.; Lu, G.; Li, S.; Liu, Y.; Xu, H.; Cui, C.; Yan, W.; Yang, Y.; Huo, F., Controlled Incorporation of Nanoparticles in Metal-Organic Framework Hybrid Thin Films. *Chem. Commun.* **2014**, *50*, 4296-4298.

42. Wang, P.; Zhao, J.; Li, X.; Yang, Y.; Yang, Q.; Li, C., Assembly of ZIF Nanostructures around Free Pt Nanoparticles: Efficient Size-Selective Catalysts for Hydrogenation of Alkenes under Mild Conditions. *Chem. Commun.* **2013**, *49*, 3330-3332.
43. Yang, Y.; Wang, F.; Yang, Q.; Hu, Y.; Yan, H.; Chen, Y.-Z.; Liu, H.; Zhang, G.; Lu, J.; Jiang, H.-L.; Xu, H., Hollow Metal-Organic Framework Nanospheres via Emulsion-Based Interfacial Synthesis and Their Application in Size-Selective Catalysis. *ACS Appl. Mater. Interfaces* **2014**, *6*, 18163-18171.
44. Rösler, C.; Dissegna, S.; Rechac, V. L.; Kauer, M.; Guo, P.; Turner, S.; Ollegott, K.; Kobayashi, H.; Yamamoto, T.; Peeters, D.; Wang, Y.; Matsumura, S.; Van Tendeloo, G.; Kitagawa, H.; Muhler, M.; Llabrés i Xamena, F. X.; Fischer, R. A., Encapsulation of Bimetallic Metal Nanoparticles into Robust Zr-Based Metal-Organic Frameworks: Evaluation of the Catalytic Potential for Size-Selective Hydrogenation. *Chem. Eur. J.* **2016**.
45. Aijaz, A.; Zhu, Q.-L.; Tsumori, N.; Akita, T.; Xu, Q., Surfactant-Free Pd Nanoparticles Immobilized to a Metal-Organic Framework with Size- and Location-Dependent Catalytic Selectivity. *Chem. Commun.* **2015**, *51*, 2577-2580.
46. Chen, J.; Liu, R.; Guo, Y.; Chen, L.; Gao, H., Selective Hydrogenation of Biomass-Based 5-Hydroxymethylfurfural over Catalyst of Palladium Immobilized on Amine-Functionalized Metal-Organic Frameworks. *ACS Catal.* **2015**, *5*, 722-733.
47. Liu, H.; Li, Y.; Jiang, H.; Vargas, C.; Luque, R., Significant Promoting Effects of Lewis Acidity on Au-Pd Systems in the Selective Oxidation of Aromatic Hydrocarbons. *Chem. Commun.* **2012**, *48*, 8431-8433.
48. Liu, H.; Liu, Y.; Li, Y.; Tang, Z.; Jiang, H., Metal-Organic Framework Supported Gold Nanoparticles as a Highly Active Heterogeneous Catalyst for Aerobic Oxidations of Alcohols. *J. Phys. Chem. C* **2010**, *114*, 13362-13369.
49. Cirujano, F. G.; Leyva-Pérez, A.; Corma, A.; Llabrés i Xamena, F. X., MOFs as Multifunctional Catalysts: Synthesis of Secondary Arylamines, Quinolines, Pyrroles, and Arylpyrrolidines over Bifunctional MIL-101. *ChemCatChem* **2013**, *5*, 538-549.
50. Cirujano, F. G.; Llabrés i Xamena, F. X.; Corma, A., MOFs as Multifunctional Catalysts: One-Pot Synthesis of Menthol from Citronellal over a Bifunctional MIL-101 Catalyst. *Dalton Trans.* **2012**, *41*, 4249-4254.
51. Pan, Y.; Yuan, B.; Li, Y.; He, D., Multifunctional Catalysis by Pd@MIL-101: One-Step Synthesis of Methyl Isobutyl Ketone over Palladium Nanoparticles Deposited on a Metal-Organic Framework. *Chem. Commun.* **2010**, *46*, 2280-2282.
52. Li, X.; Guo, Z.; Xiao, C.; Goh, T. W.; Tesfagaber, D.; Huang, W., Tandem Catalysis by Palladium Nanoclusters Encapsulated in Metal-Organic Frameworks. *ACS Catal.* **2014**, *4*, 3490-3497.
53. Zhao, M.; Deng, K.; He, L.; Liu, Y.; Li, G.; Zhao, H.; Tang, Z., Core-Shell Palladium Nanoparticle@Metal-Organic Frameworks as Multifunctional Catalysts for Cascade Reactions. *J. Am. Chem. Soc.* **2014**, *136*, 1738-1741.
54. Wang, X.; Li, M.; Cao, C.; Liu, C.; Liu, J.; Zhu, Y.; Zhang, S.; Song, W., Surfactant-Free Palladium Nanoparticles Encapsulated in ZIF-8 Hollow Nanospheres for Size-Selective Catalysis in Liquid-Phase Solution. *ChemCatChem* **2016**, *8*, 3224-3228.

55. Ke, F.; Zhu, J.; Qiu, L. G.; Jiang, X., Controlled Synthesis of Novel Au@MIL-100(Fe) Core-Shell Nanoparticles with Enhanced Catalytic Performance. *Chem. Commun.* **2013**, *49*, 1267-1269.
56. Schlickum, U.; Decker, R.; Klappenberger, F.; Zopellaro, G.; Klyatskaya, S.; Ruben, M.; Silanes, I.; Arnau, A.; Kern, K.; Brune, H.; Barth, J. V., Metal-Organic Honeycomb Nanomeshes with Tunable Cavity Size. *Nano Lett.* **2007**, *7*, 3813-3817.
57. Grumelli, D.; Wurster, B.; Stepanow, S.; Kern, K., Bio-Inspired Nanocatalysts for the Oxygen Reduction Reaction. *Nat. Commun.* **2013**, *4*, 2904.
58. Shi, Z.; Lin, N., Structural and Chemical Control in Assembly of Multicomponent Metal-Organic Coordination Networks on a Surface. *J. Am. Chem. Soc.* **2010**, *132*, 10756-10761.
59. Stepanow, S.; Lingenfelder, M.; Dmitriev, A.; Spillmann, H.; Delvigne, E.; Lin, N.; Deng, X.; Cai, C.; Barth, J. V.; Kern, K., Steering Molecular Organization and Host-Guest Interactions Using Two-Dimensional Nanoporous Coordination Systems. *Nature materials* **2004**, *3*, 229-233.
60. Szilágyi, P. Á.; Weinrauch, I.; Oh, H.; Hirscher, M.; Juan-Alcañiz, J.; Serra-Crespo, P.; de Respinis, M.; Trzeźniewski, B. J.; Kapteijn, F.; Geerlings, H.; Gascon, J.; Dam, B.; Grzech, A.; van de Krol, R.; Geerlings, H., Interplay of Linker Functionalization and Hydrogen Adsorption in the Metal–Organic Framework MIL-101. *J. Phys. Chem. C* **2014**, *118*, 19572-19579.
61. Decker, R.; Schlickum, U.; Klappenberger, F.; Zopellaro, G.; Klyatskaya, S.; Ruben, M.; Barth, J. V.; Brune, H., Using Metal-Organic Templates to Steer the Growth of Fe and Co Nanoclusters. *Appl. Phys. Lett.* **2008**, *93*, 243102.

# Chapter 2

---

## Characterisation Techniques

## 2.1 Introduction

Multiple characterisation techniques were used towards the synthesis of robust, active and selective catalysts consisting of metal nanoparticles within Lewis acidic metal organic frameworks. The use of multiple techniques for a single material gives insight into the structure, porosity, size and composition of these catalysts. The various techniques utilized to characterise these materials are described in section 2.2.

The techniques used in the investigation and characterisation of molecular assemblies of metal organic coordination networks on single crystal gold surfaces are discussed in section 2.3.

## 2.2 Characterisation Techniques: Immobilised Nanoparticles in MOF

The theory behind the characterisation techniques used to develop and characterise the materials discussed in Chapters 3, 4, 5 and 6 are discussed in this sub chapter. A combination of multiple complementary techniques allows for a better overall understanding of the material characteristics.

### 2.2.1 Powder X-ray Diffraction

X-ray diffraction (XRD) is a widely available technique used to elucidate crystal structures and determine particle sizes. Moreover, it can be used to identify known crystalline phases and determine unit cells. In this work XRD was used exclusively for pattern matching. Materials of known crystal phases were synthesized and their phase was determined to be that desired (or not) based on comparing previously published and databased XRD patterns with the synthesised material patterns.

Crystalline materials possess a 3-dimensional order of atoms, and their unit cell is the smallest repeating unit. In this technique, X-rays of a well-defined wavelength, commonly Cu  $K\alpha_1$  at 1.5406 Å, are passed through a sample. The X-ray waves interfere both constructively and destructively while passing through the sample. These interferences lead to a diffraction pattern, which is highly material specific. For known materials, diffraction patterns can be found in large databases like the International Centre for Diffraction Data (ICDD) or the Cambridge Structural Database (CSD).

Bragg's Law is used to find the spacing between planes of a crystalline material and dictates the diffraction pattern for any given material. Figure 2.1 shows X-rays diffracting from a sample. The difference in path length between the two waves is an integral number of wavelengths. The d-spacing can be calculated by knowing the angle of incidence ( $\theta$ ) and the X-ray wavelength ( $\lambda$ ) as shown by equations 2.1 and 2.2.

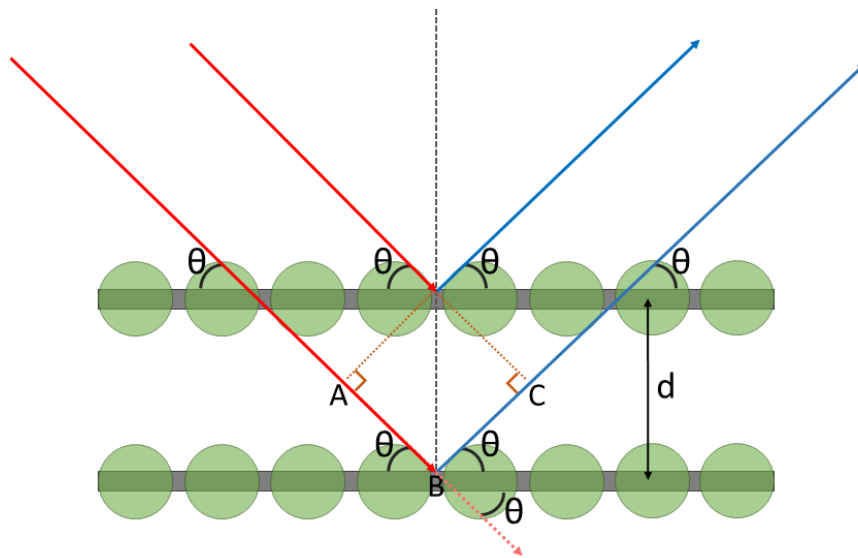


Figure 2.1 Bragg's Law diagram showing the incoming (red) and diffracting X-rays (blue) from planes of atoms (grey).  $\theta$  is one half of the scattering angle  $2\theta$ .

$$AB+BC=2d \sin \theta \quad 2.1$$

$$n\lambda=2d \sin \theta \quad 2.2$$

By loading a powder sample, which has randomly distributed crystal orientations, the X-rays that pass through the sample will show peaks corresponding to all lattice plane d-spacings of symmetry-allowed reflections. Because there is a statistically infinite number of orientations within a non-preferentially oriented crystalline powder, the X-ray will interact with all the planes within a sample. Within this work there are two geometrical setups used to collect the diffraction patterns, shown in Figure 2.2. Transmission mode and reflection mode provide similar data; however, less sample is required for transmission mode because the sample holder is a thin capillary rather than a large disc. In transmission mode the capillary is spun in order to increase the signal to noise ratio of the diffractogram and remove issues of preferred orientation.

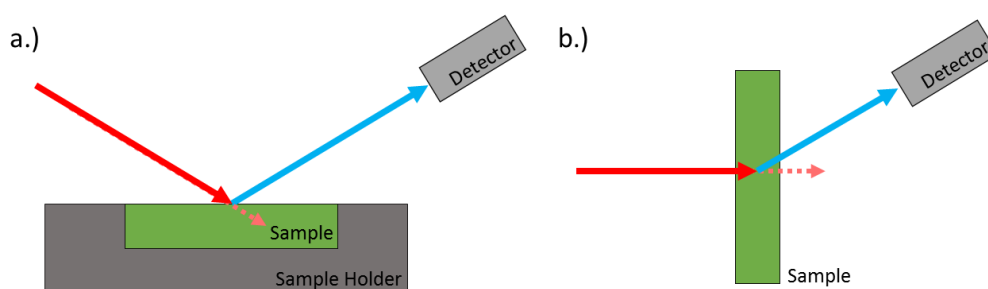


Figure 2.2 The two Powder XRD geometries used in this thesis. a.) reflection mode and b.) transmission mode.

### 2.2.2 Nitrogen Adsorption<sup>1-5</sup>

Gas adsorption measurements can be used to determine pore volume, surface area, pore size distribution, pore geometry and connectivity of pores in solid samples. These parameters are important for developing catalysts because highly porous materials are sought after for their large surface areas and low diffusion limitations.

In a gas adsorption isotherm, the amount of gas adsorbed is plotted against the relative pressure of the gas at a fixed temperature. In this thesis, nitrogen adsorption isotherms performed at 77 K will be presented. Traditionally six types of isotherms are defined by IUPAC<sup>1</sup>, shown in Figure 2.3, however many materials do not fit into just one defined isotherm type.

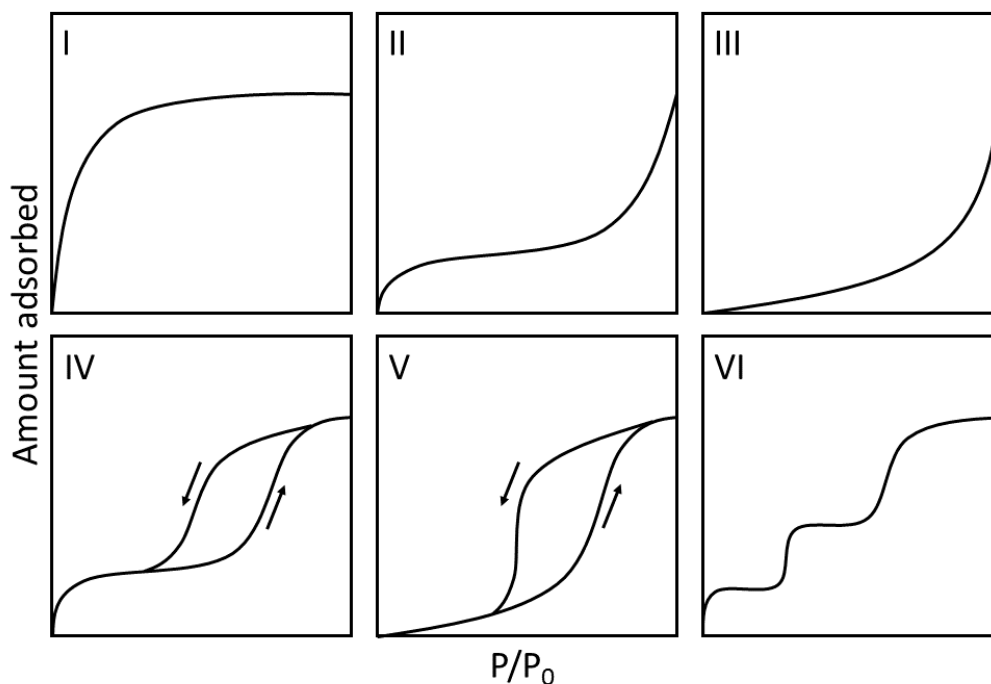


Figure 2.3 The six types of adsorption isotherms defined by IUPAC.

Type I isotherms are typical of microporous (pores less than 2 nm) materials, and clearly show the filling of the pores eventually reaching a maximum adsorption value. Type II and III isotherms are typical of nonporous materials and weak adsorbate-adsorbent interactions respectively. Type IV and V isotherms are commonly seen for mesoporous (pore size between 2 nm and 50 nm) materials, the latter showing weak adsorbate-adsorbent interactions. Type VI shows a multi-step adsorption isotherm, indicating several different pore filling events. The obvious characteristic seen in type IV isotherms of mesoporous materials is a hysteresis loop appearing at  $P/P_0 > 0.4$ . This hysteresis loop appears due to capillary condensation in the pores, causing a large difference in adsorption and desorption of the adsorbent within the mesopores. Further analysis of this hysteresis can elucidate information on the pore shape. However, for most mesoporous MOFs, this hysteresis is not seen because the pore size is less than that at which the hysteresis occurs in  $N_2$  isotherms at 77 K. A typical nitrogen adsorption isotherm for the mesoporous MOF MIL-101(Cr) prepared in this thesis is shown in Figure 2.4.

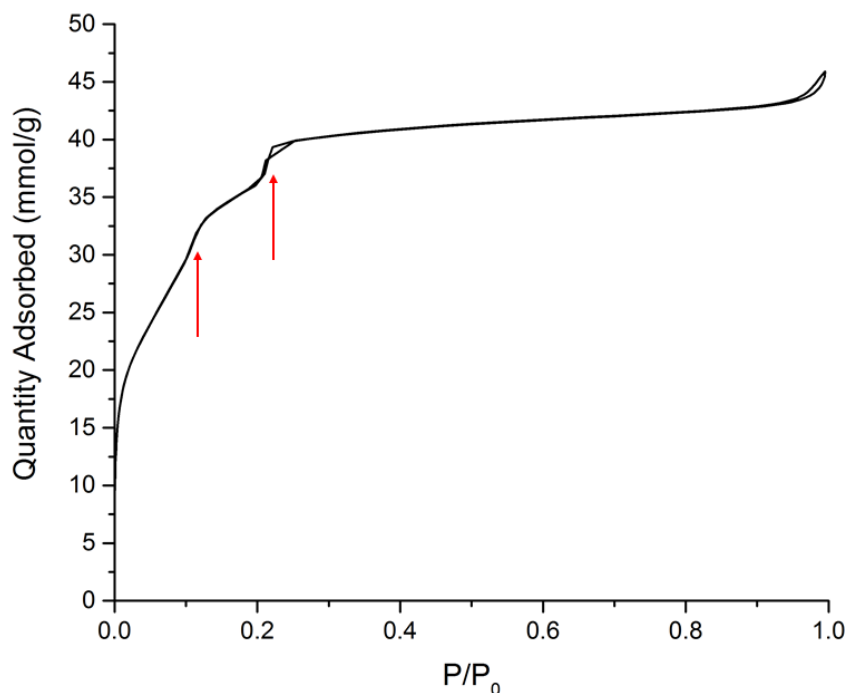


Figure 2.4 MIL-101(Cr) N<sub>2</sub> adsorption at 77 K. The red arrows indicate the filling of the small and large cages.

There are two significant inflection points which show the small (2.9 nm) cages filling ( $P/P_0 \approx 0.15$ ) and the large (3.4 nm) cages filling ( $P/P_0 \approx 0.25$ ). The slope of the isotherm minimises at the point of maximum adsorption; around 42 mmol g<sup>-1</sup> in Figure 2.4. The small increase in adsorption (and hysteresis in desorption) around  $P/P_0 \approx 1$  is due to the overall MOF crystal shape, causing macroporous (pores larger than 50 nm) voids in between the crystals when packed in the tube. Because of this it can be ignored with respect to the MOF pore adsorption. This maximum quantity of gas adsorbed is directly related to the pore volume ( $V_{\text{pore}}$ ) of the sample, given by Equation 2.3, which is extremely important to the double solvents nanoparticle deposition method described in Chapters 3 and 4.  $A_m$  is the maximum quantity adsorbed, read from the plot,  $M_{\text{N}_2}$  is the molar weight of nitrogen and  $\rho_{\text{N}_2}$  is the density of liquid nitrogen at 77 K. For MIL-101(Cr) the pore volume calculates to 1.45 cm<sup>3</sup> g<sup>-1</sup>.

$$V_{\text{pore}} = (A_m * M_{\text{N}_2}) / (1000 * \rho_{\text{N}_2}) \quad 2.3$$

The Brunauer, Emmett and Teller (BET) theory is commonly used to determine surface area of materials. The theory was developed to explain the type II isotherm obtained from physisorbing molecules on a flat surface. This theory gives the surface area of a material based on the amount of gas, commonly N<sub>2</sub>, that physisorbs in a multilayer to the surface as the adsorbate pressure increases. The theory assumes that the layer at the interface with the vapour and the vapour are in dynamic equilibrium with each other. This means that in a system where there is exactly one monolayer of adsorbate on the material surface, it is in dynamic equilibrium with the adsorbate vapour phase. In practice there is no specific pressure for an adsorbate at which an exact monolayer forms, but the BET theory can be useful in predicting the number of molecules necessary for an exact monolayer. With this prediction the surface area can be determined on an area per mass basis. BET analysis is useful for non-porous and mesoporous materials quantitatively, and useful qualitatively for microporous materials. In the case of mesoporous materials like MIL-101(Cr), the BET calculation is performed in the P/P<sub>0</sub> range before the first inflection point (0.05 to 0.15).

### 2.2.3 Transmission Electron Microscopy<sup>6-7</sup>

Transmission electron microscopy (TEM) was developed because of the need to view objects smaller than is possible using visible-light microscopy. A high intensity electron beam, 200 kV in this work, penetrates and passes through a very thin sample in order to view the sample on a nano-scale. When using photons, as in visible-light microscopy, the smallest object that can be observed is approximately found using the Rayleigh equation, seen in equation 2.4.

$$\delta = \frac{0.61\lambda}{\mu \sin \beta} \quad 2.4$$

In this equation,  $\delta$  is the smallest distance that can be resolved,  $\lambda$  is the wavelength of light,  $\mu$  is the refractive index of the medium and  $\beta$  is the semi-angle of reflection. If the denominator is approximated as 1 and a wavelength of light in the middle of the visible-light spectrum, 550 nm, is used it is found that the best resolution achieved is around 335 nm. While this is good for some applications, the nanoparticles

synthesised in this thesis range between 2-11 nm; much too small to view with visible-light microscopy.

When using electrons instead of photons the resolution achieved is much better. Using the de Broglie equation, seen in equation 2.5, we can calculate for an electron source (E, in eV) of 100 keV the wavelength ( $\lambda$ , in nm) would be around 4 pm.

$$\lambda \sim \frac{1.22}{E^{0.5}} \quad 2.5$$

Using this wavelength in the Rayleigh equation gives a resolution of approximately 0.002 nm. This is definitely small enough to view samples on an atomic level, but is only a theoretical resolution because lens distortions in the TEM cause a reduced overall resolution. The Jeol JEM-2011 TEM used in this thesis has a maximum resolution of 0.18 nm.

Figure 2.5 shows a representative diagram of a TEM. The electron gun is commonly made of either a tungsten filament, a LaB<sub>6</sub> crystal, or a field emission gun. In this work a LaB<sub>6</sub> crystal was used for its ability to operate at a much lower temperature due to its smaller work function when compared to a tungsten filament.<sup>8</sup> A series of electromagnetic lenses, called condenser lenses, direct the electron beam towards the sample. For this work the samples are ground with acetone and dispersed on a 3 mm holey carbon grid on Cu. The transmitted electrons have been scattered due to their interaction with the sample. The transmitted electron beam is focussed by the objective lenses to form an image. Next, the beam passes through projector lenses which control the magnification in order to create an image on the screen that gives structural information. The current passing through the projector lenses can be changed to view either a diffraction pattern or an image. The screen to view the image is phosphorescent and gives off photons when excited with electrons. The screen can best be viewed using the viewing chamber. Putting the screen up (indicated by the dashed lines) allows the beam to hit a CCD camera in order to collect the image.

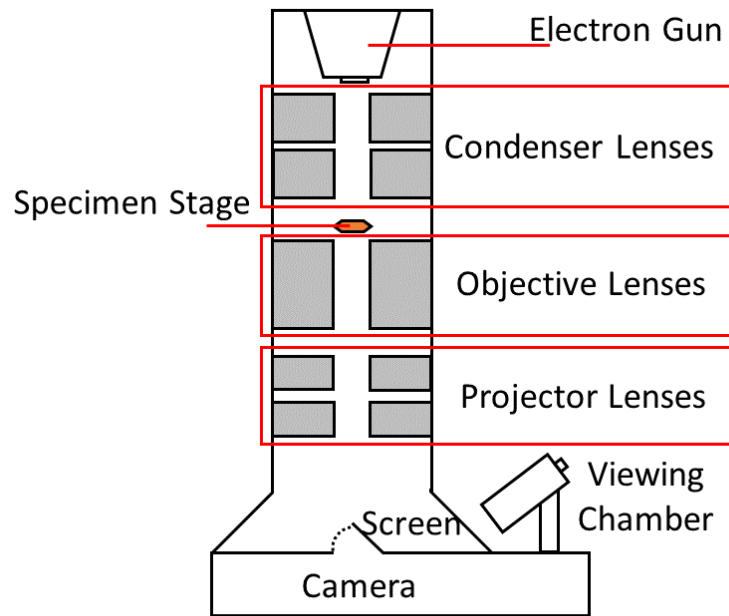


Figure 2.5 Schematic of a TEM which shows the lenses that the electron beam is conditioned by before and after interacting with the sample on the specimen stage.<sup>8</sup>

As previously mentioned, the electromagnetic lenses cause distortions within the images and lead to reduced resolution. The distortions caused by imperfections in the electromagnetic lenses can be categorised into 4 groups: spherical aberrations, chromatic aberrations, image distortions and astigmatism. In practice, given that the sample is thin enough that the chromatic aberrations are negligible, spherical aberration presents the main limitation to the resolution achieved in TEM. This occurs due to the electrons refracting differently at the edges of the lens compared to the centre. As a result, the beams do not coalesce into a single point. More advanced lenses have been developed to help remove spherical aberrations which reduce the number of electrons refracting at the edges, thus allowing the beam to recombine to a single point. However, in this work a spherical aberration corrector was not used, and instead some spherical aberration was corrected by under focusing the objective lens slightly, allowing for a different viewing plane.

Image contrast in TEM can be obtained by several mechanisms depending on the imaging mode used. In this work bright field imaging mode was used exclusively. This mode shows thicker or higher atomic number areas as darker. This is because the

interaction between the electron beam and thicker areas or areas with higher atomic number elements is stronger, meaning fewer electrons transmit in these areas. As always, when viewing a sample with TEM it is important to take into account the fact that a 3D object is being projected onto a 2D plane. This in turn can make analysis difficult since the z-axis can only be probed by tilting the whole sample.

Particle size and particle size distributions can easily be measured and calculated using images from the TEM. Statistical relevance should be at the forefront of each image obtained when showing the representation of a sample, which often means taking many images of different areas within the sample to get an overall idea of the bulk material. As TEM is best used for imaging small thin areas of the sample, it is often possible to obtain images which may not be representative of the sample as a whole.

### **2.2.4 Scanning Electron Microscopy<sup>9</sup>**

Scanning electron microscopy (SEM) is a microscopic technique that looks at the surface topography of a sample by scanning an electron beam over the surface. SEM is similar to TEM, however the accelerating voltage is much lower, usually around 2 kV for imaging, which does not transmit through the sample. An electron gun with usually either a tungsten or LaB<sub>6</sub> filament sends a focussed beam of electrons towards a sample and upon hitting the sample they interact. The SEM used in this thesis detects secondary electrons, which are the electrons ejected from the sample after interaction with the primary electron beam; usually weakly bound electrons from outer shells. Only secondary electrons generated from the surface escape, thus the SEM only images the surface features. Contrast from the SEM is generated because the features that protrude from the sample allow more secondary electrons to escape, thus appearing brighter. The SEM performed in this thesis was in combination with energy dispersive x-ray spectroscopy on a Jeol JSM-5600 SEM with a tungsten filament.

### **2.2.5 Energy Dispersive X-Ray Spectroscopy<sup>10</sup>**

Energy dispersive X-ray spectroscopy (EDX) was performed on samples to determine polyoxometalate (POM) loadings, metal loadings, and overall compositions in conjunction with SEM imaging.

In EDX the sample is bombarded with electrons from the SEM filament, causing the ejections of electrons within the sample. The vacancies within the sample's electron configuration are filled by higher energy shell electrons migrating to the vacancy. The energy released from this process gives characteristic X-ray emission spectra which can be used for elemental identification.

EDX is useful in elemental identification for elements larger than Be, but difficult to quantify for elements from Be to Ne ( $Z = 4$  to 10). This is because the electrons involved in X-ray generation are in the valence shell, and they are also participating in the chemical bonds of the sample. This can cause changes in the shape and position of the peaks which can cause difficulty in analysis and standards should be used to identify peak placements. Additionally, some X-ray energies overlap which can make the analysis more challenging. The overlap makes it difficult to separate relative amounts of, for instance, Pd and Cl which overlap in Pd L-level emission with Cl K-level emission, shown in Figure 2.6.

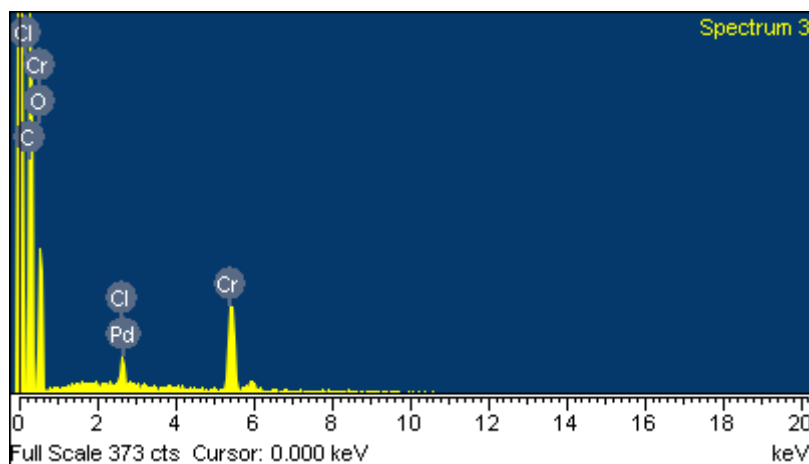


Figure 2.6 EDX spectrum of Pd NPs deposited in MIL-101(Cr).

Ideally, samples used in EDX should be stable under electron accelerating voltages ranging from 15 to 30 kV, which is sufficient to generate X-ray lines for all elements. MOFs however, depending on the type, are often damaged by the electron irradiation during both the microscopy and EDX experiments,<sup>11</sup> which can have long durations with constant electron bombardment in order to collect enough counts to obtain sufficient data. In this work an accelerating voltage of 20 kV was used and multiple areas were viewed as to not continuously observe a damaged sample. At this

accelerating voltage the penetration depth is of the order of a few microns. Because the MOF crystals used in this work are smaller than 1  $\mu\text{m}$ , the composition of the entire material is observable by EDX. However, for the same reason, it is not possible to analyse the C and O signals from the EDX with respect to the sample composition because the samples are mounted on sticky carbon tape.

### 2.2.6 X-ray Photoelectron Spectroscopy<sup>12</sup>

X-ray photoelectron spectroscopy (XPS) uses high energy X-rays to eject photoelectrons from a sample. The emitted photoelectrons are detected and give information on the binding energies of the elements present in the sample. From the binding energies, oxidation states can be elucidated. XPS is a surface sensitive technique because the chosen energy from the X-ray source causes ejected photoelectrons to have kinetic energies which cannot travel far through the sample, thus only the emission from the surface atoms is observed. Additionally, the XPS performed in this work was under UHV conditions in order to minimise photoelectron scattering and maximise the mean free path of the photoelectrons.

The basis of XPS is the measurement of ejections of electrons from core level atoms by photons from an X-ray source. The spectral outcome is plotted with binding energy on the x-axis and intensity on the y-axis. However, kinetic energy of the electron is the experimental measurement collected and the photoelectron effect relates the kinetic energy to the binding energy of the electron. Equation 2.6 shows the relationship where  $E_K$  is the kinetic energy,  $E_B$  is binding energy,  $h\nu$  is the X-ray photon energy, and  $\phi$  is the work function of the spectrometer.

$$E_B = h\nu - E_K - \phi \quad 2.6$$

The analysis depth in XPS depends on the kinetic energy of the electrons in which the inelastic mean free path,  $\lambda$ , of the electrons is related to depth at which the electrons can escape. Equation 2.7 shows the intensity,  $I$ , of the ejected electrons from a depth,  $d$ , at an emission angle of  $\theta$ . This equation can determine the thickness of a film on a substrate, assuming the film is of uniform thickness,  $d$ .

$$I = I_0 e^{\frac{-d}{\lambda \cos \theta}} \quad 2.7$$

This equation is valid for a perfectly flat, infinitely thick and uniform substrate. For the MOFs used in this thesis, which possess none of these properties, this estimation for escape depth is flawed. The highly porous MOF systems allow for significantly larger ejection depths. Equation 2.8<sup>13</sup> is the equation used to correlate ejection depths in MOF shells, used in Chapter 5. In this equation  $N_v$  is the number of valence electrons per unit cell of MOF,  $M$  is the atomic weight of the MOF and  $\rho$  is the MOF density.

$$\lambda = E/E_p^2 [\beta \ln(\gamma E) - (C/E) + (D/E^2)] \quad 2.8$$

$$E_p = 28.8(N_v \rho / M)^{1/2} \quad a$$

$$C = 1.97 - 0.91U \quad b$$

$$D = 53.4 - 20.8U \quad c$$

$$U = N_v \rho / M \quad d$$

The chemical state of the atoms dictates the exact binding energies. Higher oxidation states of elements will produce higher binding energies due to the effort in ejecting an electron from an already electron deficient atom. Additionally, for any orbital other than  $s$ , angular momentum causes spin-orbit coupling leading to doublets in the spectra. Knowing the ratio of doublet area, depending on the shell of the ejected photoelectron, the overall areas can be fitted accurately in the spectra. Table 2.1 shows the spin-orbit coupling constants and the corresponding areas they produce, given by Equation 2.9.

$$I \propto 2J+1 \quad 2.9$$

Table 2.1 Spin-orbit splitting correlation to double area ratio.

Orbital	J value	Doublet area ratio
s	1/2	n/a
p	3/2 : 1/2	2 : 1
d	5/2 : 3/2	3 : 2
f	7/2 : 5/2	4 : 3

The X-rays used as the photon source are a monochromatic beam usually from Al (Al  $K\alpha$  = 1486.6 eV) or Mg (Mg  $K\alpha$  = 1253.6 eV). The beam hits the sample and the photoelectrons are ejected. The photoelectrons travel towards an analyser unit that directs them towards the detector. For the XPS studies performed in this thesis an Al X-ray source was used and each sample was calibrated, often to Si 2p at 103.3 eV if present in the system.

### **2.2.7 Fourier Transform Infrared Spectroscopy<sup>14</sup>**

Infrared (IR) spectroscopy observes the vibrational frequencies of molecules which gives information about the molecular identification. For a vibration to be considered infrared active it must have an associated change in dipole moment.

An infrared spectrometer compares the difference in radiation intensity incident in the sample to the intensity after passing through the sample which gives rise to the IR spectrum. When the frequency of the incoming infrared beam matches the frequency of a vibration of the sample then absorption occurs. These absorptions are highly bond specific and show which bonds are present in the sample.

Fourier transform infrared spectroscopy (FTIR) gets its name because a Fourier transform is applied to the raw data to obtain the final spectrum. This is because the IR beam shines the full range of frequencies of light and measures how much is absorbed. The computer takes these data and uses Fourier transforms to work out the absorption at each wavelength. The benefit of FTIR compared to a system that measures each absorption separately is the speed of sample analysis and the enhanced signal to noise ratio in FTIR in relation to the time it takes to analyse a sample.

Within Chapters 3, 4, 5 and 6 there are two different configurations of FTIR used. In transmission FTIR, the IR beam is passed through a translucent disc, prepared by grinding the sample with KBr and pressing it with a hydraulic press. The entire depth of the sample is viewed in this experiment since the beam transmits through the sample.

The other configuration of FTIR is slightly more complicated and is explained in the sub-section below. A third type of IR experiment is explained in terms of MOCN materials in section 2.3.1.

### 2.2.7.1 Diffuse Reflectance Infrared Fourier Transform Spectroscopy

Diffuse reflectance infrared Fourier transform spectroscopy (DRIFTS) is an IR method with an alternative experimental configuration which can be used to observe surface functionalities of materials. A small amount of sample is ground with KBr and placed into a sample cup. The IR beam is focused towards the sample and interacts with the sample by bouncing off multiple particles. Eventually the IR beam is reflected from the sample cup towards an ellipsoid mirror which directs the beam towards the detector. Figure 2.7 shows the experimental setup for DRIFTS.

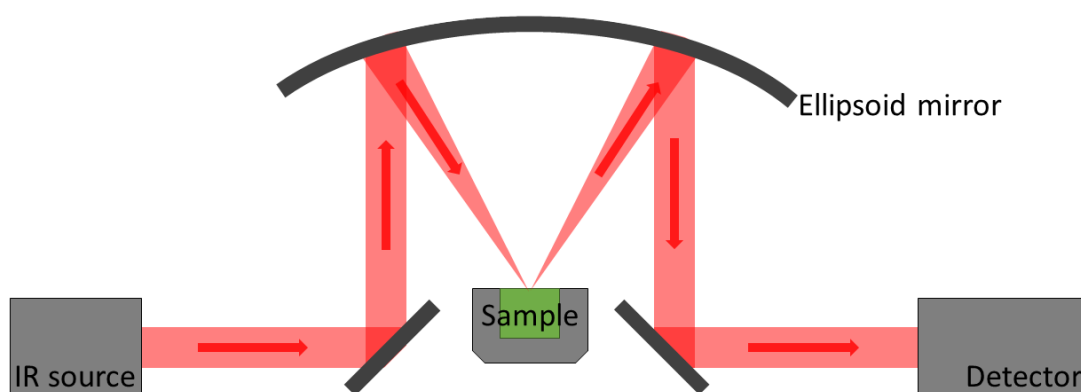


Figure 2.7 DRIFTS experimental setup. The IR beam is focused towards a sample cup containing a powder sample.

The diffuse reflectance interaction with the sample allows the surface of the material to be probed, which is an important parameter in Chapter 5 when observing silica sphere surface reactions towards the synthesis of MOF@Pd/SiO<sub>2</sub> core-shell materials.

### 2.2.8 Solution State Nuclear Magnetic Resonance Spectroscopy<sup>15</sup>

Nuclear magnetic resonance spectroscopy (NMR) is commonly used for molecular identification. For a nucleus to be NMR active its total spin must not equal to 0. Common NMR-active nuclei of choice include the dipolar ( $I=1/2$ ) nuclei, <sup>1</sup>H, <sup>13</sup>C, <sup>19</sup>F and

$^{31}\text{P}$ . The sample is introduced into a strong magnetic field where the spin of the nucleus tilts with respect to the magnetic field applied; see Figure 2.8.

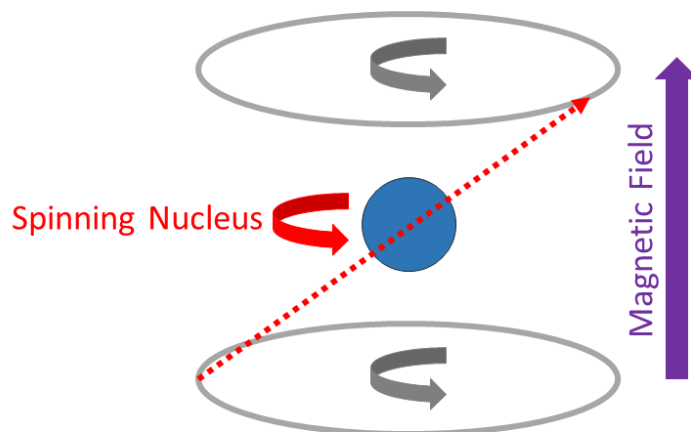


Figure 2.8 The spinning nucleus tilts with respect to the magnetic field.

When the magnetic field is discontinued, the nucleus relaxes back to its normal state and releases energy. The change of energy due to the relaxation is detected on a sensitive receiver and is transformed into a spectrum which gives a resonant frequency corresponding to a chemical shift relative to a standard, commonly  $\text{CFCl}_3$  in  $^{19}\text{F}$  NMR. Within this thesis  $^{19}\text{F}$  NMR was routinely used to determine conversions in catalysis. The most common reaction was the reductive amination of benzylamine and 4'-fluoroacetophenone. A typical NMR spectrum with each peak labelled with its corresponding compound is shown in Figure 2.9.

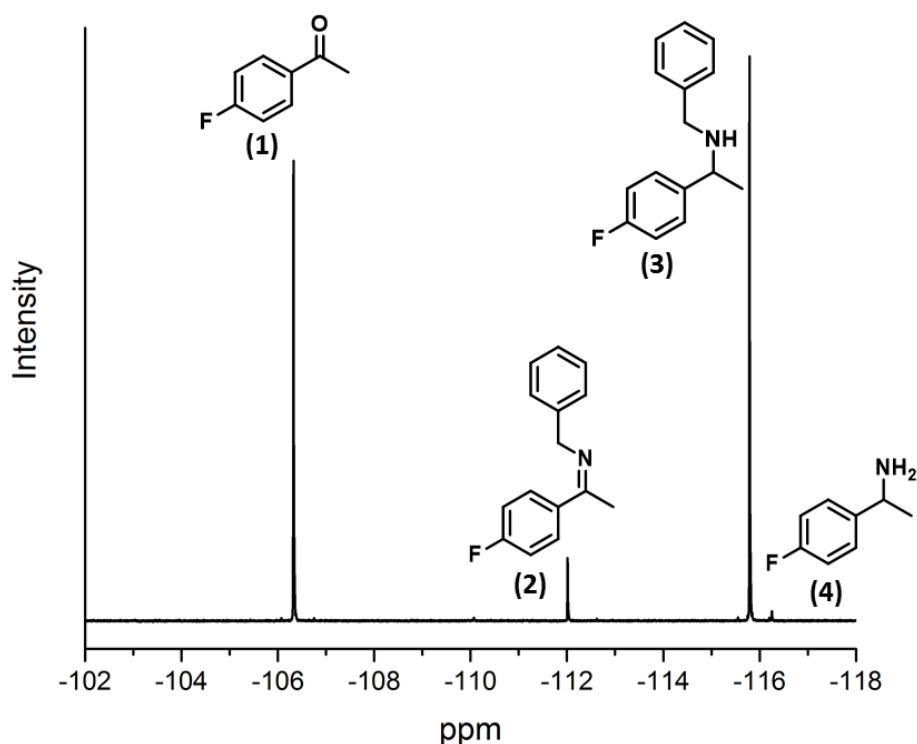


Figure 2.9 Representative  $^{19}\text{F}$  NMR from a reductive amination catalysis experiment.

For definite quantitative NMR analysis of any nuclei the magnetic field pulses must occur in a period of time longer than the relaxation time of the nucleus. In  $^1\text{H}$  NMR this is usually not an issue, as the relaxation times of most molecules is very fast. However, for nuclei such as  $^{19}\text{F}$  NMR this can become a significant issue if performing quantitative analysis when comparing compounds with different relaxation times. For this reason, a T1 test can be performed to determine the spin-lattice relaxation time of each nucleus of interest. The T1 parameter obtained by the experiment is the time that the nucleus takes to recover about 63% of its magnetic equilibrium.<sup>16</sup> A variety of pulses are applied to the sample and the magnetic moment is measured. The pulses are repeated in series of increasing time lengths to determine the relaxation time of the sample. The relaxation times for the four fluorinated molecules used in the determination of catalysis conversion for a chosen reductive amination reaction (Chapter 4) are summarised in Table 2.2. It is common to set the pulse time for an NMR experiment at 3 to 5 times the longest T1 parameter in order to ensure the nuclei is near magnetic equilibrium before the next pulse occurs.<sup>17</sup>

Table 2.2 Reductive amination catalysis  $^{19}\text{F}$  NMR T1 parameters.

Molecule	NMR shift (ppm)	T1 parameter (s)
1	-106.3	3.3
2	-112.0	2.9
3	-115.8	2.8
4	-116.3	3

## 2.3 Characterisation Techniques: Metal Organic Coordination Networks

A metal organic coordination network assembly was observed on a Au(111) single crystal by depositing chromium hexacarbonyl and *p*-terphenyldinitrile. The specific deposition and synthesis methods can be found in the corresponding chapter, while the theory and limitations of the surface science characterisation techniques are described here.

### 2.3.1 Reflection Absorption Infrared Spectroscopy<sup>18</sup>

Reflection absorption infrared spectroscopy (RAIRS) is a vibrational spectroscopy technique which gives information about orientation of molecules on a highly reflective surface. RAIRS can also give insight into bond types due to the characteristic molecular bond vibration frequencies. This method can be applied in both ultra-high vacuum (UHV) systems as well as at ambient pressure, which makes it widely applicable to many systems.

A RAIRS experiment begins by directing an infrared beam to the metal surface at an angle near parallel to the surface, called the incidence angle. This beam can be decomposed into two vectors;  $E_{ip}$  and  $E_{is}$ . The vector  $E_{ip}$  corresponds to the field perpendicular to the plane of incidence, while  $E_{is}$  corresponds to the field parallel to the plane of incidence, shown in Figure 2.10.

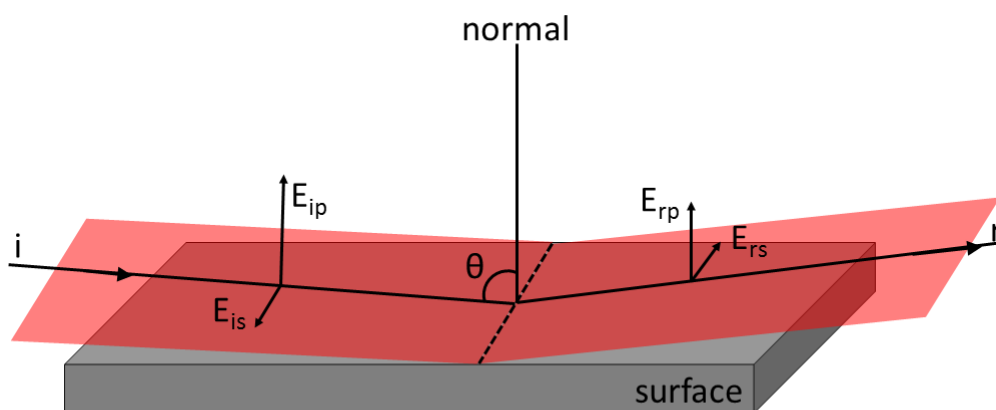


Figure 2.10 RAIRS geometry showing the parallel (s) and perpendicular (p) components to the incident (i) and reflected (r) beams.

Analogous to the incident beam, the reflected beam can also be decomposed into two vectors;  $E_{rp}$  and  $E_{rs}$ . The parallel component has a phase shift of nearly  $180^\circ$  upon reflection, which leads to a cancellation of these two vectors. Practically, this means that the s-polarised component does not interact with the surface. However, the perpendicular component has a phase shift highly dependent on the angle of incidence, with the maximum enhancement commonly occurring between  $75^\circ$  and  $88^\circ$ . Due to the interaction of the perpendicular component of the beam with the surface, molecules on the surface must vibrate with a dipole moment that has a perpendicular component in order to be IR active. This is commonly referred to as the surface selection rule, which is depicted in Figure 2.11. Surface selection rules apply to conducting surfaces due to the free electrons which create the image dipole.

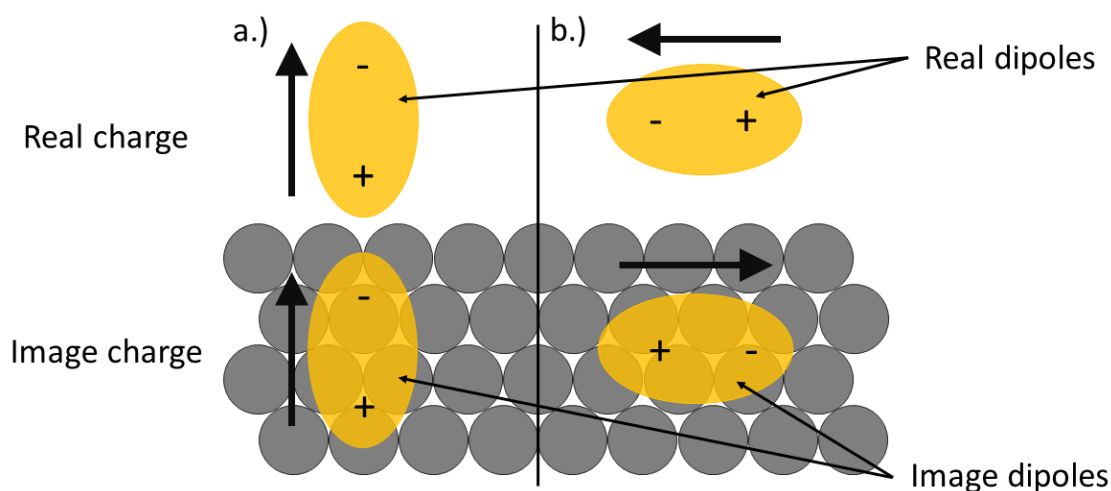


Figure 2.11 Surface selection rules due to the orientation of the molecule on the surface. (a.) a dipole perpendicular to the surface leads to an enhancement by the image dipole, while (b.) a dipole parallel to the surface is cancelled out by its image dipole. Adapted from <sup>18</sup>.

In the RAIRS experiments performed in this work, the Au (111) single crystal was in a UHV atmosphere and the IR beam was directed to and collected from the surface through viewport flanges.

### 2.3.2 High Resolution Electron Energy Loss Spectroscopy<sup>19</sup>

High resolution electron energy loss spectroscopy (HREELS) is a UHV technique measuring the energy loss of electrons when inelastically scattering from a surface. In this technique a beam of electrons is generated and passed through a monochromator in order to have a well-defined and large electron flux. The electrons then hit and scatter from the surface and are subsequently collected in an electrostatic analyser and detector to be processed into a spectrum. A simplified diagram of the HREELS setup is shown in Figure 2.12.

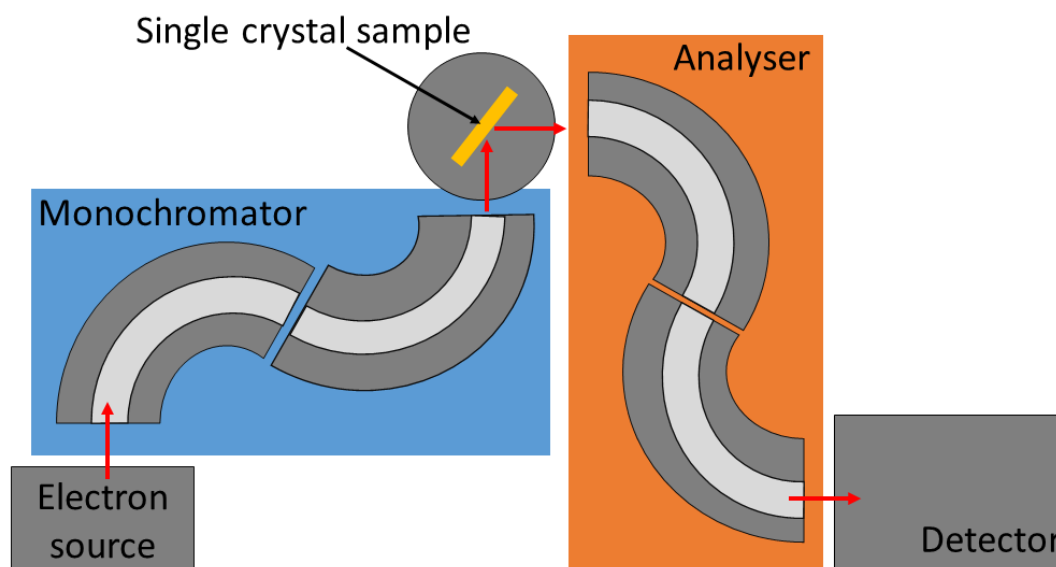


Figure 2.12 HREELS setup showing the monochromator and analyser units. The single crystal is mounted on a rod that turns so that the specular position can be found without re-tuning the lenses.

Upon the incident electrons hitting the surface, the majority of electrons elastically scatter from the surface, leading to a large peak with zero energy loss in the spectrum. However, magnifying the area along the tail of the elastic peak shows energy loss features which corresponds to the electronic excitation of the sample. The excitations within the sample lead to a decrease of kinetic energy in the electrons interacting with the sample. The magnitude of energy lost from the electrons corresponds to the vibrational mode of the bonds on the surface.

In addition to the molecular vibrations, which indicate the bonds present on a surface, bond orientation can also be elucidated using HREELS. When running the experiments with specular geometry, meaning the angle of incidence is equivalent to the angle of scattering, the same surface selection rules as in RAIRS apply (see Figure 2.11). This means that only vibrations with dipole moments that have a component perpendicular to the surface appear. By changing the specular geometry to off specular, an increase or decrease in the intensity of vibrations can occur, thus giving information on the orientation of the adsorbed molecules on the surface.

The benefit of HREELS over RAIRS is that HREELS offers a higher sensitivity and wider energy window, meaning that in ideal conditions vibrations of ligand to metal bonds

can be detected on the surface. Statistical software can be used to recover spectra from instrumental broadening<sup>20-21</sup> and commonly leads to overall resolutions of the elastic peak around  $50 \text{ cm}^{-1}$  at full width half maximum (FWHM).

### 2.3.3 Scanning Tunneling Microscopy<sup>18, 22-23</sup>

Scanning tunneling microscopy (STM) is a scanning probe microscopy technique invented by IBM in 1981 and whose inventors earned the Nobel Prize in Physics in 1986. STM can be used in either UHV or ambient conditions, the latter is useful for imaging liquid-solid or gas-solid interfaces. A tip, which ideally has a single atom at its apex, is brought within ångströms of a conductive surface and a potential difference is applied. The potential difference causes electrons to tunnel between tip and surface which in turn create images due to slight differences between current while scanning over the surface. A simplified diagram of these principles can be seen in Figure 2.13.

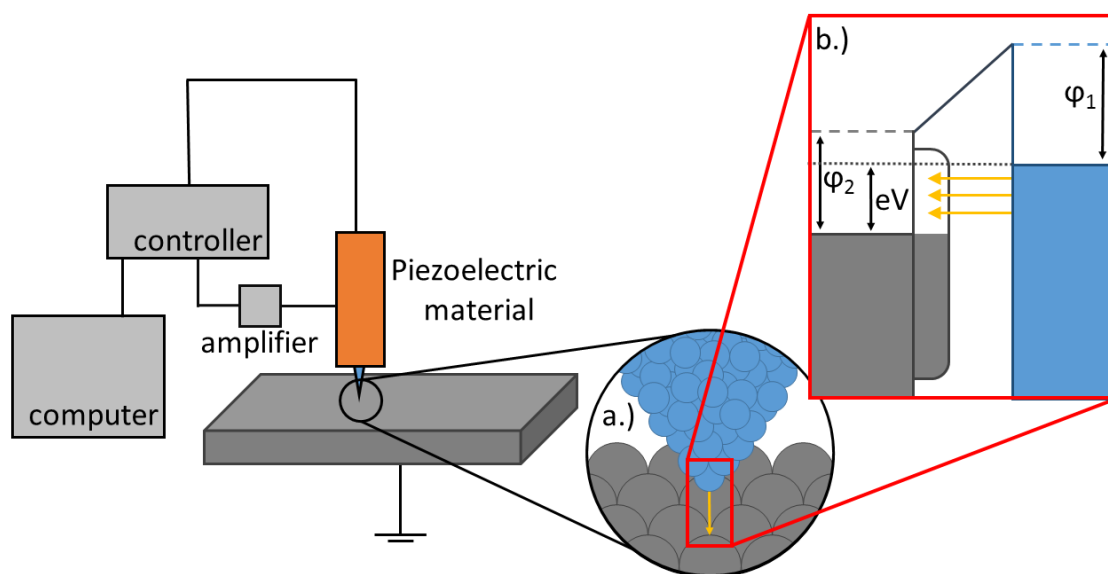


Figure 2.13 STM setup and principles. Adapted from references 18, 23. The general figure shows the setup of the scanning system. The tip, attached to a piezoelectric material, is scanned across the surface. The tunneling current from the tip to the surface is measured, amplified and used to control the tip-to-surface distance. A.) shows the atomically sharp tip at a small distance away from the surface. B.) shows the energy diagram of the tip (blue) and the surface (grey). A positive tip bias is shown, therefore electrons tunnel from tip to surface.

The electron tunneling current depends on the distance from tip to surface and decreases exponentially as the tunneling gap increases, as shown in Equation 2.10.

This relationship causes a large change in current with very small changes in tip-to-surface distance, seen in Figure 2.14.

$$I = C_1 U e^{-C_2 D} \quad 2.10$$

Where  $I$  is the tunneling current,  $C_1$  and  $C_2$  are constants,  $U$  is the tunneling bias and  $D$  is the distance between tip and surface.

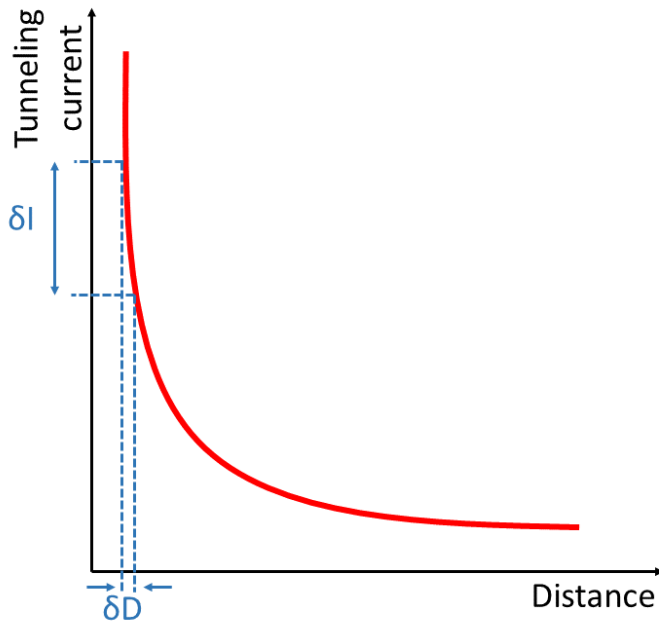


Figure 2.14 The relationship between tunneling current and tip-to-surface gap distance.

In order to obtain the necessary precision and control to achieve small distances between tip and surface, the tip is attached to a piezoelectric material. The piezoelectric tube allows small changes in voltage to either expand or contract the material, thus keeping the tip close to the surface. STM can be operated in either constant height mode, where the tip is a constant distance from the surface, or constant current mode, where the tip changes height to keep a constant current across the surface. To achieve constant current, the tunneling current feedback is attached to the voltage control on the piezoelectric tube. Constant current mode is best to use when dealing with not perfectly flat surfaces (i.e. possibility of multilayer adsorption on a surface) so that the tip is not damaged, and is the mode used within this work. The resolution achieved in STM is highly dependent on tip conditions. Ideally, a tip's apex will have a single atom, allowing for resolutions commonly around 1 Å. This

allows for atomic resolution of molecular adsorption on surfaces. However, due to the fact the STM uses current to form images, it is important to note that the images obtained do not necessarily correspond to structure, but rather to electronic state instead. This means that STM is often coupled with DFT calculations to map out possible HOMO and LUMO states when trying to elucidate molecular structures on a surface.

Additionally, if tip conditions are not ideal, as often is the case under experimental conditions, a tip can have multiple atoms as an apex, leading to poor resolution, or even two apices. In the case of a double tip, images obtained have identical features with an equivalent distance between them. When the tip is not in optimal condition it can be manually pulsed to achieve a better tip, and therefore better image resolution. Pulse treatments to the tip include quickly increasing and decreasing the bias voltage to encourage contaminants off the tip, or colliding the tip to the surface to condition the tip.

## 2.4 References

1. Sing, K. S. W.; Everett, D. H.; Haul, R. A. W.; Moscou, L.; Pierotti, R. A.; Rouqu  rol, J.; Siemieniewska, T., Reporting Physisorption Data for Gas/Solid Systems with Special Reference to the Determination of Surface Area and Porosity. *Pure Appl. Chem.* **1985**, *57*, 603-619.
2. Brunauer, S.; Emmett, P. H.; Teller, E., Adsorption of Gases in Multimolecular Layers. *J. Am. Chem. Soc.* **1938**, *60*, 309-319.
3. Lowell, S.; Shields, J. E., *Powder Surface Area and Porosity*. Springer: 1991.
4. D  ren, T.; Baeb, Y.-S.; Snurr, R. Q., Using Molecular Simulation to Characterise Metal–Organic Frameworks for Adsorption Applications. *Chem. Soc. Rev.* **2009**, *38*, 1237–1247.
5. Rouquerol, F.; Rouquerol, I.; Sing, K., Adsorption by Powders and Porous Solids Principles, Methodology and Applications. Academic Press: London, 1999.
6. Williams, D. B.; Carter, C. B., *Transmission Electron Microscopy*. Springer: 2009.
7. Reimer, L.; Kohl, H., *Transmission Electron Microscopy: Physics of Image Formation*. 5 ed.; Springer: 2008.
8. Putnis, A., *Introduction to Mineral Sciences*. Cambridge University Press: Hampshire, 1992.
9. Chorkendorff, I.; Niemantsverdriet, J. W., *Concepts of Modern Catalysis and Kinetics*. Wiley-VCH Verlag GmbH & Co.: 2003.
10. Niemantsverdriet, J. W., *Spectroscopy in Catalysis*. Wiley-VCH Verlag GmbH & Co. KGaA, Weinheim, Germany: 2007.
11. Meilikhov, M.; Yusenko, K.; Esken, D.; Turner, S.; van Tendeloo, G.; Fischer, R. A., Metals@MOFs - Loading MOFs with Metal Nanoparticles for Hybrid Functions. *Eur. J. Inorg. Chem.* **2010**, *2010*, 3701-3714.
12. Watts, J. F.; Wolstenholme, J., *An Introduction to Surface Analysis by XPS and Aes*. John Wiley & Sons Ltd.: 2003.
13. Tanuma, S.; Powell, C. J.; Penn, D. R., Calculations of Electron Inelastic Mean Free Paths. V. Data for 1 Organic Compounds over the 50-2000 eV Range. *Surf. Interface Anal.* **1994**, *21*, 165-176.
14. Stuart, B., *Infrared Spectroscopy: Fundamentals and Applications*. John Wiley & Sons Ltd.: 2004.
15. Burrows, A.; Holman, J.; Parsons, A.; Pilling, G.; Price, G., *Chemistry3*. Oxford University Press: New York, 2009.
16. Bloembergen, N.; Purcell, E. M.; Pound, R. V., Relaxation Effects in Nuclear Magnetic Resonance Absorption. *Phys. Rev.* **1948**, *73*, 679-712.
17. Freeman, R.; Hill, H. D. W., Fourier Transform Study of NMR Spin-Lattice Relaxation by Progressive Saturation. *J. Chem. Phys.* **1971**, *54*, 3367-3377.
18. Attard, G.; Barnes, C., *Surfaces*. Oxford University Press: New York, 2004.
19. Richardson, N. V., High Resolution Electron Energy Loss Spectroscopy. *Curr. Opin. Solid State Mater. Sci.* **1997**, *2*, 517-524.
20. Frederick, B. G.; Jones, T. S.; Pudney, P. D. A.; Richardson, N. V., HREELS and RAIRS a Complete Vibrational Study of the Surface Benzoate Species Adsorbed on Copper. *J. Electron. Spectrosc. Relat. Phenom.* **1993**, *64-65*, 115-122.

21. Frederick, B. G.; Richardson, N. V., Comment on “Ultrahigh Resolution Electron Energy Loss Spectroscopy”. *Phys. Rev. Lett.* **1994**, *73*, 772-772.
22. Chen, C. J., *Introduction to Scanning Tunneling Microscopy*. Oxford University Press: 2008.
23. Hosokawa, M.; Nogi, K.; Naito, M.; Yokoyama, T., *Nanoparticle Technology Handbook*. 2007.

# **Chapter 3**

---

Metal Nanoparticle Deposition and Formation in MOF Supports:  
Synthesis and Characterisation of Multifunctional Materials

### 3.1 Introduction

Catalytically active acid sites in metal-organic frameworks (MOFs) can arise either from the functionality of the linker or from the metal node. Some MOFs have well-defined active sites at coordinatively unsaturated sites within the framework which can behave as heterogeneous acid catalysts as well as act as a structural component of the MOF material.<sup>1</sup> This heterogeneity is beneficial when compared to homogeneous catalyst analogues due to the ease of separation of catalyst from reactants and products.

Adding an alternate functionality, such as metal nanoparticles (MNPs), can enable the material to catalyse multiple reactions. An ideal MOF support host for bifunctional catalysis should possess both acidity and large pores. The large pore materials enable the MNPs to form within the MOF structure and allows for mass transfer to occur without diffusional limitation during the catalysis. Immobilisation of MNPs within a MOF structure that contains cages can minimise the agglomeration of MNPs because they cannot traverse through the narrower MOF windows.

MIL-101(Cr) is the MOF of choice in Chapters 3 and 4. MIL-101(Cr) is a mesoporous MOF with a hierarchical MTN framework. This MOF is comprised of two mesoporous cages; a small cage of 2.9 nm with pentagonal openings of 1.2 nm and a large cage with a diameter of 3.4 nm and pentagonal and hexagonal windows of 1.2 and 1.6 nm.<sup>2</sup> MIL-101(Cr) was initially synthesised using HF, which is highly corrosive and toxic. Since the initial discovery of MIL-101(Cr), other preparations have been reported that eliminate the HF usage and still produce highly crystalline and porous materials.<sup>3-4</sup> Other than its mesoporosity, another benefit of using MIL-101(Cr) as a support for immobilisation of metal nanoparticles is its high thermal (up to 275°C) and chemical stability.<sup>4</sup> MIL-101(Cr) is stable in water and other organic solvents, making it widely applicable for many deposition techniques.

Another MOF used for immobilisation of MNPs in this chapter is MIL-100(Sc). This MOF has the same overall MTN structure as MIL-101, but trimesic acid is used as the linker instead of terephthalic acid in MIL-101. This in turn makes the windows and cages smaller. The small cage of MIL-100(Sc) is 2.5 nm and the large cage is 3.0 nm, with windows of 0.5 nm (pentagonal) and 0.9 nm (hexagonal). The Sc<sup>3+</sup> nodes instead of

$\text{Cr}^{3+}$  makes MIL-100(Sc) a better Lewis acid catalyst than MIL-101(Cr). MIL-100(Sc), however, is less stable due to the more facile ligand exchange when compared to the more inert Cr nodes.<sup>5</sup> The analogous MIL-101(Sc) also suffers from facile ligand exchange. This MOF is not stable upon solvent removal and recrystallizes into MIL-88B upon heating.<sup>5</sup>

There are multiple techniques available for deposition of MNPs within metal-organic frameworks. The top down methodology for creating these multifunctional materials is a widely used strategy. Ideally in this strategy small metal nanoparticles are immobilised within the porous network of the MOF support. Metal salts are deposited in the MOF and then reduced to form well-dispersed MNP/MOF materials. This allows for small nanoparticles to be created, less than 3.4 nm in the case of MIL-101(Cr) materials. Because the MIL-100 and MIL-101 structures are composed of smaller windows to access large cages, MNPs can be immobilised within the cages without easy diffusion out. For example, nanoparticles larger than 1.6 nm will not be able to agglomerate following the same pathway as compared to nanoparticles on a flat surface because the large cage of MIL-101(Cr) has windows of 1.6 nm and 1.2 nm. The agglomeration of nanoparticles during catalysis often leads to deactivation of the catalyst, so minimising agglomeration processes yields a more stable and recyclable catalyst. The isolation of MNPs inside the MOF pores helps maintain the nanoparticle size during catalysis by preventing agglomeration, as outlined above. Of course, other mechanisms for nanoparticle deactivation during catalysis still exist and will be discussed further in Chapter 4.

Several top-down strategies have been used within MIL-101(Cr) for nanoparticle deposition as previously detailed in Chapter 1. The two methods discussed in this chapter are solution impregnation and a modified incipient wetness impregnation by a double solvents deposition method.

Solution impregnation was accomplished in a study by Zlotea *et al.*<sup>6</sup> where MIL-100(Al) was used as the support for Pd nanoparticles. In this work  $\text{H}_2\text{PdCl}_4$  was made by dissolving  $\text{PdCl}_2$  in a HCl solution. The MOF was then impregnated by stirring it in the tetrachloropalladic acid solution for 3 hours. This enables the  $\text{H}_2\text{PdCl}_4$  to interact

with the MOF crystals and enter the pores. The resulting material was dried and then reduced in a flow of hydrogen. It was calculated that 10% of the nanoparticles formed are larger than the available pore size, meaning at least 10% are located on the surface of the MIL-100(Al). The structure of the MOF remains crystalline, but there is a discernible peak broadening, indicating a possible slight loss of crystallinity of the MIL-100(Al).

The initial procedure for a modified incipient wetness deposition, called the double solvents method, was developed by Aijaz *et al.* for Pt MNPs in MIL-101(Cr).<sup>7</sup> In this method a small volume of aqueous metal salt solution is deposited within the MIL-101(Cr) pores by capillary force, which prevents metal from being deposited on the MOF external surface. The nanoparticles formed are in the size range of 1.2 to 3.0 nm, well within the cage sizes of MIL-101(Cr). Since the initial publication with Pt MNPs, the double solvent method has been reported for use in synthesising Pd, Ag, PdAg, Ni, Au and NiAu MNPs in MIL-101(Cr).<sup>8-9</sup>

This chapter discusses the synthesis and optimisation of the MOF support formation and the top-down MNP deposition procedures. Section 3.3.1 discusses the optimisation of MOF formation and preparation for nanoparticle deposition. Section 3.3.2 discusses the strategies for top-down nanoparticle deposition to achieve well-defined nanoparticles within the MOF. The materials discussed in this chapter are used as catalysts in Chapter 4.

## 3.2 Experimental

### 3.2.1 MOF Synthesis

#### 3.2.1.1 MIL-101(Cr)

Following a modified procedure reported by Férey *et al.*<sup>2</sup> CrCl<sub>3</sub>·6H<sub>2</sub>O (Fisons, 95%), terephthalic acid (Aldrich, 98%) and water were combined in a 1:1:400 molar ratio, respectively, within a Teflon-lined stainless steel autoclave. A typical synthesis combined 0.3 g CrCl<sub>3</sub>·6H<sub>2</sub>O and 0.187 g terephthalic acid with 8.2 ml water. The solution was mixed for 10 minutes, then sealed and heated to 220°C for 8 hours. Upon cooling to room temperature, the solution was centrifuged and the supernatant was

decanted. The solid was further purified by heating in ethanol for 24 hours, then centrifuged and dried at 70°C in air overnight.

### **3.2.1.2 MIL-100(Sc)**

Aqueous scandium chloride solution was prepared by stirring the desired quantity of  $\text{Sc}_2\text{O}_3$  (Stanford Materials Corporation, 99.99%) in concentrated HCl at 50°C until the solution is opaque white (usually around 8 hours) then heat up to 70°C for 1-2 hours. A small amount of water is added while heating and stirring, which turns to a clear solution upon reaction completion. The solution is then diluted to the desired molarity and kept as a stock solution. This solution was then used as the scandium source for the synthesis of MIL-100(Sc).

Autoclave synthesis: Using a procedure modified from that of Mitchell *et al.*<sup>5</sup> aqueous scandium chloride solution (1.5 M), benzene-1,3,5-tricarboxylic acid (trimesic acid, Alfa Aesar, 98%), and DMF (Alfa Aesar, 99%) were combined in a 1:0.5:260 molar ratio, respectively, within a Teflon-lined stainless steel autoclave. A typical preparation combined 0.66 ml  $\text{ScCl}_3$  solution (1.5 M) and 0.1 g trimesic acid with 20 ml DMF. The solution was stirred for 10 minutes, then sealed and heated to 150°C for 48 hours. The resulting solid was centrifuged, supernatant decanted, and washed with ethanol three times. The MOF material was then dried at 70°C overnight in air.

Reflux synthesis: Using an overall molar ratio of 1:0.5:260 of  $\text{ScCl}_3$  (1.5 M), 1,3,5-tricarboxylic acid (trimesic acid, Alfa Aesar, 98%) and DMF (Alfa Aesar, 99%), 1,3,5-tricarboxylic acid was dissolved in DMF within a round bottom flask. A typical preparation combined 0.66 ml  $\text{ScCl}_3$  solution (1.5 M) and 0.1 g trimesic acid with 20 ml DMF. Then  $\text{ScCl}_3$  was added and refluxed at 140°C for 16 hours. The resulting solid was centrifuged, supernatant decanted, and washed with ethanol three times. The MOF material was then dried at 70°C overnight in air.

Microwave conditions: In a microwave vial,  $\text{ScCl}_3$  solution (1.5 M), 1,3,5-tricarboxylic acid (trimesic acid, Alfa Aesar, 98%) and DMF (Alfa Aesar, 99%) were combined in a molar ratio of 1:0.5:260. A typical preparation combined 0.2 ml  $\text{ScCl}_3$  (1.5 M) and 0.0302 g trimesic acid with 6 ml DMF. The vial was then sealed and microwave

irradiated at 140°C for 30 minutes, with a 2 minute pre-heat stir period. The resulting solid was centrifuged, supernatant decanted, and washed with ethanol three times. The MOF material was then dried at 70°C overnight in air.

### 3.2.1.3 MIL-100(Fe)

MIL-100(Fe) was synthesised using a modified microwave procedure reported by Márquez *et al.*<sup>10</sup> using an iron chloride hexahydrate (Sigma Aldrich, 97%): 1,3,5-tricarboxylic acid (trimesic acid, Alfa Aesar, 98%): water ratio of 1:0.5:185. Typically, 1.62 g FeCl<sub>3</sub>·6H<sub>2</sub>O was mixed with 0.56 g trimesic acid in 20 ml of water. The reaction was then heated to 130°C and kept at this temperature for 5.5 minutes. The mixture was cooled then centrifuged. The resulting solid was washed three times with ethanol before being dried at 70°C overnight in air.

## 3.2.2 Metal Nanoparticle Deposition

Solution impregnation of Pd was achieved using a modified procedure described by Zlotea *et al.*<sup>6</sup> A H<sub>2</sub>PdCl<sub>4</sub> solution was prepared by mixing the desired amount of PdCl<sub>2</sub> (Sigma Aldrich, 99.999%) into a 10% v/v HCl aqueous solution. Upon dissolving, MOF was added to the solution and stirred for 3 hours. The mixture was filtered and dried in air at 70°C. The sample was then transferred to an alumina boat and reduced under a flow of 5% H<sub>2</sub>/N<sub>2</sub> for 2 hours at 200°C with a ramp of 1.5°C min<sup>-1</sup>.

Metal nanoparticles were also deposited by a similar method developed by Aijaz *et al.*<sup>7</sup> The as-prepared MOF was activated under vacuum at 150°C for 16 hours. The MOF was then combined with dry hexane under inert atmosphere and sonicated for 30 minutes to disperse the MOF crystals within the hexane solution. The desired amount of PdCl<sub>2</sub> (Sigma Aldrich, 99.999%), HAuCl<sub>4</sub> (Sigma Aldrich, 99.999%), RuCl<sub>3</sub> (Sigma Aldrich, Ru content 45-55%) or PtCl<sub>4</sub> (Sigma Aldrich, ≥99.99%) was dissolved in H<sub>2</sub>O that equates to 85% of the available pore volume of the MOF and added dropwise to the MOF suspension while vigorously stirring. The solution was left to dry in air for 24 hours at room temperature, then activated at 150°C under vacuum for 16 hours. The activated material was then transferred to an alumina boat and reduced under a flow of 5% H<sub>2</sub>/N<sub>2</sub> for 2 hours at 200°C (ramp of 1.5°C min<sup>-1</sup>) to produce the final MNP in

MOF material. Elemental analysis on Pd loadings in MIL-101(Cr) was performed by Mikroanalytisches Laboratorium Kolbe. The actual loadings determined by elemental analysis are presented.

### **3.3 Metal Nanoparticle in MOF Catalyst Characterisation**

#### **3.3.1 Optimisation of MOF Synthesis**

The preparation of the MOF support is an integral part of the catalyst synthesis. A MOF with a large surface area and pore volume allows for more nanoparticles to be dispersed throughout the support. Because of this, any contamination by unreacted linkers or high boiling point solvents used during the synthesis, should be removed to give the best support material.

##### **3.3.1.1 MIL-101(Cr)**

Unreacted terephthalic acid used in the MIL-101(Cr) synthesis either crystallises during heating or contaminates the MOF pores. The removal of excess terephthalic acid during purification of MIL-101(Cr) is an important step to achieve the high surface area material desired.

A simple vacuum filtration and wash leaves crystallised terephthalic acid in the material. However, it was determined that centrifugation of the reaction solution leads to less terephthalic acid in the final support material. Figure 3.1 shows the difference in peak intensity for terephthalic acid around  $18^\circ 2\theta$ . For this reason, centrifugation and subsequent washing was performed on all MOF materials.

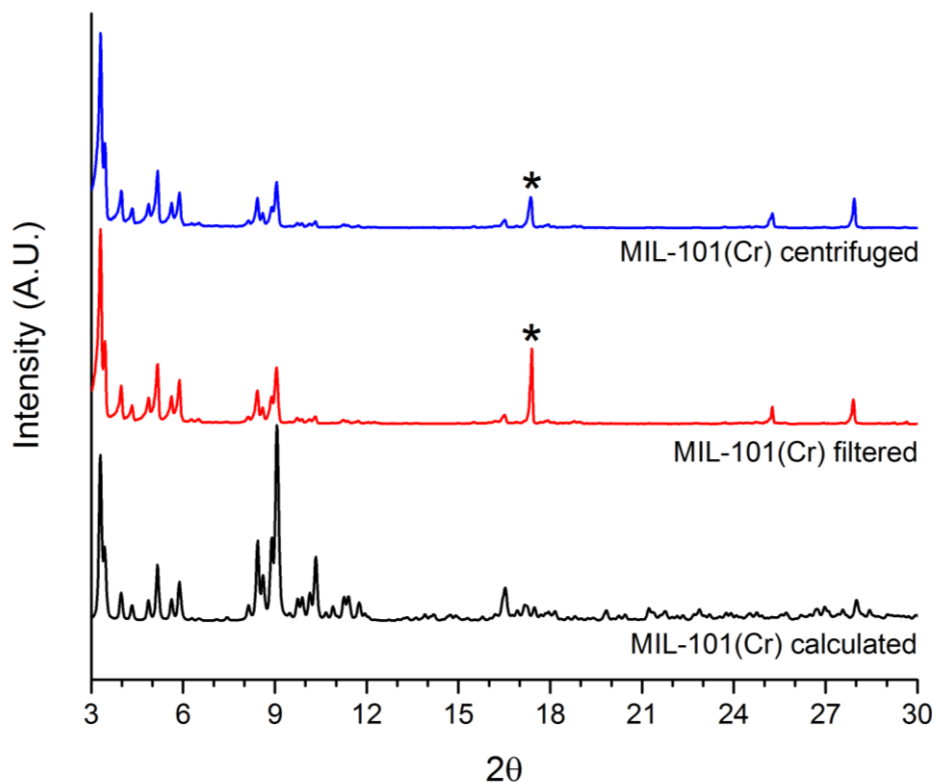


Figure 3.1 XRDs of filtered and centrifuged MIL-101(Cr) materials. Note the intensity of the peak due to excess terephthalic acid (\*) decreases from filtration to centrifugation.

To further remove excess terephthalic acid from the MIL-101(Cr) pores, an ethanol wash was performed on the previously centrifuged and washed material. In this procedure MIL-101(Cr) and ethanol were refluxed for 24 hours. This allows for the terephthalic acid to dissolve in the EtOH solution. The surface area of the as prepared material compared to the ethanol washed material nearly doubles from  $1614 \text{ m}^2 \text{ g}^{-1}$  to  $3013 \text{ m}^2 \text{ g}^{-1}$ , as seen in Figure 3.2. The typical pore volume achieved after the EtOH washing procedure is  $1.45 \text{ cm}^3 \text{ g}^{-1}$ .

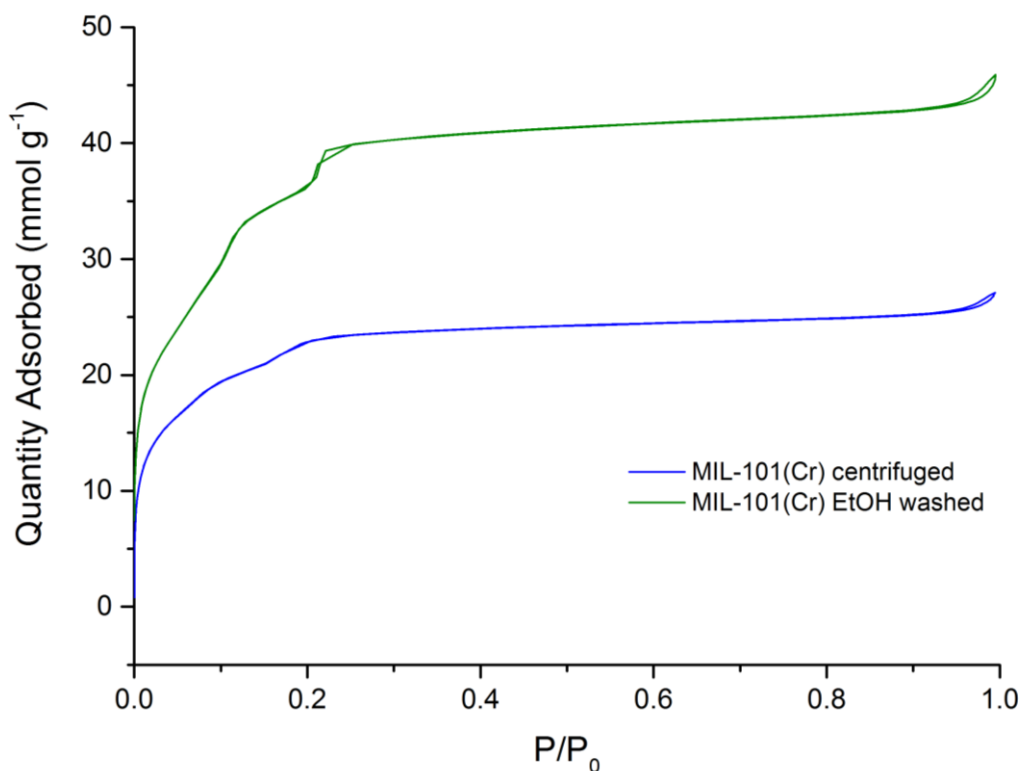


Figure 3.2 N<sub>2</sub> adsorption isotherms showing the increase of surface area after the EtOH washing procedure.

The MOF remains crystalline after the procedure, as shown in Figure 3.3. The broadening of peaks is possibly due to a change from reflection to transmission X-ray diffractometer mode with a shorter collection time. Alternatively, the broadening of the peaks could be due to the MOF crystals becoming smaller through grinding of the MOF crystals with the magnetic stir bar during the EtOH wash procedure. After the synthesis and purification of MIL-101(Cr) detailed above the support material is ready for metal nanoparticle deposition.

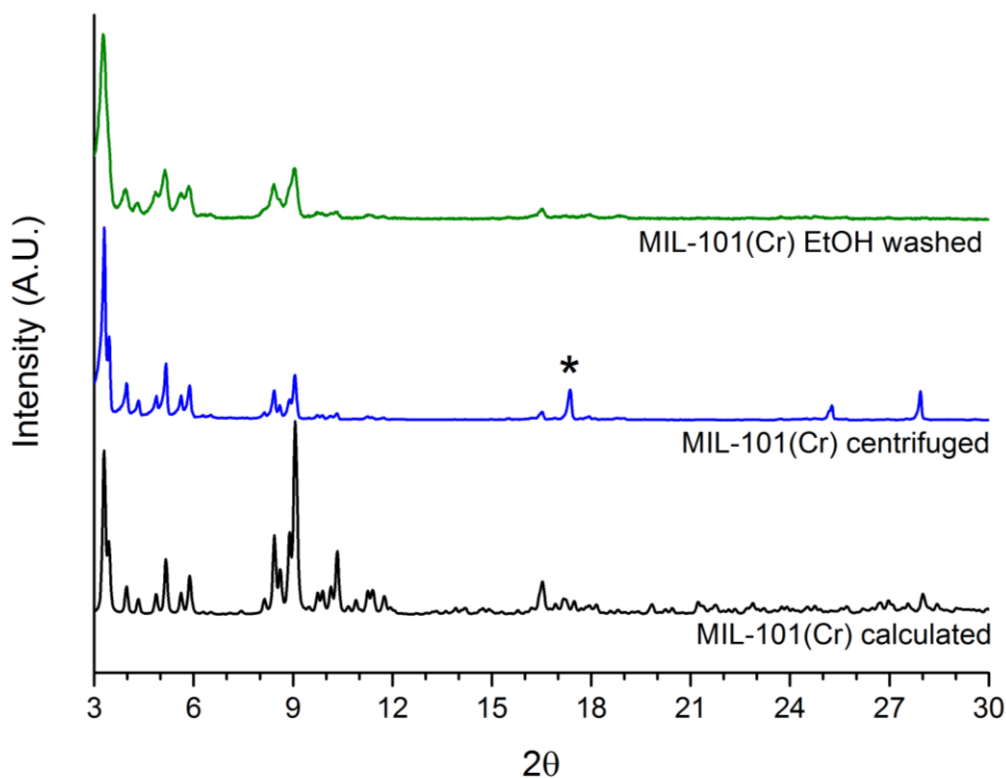


Figure 3.3 XRD of MIL-101(Cr) after centrifugation and after the subsequent EtOH wash procedure. Note the peak corresponding to terephthalic acid (denoted with \*) has diminished after the EtOH wash.

### 3.3.1.2 MIL-100(Sc)

MIL-100(Sc) was prepared three separate ways: autoclave, reflux and microwave. In all synthetic methods the desired MOF was formed, indicated by XRD shown in Figure 3.4. The decreased signal to noise ratio seen in the reflux synthesis method is probably due to the shorter XRD acquisition time, but may be due to a slight decrease in crystallinity when compared to the autoclave and microwave preparations. The microwave synthesis method takes a fraction of the time compared to the other two approaches, and was chosen as the MIL-100(Sc) synthesis method of choice. MIL-100(Sc) is synthesised in DMF, which is hazardous to health and has a high boiling point which complicates its removal. For this reason, upon completion the MOF was centrifuged and washed with ethanol three times. This replaces the DMF within the pores with ethanol. All preparation methods yielded materials with similar nitrogen adsorption; a typical isotherm is shown in Figure 3.5. The calculated pore volume is around  $0.8 \text{ cm}^3 \text{ g}^{-1}$  and surface area of approximately  $1600 \text{ m}^2 \text{ g}^{-1}$ . The smaller pore volume and

surface area from MIL-100(Sc) compared to MIL-101(Cr) is due to the use of trimesic acid rather than terephthalic acid for the MOF synthesis. After the EtOH replacement, the MOF was dried in air and ready for subsequent MNP deposition.

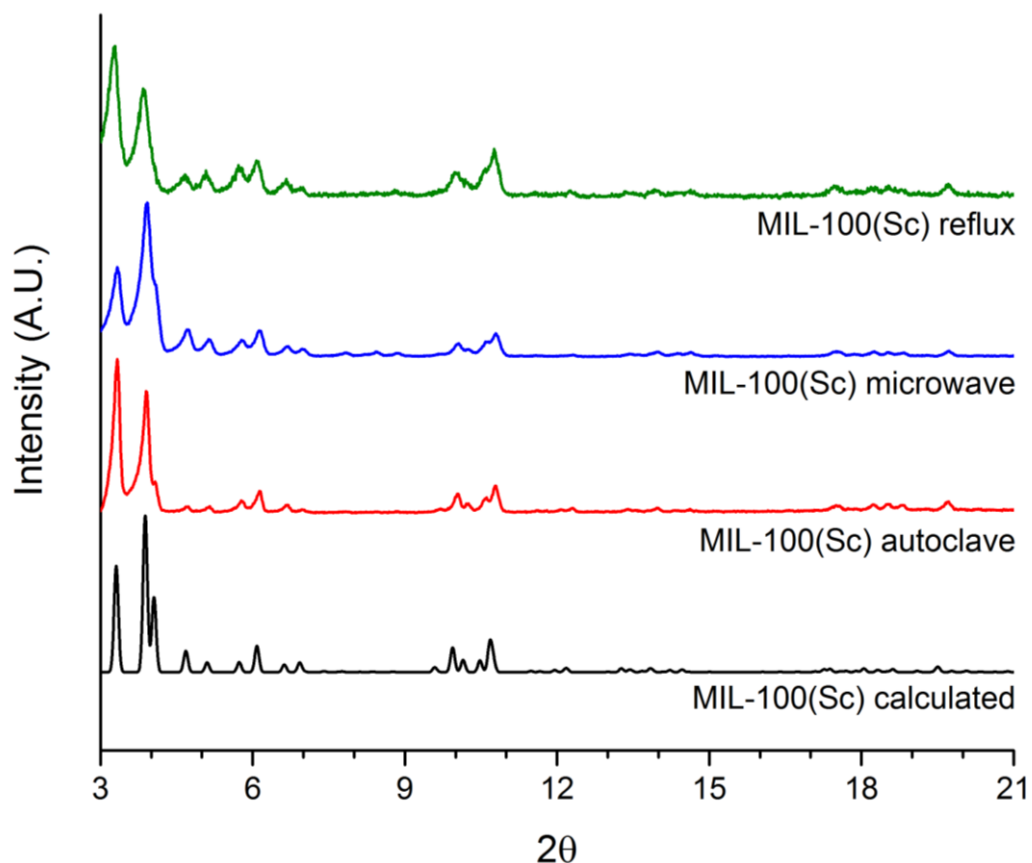


Figure 3.4 MIL-100(Sc) prepared by autoclave, microwave, and reflux. MIL-100(Sc) calculated pattern was determined by using MIL-100(Cr) cif file and changing the unit cell parameter defined by Mitchell *et al.*<sup>11</sup>

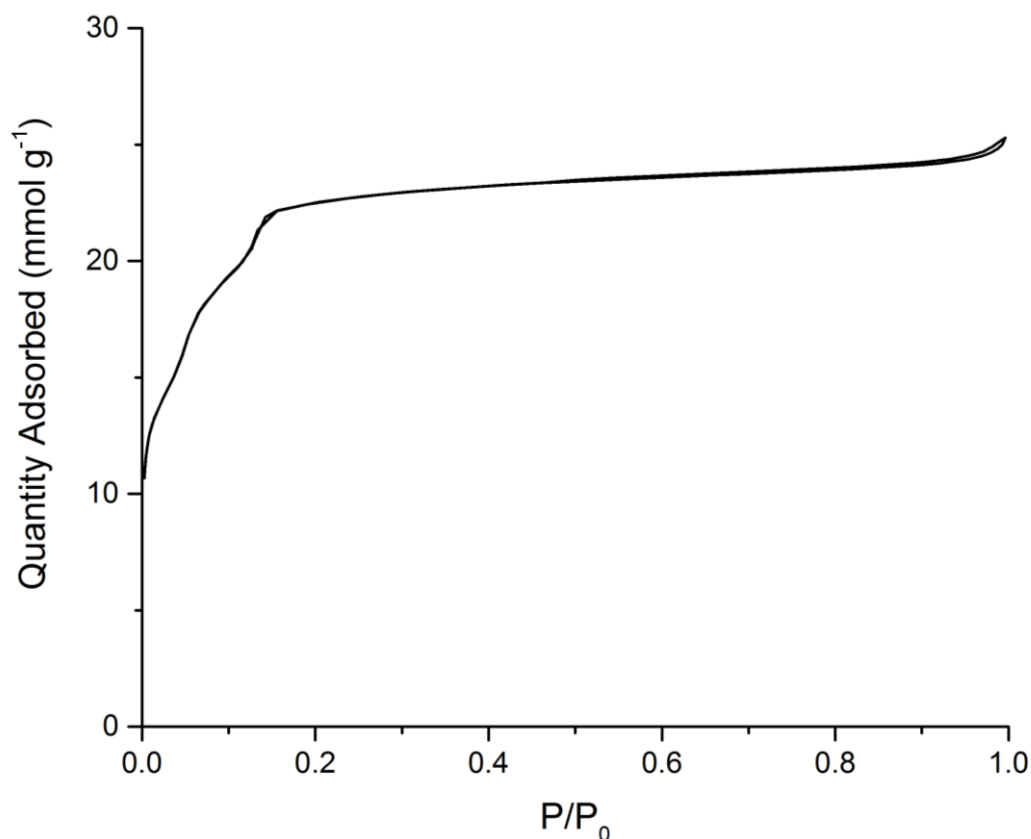


Figure 3.5 MIL-100(Sc) nitrogen adsorption isotherm.

### 3.3.2 Optimisation of MNP Deposition

Metal nanoparticle deposition was attempted using two different approaches, followed by optimisation of the most promising method.

#### 3.3.2.1 Solution Impregnation

Solution impregnation of Pd was initially tried on MIL-101(Cr). In this method, adapted from Zlotea *et al.*<sup>6</sup>, PdCl<sub>2</sub> and HCl are mixed together to form H<sub>2</sub>PdCl<sub>4</sub>. This solution is diluted with water and the MOF is introduced. The solution is stirred for 3 hours to allow the Pd salt to enter the MOF pores. A downside using this method is that the acidic conditions lead to a dramatic reduction in the crystallinity of the support material, as can be seen in Figure 3.6.

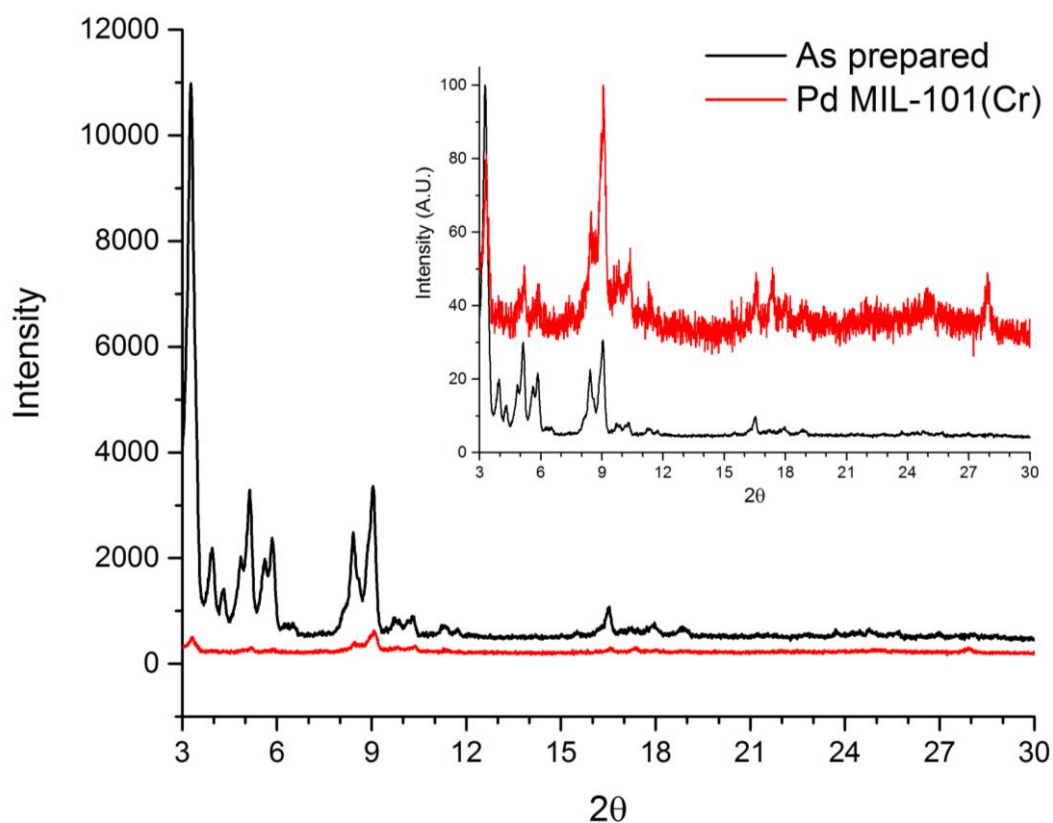


Figure 3.6 MIL-101(Cr) before and after Pd solution impregnation procedure. The main plot shows the large decrease in intensity. Inset shows the relative intensities which have the characteristic MIL-101(Cr) peaks still within the material after deposition.

If this method were to be used, more experiments into altering the HCl concentration need to be completed in order to maintain MOF crystallinity. Additionally, this method would be unlikely to be versatile when extended to different MNPs and MOFs. The stability of MOFs under acidic conditions is very MOF dependent and would require individual optimization. Additionally, solution impregnation does not offer any control over depositing the MNPs within the pores of the MOF, and once optimised would likely form MNPs on both the surface and within the pores. For this reason, the solution impregnation technique was not optimised further and instead the double solvents deposition technique was used.

### 3.3.2.2 Double Solvents Deposition

The double solvents technique, developed by Aijaz *et al.*<sup>7</sup>, utilizes the hydrophilic nature of the coordinatively unsaturated sites within the MOF to strategically deposit MNPs within the MOF pores. The MOF is first activated and then dispersed in a

nonpolar solvent (hexane) by sonication. This enables the nonpolar solvent to surround the MOF crystals as well as break up large MOF agglomerates in the hexane solution. A fine powder of MOF dispersed in the hexane enables more homogeneous capillary action within each crystal for the next step. Next, an aqueous metal salt solution with the volume of 85% of the available MOF pore volume is slowly added to the MOF/hexane dispersion while stirring vigorously. The hydrophilic nature of the MOF pores attracts the aqueous metal salt solution while the nonpolar solvent does not allow the metal salt solution to leave upon entering the pores. After drying and another activation procedure, the MOF material is placed in a tube furnace and the metal salt is reduced to the desired MNPs under a flow of 5% H<sub>2</sub> in N<sub>2</sub> at 200°C. A scheme showing the steps of the double solvents deposition method can be seen in Figure 3.7.

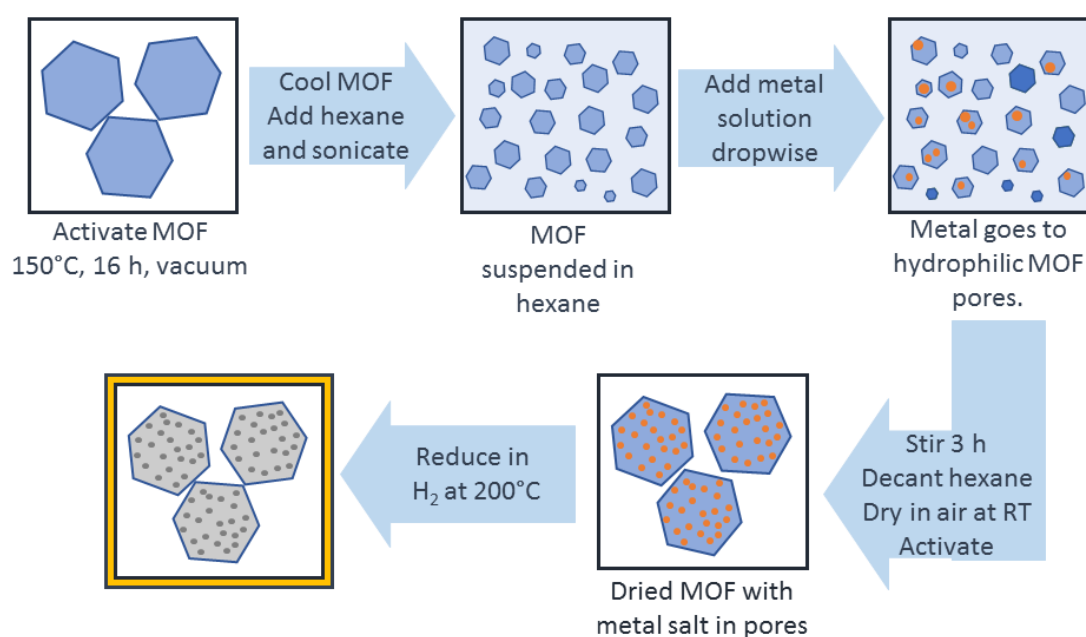


Figure 3.7 Double solvents method for MNP deposition. Adapted procedure developed by Aijaz *et al.*<sup>7</sup>

The steps after the metal salt solution is dispersed in the pores dictate the size and location of the MNPs. If the material is dried in air until the hexane evaporates, followed by reduction, the MNPs are large and are likely to form on the MOF crystal surface rather than be dispersed only in the pores, seen in Figure 3.8a. The step of drying in air to evaporate the hexane and then a second activation under vacuum is critical for the preparation of small, well-dispersed MNPs, shown in Figure 3.8b.

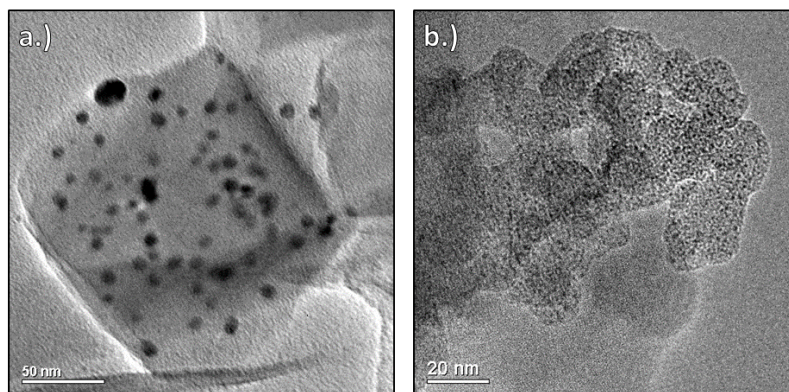


Figure 3.8 Pd in MIL-101(Cr). (a.) TEM of Pd/MOF without a second activation and (b.) with a second activation before reduction.

This deposition method maintains the crystallinity of the MOF as long as the MOF is stable under aqueous conditions. The expansion towards other aqueous stable MOFs is possible, in theory, by altering the amount of aqueous solution, dictated by the MOF pore volume. Exchanging the type of MNP and loadings can be achieved by having a metal salt that is soluble in water and changing the overall concentration of metal salt solution. MNPs consisting of Pd, Au, Pt and Ru have successfully been deposited in MIL-100(Sc) and MIL-101(Cr), seen in Figure 3.9. Au MNPs, in particular, are larger than the other metal particles. This is likely due to the relative ease of reducibility and the greater mobility of Au.

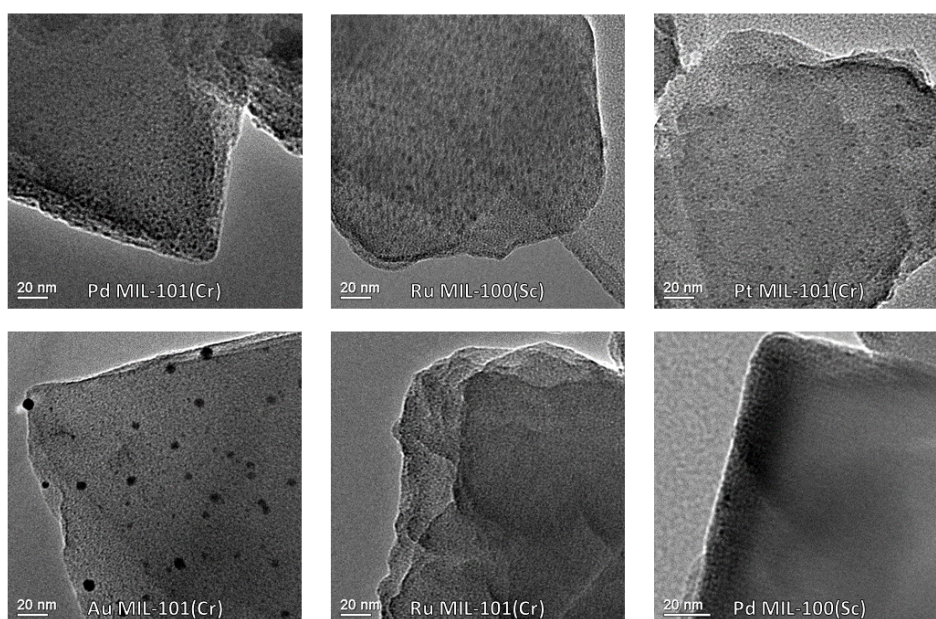


Figure 3.9 MNPs in MOF using the double solvents method for deposition.

Additionally, bimetallic 50:50 PdAu nanoparticles were deposited in MIL-101(Cr). Although the extent of alloying present in this sample, if any, is not determined, EDX shows approximately 1:1 PdAu within the sample. The EDX was averaged over multiple spectra, as the loadings were not constant through the sample. This may be due to areas of Au-rich NPs and areas of Pd-rich NPs within the MOF. Elemental analysis should be performed to get a more accurate total loading. Additionally, extended X-ray absorption fine structure analysis (EXAFS) could indicate the extent of alloying in the nanoparticles. Figure 3.10 shows a representative TEM image as well as an EDX spectrum.

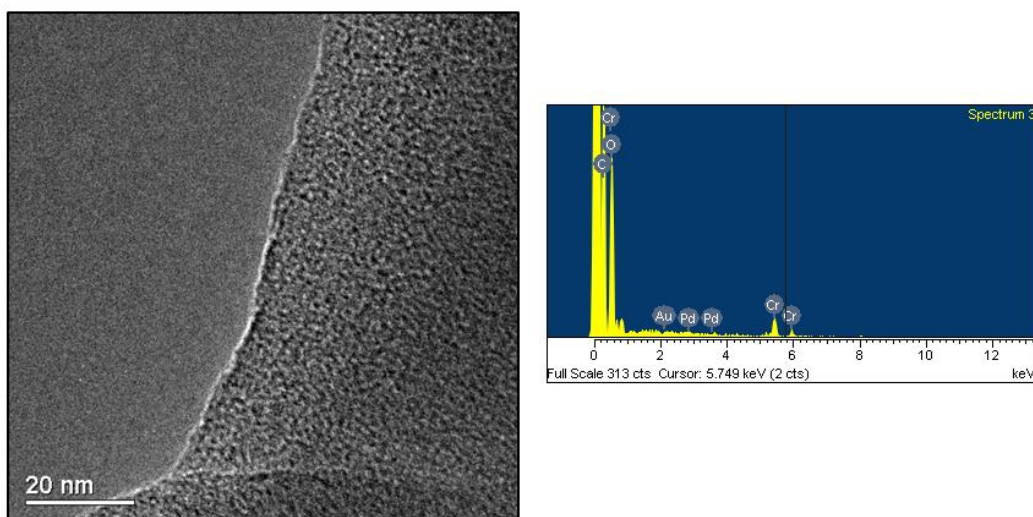


Figure 3.10 TEM image and representative EDX spectrum for 50:50 PdAu MNPs in MIL-101(Cr).

Extensive characterisation of the Pd MIL-101(Cr) materials has been performed. Four MNP loadings of 0.2 wt%, 0.4 wt%, 0.5 wt% and 1.0 wt% were successfully deposited within MIL-101(Cr). Figure 3.11 shows TEM images for the four loadings. In each loading the well-defined crystal edges of the MOF are apparent.

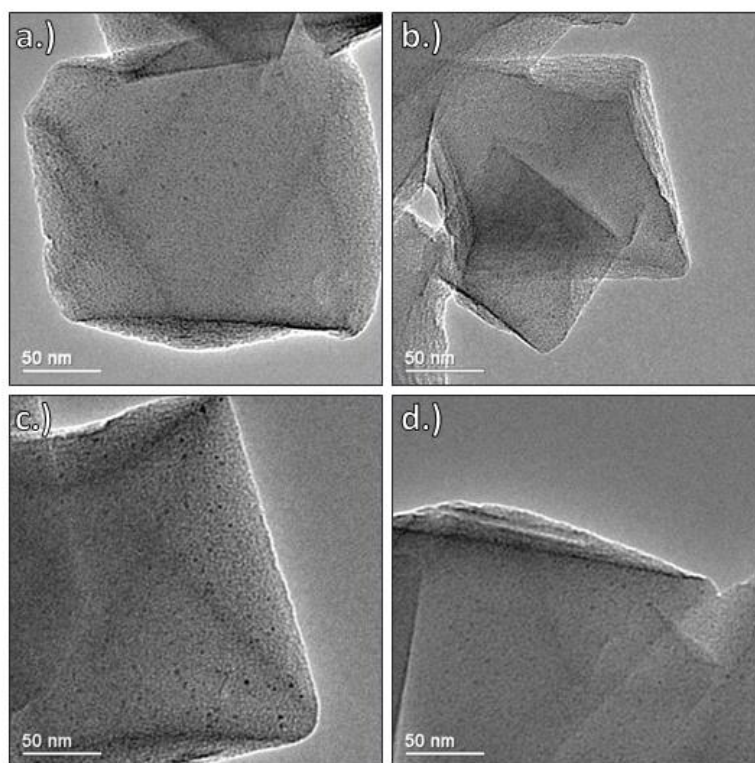


Figure 3.11 Pd in MIL-101(Cr). (a.) 0.2 wt%, (b.) 0.4 wt%, (c.) 0.5 wt% and (d.) 1.0 wt%.

The size distribution of the MNPs, seen in Figure 3.12, has been determined for each loading. In each material over 100 nanoparticles were hand-counted in order to give the size distribution. The hand-counting was deemed necessary because computer-assisted counting proved to be difficult with the uneven (porous) supports.<sup>12</sup> 0.4 wt% Pd in MIL-101(Cr) has more particles with smaller diameters, possibly due to the enhanced TEM resolution achieved whilst imaging this sample. However, when considering the standard deviation of the particle size in each loading shown in Figure 3.13, it was determined all samples have particles that are the same average size within error. In each case the MNP size is roughly the same, this means that as the loadings grow larger the difference is the number of nanoparticles within the material, not the size of the nanoparticles. The MOF successfully immobilises the MNPs as well as limits their size due to the inner pore structure. MIL-101(Cr) has pore cages of 2.9 nm and 3.4 nm in diameter, which are both larger than the average MNP size in each loading. Table 3.1 shows a summary of the physical properties of the materials with varying loading.

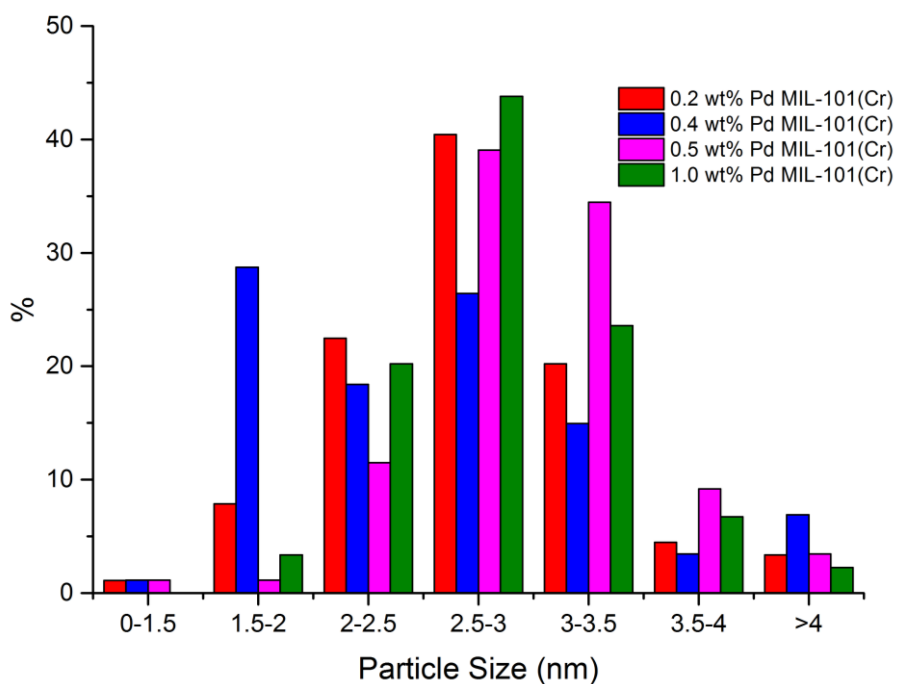


Figure 3.12 0.2-1.0 wt% Pd in MIL-101(Cr) size distributions. Values are taken from multiple TEM images for each sample.

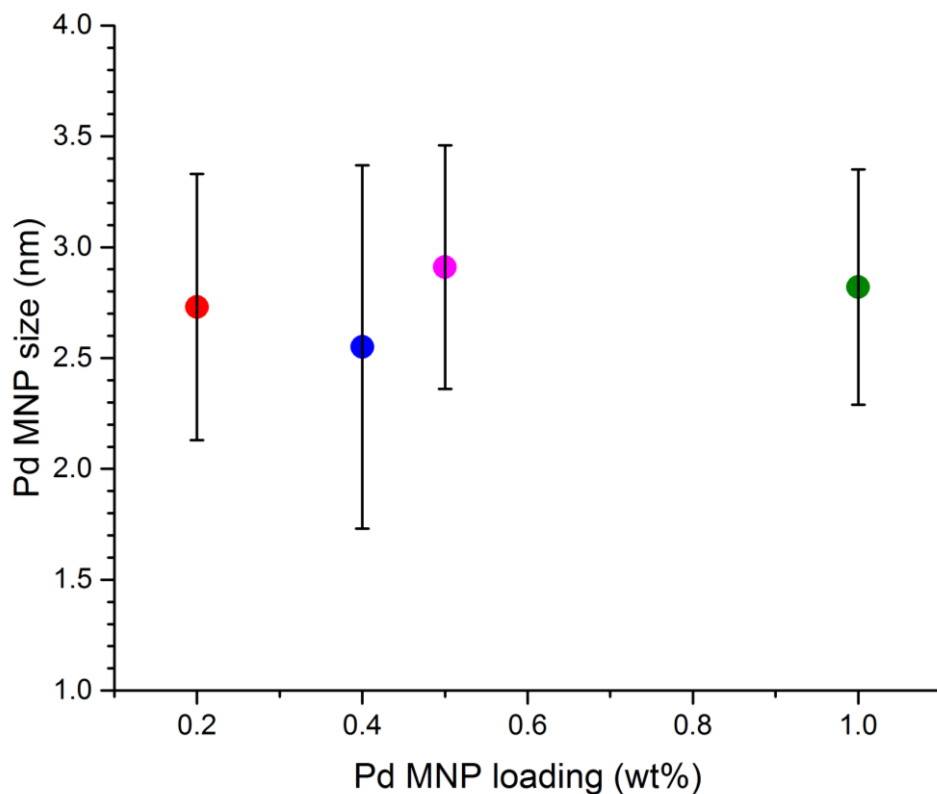


Figure 3.13 Average MNP size with each sample's standard deviation for 0.2-1.0 wt% Pd in MIL-101(Cr).

Table 3.1 Summary of physical properties of Pd in MIL-101(Cr) materials.

Pd Loading (wt%)	BET surface area ( $\text{m}^2 \text{g}^{-1}$ )	Pore volume ( $\text{cm}^3 \text{g}^{-1}$ )	Average Pd size (nm)	Standard deviation
0	3014	1.45	n/a	n/a
0.2	3292	1.61	2.7	0.60
0.4	3061	1.52	2.6	0.82
0.5	3226	1.60	2.9	0.55
1.0	3253	1.63	2.8	0.53

Compared to the parent MIL-101(Cr) material, the MNP loaded materials show a slight increase in  $\text{N}_2$  adsorption, seen in Figure 3.14. This is likely because of the fact that during the double solvents procedure more impurities are washed out from the pores of MIL-101(Cr), leading to higher adsorptions. The pore volume ranges from  $1.45 \text{ cm}^3 \text{ g}^{-1}$  for the parent MOF material to  $1.63 \text{ cm}^3 \text{ g}^{-1}$  for the 1.0 wt% Pd sample. In the original paper for the synthesis for MIL-101(Cr) by Férey *et al.*<sup>2</sup> it was discussed that their pore volumes varied between  $1.5$  and  $1.9 \text{ cm}^3 \text{ g}^{-1}$ , mainly determined by the amount of terephthalic acid within the pore system, which means all materials fit into this range even with the nanoparticles added to the system.

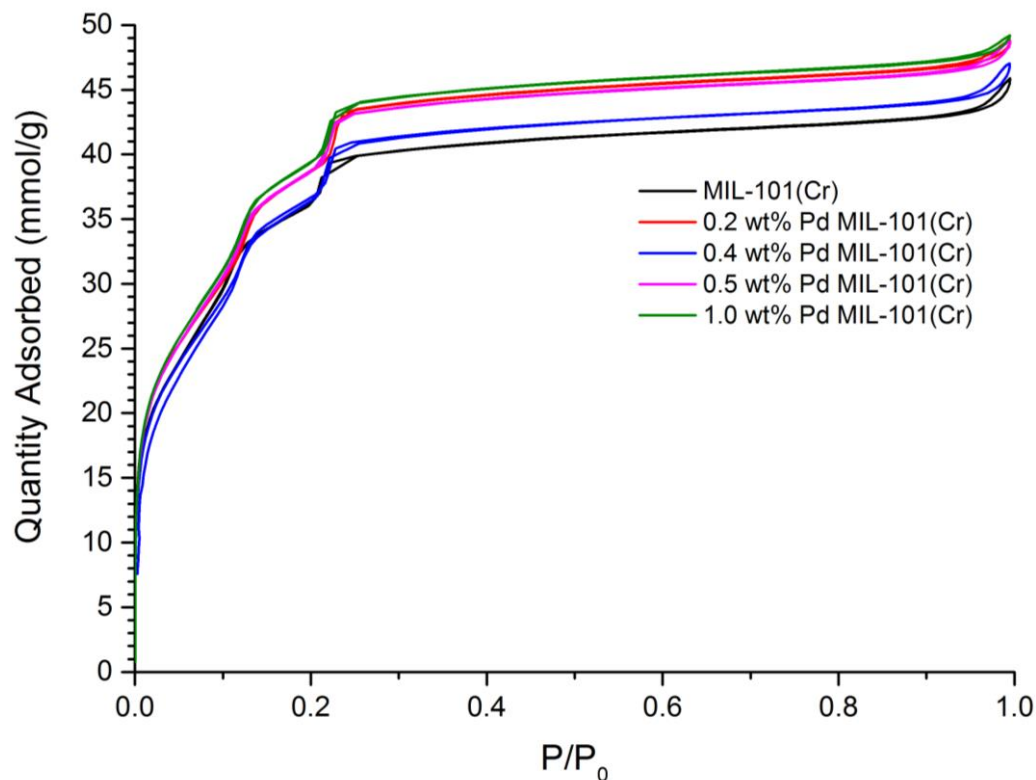


Figure 3.14 N<sub>2</sub> adsorption isotherms for 0.2-1.0 wt% Pd in MIL-101(Cr) materials.

As previously mentioned, the MOF remains crystalline throughout the deposition procedure, seen in XRD patterns in Figure 3.15, and there is no significant difference between the loadings within the MOF XRD patterns. The Pd XRD peaks are not visible, even at larger loadings, seen in Figure 3.16 for 1.0 wt% Pd in MIL-101(Cr). This is likely because the MNPs are very small and the peaks are so broad that they disappear into the background noise as well as the small overall amount of MNP in the system. Even attempts of long acquisition times did not lead to identifiable MNP peaks.

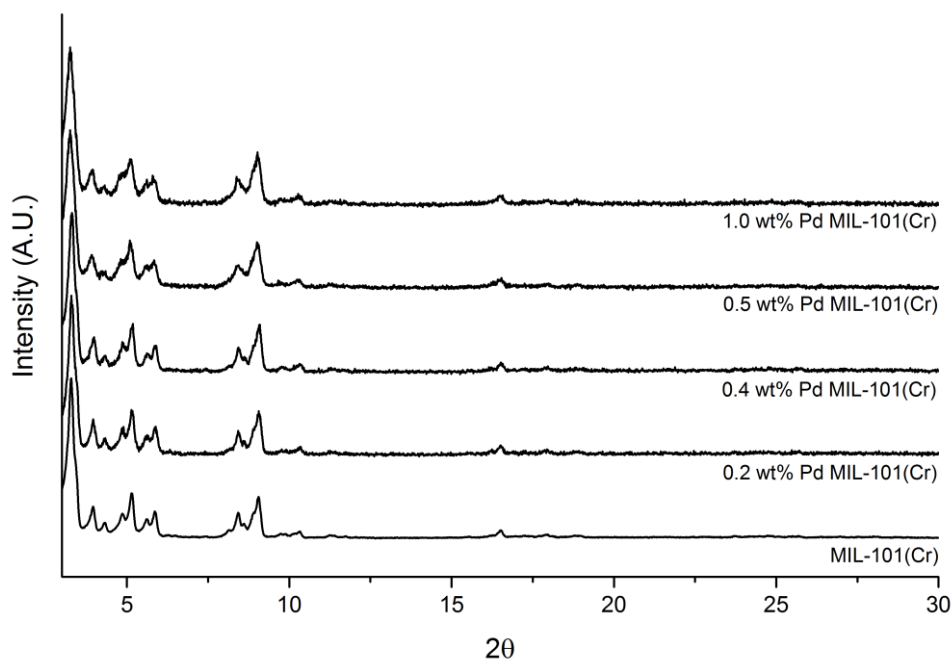


Figure 3.15 XRD patterns of Pd loaded materials. The apparent increase in noise is due to diffractometer configuration change and shorter acquisition times, as the TEM indicates highly crystalline materials remain.

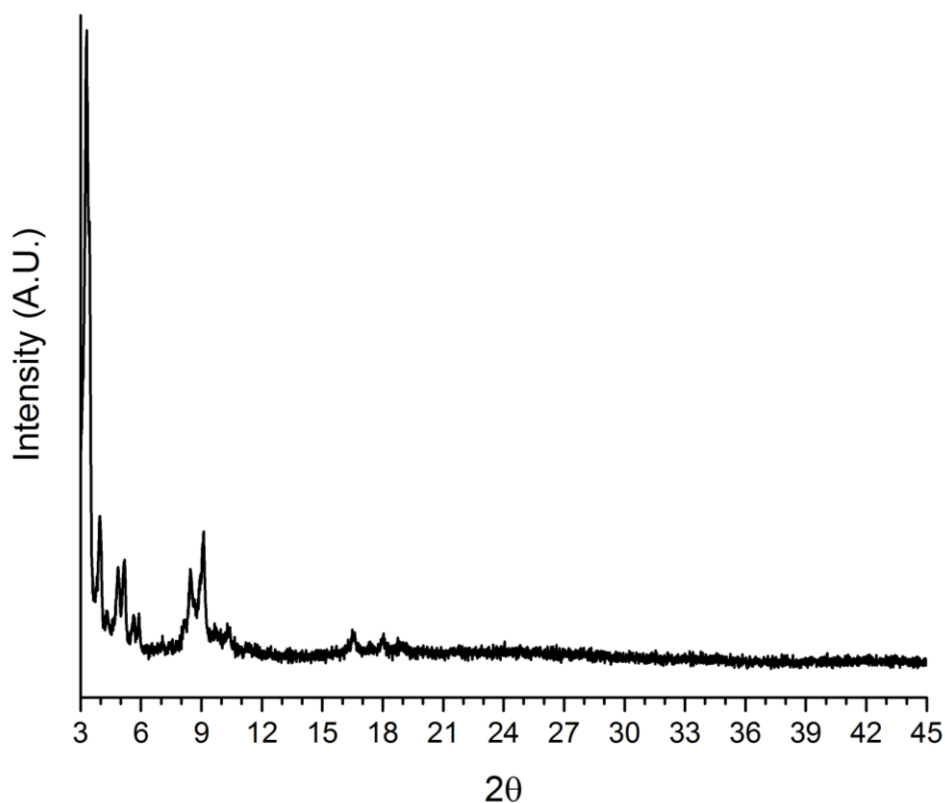


Figure 3.16 1.0 wt% Pd in MIL-101(Cr) extended XRD pattern. Pd(111), the most intense Pd peak, should appear at a  $2\theta$  of 40.1.

XPS was attempted on the Pd in MIL-101(Cr) materials to determine the overall percentage of Pd<sup>0</sup> and PdO within the MNPs. However, this was not conclusive since it did not show any signal for Pd within the system. The Pd NPs are well-dispersed through the MOF crystals, so it is possible there is not a sufficient amount of Pd within the XPS analysis depth of a few nanometers to generate a large enough signal. Extended acquisition times were attempted with the same result. The composition of the MOF support material, however, was readily identifiable by XPS, shown in Figure 3.17.

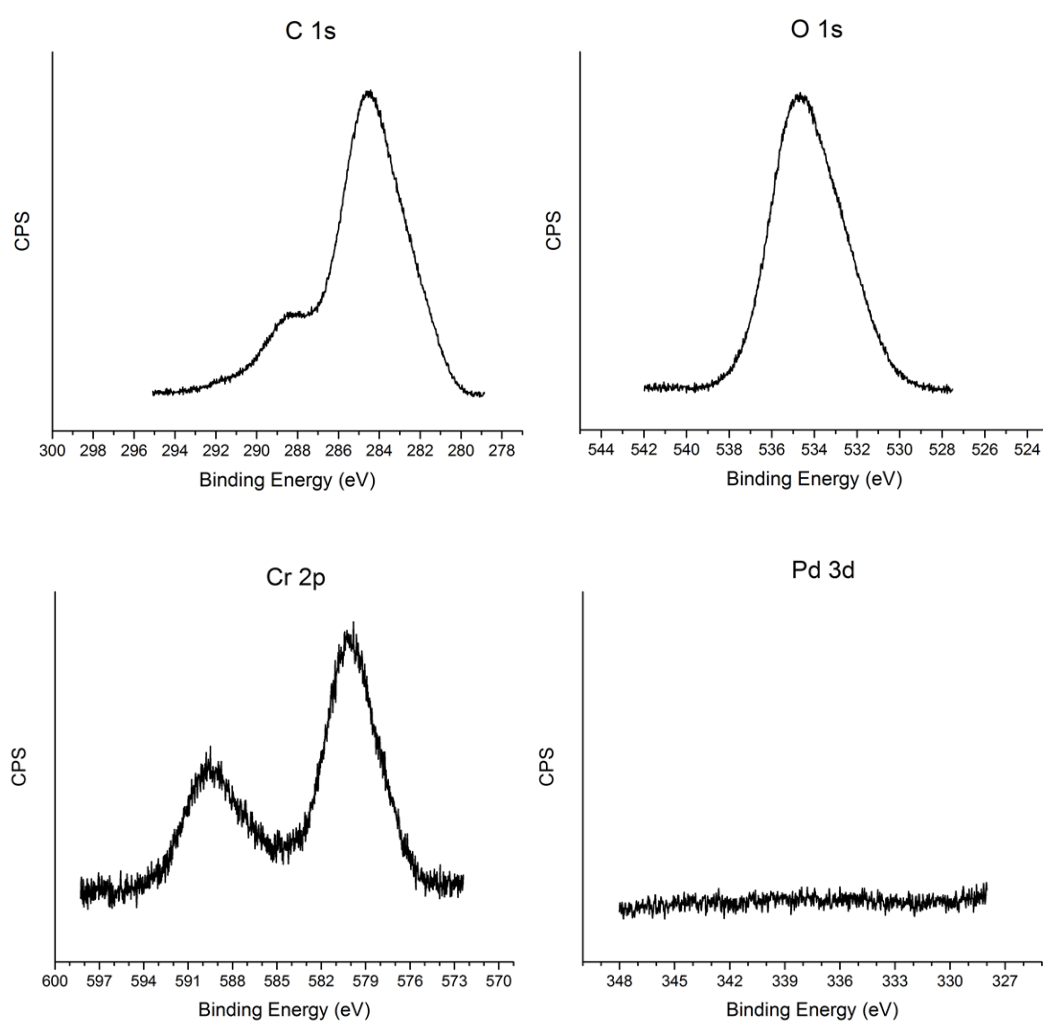


Figure 3.17 XPS of 1.0 wt% Pd MIL-101(Cr)

As previously seen in Figure 3.9, MIL-100(Sc) was also used as a support for MNP deposition. MIL-100(Sc) appears to have small, well-dispersed MNPs within its structure similar to the MIL-101(Cr) materials. However, a size distribution plot, shown for Ru in MIL-100(Sc) in Figure 3.18, indicates many of the MNPs, although small, are not within the size range of the MIL-100(Sc) cages. The large cage of MIL-100(Sc) is 3 nm, which means only 13% of the nanoparticles are small enough to be within a single MOF cage. The average nanoparticle size for the Ru MIL-100(Sc) sample is 3.5 nm. The MNPs are well-dispersed, seen in Figure 3.9, which might indicate some degradation of the MOF crystallinity to allow for a single nanoparticle to consume more than one cage. The XRDs in Figure 3.19 show a significant change in intensity of the peaks in the low  $2\theta$  region, indicating a change in the long-range order of the MOF. The peaks are not significantly broader after nanoparticle deposition, and the MOF remains the same crystalline phase.

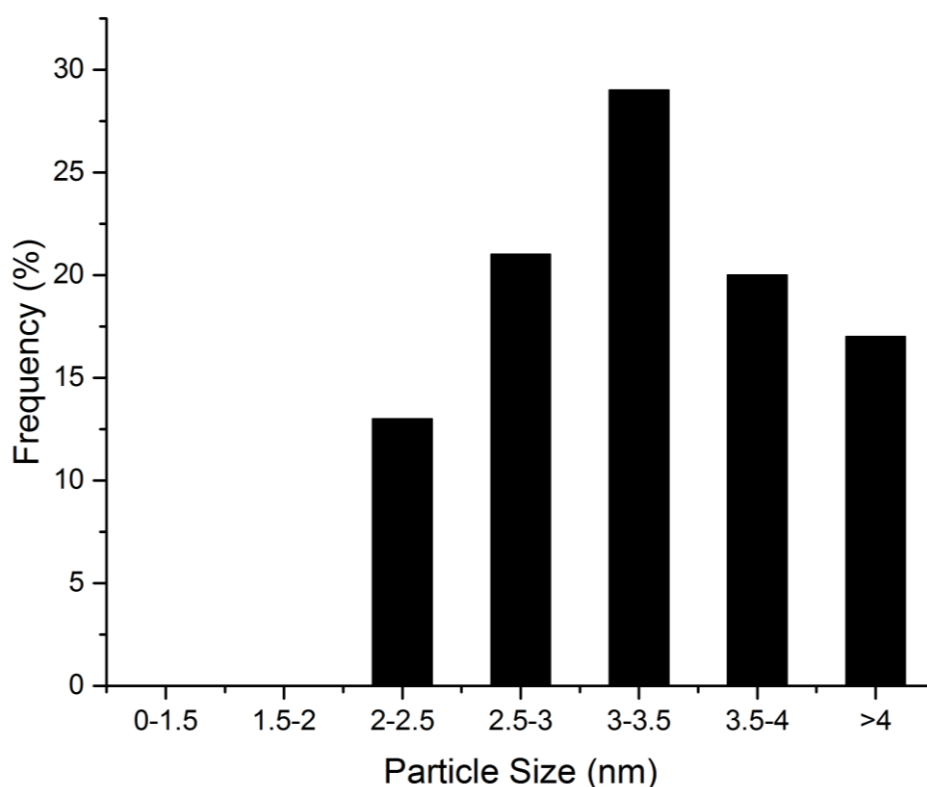


Figure 3.18 Ru MIL-100(Sc) MNP size distribution. Only 13% of the MNPs are within the sizes of the available cages. Values calculated from 70 MNPs from 4 separate TEM images.

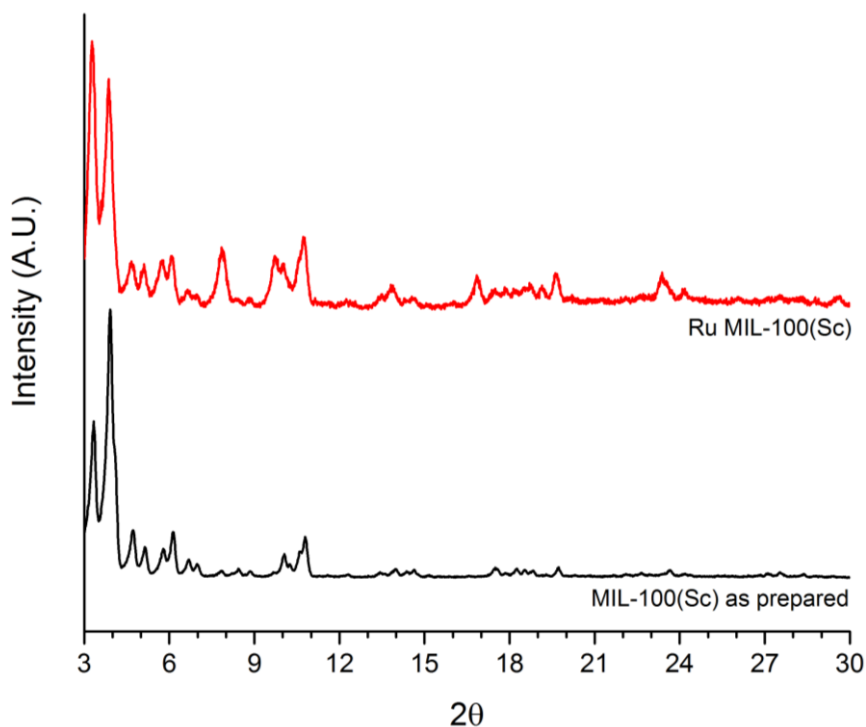


Figure 3.19 Ru MIL-100(Sc). The overall intensities of the peaks have changed, but the MIL-100(Sc) structure remains throughout the MNP deposition.

The TEM images for Pd MIL-100(Sc), previously seen in Figure 3.9, show an overall smaller average size of 3.3 nm and 59% of counted nanoparticles were within MOF cage size. However, only a small amount of MNPs were counted due to the reduced resolution achieved in the TEM, thus making the statistics less reliable than the Ru MIL-100(Sc) sample. The large number of MNPs outside the MIL-100(Sc) pore structure may be due to the small window size when compared to MIL-101. MIL-100(Sc) has a hexagonal window of 0.9 nm and pentagonal window of 0.5 nm which may hinder the metal salt diffusion within the pores during deposition.

Other MOF systems, such as MOF-808(Hf), MIL-101(Cr)-SO<sub>3</sub>H and MIL-100(Fe) were also used as supports for double solvents deposition. MOF-808(Hf), provided by Mr. Ram Prasad, was attempted as a Pd MNP support through the double solvents method but no metal nanoparticles were observed in either TEM or by EDX. The material shows the correct XRD peaks after deposition and reduction, as seen in Figure 3.20, however a significant change in surface area from 1000 m<sup>2</sup> g<sup>-1</sup> to 244 m<sup>2</sup> g<sup>-1</sup> was observed, seen in Figure 3.21. This may indicate MOF-808(Hf) is losing crystallinity throughout the deposition technique and becoming less porous. The TEM images of

Figure 3.22, show no MNPs. MOF-808 has an opening diameter of 1.4 nm and an inner pore diameter of 1.8 nm.<sup>13</sup> This should be large enough for the PdCl<sub>2</sub> to enter the porous network. The obtained results indicate that it is possible that the internal structure of the MOF is diminishing.

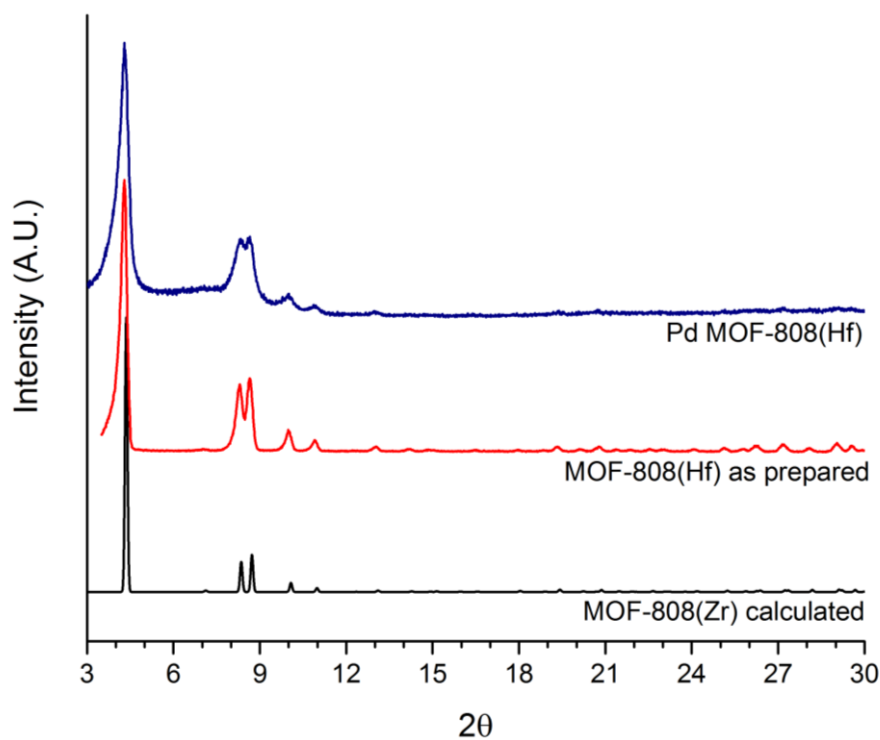


Figure 3.20 Pd MOF-808(Hf) XRD after double solvents deposition and reduction.

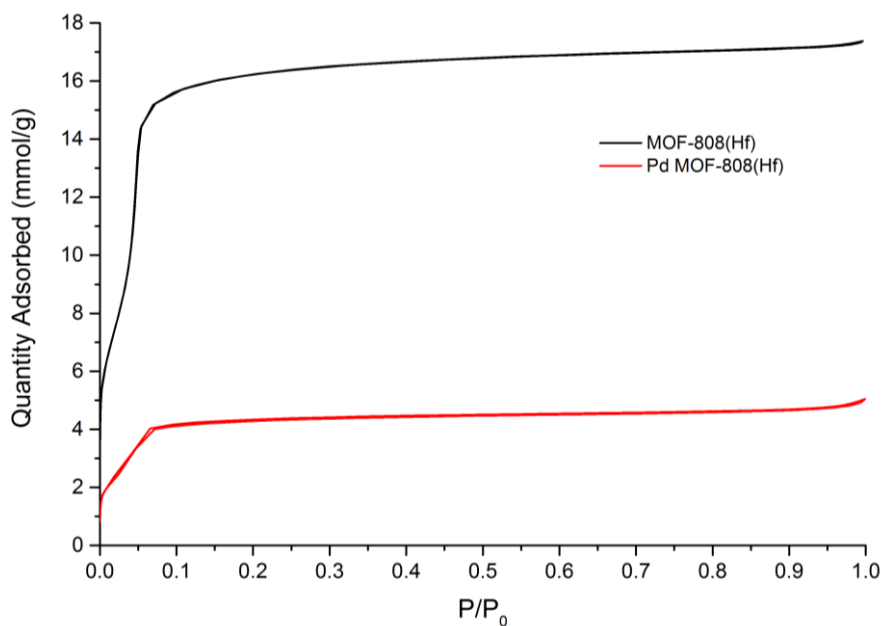


Figure 3.21 N<sub>2</sub> adsorption isotherms showing the decrease in surface area after the Pd deposition procedure. Isotherms were collected by Mr. Ram Prasad.

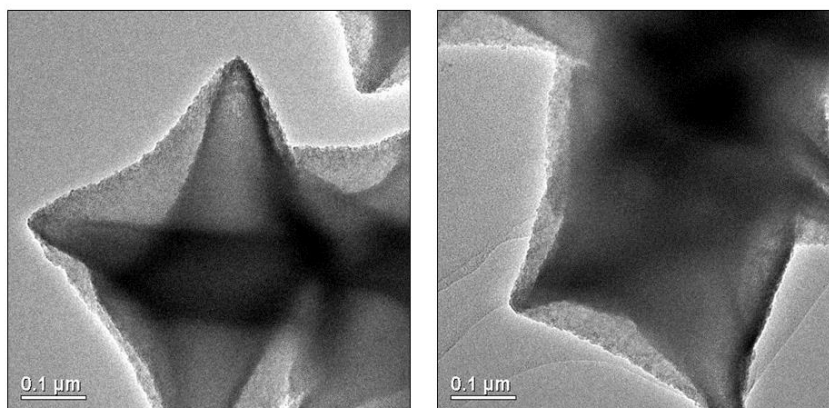


Figure 3.22 Pd MOF-808(Hf) TEM images showing the MOF-808 material, but no apparent MNPs.

MIL-101(Cr)-SO<sub>3</sub>H, also provided by Mr. Ram Prasad, was thought as a good candidate due to the additional acidity the SO<sub>3</sub>H group provides, which might lead to an enhancement in catalysis. However, this MOF was not as stable as the parent MIL-101(Cr), and the change from terephthalic acid to SO<sub>3</sub>H-functionalised terephthalic acid proved to be detrimental to the stability needed for nanoparticle deposition. The lack of stability compared to MIL-101(Cr) has previously been shown, however it was determined the MIL-101(Cr)-SO<sub>3</sub>H structure can withstand up to

300°C,<sup>14</sup> which was initially thought to be stable enough for the double solvents deposition procedure. The resulting material showed no crystallinity.

MIL-100(Fe) was also attempted for use as a support for Pd MNPs. However, this support material was also not able to withstand the MNP deposition procedure, and became amorphous after MNP reduction.

### **3.4 Conclusions and Outlook**

MIL-101(Cr) was successfully prepared and optimised to obtain a highly porous MOF for MNP support. The optimised preparation of MIL-101(Cr) included centrifugation of the reaction mixture and further washing by heating in ethanol. These steps help reduce the amount of excess terephthalic acid left in the pores of the MOF. Removing the unreacted terephthalic acid leads to a more porous material, which is beneficial for subsequent MNP deposition.

MIL-100(Sc) was prepared in three different ways; autoclave, reflux and microwave. All three methods produced crystalline materials. The microwave approach was the preferred method of choice due to the speed of preparation when compared to the other two methods.

Metal nanoparticle deposition was performed using two different approaches. Metal nanoparticle deposition by solution impregnation led to significant degradation of the MIL-101(Cr) support material, and was not further optimised. The double solvents method, a modified incipient wetness approach, was found to produce dispersed and small MNPs within the MOF.

Various loadings of metal into MIL-101(Cr) were examined. Pd loadings of 0.2, 0.4, 0.5 and 1.0 wt% were prepared and characterised. These materials show the same nanoparticle size within the MOF material, indicating that altering the loading amount changes the number of metal nanoparticles rather than the size of the nanoparticles. The MNP/MOF materials remained crystalline and highly porous. XPS was shown to be unsuitable for determining the oxidation state of the Pd particles, due to the immobilisation of the MNPs within the MOF pores rather than on the surface.

Depositing Ru into MIL-100(Sc) led to nanoparticles which were too large to fit within the intact MOF cages. Using Pd led to a smaller overall nanoparticle size, but an estimated 40% of MNPs are still too large to fit within the 3 nm large cage.

Other MOF systems were attempted, but in most cases led to amorphous materials, probably due to the combination of limited stability in water as well as instability to heating during the deposition procedure. Catalytic investigation of the successful MNP/MOF materials is discussed in Chapter 4.

It appears that MIL-101(Cr) is unique among the MOFs examined in its capability to withstand the water and heat treatments necessary for double solvent deposition. It was the only MOF tried which obtained well-defined MNP in MOF catalysts. However, further studies should be performed with different MOFs to develop alternate MNP/MOF systems. For this, the MOF must be stable in aqueous solutions as well as stable at 200°C for prolonged periods, due to the necessary step of MNP reduction. Recently reported mesoporous MOFs with Zr clusters have shown significant thermal and chemical stability, as well as Lewis acidity, and may be good candidates for the double solvents deposition method.

### 3.5 References

1. Lee, J.; Farha, O. K.; Roberts, J.; Scheidt, K. A.; Nguyen, S. T.; Hupp, J. T., Metal-Organic Framework Materials as Catalysts. *Chem. Soc. Rev.* **2009**, *38*, 1450-1459.
2. Férey, G.; Mellot-Draznieks, C.; Serre, C.; Millange, F.; Dutour, J.; Surblé, S.; Margiolaki, I., A Chromium Terephthalate-Based Solid with Unusually Large Pore Volumes and Surface Area. *Science* **2005**, *309*, 2040-2042.
3. Zhao, T.; Jeremias, F.; Boldog, I.; Nguyen, B.; Henninger, S. K.; Janiak, C., High-Yield, Fluoride-Free and Large-Scale Synthesis of MIL-101(Cr). *Dalton Trans.* **2015**, *44*, 16791-801.
4. Bhattacharjee, S.; Chen, C.; Ahn, W.-S., Chromium Terephthalate Metal-Organic Framework MIL-101: Synthesis, Functionalization, and Applications for Adsorption and Catalysis. *RSC Adv.* **2014**, *4*, 52500-52525.
5. Mitchell, L.; Gonzalez-Santiago, B.; Mowat, J. P. S.; Gunn, M. E.; Williamson, P.; Acerbi, N.; Clarke, M. L.; Wright, P. A., Remarkable Lewis Acid Catalytic Performance of the Scandium Trimesate Metal Organic Framework MIL-100(Sc) for C–C and C=N Bond-Forming Reactions. *Catal. Sci. Tech.* **2013**, *3*, 606-617.
6. Zlotea, C.; Campesi, R.; Cuevas, F.; Leroy, E.; Dibandjo, P.; Volkringer, C.; Loiseau, T.; Férey, G.; Latroche, M., Pd Nanoparticles Embedded into a Metal-Organic Framework: Synthesis, Structural Characteristics, and Hydrogen Sorption Properties. *J. Am. Chem. Soc.* **2010**, *132*, 2991-2997.
7. Aijaz, A.; Karkamkar, A.; Choi, Y. J.; Tsumori, N.; Ronnebro, E.; Autrey, T.; Shioyama, H.; Xu, Q., Immobilizing Highly Catalytically Active Pt Nanoparticles inside the Pores of Metal-Organic Framework: A Double Solvents Approach. *J. Am. Chem. Soc.* **2012**, *134*, 13926-9.
8. Zhu, Q. L.; Li, J.; Xu, Q., Immobilizing Metal Nanoparticles to Metal-Organic Frameworks with Size and Location Control for Optimizing Catalytic Performance. *J. Am. Chem. Soc.* **2013**, *135*, 10210-10213.
9. Chen, Y.-Z.; Zhou, Y.-X.; Wang, H.; Lu, J.; Uchida, T.; Xu, Q.; Yu, S.-H.; Jiang, H.-L., Multifunctional PdAg@MIL-101 for One-Pot Cascade Reactions: Combination of Host-Guest Cooperation and Bimetallic Synergy in Catalysis. *ACS Catal.* **2015**, *5*, 2062-2069.
10. García Márquez, A.; Demessence, A.; Platero-Prats, A. E.; Heurtaux, D.; Horcajada, P.; Serre, C.; Chang, J.-S.; Férey, G.; de la Peña-O'Shea, V. A.; Boissière, C.; Grosso, D.; Sanchez, C., Green Microwave Synthesis of MIL-100(Al, Cr, Fe) Nanoparticles for Thin-Film Elaboration. *Eur. J. Inorg. Chem.* **2012**, *2012*, 5165-5174.
11. Mitchell, L.; Williamson, P.; Ehrlichova, B.; Anderson, A. E.; Seymour, V. R.; Ashbrook, S. E.; Acerbi, N.; Daniels, L. M.; Walton, R. I.; Clarke, M. L.; Wright, P. A., Mixed-Metal MIL-100(Sc,M) (M=Al, Cr, Fe) for Lewis Acid Catalysis and Tandem C-C Bond Formation and Alcohol Oxidation. *Chem. Eur. J.* **2014**, *20*, 17185-17197.
12. Gontard, L. C.; Ozkaya, D.; Dunin-Borkowski, R. E., A Simple Algorithm for Measuring Particle Size Distributions on an Uneven Background from TEM Images. *Ultramicroscopy* **2011**, *111*, 101-106.
13. Jiang, J.; Gándara, F.; Zhang, Y.-B.; Na, K.; Yaghi, O. M.; Klemperer, W. G., Superacidity in Sulfated Metal-Organic Framework-808. *J. Am. Chem. Soc.* **2014**, *136*, 12844-12847.

14. Zhang, D.; Ye, F.; Guan, Y.; Wang, Y.; Hensen, E. J. M., Hydrogenation Of  $\gamma$ -Valerolactone in Ethanol over Pd Nanoparticles Supported on Sulfonic Acid Functionalized MIL-101. *RSC Adv.* **2014**, *4*, 39558-39564.

# Chapter 4

---

Multifunctional MOF and MNP/MOF Materials:

The Influence of the MOF Support on MNP Catalysis and Tandem

MNP/MOF Catalysis

## 4.1 Introduction

After synthesis and characterization of the multifunctional MOF-supported metal nanoparticle catalysts discussed in Chapter 3, the materials were screened in various catalytic applications. The benchmark reaction which was found to be a good probe of both Lewis acid site and MNP site was a reductive amination reaction.

A similar reaction has been reported by Cirujano *et al.* and Chen *et al.* with MNP deposited in MIL-101(Cr), the latter during the course of the work of this thesis.<sup>1-2</sup> In the results published by Cirujano *et al.* the one-pot tandem reductive amination was catalysed by Pd or Pt MNPs within MIL-101(Cr). In the first step, the metal nanoparticles reduced nitrobenzene to aniline in the presence of hydrogen. Next, an imine was formed by a condensation reaction between the previously formed amine and an aldehyde or ketone, catalysed by the MIL-101(Cr) Lewis acid sites. Finally, the imine underwent reduction on the Pd or Pt MNP to form a desired secondary amine. The general reaction schemes can be seen in Figure 4.1.

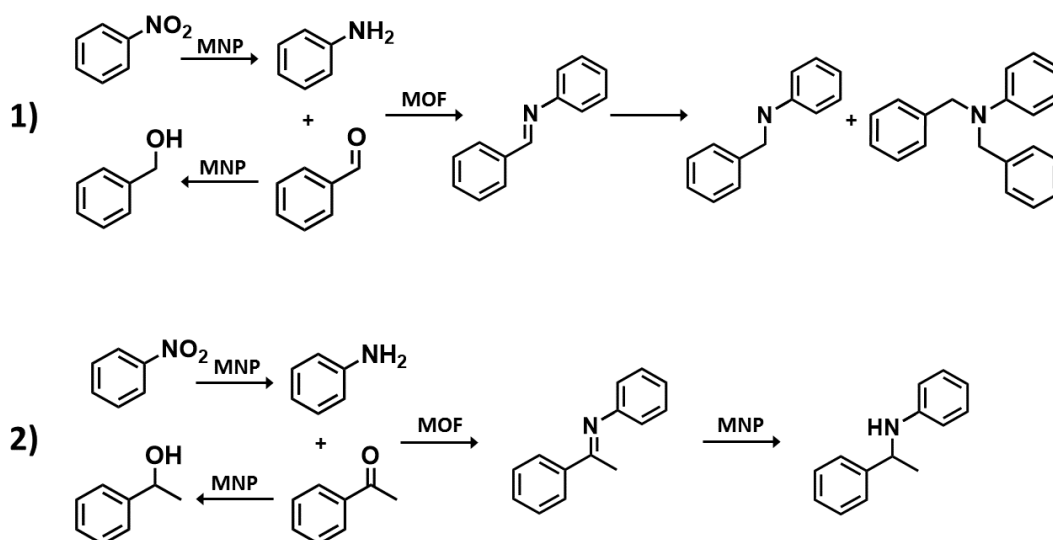


Figure 4.1 Two reductive amination schemes to form secondary arylamines. Reaction 1 begins with nitrobenzene and benzaldehyde. Reaction 2 begins with nitrobenzene and acetophenone. In the work by Cirujano *et al.* the reactions are performed at 110 °C and 5 bar H<sub>2</sub>.

In the Cirujano *et al.* work the metal nanoparticles were synthesized using two different approaches within MIL-101(Cr). In the first method, an incipient wetness procedure using aqueous solutions of Pd(NO<sub>3</sub>)<sub>2</sub>·2H<sub>2</sub>O or K<sub>2</sub>PtCl<sub>4</sub> was added to MIL-

MIL-101(Cr) and then reduced to form MNPs. Another approach was attempted which begins with the synthesis of MIL-101(Cr)-NH<sub>2</sub> as the support material. Subsequently, the Pd or Pt was added dropwise to a slurry of acetonitrile and MOF. The Pd or Pt in MIL-101(Cr) materials synthesized using the incipient wetness procedure were found to perform worse than the materials which utilised the -NH<sub>2</sub> functionality. When performing reaction 1, depicted in Figure 4.1, using the Pd in MIL-101(Cr)-NH<sub>2</sub> at 110 °C and 5 bar H<sub>2</sub>, full conversion was obtained in 6 hours with an overall selectivity of 90% to the desired 2° amine. Comparing the incipient wetness deposition Pd MIL-101(Cr) material, full conversion was also achieved after 6 hours but with a lower selectivity of only 75% to the desired 2° amine. In the case of the more challenging reaction 2 (see Figure 4.1) under the same conditions, the Pd in MIL-101(Cr)-NH<sub>2</sub> obtained full conversion in 60 hours with 93% selectivity to the 2° amine. The Pd in MIL-101(Cr) material on the other hand, obtained full conversion in 70 hours with 82% selectivity towards the desired 2° amine. This change in selectivity was proposed to be due to not only the change in size and dispersion of the metal nanoparticles between the unfunctionalised and functionalised MIL-101(Cr), but also likely due to the change of the support itself.

Chen *et al.* utilized PdAg nanoparticles in MIL-101(Cr) in multifunctional tandem reactions.<sup>2</sup> In this report the catalysts are made using the double solvent nanoparticle deposition method, as discussed and demonstrated in Chapter 3. The same reductive amination reactions which have been investigated in the Cirujano *et al.* work were also utilised here in which both the MIL-101(Cr) acid sites and the PdAg sites act as separate active catalysts. The Pd MNPs synthesised in the Chen *et al.* study are much less selective than the Pd MIL-101(Cr) catalysts published by Cirujano *et al.*, even at a lower pressure of 2 bar. It was found, however, that the selectivity of the reaction towards the desired secondary amine could be tuned by utilizing bimetallic PdAg MNPs and varying the ratio of the two metals. Using a Pd<sub>2</sub>Ag<sub>1</sub> MIL-101(Cr) catalyst, 99% conversion was achieved in 10 hours with an 85% selectivity towards the desired 2° amine for the reaction starting from nitrobenzene and benzaldehyde. In the more challenging reaction starting with nitrobenzene and acetophenone, the Pd<sub>2</sub>Ag<sub>1</sub> MIL-

101(Cr) catalyst achieved 65% conversion in 30 hours with 71% selectivity towards the desired 2° amine product. It is difficult to compare the two literature reported catalysts because of the slightly different reaction conditions and times. It would be interesting to see the selectivity of the PdAg catalyst at full conversion of the more challenging reaction and to know at what time the full conversion occurs.

Herein, a similar multi-step reductive amination reaction was investigated as a model reaction in order to tune selectivity and activity towards the 2° amine product, shown in Figure 4.2. In this work, fluorine-containing substrates are chosen in order to readily monitor the reaction progress by  $^{19}\text{F}$  NMR. This reaction progression was identified with a combination of  $^{19}\text{F}$  NMR and GC analysis.

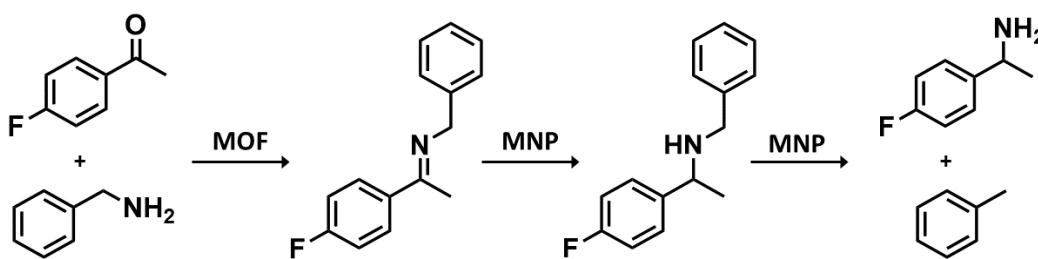


Figure 4.2 Reductive amination reaction used in this work.

The first step of the tandem reaction is the condensation of 4'-fluoroacetophenone and benzylamine facilitated by the Lewis acid site in the MOF to form an imine. The imine formation is accelerated by using an excess of benzylamine (2 equiv.).<sup>3</sup> The imine then reacts on the palladium nanoparticle surface to reduce to the desired secondary amine in the presence of hydrogen. Under certain conditions, the palladium nanoparticles can catalyse further reaction of the desired 2° amine product leading to decomposition into a primary amine and toluene. The goal was to minimize the decomposition of the desired product while maximising the rates of the other reactions to obtain high activity and selectivity towards the 2° amine. To achieve the desired high selectivity, a balance between active MOF sites as well as active metal nanoparticles is necessary.

Within this chapter, the results of the reductive amination reaction catalysed by Pd in MIL-100(Sc) and MIL-101(Cr) at 50 °C are given (section 4.3). From these findings, Pd in

MIL-101(Cr) was synthesised with different MNP loadings and tested at higher temperatures (90 °C) to achieve full conversion (section 4.4). The nanoparticles in MOF catalysts were also tested in other reactions to investigate the activity and selectivity of these multifunctional systems (section 4.5). Finally, addition of polyoxometalates to the MOF materials was investigated in order to increase acidity of the MOF support and stabilise the MOF structure. These modified MOF materials were then tested in metal nanoparticle deposition procedures in an attempt to synthesise a more active multifunctional catalyst (section 4.6).

## 4.2 Experimental

### 4.2.1 Reductive Amination Catalysis Testing

In a typical catalysis run 5 mol% MOF catalyst (activated at 150 °C for 4 hours under vacuum) was combined with dry hexane under a nitrogen atmosphere. Catalyst amount was calculated using the full MOF molecular weight using the molar quantity of 4'-fluoroacetophenone used in the catalysis. 4'-fluoroacetophenone and benzylamine were added to the mixture in a 1:2 molar ratio. Three reaction scales were used, with the smallest total amount in kinetic experiments and the largest in recycling experiments to be able to easily recover catalyst for the next run. Typical reaction amounts for MIL-101(Cr) catalysts can be found in Table 4.1.

Table 4.1 Typical reaction amounts for each type of reductive amination catalysis run.

Reaction Type	MIL-101(Cr) (mg)	4'-fluoroacetophenone (ml)	benzylamine (ml)
Kinetics	2	0.0071	0.0127
Typical	10	0.03	0.06
Recycling	20	0.07	0.13

The vials were sealed, pierced with needles then loaded into a stainless steel autoclave and pressurised with H<sub>2</sub> to 10 bar. The autoclave was then placed into a heated oil bath and kept at the desired temperature for the duration of the reaction. The reaction was stopped by placing the autoclave in a water bath to cool quickly, then depressurised. Upon cooling and depressurising the autoclave was opened and the

vials were centrifuged to separate the catalyst from the reaction mixture. Minimal solvent loss was observed in each scale of reaction. Conversions and selectivities were determined using  $^{19}\text{F}$  NMR on a Bruker AV 400 machine and gas chromatography on a Thermo Trace GC ultra was used to qualitatively observe other non-fluorinated species. The following GC conditions were used: with a Restek RTX-1 (30 m x 0.25 mm x 0.25  $\mu\text{m}$ ) column, 50  $^{\circ}\text{C}$  start, ramp 8  $^{\circ}\text{C min}^{-1}$  to 70  $^{\circ}\text{C}$ , hold 2 min. Ramp 20  $^{\circ}\text{C min}^{-1}$  to 300  $^{\circ}\text{C}$ , hold 1 min.

#### 4.2.1.1 Secondary Reactions

Through GC analysis it was observed that in the cases where there is a large  $1^{\circ}$  amine concentration, the benzylamine is not present in double the concentration of 4'-fluoroacetophenone. This implies that another reaction is occurring on the Pd MNPs which converts benzylamine into toluene and ammonia. This also seemed to be confirmed in GC by the fact that the toluene and  $1^{\circ}$  amine were not present in a 1:1 ratio. This implies that the decomposition of the  $2^{\circ}$  amine is not the sole pathway to toluene formation. The suggested reaction pathway for the decomposition of benzylamine is shown in Figure 4.3. However, the consumption of benzylamine does not seem to drastically compete with the imine formation reaction, as it is only observed at long reaction times, after the consumption of the 4'-fluoroacetophenone.

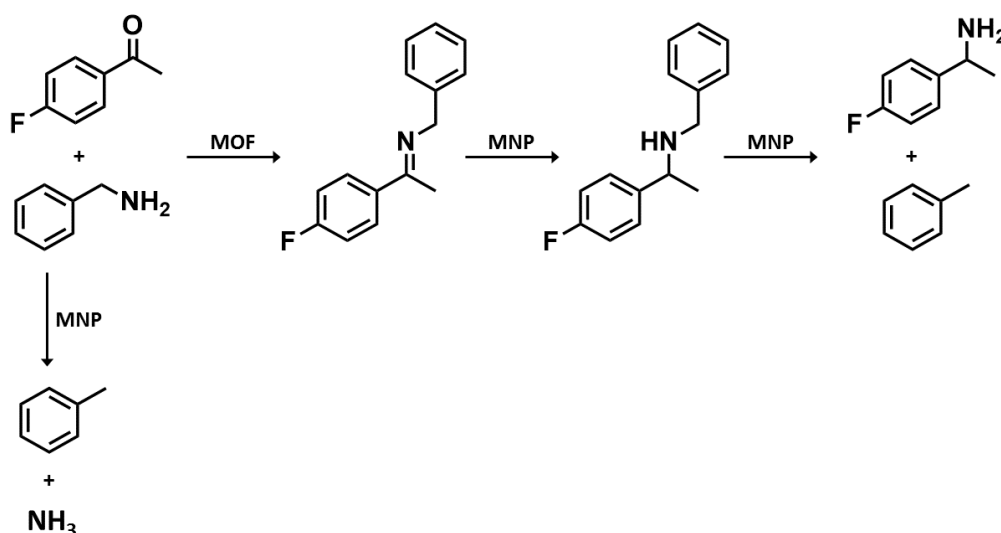


Figure 4.3 Tandem reaction with the decomposition of benzylamine. This alternative benzylamine reaction is observed when the activity of the Pd is very high.

Representative GC traces, showing the formation of toluene, primary fluorinated amine, and the lack of 1:1 ratio between these two species can be seen in Figure 4.4.

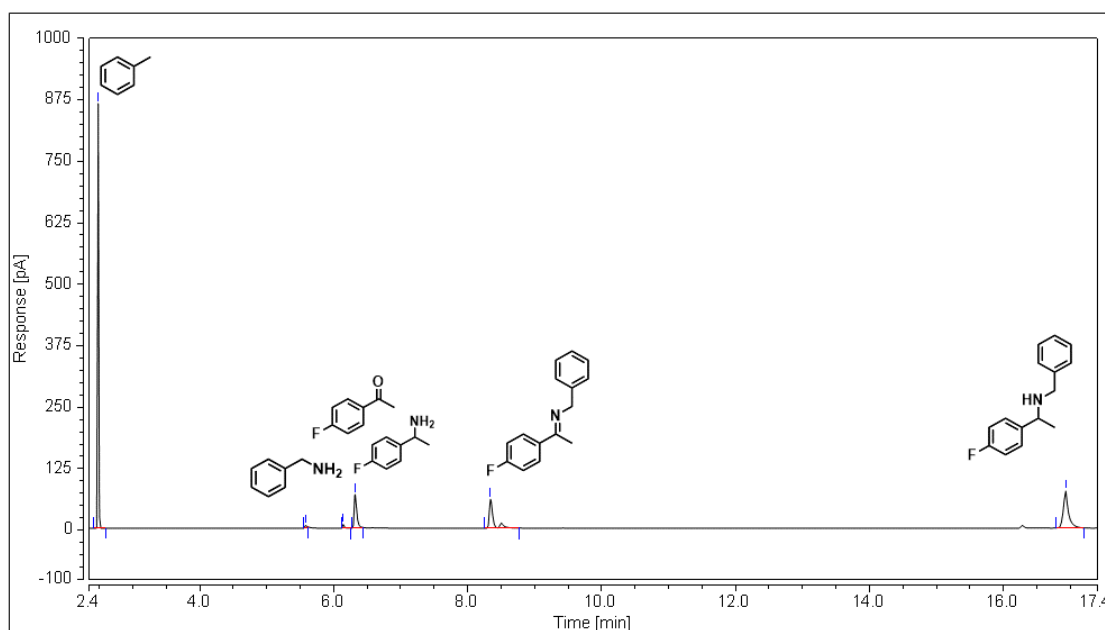


Figure 4.4 Representative GC analysis from 0.5 wt% Pd in MIL-101(Cr) after a 16 hour reductive amination reaction at 90 °C. The large toluene signal as well as the diminished benzylamine signal indicate the alternate reaction pathway.

In attempts to track this reaction, the tandem reaction was performed at 90 °C with 4-fluorobenzylamine instead of benzylamine, shown in Figure 4.5. By using the fluorinated analogues of both substrates, the overall reaction can be readily monitored using  $^{19}\text{F}$  NMR.

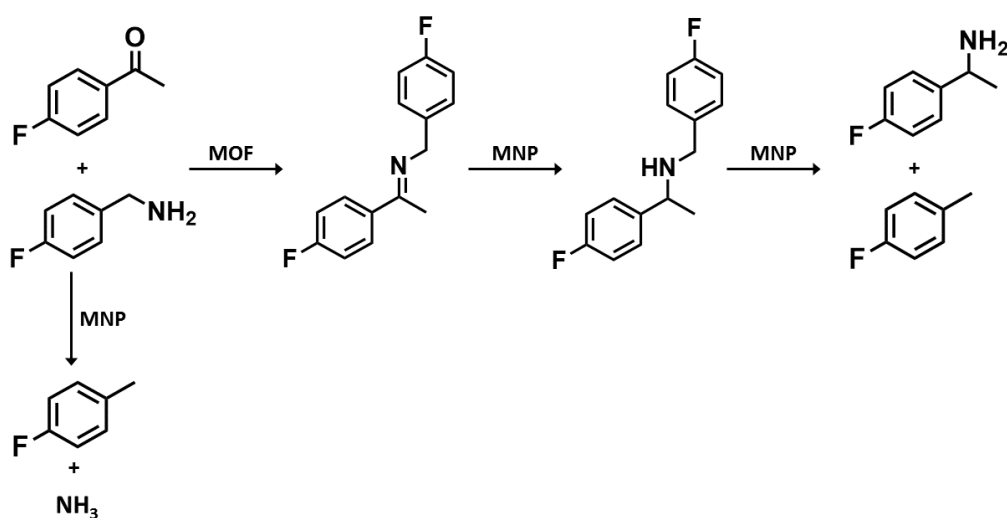


Figure 4.5 Modified tandem reaction scheme using fluorinated benzylamine.

Using the 1.0 wt% Pd MIL-101(Cr) catalyst, which previously showed the largest consumption of benzylamine through GC, the reaction was analysed after a reaction time of 16 hours. The  $^{19}\text{F}$  NMR showed two signals, as expected, for both the imine and 2° amine products. However, no decomposition of 2° amine to 1° amine occurred and no decomposition of 4-fluorobenzylamine into 4-fluorotoluene was observed. Possibly the higher electronegativity of the fluorine group has an influence that prevents decomposition on the Pd MNP, preventing this side-reaction. Comparing this result to previous reductive amination experiments published by Cirujano *et al.*<sup>1</sup>, this could be the reason the ketone is not reduced to an alcohol as described. The difference between the two reductive amination reactions is that Cirujano and coworkers did not use fluorinated species to track the reaction through  $^{19}\text{F}$  NMR.

Interestingly, in the work by Cirujano *et al.* no decomposition of the 2° amine was mentioned. Yap *et al.* published a report of a similar reductive amination reaction performed by Pd/C where it was found that the decomposition of 2° amine to 1° amine does occur.<sup>4</sup> It is possible that when following the reaction by GC, since the retention times for the 1° amine and the alcohol product are similar, there might be overlap between the two peaks. Alternatively, the difference in preparation of the Pd MIL-101(Cr) catalysts could provide enough change to allow for this alternative decomposition pathway.

#### 4.2.2 Citronellal to Menthol

In a typical reaction, 8 mol% MOF catalyst, calculated by the total MOF molecular weight compared to the molar amount of ( $\pm$ )-citronellal, was added to 3 ml dry cyclohexane with ( $\pm$ )-citronellal. The reaction vial was sealed then pierced with needles. The vial was then placed into an autoclave and pressurised to 8 bar H<sub>2</sub>. The reaction was heated at 80 °C for 16 hours. The reaction was quenched by placing the autoclave in cold water and upon cooling the vessel was depressurised. The vials were removed and centrifuged to separate catalyst from reaction mixture. The conversions and selectivities were determined by GC analysis with a Thermo Trace GC ultra. GC conditions: with a Restek RTX-1 (30 m x 0.25 mm x 0.25  $\mu$ m) column, 80 °C isothermal for 20 minutes.

#### 4.2.3 Chloronitrobenzene to Chloroaniline

Typically, 3 mol% MOF catalyst, calculated by the total MOF molecular weight compared to the molar amount of chloronitrobenzene, was added to a glass vial with 0.5 mmol chloronitrobenzene in 5 ml dry toluene solution. The vial was sealed and pierced with needles. The vial was then placed into an autoclave and the autoclave was sealed and pressurised to 10 bar H<sub>2</sub>. The vessel was heated for the desired time. After reaction, the reaction was quenched by placing the autoclave into cold water. Upon cooling, the autoclave was depressurised and opened. The vials were removed and centrifuged to separate the catalyst from the reaction mixture. The conversions and selectivities were determined by GC analysis with a Thermo Trace GC ultra. GC conditions: with a Restek RTX-1 (30 m x 0.25 mm x 0.25  $\mu$ m) column, 50 °C, ramp 8 °C min<sup>-1</sup> to 70 °C, hold 2 min. Ramp 20 °C min<sup>-1</sup> to 300 °C, hold 1 min.

#### 4.2.4 Autoclave Temperature Discrepancy

Initially setting the oil bath temperature to the desired temperature of the reaction when using the stainless steel autoclave led to significantly less conversion than when performed without the autoclave. An alternate autoclave with a thermocouple port was used to calibrate the internal temperature with the oil bath temperature and it was determined that a 20 °C discrepancy was apparent at both 50 °C and 90 °C. The oil bath temperature had to be set to 70 °C and 110 °C respectively to allow for the

desired internal temperature. This calibration was used in all subsequent reactions. The discussed reaction temperature will be the internal autoclave temperature, not the oil bath temperature.

#### 4.2.5 NMR Methods

$^{19}\text{F}$  NMR was used to determine the conversions in the reductive amination catalysis. Because of this, 4'-fluoroacetophenone, N-[1-(4-fluorophenyl)ethylidene]-benzenemethanamine (intermediate imine), 4-fluoro- $\alpha$ -methyl-N-(phenylmethyl)-benzenemethanamine ( $2^\circ$  amine), and 4-fluoro- $\alpha$ -methyl-benzenemethanamine ( $1^\circ$  amine) were visible in the NMR spectra. The NMR peaks assigned to each species can be seen in Table 4.2. Kinetics were determined by independently timed experiments. A representative  $^{19}\text{F}$  NMR of various times within the 0.4 wt% Pd in MIL-101(Cr) can be seen in Figure 4.6.

Table 4.2  $^{19}\text{F}$  NMR peak assignments for the fluorinated species within the reductive amination reaction.

Molecule	NMR shift (ppm)
4'-Fluoroacetophenone	-106.3
Imine	-112.0
$2^\circ$ Amine	-115.8
$1^\circ$ Amine	-116.3

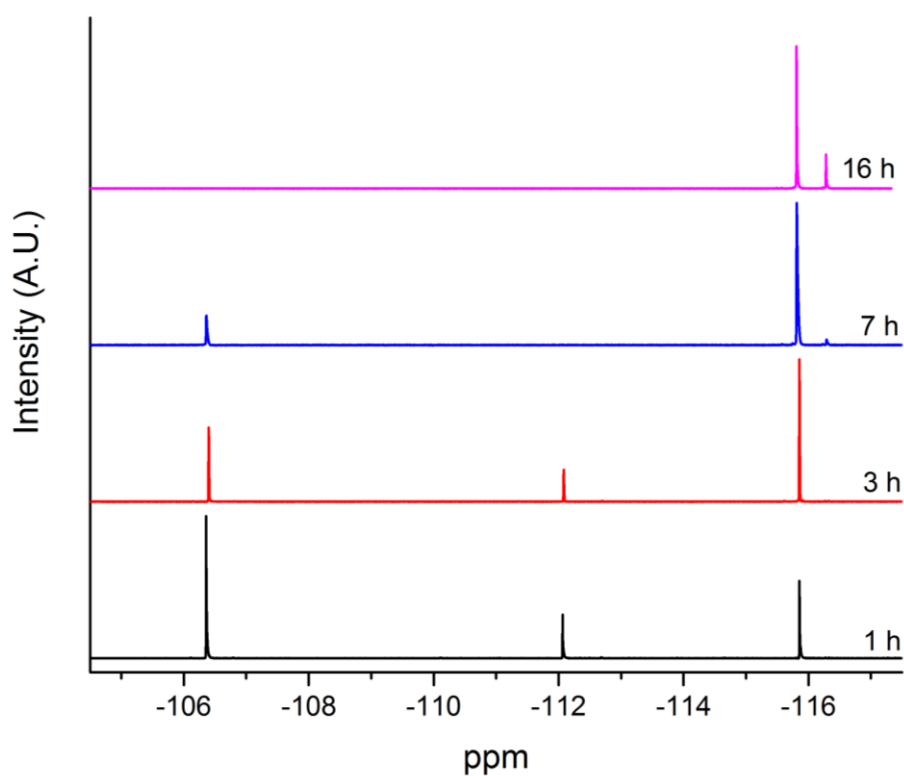


Figure 4.6 0.4 wt% Pd in MIL-101(Cr)  $^{19}\text{F}$  NMR spectra from various timed reactions at 90 °C.

#### 4.2.5.1 Validity of $^{19}\text{F}$ NMR for Conversions

A T1 test was performed on the reaction mixture with all products in the solution. The plot seen in Figure 4.7 shows how each molecule relaxes with time.

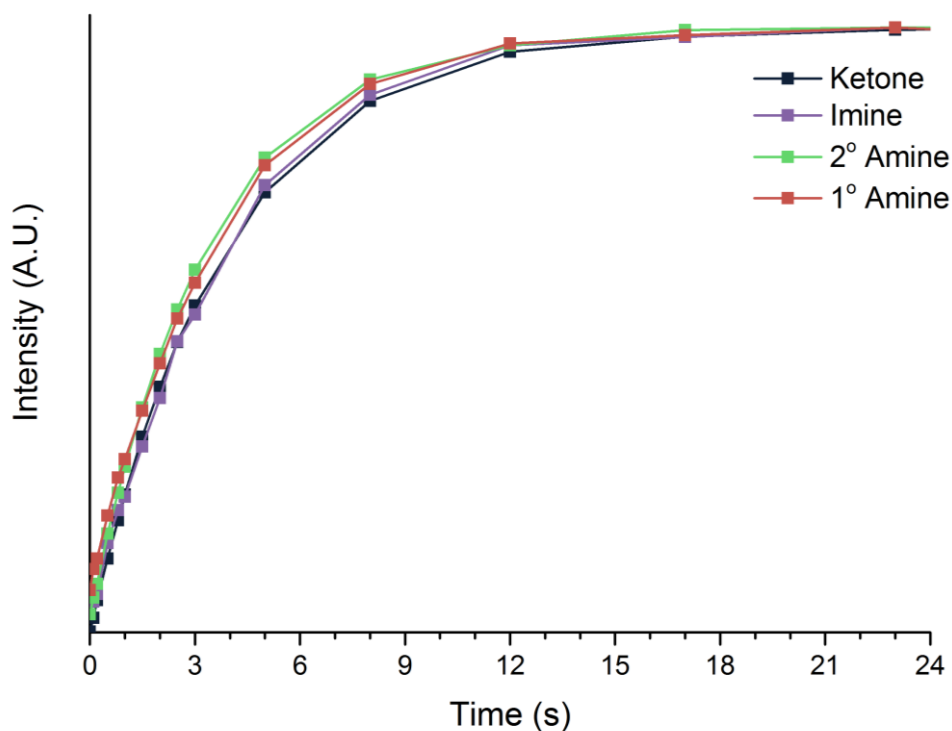


Figure 4.7  $^{19}\text{F}$  NMR  $T_1$  relaxation plots for the fluorinated molecules within the reductive amination reaction.

Each molecule has a very similar profile. This shows that the full relaxation between pulses should be around 17 seconds (3-5 times the longest  $T_1$ ), as discussed in Chapter 2. However, because of the similarity of the profiles, the error when using a shorter pulse time is small. Due to the long duration it would take to perform  $^{19}\text{F}$  NMR experiments with the long pulse time, a short pulse time of 1 second was used instead. Testing the difference between the two experiments, it is determined that an error of approximately  $\pm 1\%$  exists.

### 4.3 Reductive Amination: Low Temperature (50 °C) Catalysis

Based on an adapted procedure by Mitchell *et al.*<sup>3</sup> MIL-100(Sc) and MIL-101(Cr) were initially tested in the imine synthesis without nanoparticles involved. It was determined that after 8 hours both MOFs performed similarly in hexane at 50 °C as they did in toluene at 90 °C (Table 4.3, entries 1-2 and 4-5). Adding 1 wt% Pd MNPs to the system increased the imine formation conversion after 8 hours (Table 4.3 entry 3

and 6). This indicates that the Pd MNPs must play a role in the enhancement of the acid sites and a cooperative effect might take place. From these results, hexane was the chosen solvent for subsequent reactions because similar conversions were achieved while maintaining lower temperature.

Table 4.3 Imine formation reaction conversions with MIL-101(Cr) and MIL-100(Sc) with and without MNPs added. 5 mol% MOF catalyst, 8 hours, 1 bar N<sub>2</sub>.

Entry	MOF	Temperature (°C)	Solvent	Conversion (%)
1	MIL-101(Cr)	90	toluene	50
2	MIL-101(Cr)	50	hexane	49
3	Pd MIL-101(Cr)	50	hexane	66
4	MIL-100(Sc)	90	toluene	71
5	MIL-100(Sc)	50	hexane	71
6	Pd MIL-100(Sc)	50	hexane	76

To ensure the catalyst was not operating under diffusion limitation, a stir speed test was performed. In this test, a series of imine formation reactions using MIL-101(Cr) were performed while varying stir speeds for 6 hours at 50 °C under N<sub>2</sub>. If the reaction was to be diffusion limited, a trend should be apparent where a higher stir speed would lead to higher catalytic activity. Five stir speeds were examined: 0, 100, 200, 400 and 600 rpm. The results for the diffusion limitation test are shown in Figure 4.8. There is no apparent trend between stir speeds, and all conversions are consistent. The small differences in conversion are likely because of experimental errors which arise from repeating reactions independently. To maintain consistency throughout experiments, all catalytic reactions were performed with a stir speed of 400 rpm.

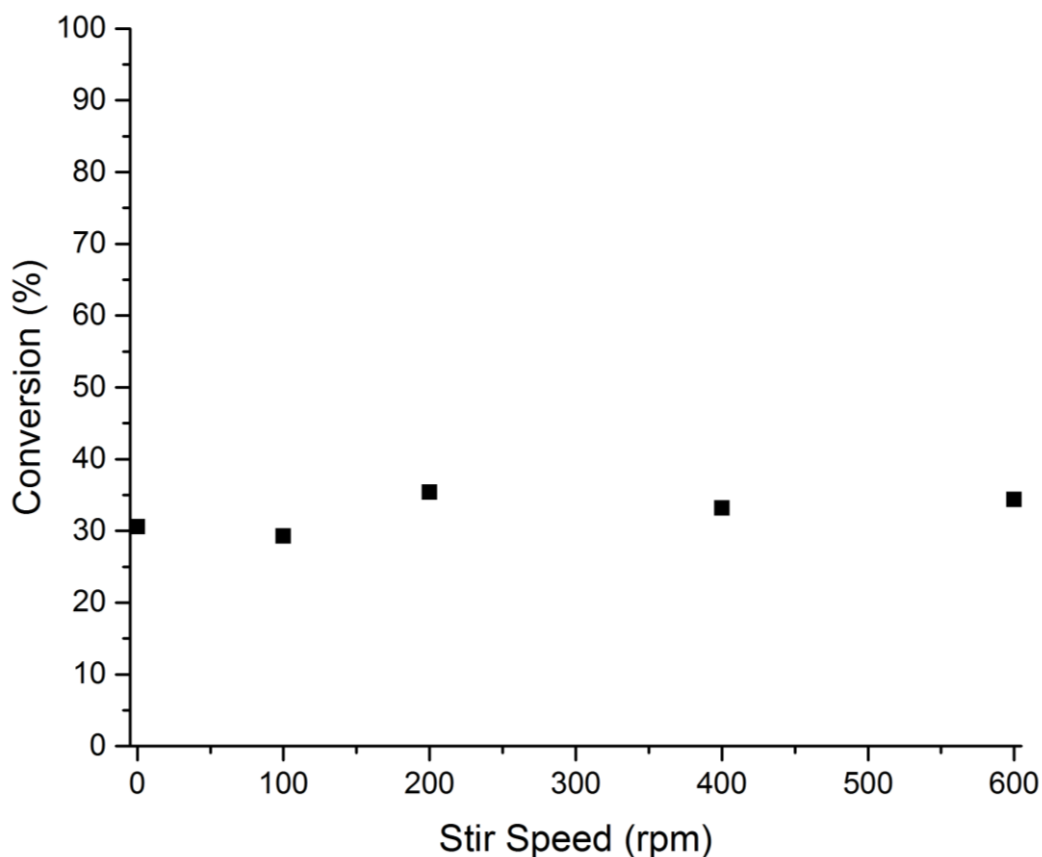
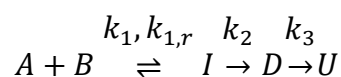


Figure 4.8 Diffusion limitation test by varying stir speed of the reaction.

### 4.3.1 Kinetics

The 1.0 wt% Pd MIL-101(Cr) material was examined in the full tandem reaction. After 16 hours, the catalyst converts 65% of the 4'-fluoroacetophenone. The selectivity of the reactions is 9 % to imine, 91% to 2° amine and less than 1% to 1° amine.

Next, the amine formation was monitored in time in order to gain insight into kinetics of the overall reaction. The reaction was repeated and the conversion was determined after 3, 4 and 5 hours to investigate the initial steps of the reaction. Figure 4.9 shows the reaction progression over time. The data were fitted with help of MATLAB running a numerical model using ordinary differential rate equations. The reaction rate constants can be changed for each reaction in the multi-tandem catalysis and the program solves the set of differential equations accordingly. The series of differential equations used to fit the data are shown in Equations 4.1 to 4.4.



$$\frac{dC_A}{dt} = -k_1 C_A C_B + k_{1,r} C_I \quad 4.1$$

$$\frac{dC_I}{dt} = k_1 C_A C_B - k_{1,r} C_I - k_2 C_I \quad 4.2$$

$$\frac{dC_D}{dt} = k_2 C_I - k_3 C_D \quad 4.3$$

$$\frac{dC_U}{dt} = k_3 C_D \quad 4.4$$

The imine formation is modelled as a reversible reaction where the Lewis acid site can both form and decompose the imine species. The rate at which the imine is reduced to the 2° amine drives the imine formation forward by Le Châtelier's principle. The two reactions that take place on the Pd surface are modelled as pseudo-first order reactions. At 50 °C the reaction to the undesired 1° amine product is set at  $k_3 = 0 \text{ h}^{-1}$ , simplifying the set of differential equations. The values determined as a plausible fit of the 50 °C kinetic data are  $k_1 = 1 \text{ M}^{-1}\text{h}^{-1}$ ,  $k_{1,r} = 0.005 \text{ h}^{-1}$  and  $k_2 = 0.18 \text{ h}^{-1}$ .

By extrapolation after numerically fitting the data as best as possible, it is determined that the reaction would take over 90 hours to achieve full consumption of 4'-fluoroacetophenone (see Figure 4.10). After 16 hours the amount of 1° amine is negligible so is not incorporated into the set of differential equations. However, if the reaction were to run until completion, this variable might eventually play a role in the experimental outcome.

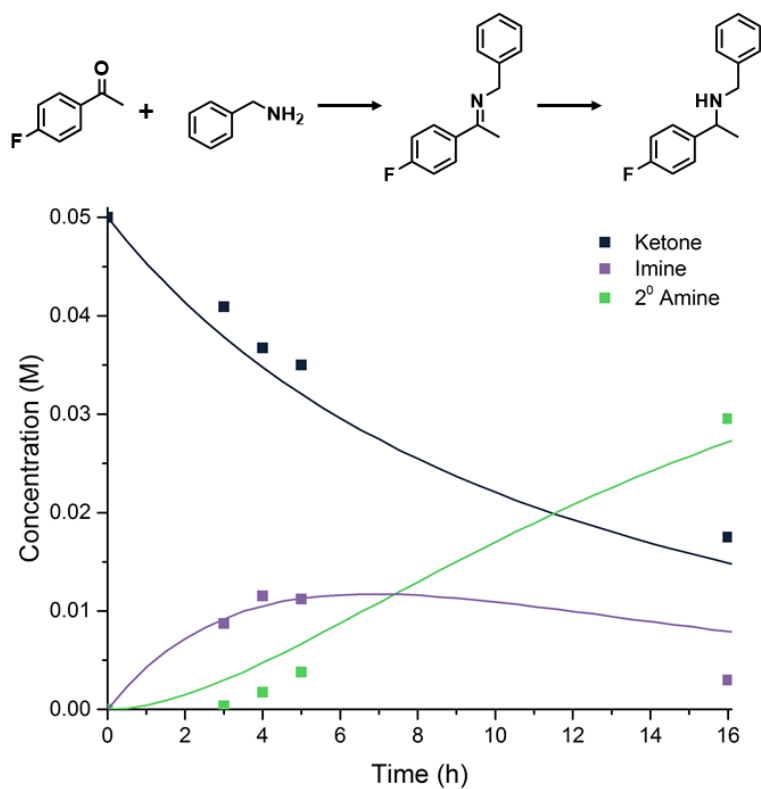


Figure 4.9 Reaction progress at 50 °C using 1.0 wt% Pd MIL-101(Cr).

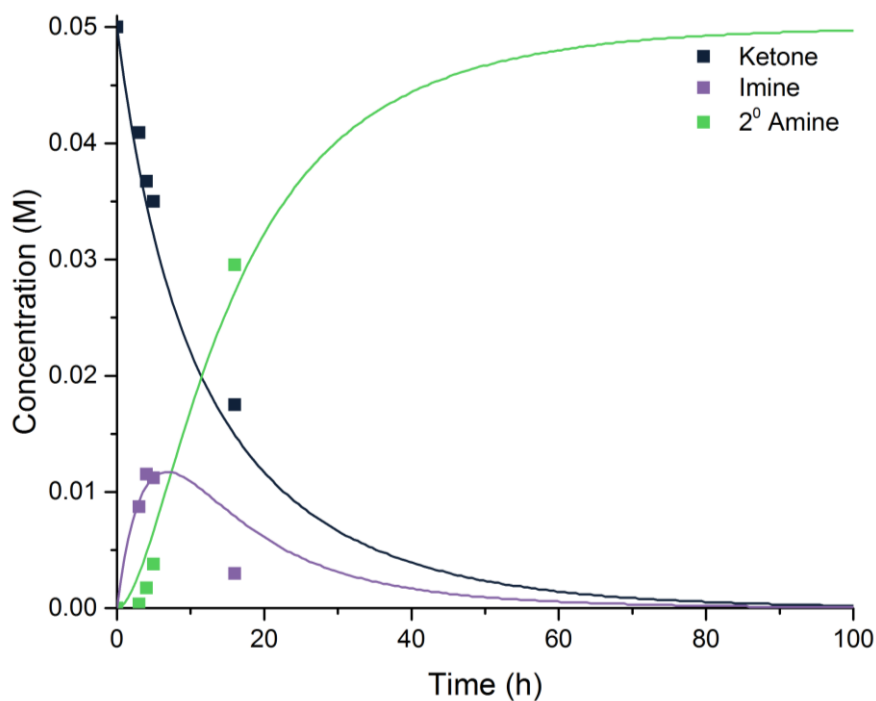


Figure 4.10 Extrapolation on time using the same rate constants from Figure 4.9. The reaction would reach full consumption of 4'-fluoroacetophenone at around 90 hours.

Looking at the discrepancy between the experimental and numerical data it can be seen that the imine formation behaves differently from what the model suggests. If the model is fitted with a higher concentration of imine, shown in Figure 4.9, the decrease of the imine concentration does not seem to follow the correct trend. This is due to the more complex reaction situations where a lot of other factors and interplays are involved which are not included in the model. In this case, an induction effect might take place, where a concentration of imine builds until the Pd MNPs start quickly reacting it towards the 2° amine. Because of this discrepancy, the rate of formation of the 2° amine in the model initially appears to be higher than experimentally determined. Clearly, there are more variables in the reaction than the series of ordinary differential equations accounts for. Still, when taking in account the ideality of the equations compared to the complexity of the experimental conditions, the curves are in close agreement.

#### 4.3.2 Recyclability and Leaching Test

To determine if the multifunctional materials were viable heterogeneous catalysts, recyclability experiments were performed with 1.0 wt% Pd MIL-101(Cr) and 1.0 wt% Pd MIL-100(Sc). In each case the MOF is activated at 150 °C for 6 hours under vacuum. The reaction is carried out for 16 hours under 10 bar of H<sub>2</sub>. The catalyst is removed from the reaction solution by centrifugation, washed with ethanol, and reactivated for the next cycle.

Pd MIL-100(Sc) was very active in the initial run, achieving 88% conversion over the 16 hours with 90% selectivity to the 2° amine product. Upon recycling, the catalyst performed significantly worse. In this case, the conversion was only 38% and no reduction to 2° amine product was detected. This indicates that the Pd MIL-100(Sc) catalyst is not a good candidate for catalytic recycling. The Pd MIL-100(Sc) catalyst was examined before and after catalysis using TEM. It could be seen that large agglomerates of Pd MNPs are observed after the reaction, showing that the MOF is not stable enough under catalysis conditions to support the immobilised MNPs. The TEM images are shown in Figure 4.11.

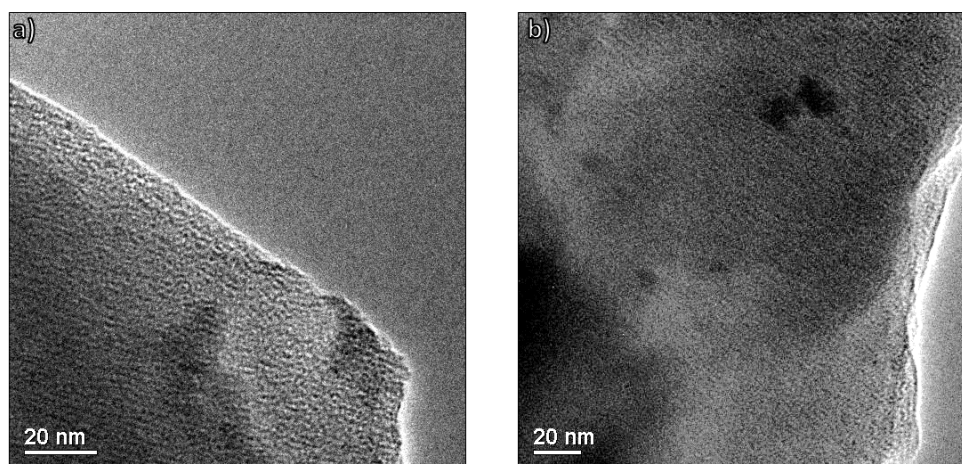


Figure 4.11 Pd MIL-100(Sc) (a) before and (b) after catalysis.

Pd MIL-101(Cr) performed much better in catalytic recycling than its MIL-100(Sc) counterpart. The catalyst can be used three times with minimal loss of activity and selectivity, shown in Figure 4.12. After the third run, the drop in conversion is 6% and there is no significant change in selectivity of the desired 2° amine product. Looking at TEM images, shown in Figure 4.13, it can be seen that after catalysis the small metal nanoparticles are still well dispersed throughout the MOF support although the size distribution has shifted slightly to larger particles. Observing the MNP size distribution in Figure 4.14 after the third recycle, it is determined that 80% of the MNP that were within the MIL-101(Cr) cage size range remain in this range after 3 catalytic cycles. This demonstrates that MIL-101(Cr) is a suitable support for the immobilisation of MNPs.

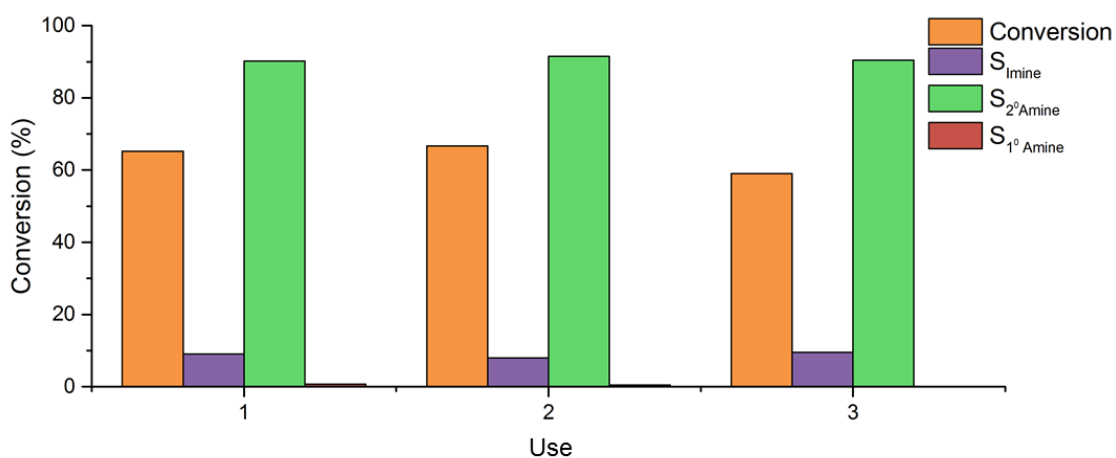


Figure 4.12 1.0 wt% Pd MIL-101(Cr) recyclability. Overall the drop in conversion between runs 1 and 3 is 6%.

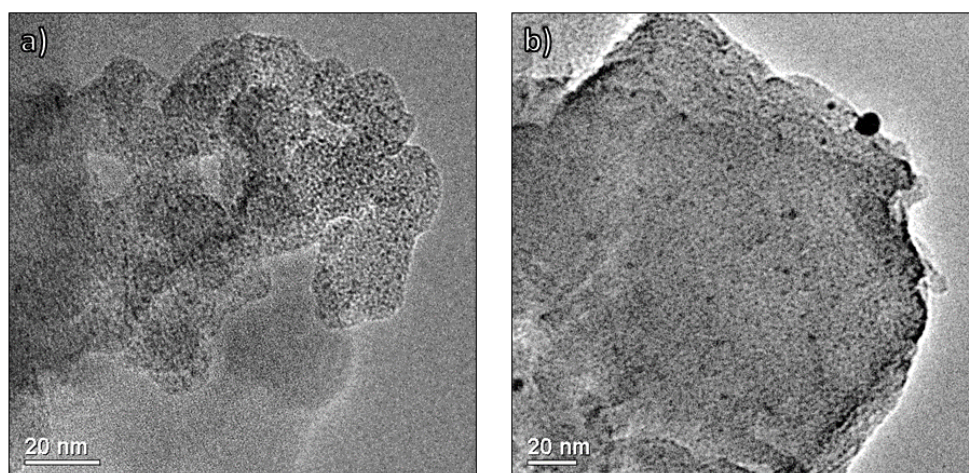


Figure 4.13 Pd MIL-101(Cr) (a) as prepared and (b) after 3 catalysis runs.

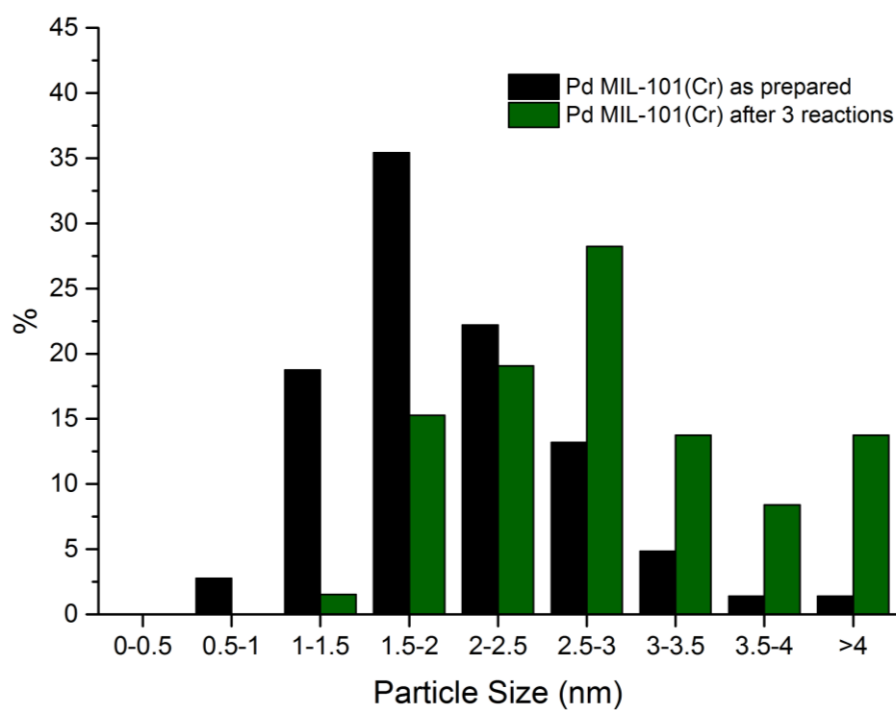


Figure 4.14 Pd MIL-101(Cr) MNP size distribution before and after recycling experiments.

It is also determined that the catalyst remains crystalline after the recycles, seen in Figure 4.15, showing that the stability of the MIL-101(Cr) support is advantageous for multifunctional catalysis.

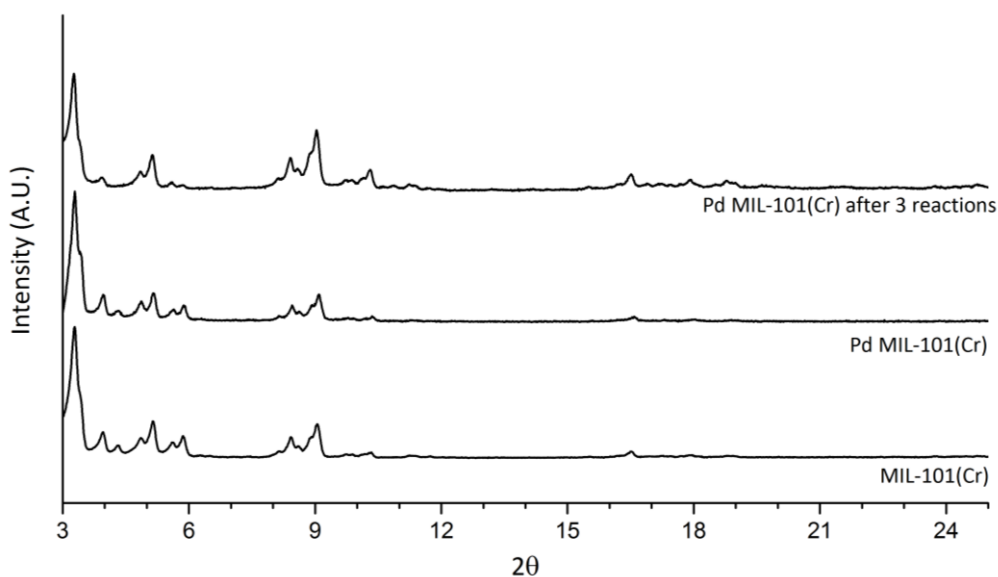


Figure 4.15 Pd MIL-101(Cr) XRD patterns before and after recycling experiments.

In order to determine metal leaching, a hot filtration test was performed on the 1.0 wt% Pd MIL-101(Cr) sample. In this experiment, 10 identical vials were prepared. All vials were put under reaction conditions and allowed to react for 3 hours. After this time elapsed, 5 of the vials were removed and the reaction mixtures were centrifuged. One vial content was used to find the conversion at 3 hours and the other four vial contents were placed back in clean vials. All vials were placed under reaction conditions again. At the end of every hour of reaction, two vials were removed. One with the catalyst still in the solution, and one of the centrifuged solution mixture. If any leached species were to be in the reaction solution, the vial with the catalyst removed would continue to react. Figure 4.16 shows the hot filtration test performed.

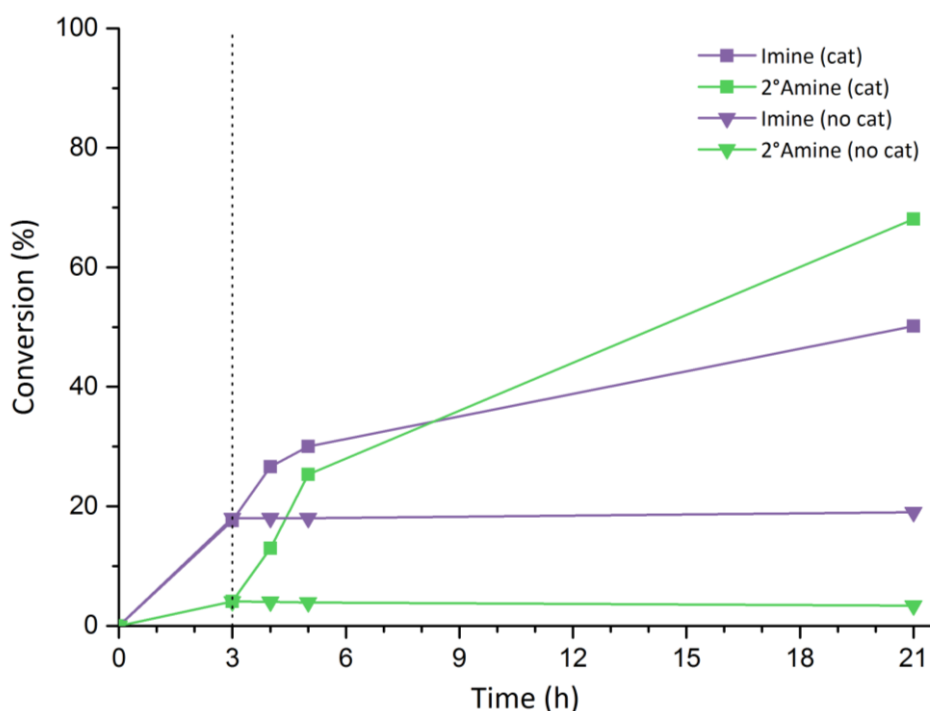


Figure 4.16 Hot filtration test on 1.0 wt% Pd MIL-101(Cr). The vertical dotted line at 3 hours represents the time which the catalyst was removed from half of the reaction vials.

This test shows that after the catalyst removal at 3 hours the reaction without catalyst does not progress any further. Neither the imine formation, catalysed by the MOF Lewis acidic sites, nor the reduction to the 2° amine by the MNPs occur after centrifugation. This demonstrates the Pd MIL-101(Cr) material operates as a heterogeneous catalyst and no active leached metal species are present in solution.

#### 4.4 Reductive Amination: High Temperature (90 °C) Catalysis

Starting with 1.0 wt% Pd in MIL-101(Cr) at 50 °C, full conversion is not achieved even after 16 hours of reaction. At 50 °C high selectivity to the desired 2° amine is obtained but only 65% of the starting 4'-fluoroacetophenone has reacted after this time. As shown previously, the kinetic model suggests that it would take around 90 hours to reach full consumption of 4'-fluoroacetophenone at the 50 °C reaction conditions.

The reaction temperature was increased to 90 °C in order to push the reaction to completion. At this elevated temperature, the undesired 1° amine is obtained as the major product. In an attempt to increase the selectivity to the desired 2° amine product, bimetallic 1:1 PdAu MNPs were deposited in MIL-101(Cr) while maintaining

the same total metal loading of 1.0 wt%. Full characterisation of this material was not accomplished, hence the extent of bimetallic alloying is unknown. Extended X-ray absorption fine structure (EXAFS) would be a good technique for characterisation of these materials, which elucidates nearest neighbours of each atom, thus indicating the extent of alloying. Nevertheless, using this material in catalysis an increased selectivity towards the desired product was observed (Table 4.4 entry 2). With this result in hand, a control experiment was performed using 0.5 wt% Pd in MIL-101(Cr), and tested in catalysis. If the PdAu alloy was in fact tuning the catalysis towards the desired 2° amine, then this material should perform better than just using half the amount of Pd metal. However, this was not the case. In fact, just using 0.5 wt% Pd gave similar results as 1.0 wt% 50:50 PdAu, shown in Table 4.4. Instead of tuning the reaction with bimetallic MNPs, it was determined that it should be possible to tune the reaction by simply adjusting the overall amount of active MNPs within the MOF support.

Table 4.4 Tandem catalysis results showing 1:1 1.0 wt% PdAu MIL-101(Cr) behaves similarly to 0.5wt% Pd MIL-101(Cr) at 5 mol% MOF catalyst, 90 °C, 10 bar H<sub>2</sub>, 16 hours.

Entry	MNP Loading (wt%)	Conversion (%)	Selectivity (%)		
			Imine	2° Amine	1° Amine
1	1.0 Pd	100	0	9	91
2	1.0 PdAu (1:1)	100	0	83	17
3	0.5 Pd	95.2	0	75	25

#### 4.4.1 Achieving Full Conversion and High Selectivity

Increasing the reaction temperature to 90 °C strongly increases the conversion of 4'-fluoroacetophenone using the same catalyst, giving full conversion after the same time. However, the increase in temperature leads to a decrease in selectivity and now the hydrogenolysis of the secondary amine is observed to dominate. In the experiments, which show the 1° amine as the main product, the decomposition of benzylamine into toluene and ammonia is observed, as determined using GC analysis. This does not appear to affect the imine formation, however, as the consumption of 4'-fluoroacetophenone still reaches 100%. This indicates there is an overall increased

activity of the palladium nanoparticles at higher temperatures and no longer is the imine functionality reduced selectively. For this reason, three lower Pd loadings were synthesised: 0.5 wt%, 0.4 wt% and 0.2 wt%. As the ratio of palladium active sites to Lewis acid active sites is reduced by decreasing the palladium loading, a shift of selectivity in the catalysis is observed.

#### 4.4.2 Optimising Pd Loadings

Comparing the 1.0 wt% Pd loading to half this amount we observe a drastic shift in selectivity to the 2° amine by 9% to 75% (Table 4.5 entries 2 and 3). By decreasing the Pd loading even more to 0.4 wt% and 0.2 wt%, the selectivity is further increased, to 87% to 90% respectively. This demonstrates that for the 16-hour reaction, an almost complete switch of selectivity from 1° amine at high loading to 2° amine at low loading is observed.

Table 4.5 Catalysis results for Pd loaded MIL-101(Cr) at 16 hours. 5 mol% MOF catalyst. 10 bar H<sub>2</sub> for 16 hours. Conversions determined by <sup>19</sup>F NMR based on consumption of 4'-fluoroacetophenone.

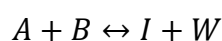
Entry	Pd Loading (wt%)	Temperature (°C)	Conversion (%)	Selectivity (%)		
				Imine	2° Amine	1° Amine
1	1.0	50	65	9	91	>1
2	1.0	90	100	0	9	91
3	0.5	90	95	0	75	25
4	0.4	90	100	0	87	13
5	0.2	90	100	0	90	10

As previously discussed in Chapter 3, the Pd MNPs within each material possess approximately the same size and distribution, thus the difference in the samples is the ratio between the Lewis acid active sites and Pd active sites. As the number of Pd sites goes down, the selectivity towards the desired product increases.

#### 4.4.3 Kinetics

Initially, the first reaction was tested without the hydrogen needed for the second reaction to occur. It was observed that the reaction appeared to reach an equilibrium, which suggests the imine formation is reversible. The reversible imine reaction was

then investigated to determine the reaction rate constants for the forward and reverse reactions. For this, the imine formation reaction was performed at varying reaction times using MIL-101(Cr) at 90 °C and 10 bar H<sub>2</sub>. The obtained data were then used to calculate and determine the forward and reverse rate constants.<sup>5</sup> Two sets of rate constants were calculated: with and without water as a variable in the equations. This means that with water the reaction is second order in both directions and without water the reaction is second order in the formation of the imine and first order in the reverse reaction. Boeker defined these equations for reversible bimolecular reactions such that the rate constants are easily solvable.<sup>5</sup> These equations are shown in Equations 4.5 with water and 4.11 without water. Using these equations and plotting Z (Equation 4.7) against time gives a straight line with a slope of m (Equation 4.8). Using the slope, it is possible to determine the reaction rate constants for both reactions shown in Equations 4.9 and 4.10 with water and Equations 4.15 and 4.16 without water. Within these equations, concentrations subscripted “e” indicate the concentration at equilibrium, and concentrations subscripted with “0” indicate the initial concentration.



$$\left[ k_1 \left( 1 - \frac{1}{K_e} \right) \right] \left[ \frac{K_e(A_e + B_e) + I_e + W_e}{(K_e - 1)} \right] t = -\ln \left( 1 - \frac{I - I_0}{I_e - I_0} \right) + \ln \left( 1 - \frac{I - I_0}{\left[ \frac{K_e(A_e + B_e) + I_e + W_e}{(K_e - 1)} \right] + I_e - I_0} \right) \quad 4.5$$

$$K_e = \frac{I_e W_e}{A_e B_e} = \frac{k_1}{k_{1,r}} \quad 4.6$$

$$Z = -\ln \left( 1 - \frac{I - I_0}{I_e - I_0} \right) + \ln \left( 1 - \frac{I - I_0}{\left[ \frac{K_e(A_e + B_e) + I_e + W_e}{(K_e - 1)} \right] + I_e - I_0} \right) \quad 4.7$$

$$m = \left[ k_1 \left( 1 - \frac{1}{K_e} \right) \right] \left[ \frac{K_e(A_e + B_e) + I_e + W_e}{(K_e - 1)} \right] \quad 4.8$$

$$k_1 = \frac{m}{\left( 1 - \frac{1}{K_e} \right) \left[ \frac{K_e(A_e + B_e) + I_e + W_e}{(K_e - 1)} \right]} \quad 4.9$$

$$k_{1,r} = \frac{k_1}{K_e} \quad 4.10$$

$$A + B \leftrightarrow I$$

$$k_1 \left[ \frac{K_e(A_e + B_e) + I_e}{(K_e - 1)} \right] t =$$

$$-\ln \left( 1 - \frac{I - I_0}{I_e - I_0} \right) + \ln \left( 1 - \frac{I - I_0}{\left[ \frac{A_e + B_e + 1}{K_e} \right] + I_e - I_0} \right) \quad 4.11$$

$$K_e = \frac{I_e}{A_e B_e} = \frac{k_1}{k_{1,r}} \quad 4.12$$

$$Z = -\ln \left( 1 - \frac{I - I_0}{I_e - I_0} \right) + \ln \left( 1 - \frac{I - I_0}{\left[ \frac{A_e + B_e + 1}{K_e} \right] + I_e - I_0} \right) \quad 4.13$$

$$m = k_1 \left[ \frac{K_e(A_e + B_e) + I_e}{(K_e - 1)} \right] \quad 4.14$$

$$k_1 = \frac{m}{\left[ \frac{K_e(A_e + B_e) + I_e}{(K_e - 1)} \right]} \quad 4.15$$

$$k_{1,r} = \frac{k_1}{K_e} \quad 4.16$$

From the calculations, the reaction rate constants were added into MATLAB programs using Equations 4.17 or 4.18. The models and experimental data are shown in Figure 4.17. The calculated rate constants when water is taken in account are  $k_1 = 2.03 \text{ M}^{-1}\text{h}^{-1}$  and  $k_{1,r} = 0.76 \text{ M}^{-1}\text{h}^{-1}$ . The calculated rate constants when water was not included are  $k_1 = 2.1 \text{ M}^{-1}\text{h}^{-1}$  and  $k_{1,r} = 0.03 \text{ h}^{-1}$ . There is almost no difference in the water being present, so the simpler model with a first order reverse reaction is used. The lack of distinction between the two models is possibly due to the fact that any water molecules which are present are likely near a Lewis acid site, thus providing an effective excess of water near the active site. This would be an equivalent situation to

when the reaction would be performed using a large excess of water, hence a first order reaction also fits the data.

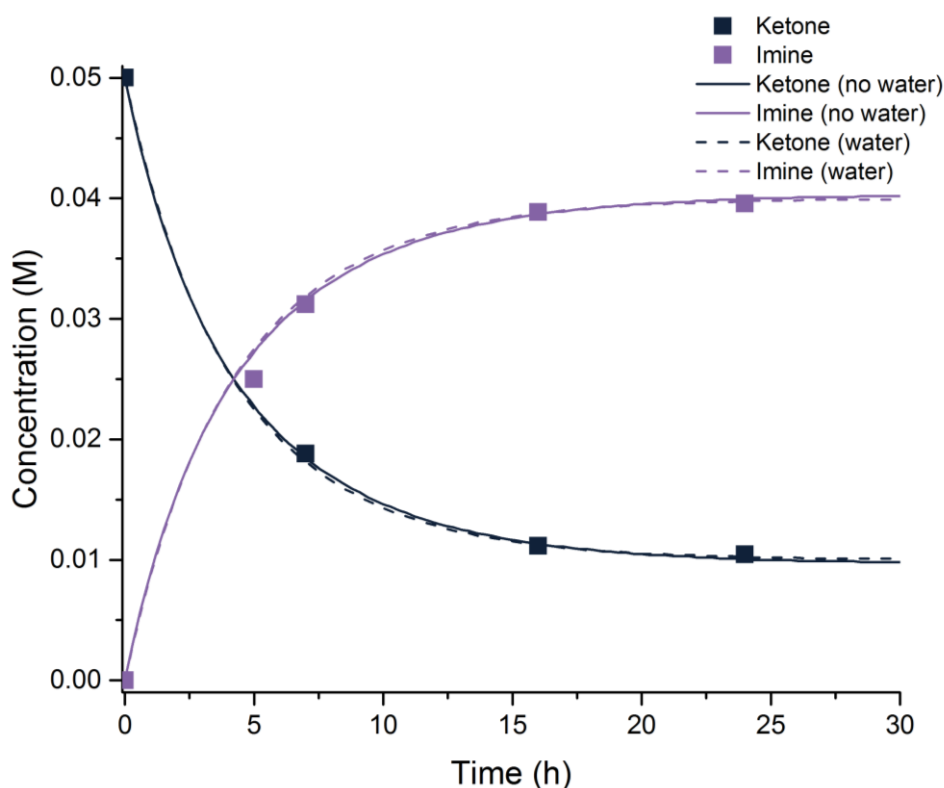


Figure 4.17 Reversible imine formation with calculated reaction rate constants including water ( $k_1= 2.03 \text{ M}^{-1}\text{h}^{-1}$ ,  $k_{1,r}= 0.76 \text{ M}^{-1}\text{h}^{-1}$ ) and not including water ( $k_1= 2.1 \text{ M}^{-1}\text{h}^{-1}$ ,  $k_{1,r}= 0.03 \text{ h}^{-1}$ ).

$$\frac{dC_A}{dt} = -k_1 C_A C_B + k_{1,r} C_I C_W \quad 4.17$$

$$\frac{dC_A}{dt} = -k_1 C_A C_B + k_{1,r} C_I \quad 4.18$$

However, when using the calculated reaction rate constants for the full tandem model system, the model no longer fits the data. The rate of consumption of ketone is far faster than predicted by the model from the reaction rate constant calculations. From this result, it was concluded that the Pd and  $\text{H}_2$  have an influence in the imine formation, although exactly how and where is unknown. To test this, the catalysis was performed under Ar atmosphere rather than  $\text{H}_2$ , which allows the Pd MIL-101(Cr) catalyst to be used while still only examining the imine formation reaction. The results, shown in Table 4.6, indicate there is a large difference between the results. Comparing

Table 4.6 entry 1 and 2, the change of gas from H<sub>2</sub> to Ar reduces the conversion from 62% to 36% even with double the amount of total catalyst. Entry 3 shows that adding Pd MNP to the MIL-101(Cr) catalyst does recover some of the activity, increasing to 50% with half the total catalyst compared to Entry 2, but the conversion is still 12% lower than just the MOF under H<sub>2</sub>. A similar trend is also observed at 16 hours, shown in entries 4-6. In fact, the change in conversion is nearly identical from the set of 7 hours to the set of 16 hours, showing that these changes alter the catalysis throughout the entire reaction length. This indicates that both the H<sub>2</sub> atmosphere and Pd MNPs influence the imine formation, although the underlying mechanism is currently not understood.

Table 4.6 Imine formation with MIL-101(Cr) with and without Pd MNPs in different pressure environments.

Entry	Catalyst	Catalyst Amount (mol%)	Pressure (bar)	Time (h)	Conversion (%)
1	MIL-101(Cr)	5	10 bar H <sub>2</sub>	7	62
2	MIL-101(Cr)	10	10 bar Ar	7	36
3	Pd MIL-101(Cr)	5	10 bar Ar	7	50
4	MIL-101(Cr)	5	10 bar H <sub>2</sub>	16	78
5	MIL-101(Cr)	10	10 bar Ar	16	52
6	Pd MIL-101(Cr)	5	10 bar Ar	16	66

While the synergy of the two active sites as well as the gas atmosphere seems to play a non-negligible role in the imine catalysis outcome, the Pd series were matched using the series of ordinary rate equations in the MATLAB program discussed in Section 4.3.1. This simplistic model fits the data with enough accuracy to visualize trends towards concerning activity and selectivity of the catalysis.

The reaction progress was monitored using the four Pd MIL-101(Cr) materials with a varying metal loading. The concentration data were then matched with a numerical solution of differential equations using MATLAB. By changing the rate constants for each reaction, the change in Pd site to Lewis acid site ratio could be investigated. The reversible imine formation was modified to best mimic the experimental data, since

the calculation of the reaction rate constants proved to be a poor fit. The formation of the imine on the Lewis acid sites appears to be the rate limiting step whereas both the reduction to the desired product and hydrogenolysis to the 1° amine occur readily on the palladium surface. The consumption of the imine varies drastically depending on the number of palladium active sites available compared to the Lewis acid sites. The overall reaction rate constants determined to be a good fit of the experimental data are shown in Table 4.7.

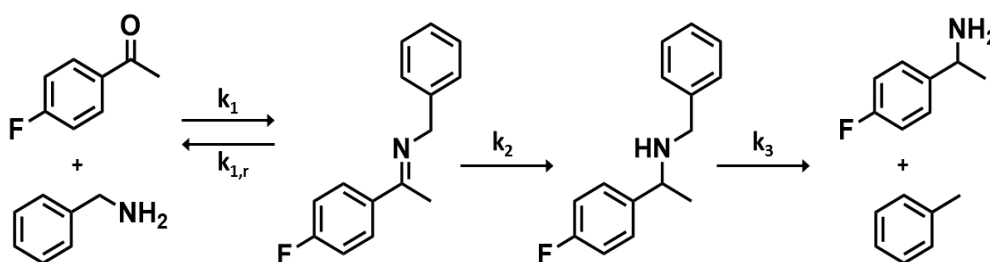


Table 4.7 The fitted reaction rate constants in the multi-tandem reaction for each Pd loaded MIL-101(Cr) catalyst.

Entry	Pd Loading (wt%)	$k_1$ ( $M^{-1}h^{-1}$ )	$k_{1,r}$ ( $h^{-1}$ )	$k_2$ ( $h^{-1}$ )	$k_3$ ( $h^{-1}$ )
1	0.2	8	1	1.1	0.01
2	0.4	8	1	2	0.011
3	0.5	8	1	2.5	0.025
4	1.0	8	1	10	0.1

Figure 4.18 shows the model to experimental fits for each loading. Comparing the models in Figure 4.19 with each other, it can be seen that the 0.4 wt% Pd MIL-101(Cr) achieves the highest yield of the desired product around 11 hours while keeping the 1° amine concentration the lowest. Tuning the ratio of palladium to Lewis acid active sites leads to the desired selectivity while maintaining good activity.

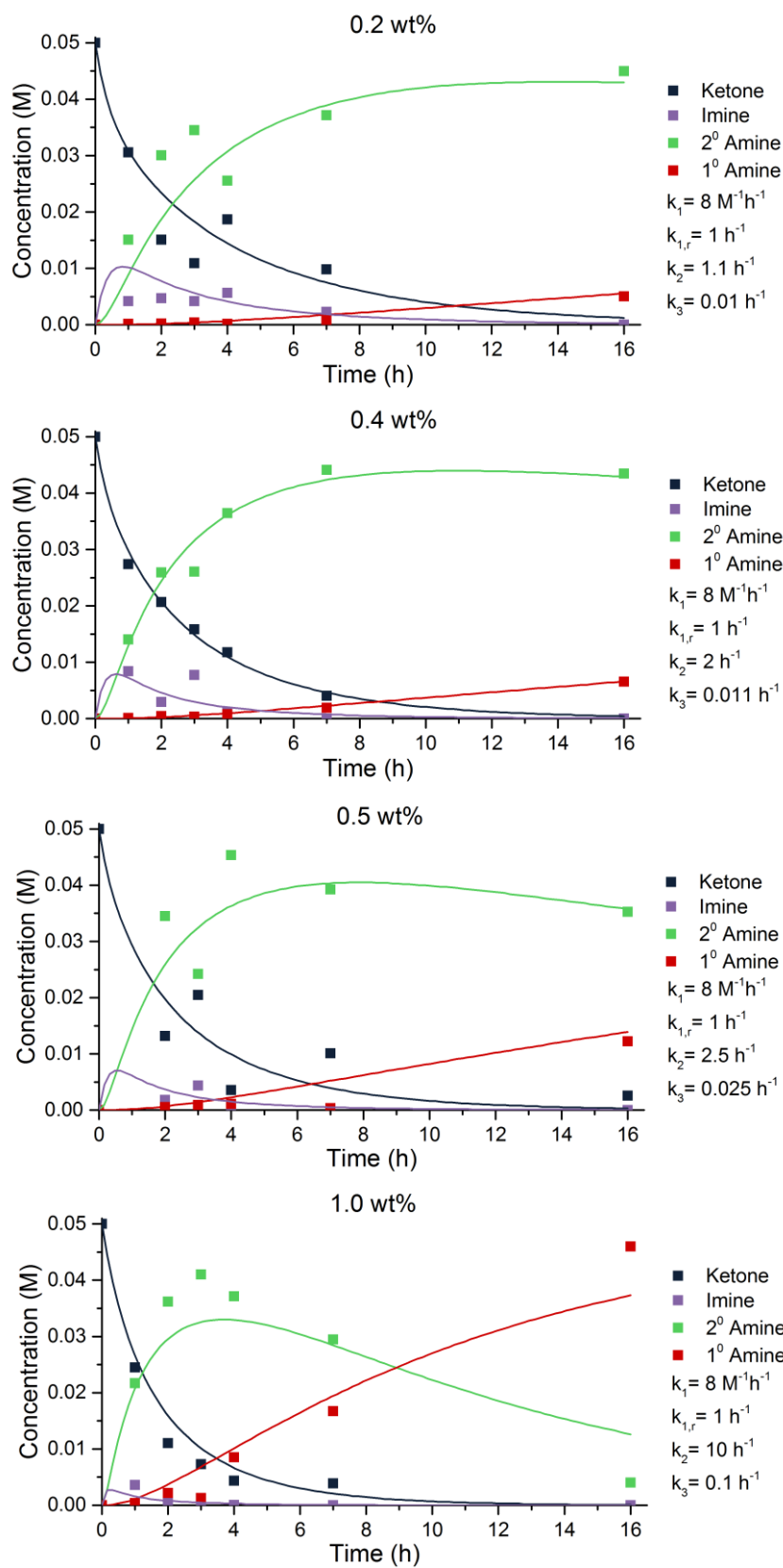


Figure 4.18 X wt% Pd MIL-101(Cr) (X=0.2-1.0) kinetic results with the corresponding MATLAB numerical model.

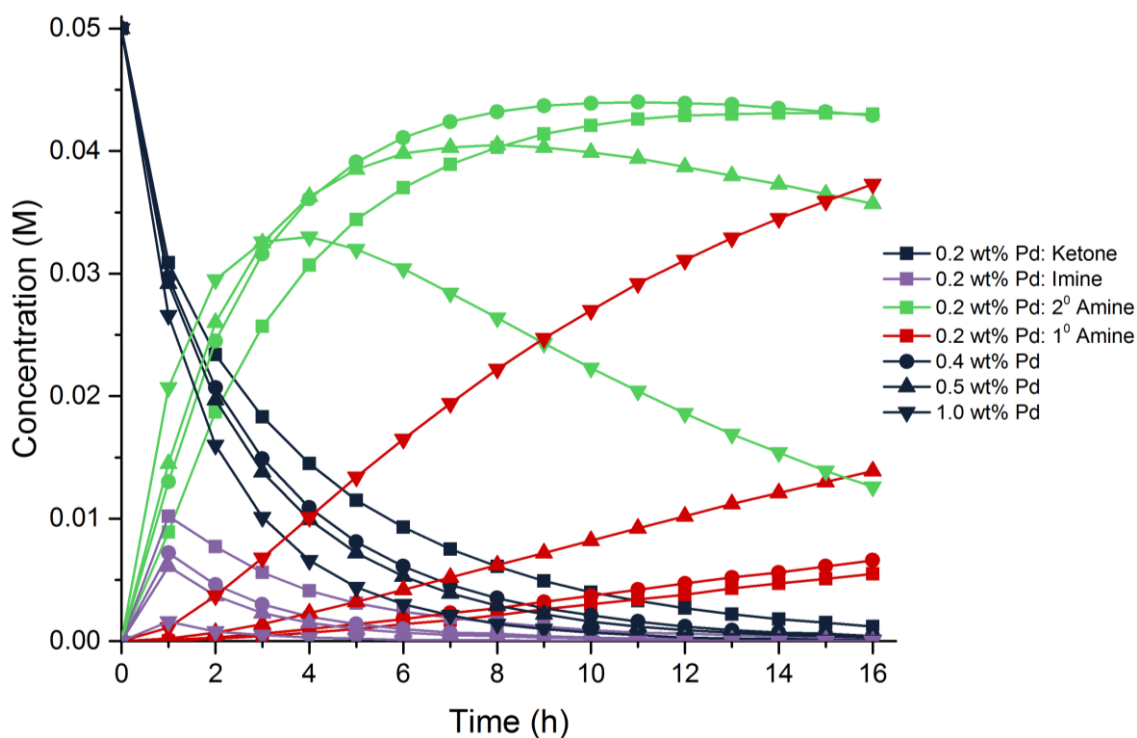


Figure 4.19 MATLAB models for 0.2, 0.4, 0.5 and 1.0 wt% Pd MIL-101(Cr) tandem reaction at 90 °C.

The reaction rate constants for MOF catalysed reactions,  $k_1$  and  $k_{-1}$ , remain the same throughout all loadings. This is because the number of active Lewis acidic sites remains the same for the MOF. The reaction rate constants for the Pd catalysed reactions,  $k_2$  and  $k_3$ , are correlated to the number of Pd sites which varies with the metal loading. The reaction rate constant that describes the conversions catalysed by Pd MNPs increases roughly 10 times with a five-fold increase of the amount of Pd (0.2 to 1.0 wt%). (The reaction rate constant is a pseudo-constant because it must include a variable which changes with the number of active sites within the catalyst.)

Comparing the catalysts tested in this reaction to similar reactions published by others it is important to realise the differences in the reaction variables. The reactions were different due to the use of fluorinated species in this work, as well as the use of benzylamine compared to aniline previously published. However, comparing to a similar reductive amination performed by Cirujano *et al.*<sup>1</sup> it was found that the reaction in this work proceeds significantly faster while obtaining similar selectivities, possibly due to the tuning of the ratio of active sites as well as reaction optimisation. Additionally, in contrast to similar multifunctional reactions performed by Chen *et al.*<sup>2</sup>

with PdAg nanoparticles in MIL-101(Cr), it is shown that the second nanoparticle metal is not necessary to tune this reaction. By lowering the overall amount of active metal the same effect can be obtained and the catalytic reaction can be tuned to the desired product.

#### **4.4.4 Recyclability and Leaching Test**

Analogous to that discussed in section 4.3.2, the recyclability and leaching was also investigated at an elevated temperature of 90 °C. 1.0 wt% Pd MIL-101(Cr) was used as the test catalyst to allow the largest changes in catalyst if leaching or sintering was to occur.

Recyclability experiments at elevated temperature proved to be significantly more difficult than at 50 °C, possibly due to the increased activity of the Pd MNPs at the higher temperature. The recyclability tests were timed at 1 hour to keep conversion low, thus being able to have a better assessment of catalyst degradation. The quenching of the reaction was performed by placing the hot autoclave into a water bath for 5 minutes before opening. Figure 4.20 shows three catalytic cycles. In cycle 2, the conversion slightly increased, but there was an overall decrease in selectivity towards both the 2° amine as well as the 1° amine. This indicates the Pd MNPs are less active during this run. By the third catalysis run the overall consumption of 4'-fluoroacetophenone decreases as well as the Pd activity. At these higher temperatures, it is likely that the Pd MNPs may have partially oxidised upon opening the autoclave, thus leading to a decrease in activity. This behaviour was also observed in another reaction with Pd MIL-101(Cr) catalysts, as discussed further in Section 4.5.2. To properly assess the reusability of this material under these conditions, the catalyst workup procedure between runs should be performed under inert conditions, minimizing contact of the Pd MNPs with oxygen.

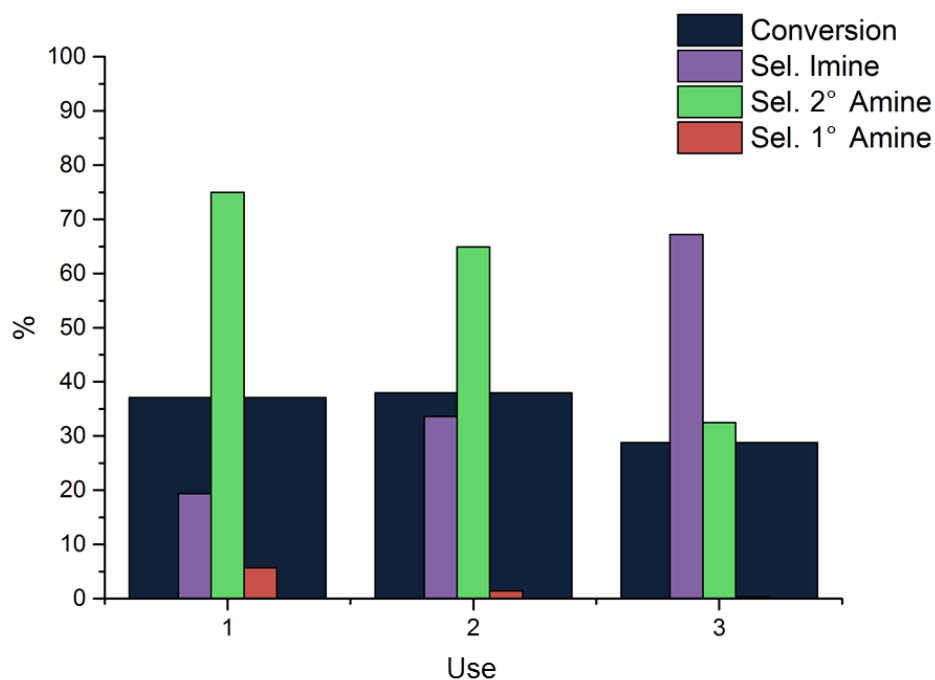


Figure 4.20 Reusability of 1.0 wt% Pd MIL-101(Cr) at 90 °C reaction temperature.

TEM images were compared before and after the catalysis, with both materials showing small Pd MNPs within crystalline MIL-101(Cr) supports, seen in Figure 4.21. The average MNP size increased from 2.8 nm to 3.0 nm, still well within the MIL-101(Cr) cage size. The confirmation of crystalline MOF after catalysis can be seen in the XRD patterns in Figure 4.22.

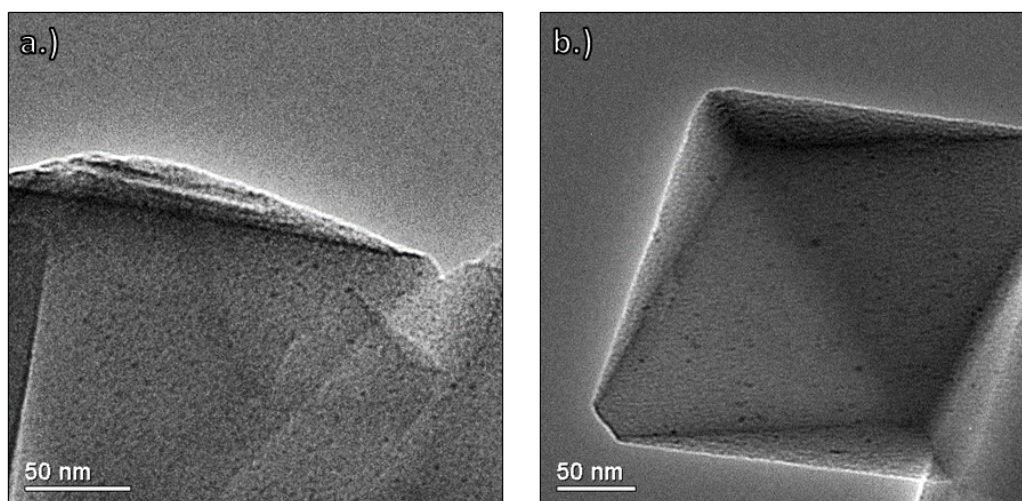


Figure 4.21 (a.) as prepared 1.0 wt% Pd MIL-101(Cr) and (b.) after catalysis at 90 °C for 16 hours.

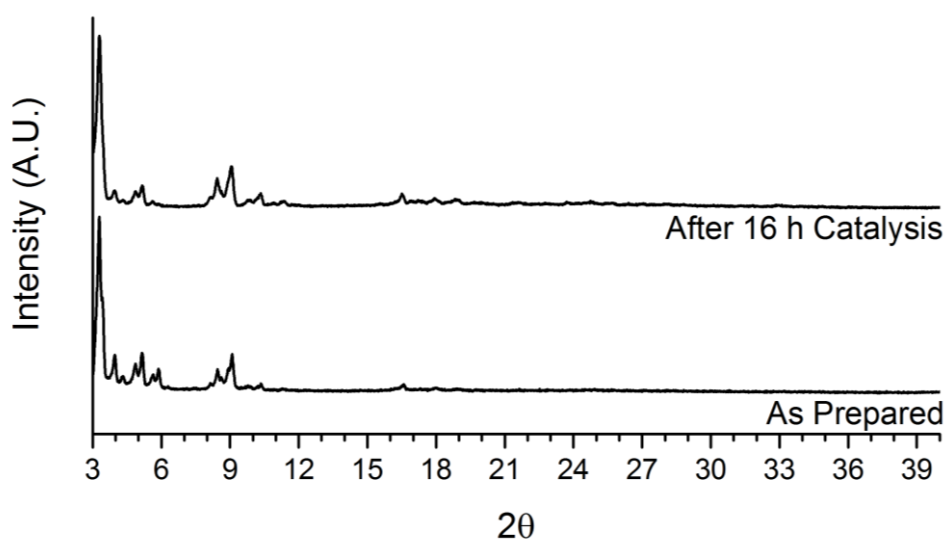


Figure 4.22 1.0 wt% Pd MIL-101(Cr) before and after catalysis at 90 °C.

The 1.0 wt% Pd MIL-101(Cr) sample was tested in a hot filtration reaction to determine the heterogeneity of the system. After 1 hour, the catalyst was removed from the reaction solution and the supernatant was placed back under reaction conditions. Figure 4.23 shows that upon removal of the solid catalyst, no reaction occurs for any of the reactions in the multi-step tandem catalysis. This indicates both the Lewis acid active sites and the palladium metal active sites catalyse their respective reactions heterogeneously and no leaching of catalytically active material seems to occur. This all seems to imply that catalyst deactivation occurs through mechanisms other than leaching of active metal and loss of crystallinity of the MOF.

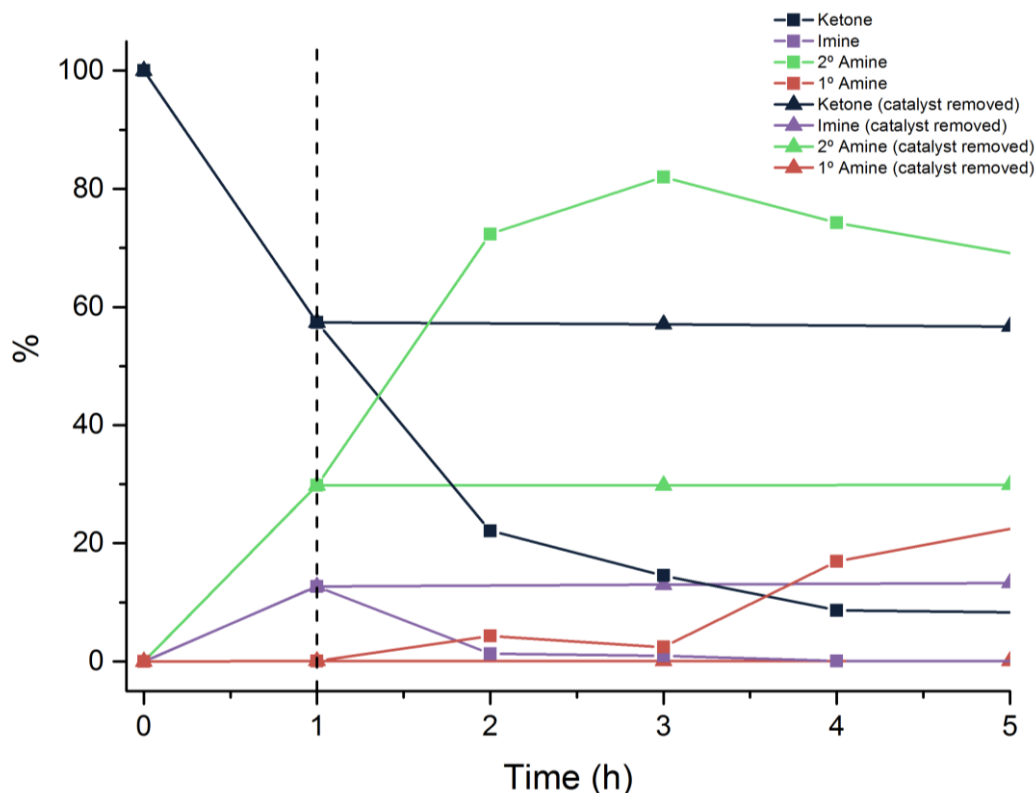


Figure 4.23 Hot filtration test on 1.0 wt% Pd MIL-101(Cr). Squares are the reaction progressing with the catalyst and triangles are the reaction proceeding after the catalyst has been removed at 1 hour.

## 4.5 Catalyst Activity in Other Reactions

### 4.5.1 Citronellal to Menthol

(-)-Menthol is a widely-used molecule in both the pharmaceutical and flavouring industry.<sup>6</sup> This product is often made industrially using enantioselective homogeneous catalysis.<sup>7</sup> Alternatively, menthol can be made by reducing isopulegols, which can be formed from citronellal. The cyclisation of citronellal to isopulegols can be achieved with Lewis acid catalysts such as scandium triflate<sup>8</sup>,  $\text{ZnCl}_2$ ,  $\text{ZnI}_2$  and  $\text{ZnBr}_2$ ,<sup>9</sup> and solid acid catalysts such as zeolites<sup>10</sup>. Researchers have investigated catalyst designs to develop a single heterogeneous catalytic material able to perform both the cyclisation and subsequent reduction to form menthol. This has been achieved with multifunctional catalysts such as metal impregnated zeolites<sup>11-12</sup> and metal impregnated silica<sup>13</sup>. The difficulty concerning enantioselective heterogeneous catalysis leads to many studies either starting with an enantiopure citronellal, or producing a racemic mixture of isopulegols and menthols. Cirujano *et al.* found an

alternate pathway to ( $\pm$ )-menthol using citronellal with a Pd or Pt MNP in MIL-101(Cr) catalyst.<sup>14</sup> It was found that the reaction could take place in one-pot, but not in tandem. The reaction pathway, shown in Figure 4.24, depicts the starting citronellal with two main pathways depending on the reaction conditions.

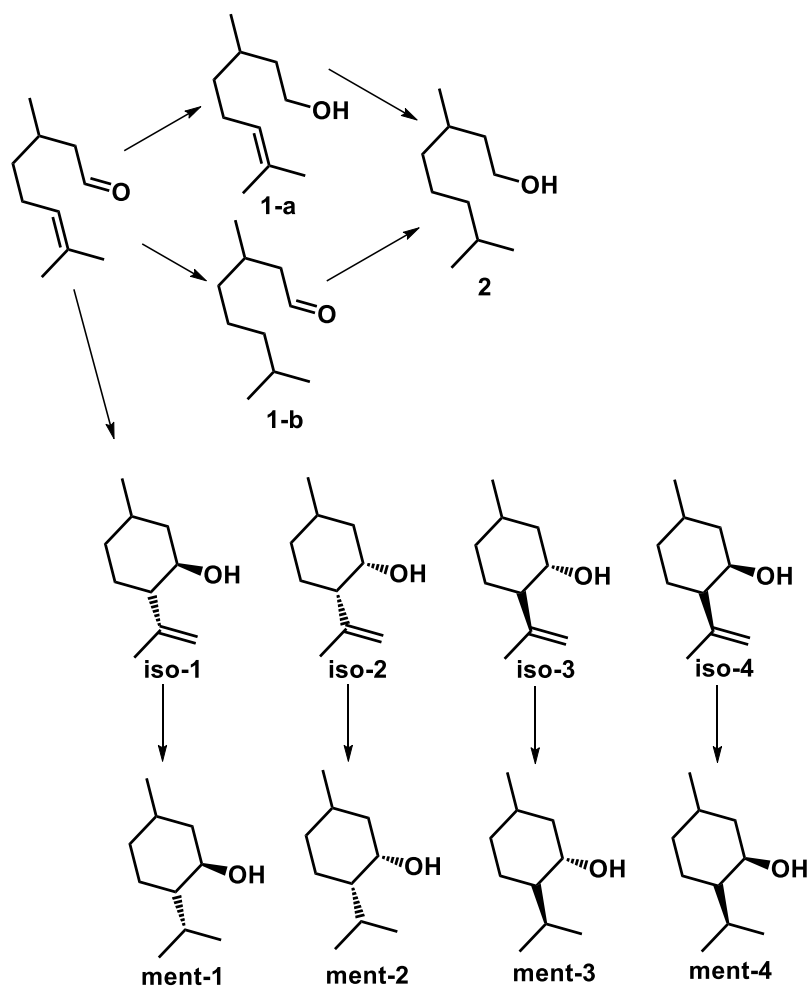


Figure 4.24 Citronellal to menthol reaction scheme.

In a reductive environment with MNPs, the citronellal can be reduced to form citronellol and 3,7-dimethyloctanal (**1-a** and **1-b**, respectively) which ultimately can be reduced further to form 3,7-dimethyloctanol (**2**). In the presence of an acid catalyst the citronellal can undergo a cyclisation reaction to form isopulegols (**iso-1-4**). Depending on the orientation of the citronellal to the acid active site, four separate diastereomers of isopulegols can be formed; ( $\pm$ )-isopulegol, ( $\pm$ )-iso-isopulegol, ( $\pm$ )-neo-isopulegol and ( $\pm$ )-neiso-isopulegol. If isopulegols are formed in the presence of a reductive catalyst, isopulegols can be reduced into menthols (**ment-1-4**). Depending on the diastereomers

of isopulegols, there are also four possible menthol diastereomers. The first menthol (**ment-1**) is the desired product, ( $\pm$ )-menthol. The publication by Cirujano *et al.* described the ability to perform the two catalysis steps sequentially. First the reaction was performed in an inert environment, thus to not allow the MNPs to reduce the citronellal to the undesired products. After the citronellal had been converted into isopulegols by the MIL-101(Cr) Lewis acid sites, the autoclave was pressurised with hydrogen gas, allowing the immobilised MNPs to reduce the isopulegols to menthols.

It would be ideal if a catalyst could be found that performs the whole sequence selectively in a single reaction environment (one-pot tandem reaction). Changing the MOF active sites to create a stronger Lewis acid, or reducing the activity of the MNPs are two strategies tried in this work. The first trials were to replicate the findings by Cirujano *et al.* and determine the similarity of performance in their catalysts to the double solvent deposition catalysts. Initially, the reaction conditions were optimised without MNPs in MIL-101(Cr), seen in Table 4.8. It was determined that using dry solvent plays a role in increasing the catalyst activity. Comparing Table 4.8 Entry 1 and 2 it is seen that using dry solvent increases the conversion by 8%. Additionally, by minimising the amount of solvent used the conversion also increases. However, the experimental setup makes it difficult to routinely use such small amounts due to small quantities of solvent evaporating during reaction and the inability of the full catalyst to be in solution when using very small amounts of solvent. Although reducing  $C_6H_{12}$  from 3 ml to 1 ml (Table 4.8 Entry 2 and 4) increases the conversion by an additional 6% it was determined that 3 ml is easier to work with and led to more reproducible results, thus it was decided to use 3 mL of solvent in subsequent reactions. The selectivity to the desired isopulegol diastereomer remains comparable regardless of activity.

Table 4.8 MIL-101(Cr) citronellal to isopulegol reaction optimisation. Reaction conditions: 8 mol% MIL-101(Cr) catalyst, 3 ml cyclohexane, 20  $\mu$ l ( $\pm$ )-citronellal, 16 hours, 8 bar H<sub>2</sub>, 80 °C. <sup>a</sup> dry cyclohexane.

Entry	Amount of C <sub>6</sub> H <sub>12</sub> (mL)	Conversion (%)	Sel. to iso-1 (%)
1	3	23	72
2	3 <sup>a</sup>	31	71
3	2 <sup>a</sup>	32	71
4	1 <sup>a</sup>	37	71
5	0.5 <sup>a</sup>	36	71
6 <sup>14</sup>	0.5	50	70

The higher conversions reported by Cirujano *et al.*, which achieved around 50% in the same time (Table 4.8 entry 6), could not be reproduced using MIL-101(Cr) in this work, so multiple other MOF materials were investigated as catalysts in order to achieve higher activity. Table 4.9 shows that higher activity can be achieved when compared to the analogous MIL-101(Cr) experiment seen in Table 4.8 Entry 2. When employing MIL-101(Cr)-NO<sub>2</sub>, where 2-nitroterephthalic acid replaces the terephthalic acid linker, the conversion is increased by 9% while keeping the same selectivity. An increased activity for isopulegol formation was also observed by Vermoortele *et al.* when using UiO-66-NO<sub>2</sub>, a Zr-based MOF with 2-nitroterephthalic acid linkers.<sup>15</sup> However, in their study, comparing UiO-66-NO<sub>2</sub> and UiO-66, the nitro functionalised MOF led to a 56-fold increase in activity in the cyclisation of citronellal. In the case of MIL-101(Cr) this difference is much smaller, but still a positive effect was observed.

For all of the other investigated catalysts, a large decrease in selectivity to the desired isopulegol was observed. Table 4.9 Entry 2 shows an 8% decrease in selectivity when polyoxometalates are also present within the MOF as acid catalysts. This is probably due to the Brønsted and Lewis acid sites available in the polyoxometalate. More discussion into these materials is found in section 4.6. Interestingly, a significant decrease in activity is observed in MIL-100(Sc) which has been shown by Mitchell *et al.*<sup>3</sup> to be an excellent acid catalyst in various reactions. Additionally, MIL-100 catalysts show a decrease in selectivity. This may be due to the limited accessibility of the metal

nodes around the trimesic acid linkers compared to the more open MIL-101 structure with terephthalic acid linkers.

Table 4.9 Citronellal to isopulegol reaction with various MOF catalysts. Reaction conditions: 8 mol% MOF catalyst, 3 ml dry cyclohexane, 20  $\mu$ l ( $\pm$ )-citronellal, 6 hours, 1 bar N<sub>2</sub>, 80 °C.

Entry	MOF	Conversion (%)	Sel. to <b>iso-1</b> (%)
1	MIL-101(Cr)-NO <sub>2</sub>	40	70
2	0.28 W/Sc PTA MIL-101(Sc)	65	62
3	MIL-100(ScFe) [XS Fe] <sup>16</sup>	31	54
4	MIL-100(Sc)	23	41
5	MIL-100(Fe)	46	64

With the aim to maintain the selectivity to the desired isopulegol, MIL-101(Cr) was used as the support for MNPs in the full tandem reaction. 1.0 wt% Pd MIL-101(Cr) was used as the catalyst for the full cyclisation and reduction reaction with the aim to form menthol. Table 4.10 shows the tandem trials with different MNP loadings. The products from the reaction go through the reduction of citronellal pathway nearly exclusively. The first hydrogenation products (**1-a,b**) are major compounds, however 45% has been reduced further to 3,7-dimethyloctanol (**2**). In attempts to minimise this reaction pathway, bimetallic MNPs were deposited in MIL-101(Cr) in two different ratios. In Entry 2 and 3 it can be seen that as the amount of Pd becomes less, the activity towards the second reduction pathway goes down. When the Pd MNPs are fully replaced with Au, the reaction still progresses towards isopulegols but no reduction occurs. These results show again that by minimising the amount of active Pd in the material the reaction can be tuned to the desired product. (The alloying of bimetallic MNP was not determined during the catalyst characterisation, so this may be an identical effect of tuning the ratio of acid site to MNP active site as previously observed in the tandem reductive amination rather than a bimetallic effect.) Table 4.10 Entry 5 shows that by reducing the H<sub>2</sub> pressure to 1 bar the first reduction pathway to produce (**1-a,b**) is active while the second reduction pathway to form (**2**) no longer occurs. This indicates that the harsher conditions are not favourable for the

desired pathway of the menthol formation and the milder 1 bar H<sub>2</sub> produces promising results. By further tuning this reaction by minimising the citronellal reduction pathways, it may be possible to develop an active and selective catalyst. However, more work in optimisation needs to be performed.

Table 4.10 MNPs MIL-101(Cr) catalysts in one-pot tandem citronellal to menthols. Reaction conditions: 8 mol% MOF catalyst, 3 ml dry cyclohexane, 20  $\mu$ l ( $\pm$ )-citronellal, 16 hours, 8 bar H<sub>2</sub>, 80 °C. <sup>a</sup> 1 bar H<sub>2</sub>.

Entry	Metal Loading	Conversion (%)	Isopulegol (%)	Menthol (%)	1 <sup>st</sup> Reduction Product (%)	2 <sup>nd</sup> Reduction Product (%)
1	Pd <sub>100</sub>	100	0	1	54	45
2	Pd <sub>75</sub> Au <sub>25</sub>	100	0	0	67	33
3	Pd <sub>50</sub> Au <sub>50</sub>	100	0	0	82	18
4	Au <sub>100</sub>	80	99	1	0	0
5	Pd <sub>100</sub> <sup>a</sup>	100	0	1	99	0

#### 4.5.2 Chloronitrobenzene to Chloroaniline

Selective hydrogenation of halonitrobenzenes is an important way to make compounds such as chloroaniline, which is widely used as a building block in the fields of pesticides, drugs and dyes.<sup>17</sup> The difficulty with these transformations is due to the dehalogenation that often occurs leading to a mixture of products. The selective reduction of halonitrobenzene to haloaniline becomes more challenging with increasing halogen size.<sup>18</sup> Additionally, the placement of the halogen moiety plays a large role in the difficulty of selective halonitrobenzene conversion, with ortho being the most difficult and meta being the easiest.<sup>18</sup>

Designing a selective and active catalyst for the conversion of chloronitrobenzene to chloroaniline is an area of intense research. Ni nanoparticles have been dispersed over various supports to address the support interaction towards the activity and selectivity.<sup>19</sup> It was determined that acidic supports, such as Al<sub>2</sub>O<sub>3</sub> and SiO<sub>2</sub>, have a higher activity than non-acidic supports like activated carbon. However, with the increased acidity the Al<sub>2</sub>O<sub>3</sub> provided, the selectivity decreased towards the desired chloroaniline. However, PdAu and Au nanoparticles deposited on Al<sub>2</sub>O<sub>3</sub> have been shown to achieve high selectivity to chloroaniline.<sup>17</sup> When the bimetallic PdAu

nanoparticles are used, the reaction rate increases when compared to the monometallic Au.

Figure 4.25 shows a simplified reaction pathway to the four products observed during the reaction. 4-Chloronitrobenzene can undergo three initial reactions in the presence of a Pd catalyst to form either chlorobenzene, nitrobenzene, or 4-chloroaniline. Nitrobenzene and 4-chloroaniline can undergo further reaction to form aniline. The desired product is 4-chloroaniline. In addition to these pathways, there are intermediates, not shown in the Figure 4.25, which also contribute to the final reaction solution. In this case, these other undesired products will be classified as one group.

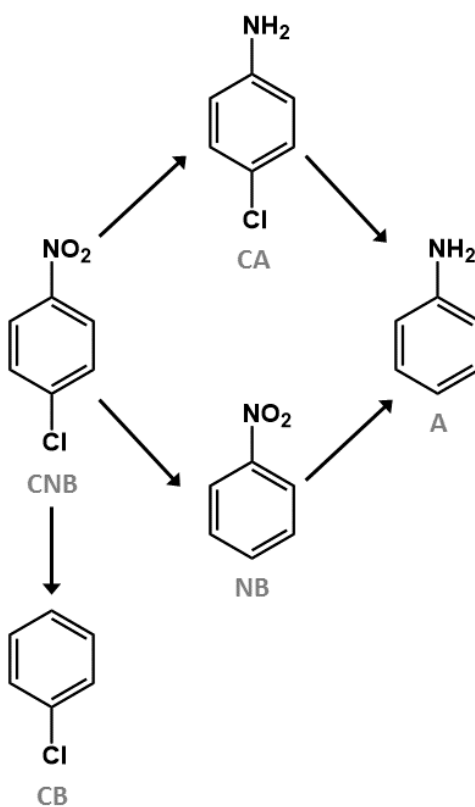


Figure 4.25 Chloronitrobenzene reaction scheme.

The chloronitrobenzene reaction was performed with 1.0 wt% Pd MIL-101(Cr) as a catalyst at 90 °C and 10 bar H<sub>2</sub>. After 16 hours the catalyst converted 16% of the chloronitrobenzene. However, the catalyst was quite unselective, leading to a mixture of chlorobenzene, nitrobenzene and aniline. After 16 hours, no chloroaniline, the desired product, was observed. Next, the reaction was monitored over time by loading

the autoclave with 5 identical vials of catalyst, solvent and chloronitrobenzene. The reaction was pressurised to 10 bar H<sub>2</sub> and was allowed to react at 90 °C for 16 hours. After this time, the reaction was stopped, the hydrogen was released and one vial was removed. Then the remaining 4 vials were placed back under reaction conditions. A vial was removed at 16, 24, 40, 48 and 64 hours. The activity of the catalyst increased and the selectivity drastically changed throughout the experiment. Figure 4.26 shows the conversion and selectivity data from this timed experiment.

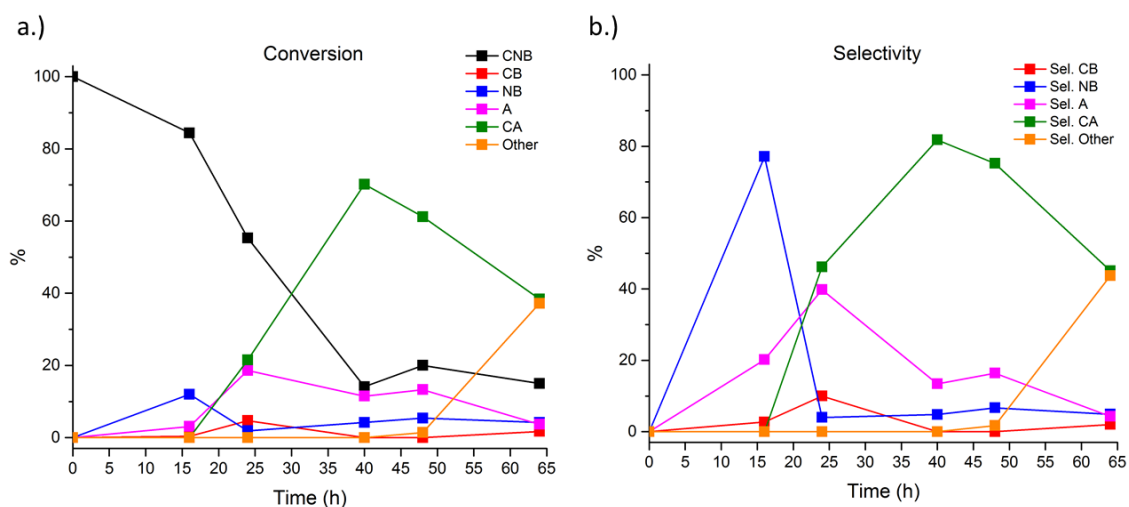


Figure 4.26 Chloronitrobenzene reaction with 1.0 wt% Pd MIL-101(Cr) catalyst. Reaction conditions: 10 mg catalyst, 78 mg chloronitrobenzene, 5 ml toluene at 90 °C and 10 bar H<sub>2</sub>. CNB: chloronitrobenzene, CB: chlorobenzene, NB: nitrobenzene, A: aniline, CA: chloroaniline

The initial result shows that the Pd is removing the chlorine functionality with great selectivity, achieving around 80% selectivity towards nitrobenzene after 16 hours. This, of course, is not the desired product. The selectivity starts to change at 24 hours, showing similar selectivities for both chloroaniline and aniline. This indicates the previously formed nitrobenzene is getting further reduced to aniline. Additionally, the Pd MNPs are no longer removing the chlorine moiety of the reactant molecule, thus giving chloroaniline. This may be due to the oxidation that inevitably occurs during depressurizing and opening of the autoclave when collecting a sample. Interestingly, upon a second oxidation (removal of a vial at 16 hours and 24 hours), the 40 hour sample becomes even more selective to the desired chloroaniline product. On one hand, it is useful that the reaction can be tuned to the desired selectivity by apparently oxidising the catalyst. On the other side, it indicates that this reaction set-up is not

useful in observing the reactions with time because the catalyst is changed with each sample observation. To avoid partially oxidising the catalyst, the experiments which are monitored as time progresses, such as in the reductive aminations previously discussed, were run with independent time intervals. This, of course, also has limitations due to minute differences and experimental error of running each experiment independently, but the catalytic results may be more valid if the assumption of homogeneous reaction setup is taken. Further oxidising the catalyst, for the 48 hour and 64 hour vial removal times shows that the catalyst loses activity for the desired chloroaniline and other side products begin to appear. Additionally, after the 40 hour vial removal the catalysts seem to lose activity, showing the overall conversion remains around 85% between 40 and 64 hours. The overall amount of oxidation plays a role in both selectivity and activity. As previously discussed in Chapter 3, the used catalysts were also examined using XPS with no success. The MNPs do not show a signal, so no progression of oxidation can be qualitatively determined.

The control experiments were performed to determine the oxidation is in fact driving the selectivity of the reaction. A 40 hour reaction was allowed to progress without interruption in order to compare the overall activity and selectivity change caused by submitting the catalyst to oxygen. In this case the reaction progressed much faster, reaching full conversion. Compared to the previous experiment where the reaction is at 80% conversion after 40 hours, a large increase in activity is observed. Additionally, at 40 hours the product selectivity was 40% chlorobenzene, 18% aniline and 42% other side products. No chloroaniline, the desired product, is observed, showing a significant difference in selectivity to the oxidised catalyst. This proves the experimental setup before has a large contribution to the activity and selectivity of the reaction.

Reusing the oxidised catalyst was attempted, however significant reduction in activity was found. Initially, a run was performed for 3 hours at reaction conditions, then the H<sub>2</sub> was vented. Immediately after venting the reaction was re-pressurised to 10 bar H<sub>2</sub> and the reaction proceeded for 16 hours. After this time, the catalyst was removed from the reaction solution, dried and reactivated under vacuum at 150 °C to be used for another catalytic chloronitrobenzene conversion reaction. Table 4.11 shows the

significant decrease in conversion from the initial run to the refreshed catalyst run. This indicates that the oxidation is detrimental to the activity of the catalysis, while the selectivity is enhanced. A controlled and selective partial oxidation of the Pd MNPs might lead to a selective and active catalyst.

Table 4.11 Reusability experiment in oxidised 1.0 wt% Pd MIL-101(Cr).

Entry	Cycle/Time (h)	Conversion (%)	Selectivity (%)				
			CB	NB	A	CA	Other
1	1/19	63.3	13.2	0	21.7	56.6	8.5
2	2/16	25.7	16.5	0	0	83.5	0

## 4.6 Catalysing and Stabilising with Polyoxometalates

The protonic form of polyoxometalates (POMs) are highly acidic solid acids which have been useful in the development of safer processes than using strong mineral acids such as HCl and HClO<sub>4</sub>.<sup>20</sup> POMs have low toxicity, high Brønsted acidity, both in strength and number of acid sites, and are more environmentally friendly than other strong acids.<sup>21</sup> The Keggin anion structure of POMs, with the general formula of [XM<sub>12</sub>O<sub>40</sub>]<sup>n-</sup> where X is the heteroatom (commonly P<sup>5+</sup> or Si<sup>4+</sup>) and M is often molybdenum or tungsten, is shown in Figure 4.27. Commercially available phosphomolybdic acid, phosphotungstic acid or silicotungstic acid are the most widely known type of Keggin polyoxometalates.<sup>20</sup>

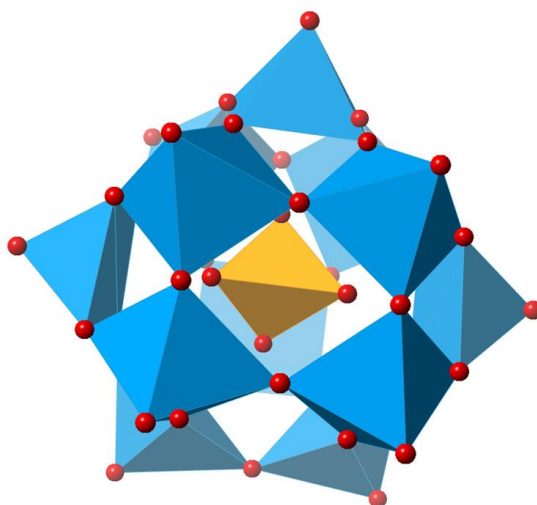


Figure 4.27 Keggin POM structure. Blue: Mo or W, orange: P or Si, red: O.

Polyoxometalates have shown to be useful in stabilising otherwise unstable MOFs.<sup>22</sup> MIL-101(Sc) is known to easily recrystallize into a less porous MOF, MIL-88B(Sc), upon heating and removal of solvent from the pores. MIL-101(Sc) would be a useful Lewis acid catalyst because of the higher acidity  $\text{Sc}^{3+}$  provides compared to  $\text{Cr}^{3+}$ . Additionally, MIL-101(Sc) has larger pores than MIL-100(Sc), which could be beneficial for MNP immobilisation. Thus, preparing a stable and active MIL-101(Sc) support is attractive. POMs have been shown to help maintain the MIL-101(Sc) structure when the MOF is synthesised in the presence of a small amount of phosphotungstic acid (PTA), but phosphomolybdic acid does not appear to have the same effect.<sup>22</sup> For this reason, PTA in MIL-101(Sc) is a potential good candidate for MNP deposition to create a highly active multifunctional material. Additionally, silicotungstic acid (STA) may also stabilise MIL-101(Sc) which could be beneficial for catalysis and subsequent MNP deposition.

In designing a multifunctional material, the tuning of the various active sites is important, as has been shown throughout this chapter. Polyoxometalates offer the possibility of changing the number of acid sites within the MOF material, which could be an alternative method to tuning the ratios of active sites. MIL-101(Cr) is a good choice of support, as previously mentioned, due to its stability and porosity. Thus, as an alternative to changing the MOF system, POMs could offer an alternative route to obtaining more acid sites within the support material which could be beneficial in increasing the overall number and strength of the acid sites relative to the immobilised metal nanoparticles.

### 4.6.1 Synthesis and Characterisation

#### 4.6.1.1 MIL-101(Sc)

Phosphotungstic acid ( $\text{H}_3\text{PW}_{12}\text{O}_{40}$ ; PTA) has previously been shown to help stabilise MIL-101(Sc).<sup>22</sup> This POM was the first tested with a series of loadings between 0.1 and 0.65 W/Sc. Table 4.12 shows the loading of PTA added during the synthesis and the amount observed from EDX in the synthesised MOF material. The results obtained from EDX are in close agreement to the PTA loadings during synthesis, showing this is a good POM for addition into MIL-101(Sc).

Table 4.12 PTA loadings in MIL-101(Sc).

Entry	W/Sc Loading	W/Sc EDX
1	0.1	0.08
2	0.2	0.22
3	0.34	0.28
4	0.5	0.56
5	0.65	0.58

All XRDs of the PTA loaded MIL-101(Sc) materials show a large diminished low angle peak when compared to the calculated MIL-101(Cr) structure and the  $2\theta$  range of 3-11 appears to have an increased background compared to the rest of the diffractogram, seen in Figure 4.28. The loss of initial peak intensity indicates a lack of long range order in the MOF crystals. This reduction of long range order increases with the loading of PTA until the largest loading where multiple other peaks appear. In this sample, the MIL-101(Sc) peaks appear much smaller than the other peaks in the 7-9° region. This separate phase is not determined at this time. The PTA MIL-101(Sc) materials show a single octahedral crystal morphology, as expected for MIL-101(Sc), as shown in a representative SEM image in Figure 4.29.

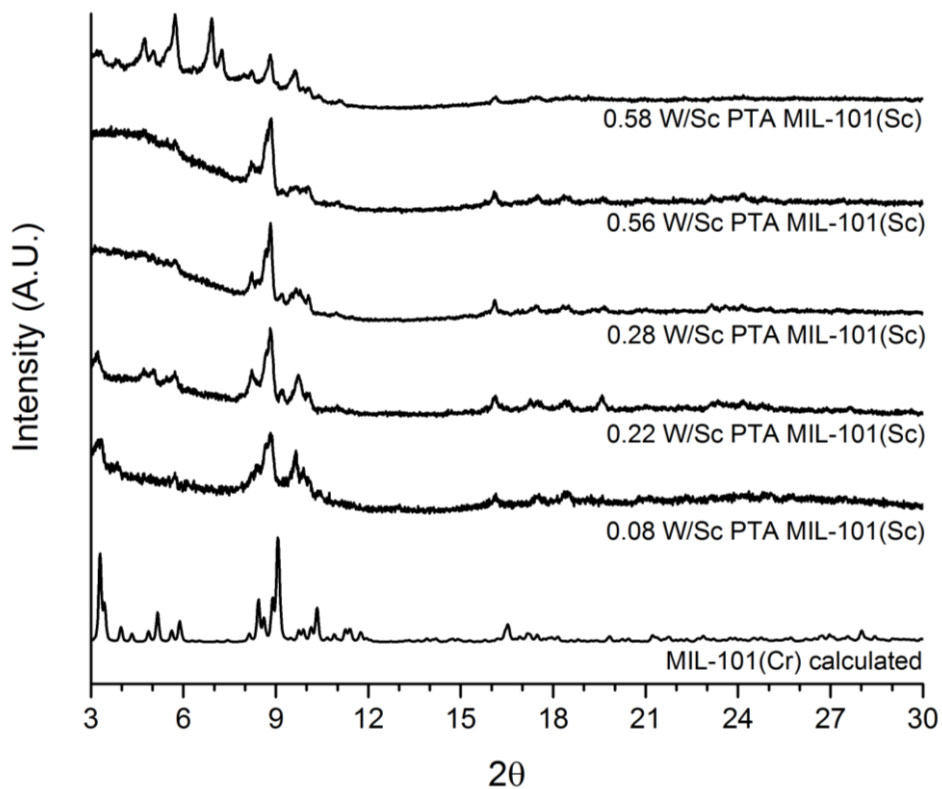


Figure 4.28 XRDs of PTA MIL-101(Sc) materials.

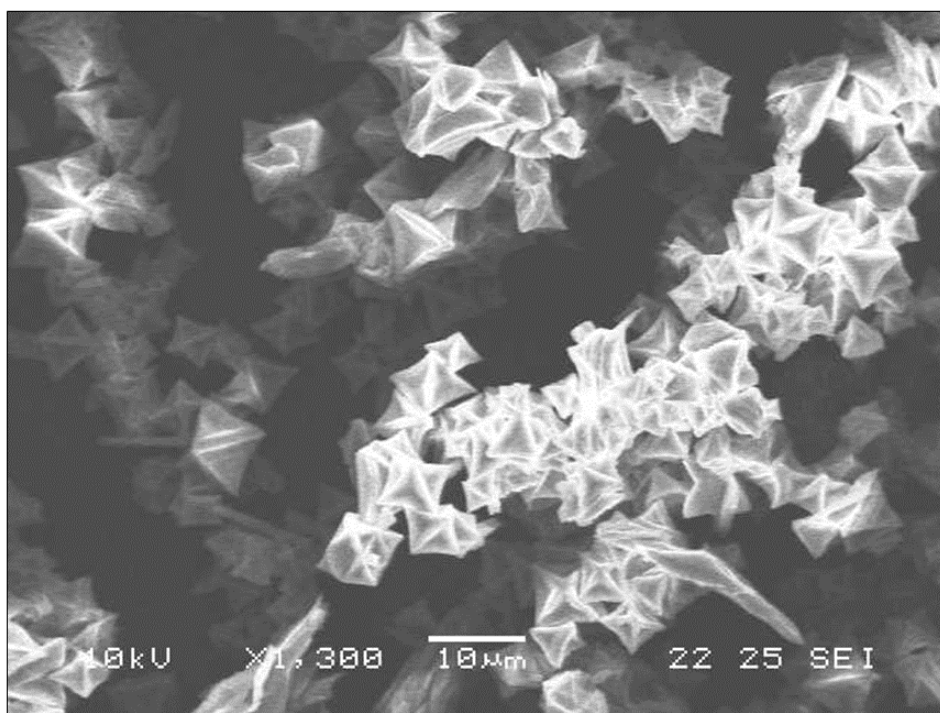


Figure 4.29 0.28 W/Sc PTA MIL-101(Sc) SEM image.

Silicotungstic acid ( $H_4[W_{12}SiO_{40}]$ ; STA) was also investigated as a stabilizing agent in MIL-101(Sc). Silicotungstic acid is used as an acid catalyst in industry for the formation of ethyl acetate and acetic acid<sup>23</sup> and is readily available. This POM was added to the preparation of MIL-101(Sc) in an identical way as PTA, in W/Sc ratios of 0.1, 0.2 and 0.34. After work-up of the material, EDX and SEM was used to gain insight into the crystal morphology and determine the overall POM loading. Table 4.13 shows the EDX loading compared to the theoretical loadings. As observed, the STA material is a less suitable candidate for POM loading in MIL-101(Sc) during the MOF synthesis because it is not possible to accurately control the amount of POM obtained in the final material.

Table 4.13 STA loadings in MIL-101(Sc).

Entry	W/Sc Loading	W/Sc EDX
1	0.1	0.35
2	0.2	0.17
3	0.34	0.20

Additionally, SEM showed that there are multiple types of crystal morphologies present, as can be seen from the representative example depicted in Figure 4.30. Ideally, MIL-101(Sc) should have an octahedral shape, but elongated rod-like crystals are also observed.

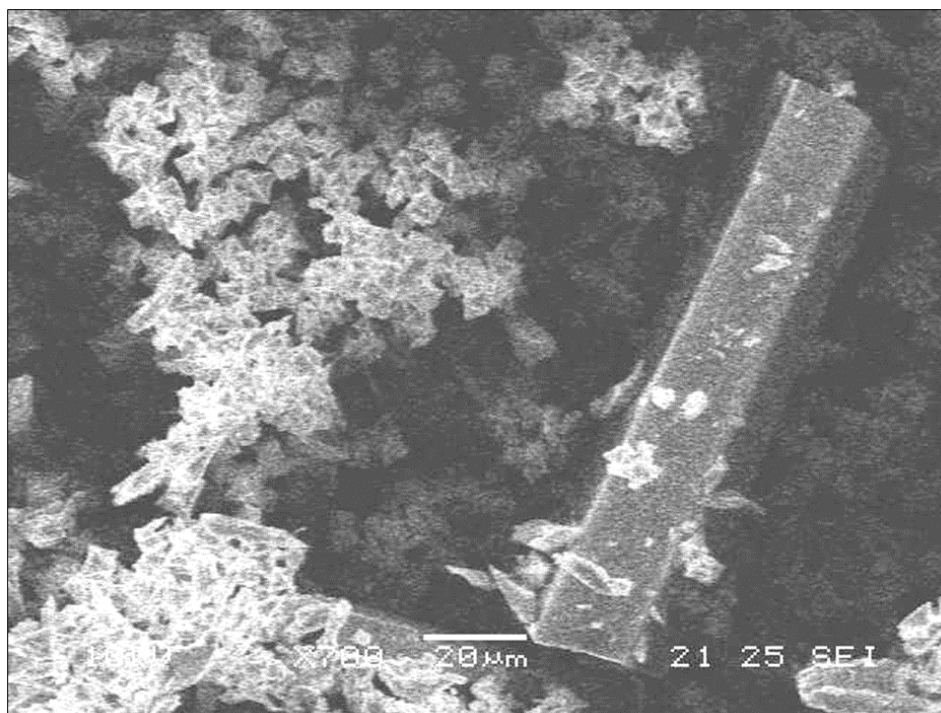


Figure 4.30 0.2 W/Sc STA MIL-101(Sc) SEM image showing multiple crystal morphologies.

The XRD patterns, seen in Figure 4.31 show very broad and low signal to noise peaks in the diffractograms which indicate poor crystallinity.

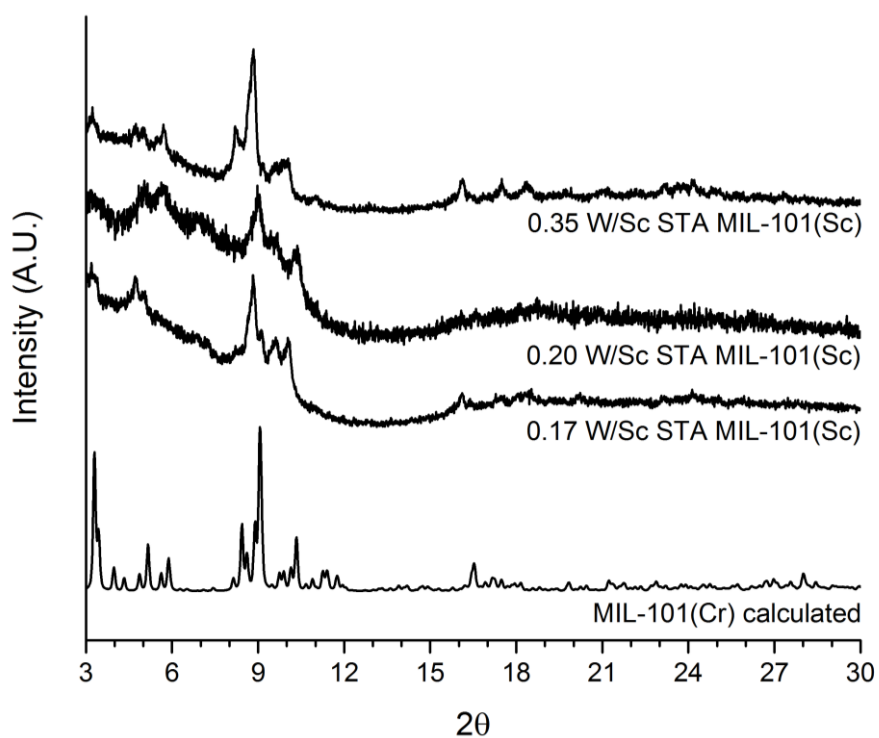


Figure 4.31 XRDs of STA MIL-101(Sc) materials.

#### 4.6.1.2 MIL-101(Cr)

MIL-101(Cr) was loaded with PTA ranging from 0.1 to 0.4 W/Cr. All materials, in Table 4.14, show a good correlation from PTA loadings to the EDX values obtained, similar to the MIL-101(Sc) case. All four POM in MOF materials show the correct peaks for the MIL-101 material, seen by PXRD in Figure 4.32. Moreover, some additional peaks are also observed in the  $2\theta$  region between  $7^\circ$  and  $8^\circ$ , which have been previously reported to be POM ordering within the MOF pores.<sup>24</sup> In this account, Bromberg *et al.* modelled PTA in three ways: 5 POMs disordered in the large cage, 5 ordered in the large cage, and POMs both in the large and small cage of the MOF. The highest calculated intensity in the 7-8 region is when the PTA is disordered in the large cage, but these calculated peaks do not necessarily agree with the experimentally observed peaks. The peak positions of the calculated ordered pattern within the large cage match much closer with the experimental data although the intensities are different. The discrepancy is suggested to be due to the possibility of PTA also being encapsulated within the small cages. The additional peaks observed in Figure 4.32 agree with this result. Additionally, the intensity of these peaks increase as the loading of PTA increases, indicating that they are indeed due to some ordering of PTA within the MOF structure.

Table 4.14 PTA loadings in MIL-101(Cr).

Entry	W/Cr Loading	W/Cr EDX
1	0.1	0.14
2	0.2	0.35
3	0.3	0.36
4	0.4	0.41

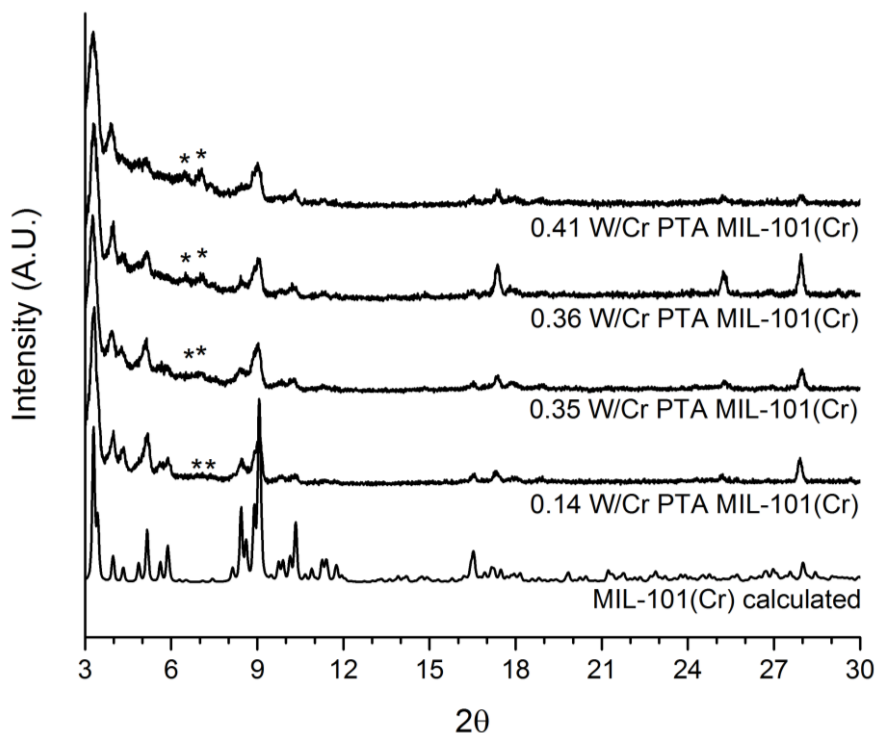


Figure 4.32 XRDs of PTA loaded MIL-101(Cr) materials. \* extra peaks from PTA in the MOF pores.

#### 4.6.2 Imine Formation Catalysis

The test reaction used to determine the stability and activity of the POM encapsulated MOF catalysts is the imine formation reaction shown in Figure 4.33. Because this is the first step in the tandem reaction discussed in detail throughout this chapter, it is a good benchmark reaction to determine whether the modified MOF material would be a good candidate for MNP deposition and subsequent multifunctional tandem catalysis. Additionally, the ease of which the reaction progress can be monitored by  $^{19}\text{F}$  NMR makes this a good choice for the initial catalytic screening.

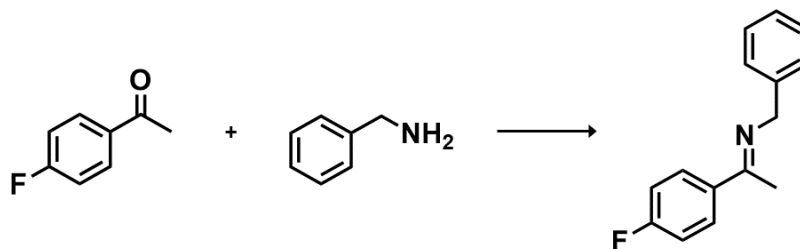


Figure 4.33 Imine formation reaction.

#### 4.6.2.1 MIL-101(Sc)

After successful loading of PTA in MIL-101(Sc) the materials were activated prior to catalysis at 120 °C under vacuum. Before being tested in the imine formation, the activated materials were first submitted for XRDs analysis. This was done to determine if the MOF material withstands the activation procedure, which involves removal of solvent from the pores, and if the material remains crystalline with coordinatively unsaturated sites. Figure 4.34 shows that for these materials the activation does not significantly decrease the crystallinity of the MIL-101(Sc) material, confirming the stabilizing effect of the POM. Additionally, the low angle peak missing in the as prepared materials appears after activation. This indicates that the long-range order of the material appears after the heat and vacuum treatment. This may be due to the water attracted by the POM in the MOF pores. The increased background in this region also appears to reduce upon the activation treatment of removing the water.

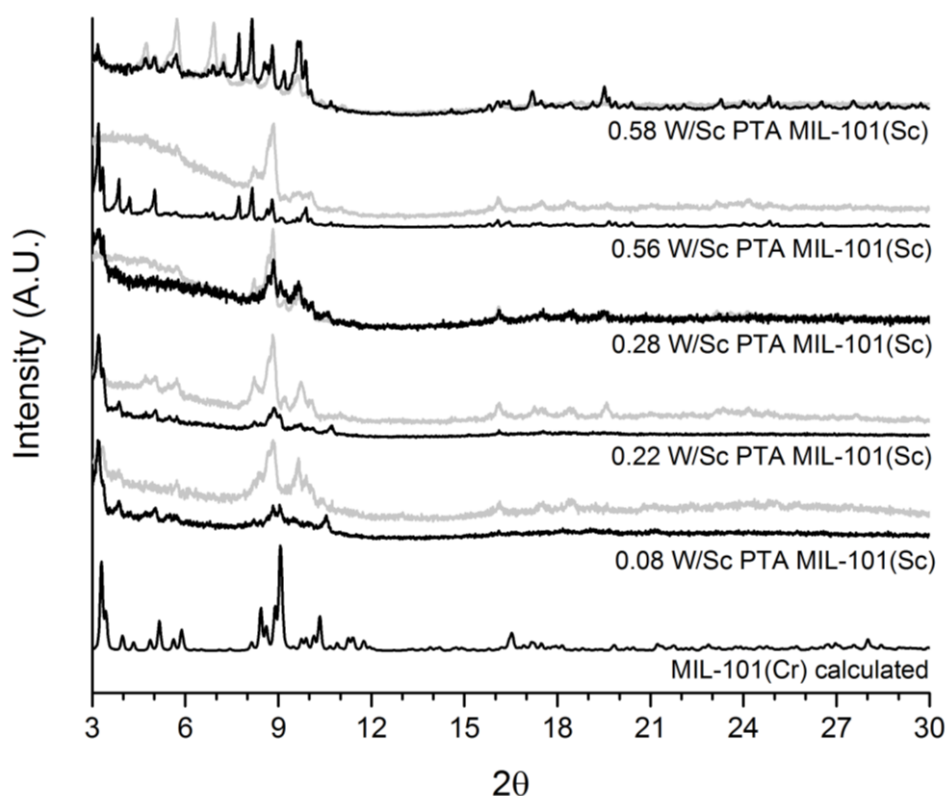


Figure 4.34 Activated PTA MIL-101(Sc) materials. Activation took place under vacuum at 120 °C for 16 hours. Light grey data set is the as prepared material and black data set is the activated material.

Next, the materials were tested as catalysts in the imine formation reaction. Table 4.15 shows the results for the catalytic materials with varying PTA loading for the imine formation after 8 hours of reaction at 50 °C.

Table 4.15 Imine formation conversions for PTA loaded MIL-101(Sc) catalysts. Reaction was performed at 50 °C for 8 h under N<sub>2</sub> in hexane. <sup>a</sup> analogous reaction performed by MIL-101(Cr).

Entry	W/Sc Loading	Conversion (%)
1	0.08	6.0
2	0.22	61.3
3	0.28	63.1
4	0.56	59.7
5	0.58	60.9
6 <sup>a</sup>	0	48.5

It is seen that at 0.08 W/Sc PTA the material is not a successful catalyst, likely because of the degradation of MIL-101(Sc) crystallinity during the reaction, most probably turning into nonporous MIL-88B(Sc). However, all other materials were successful in catalysis. Compared to MIL-101(Cr) the 0.22-0.58 W/Sc PTA MIL-101(Sc) materials achieve a conversion which is between 11.2 to 14.6% higher. There is no trend to the conversion with respect to the POM loading above 0.08 W/Sc. To determine if the catalyst maintains crystallinity during reaction, the 0.28 W/Sc material was examined in XRD after catalysis. Figure 4.35 shows that the material does lose some crystallinity indicated by the appearance of broad peaks and a lower signal to noise ratio in the diffractogram. However, the characteristic MIL-101 peaks are still observable after reaction and no other phase is apparent. This indicates that even during catalysis the POMs help to maintain the structure of MIL-101(Sc). Further studies into possible leaching of POMs from the MOF during catalysis need to be performed.

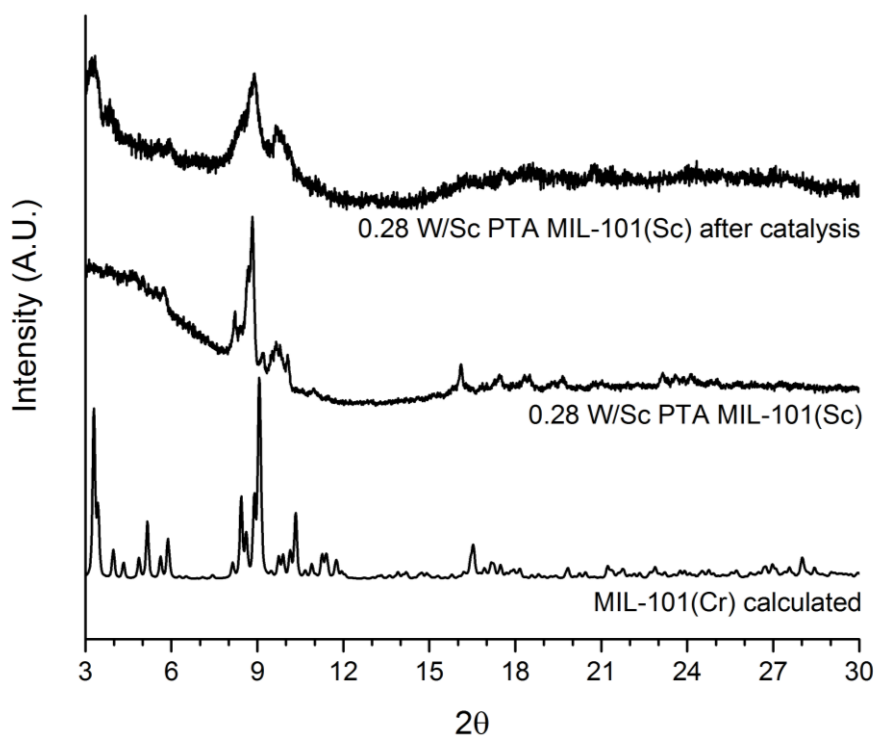


Figure 4.35 0.28 W/Sc PTA MIL-101(Sc) XRD after imine formation catalysis.

Another POM, silicotungstic acid, was also used to stabilise MIL-101(Sc). Using the 0.17-0.35 W/Sc STA MIL-101(Sc) materials in catalysis showed no real correlation between STA loading and the catalytic activity, as can be seen in Table 4.16. The STA loaded MOF catalysts achieve a higher overall conversion than the PTA loaded catalysts. However, from SEM and EDX it was determined that multiple phases of material are present in the STA loaded materials, and there is not opportunity to tune the overall amount of STA that goes into the MOF, unlike the PTA case.

Table 4.16 Imine formation results from STA loaded MIL-101(Sc) catalysts. Reaction conditions: 50 °C, 8 h, under N<sub>2</sub> in hexane. <sup>a</sup> analogous reaction performed by MIL-101(Cr).

Entry	W/Sc Loading	Conversion (%)
1	0.17	67.6
2	0.2	67.8
3	0.35	65.4
4 <sup>a</sup>	0	48.5

#### 4.6.2.2 MIL-101(Cr)

The 0.14 to 0.41 W/Cr MIL-101(Cr) materials were also examined in imine formation reaction. Figure 4.36 shows the conversion achieved with each catalyst after 8 hours of reaction. As more PTA is added to the MOF the conversion to the desired imine is decreased. Even at a relatively small loading of 0.14 W/Cr the conversion decreases from 49% with no PTA added to 40%. This means that the stabilisation of MIL-101(Cr) with PTA is detrimental to the catalytically active sites in the case of the imine formation reaction. Due to this result, the POMs in MIL-101(Cr) were not pursued further as a support material for multifunctional MNP MOF materials.

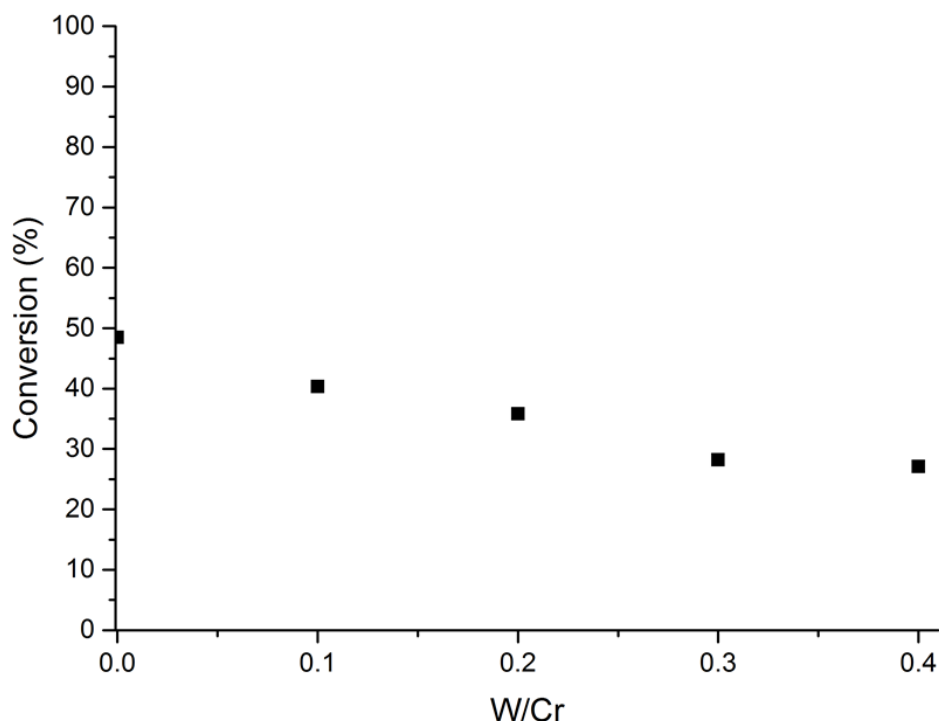


Figure 4.36 Imine formation catalysis with PTA in MIL-101(Cr)

#### 4.6.3 Nanoparticle Deposition in MIL-101(Sc)

Due to the success of PTA in MIL-101(Sc) in stabilising the structure as well as leading to good performance in catalysis, this material was then investigated for MNP deposition. The lowest successful loading of PTA, 0.22 W/Sc, was used to allow for the largest pore volume of the support material, seen in Figure 4.37. The isotherm has the typical two steps of the MTN adsorption isotherm, showing the filling of the small and

large cage at around 0.15  $P/P_0$  and 0.2  $P/P_0$  respectively. This indicates that the POM does not fill either cage completely, which would change the overall isotherm shape.

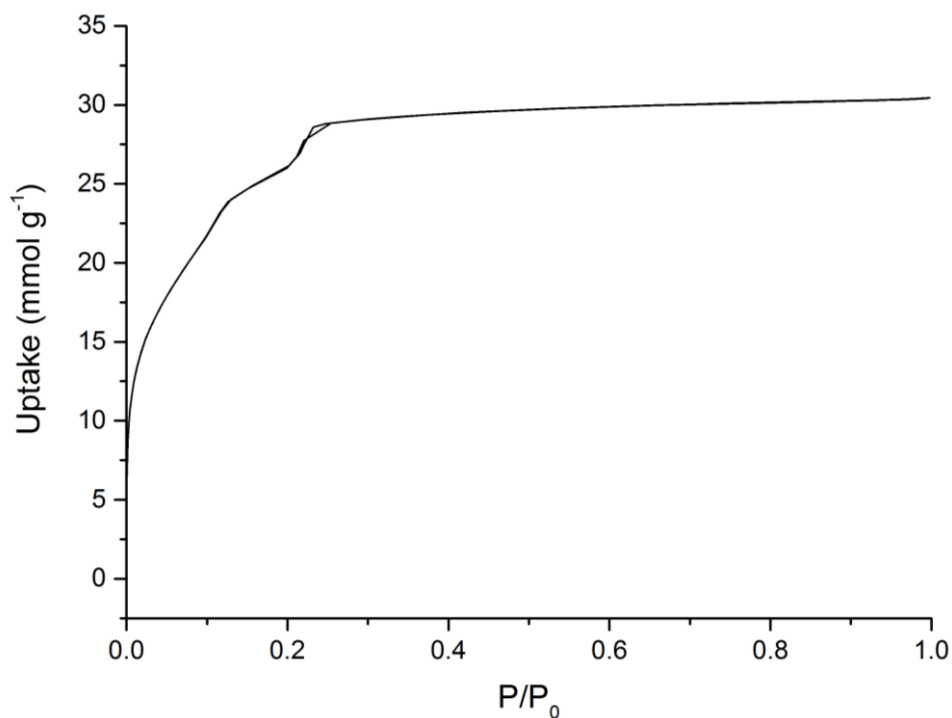


Figure 4.37  $\text{N}_2$  adsorption at 77 K of 0.22 W/Sc PTA MIL-101(Sc).

An initial deposition experiment was performed and it was attempted to load the material with 1.0 wt% Pd. The MOF did not withstand the Pd deposition procedure and a mostly amorphous material was obtained, shown by XRD patterns in Figure 4.38. The peaks starting at  $9^\circ$  could be MIL-88B, the more stable Sc and terephthalic acid MOF. Another attempt was tried with a lower Pd loading of 0.6 wt% with the same results. While the PTA stabilised material can successfully be used in catalysis, it is not stable enough to withstand the double solvents deposition procedure.

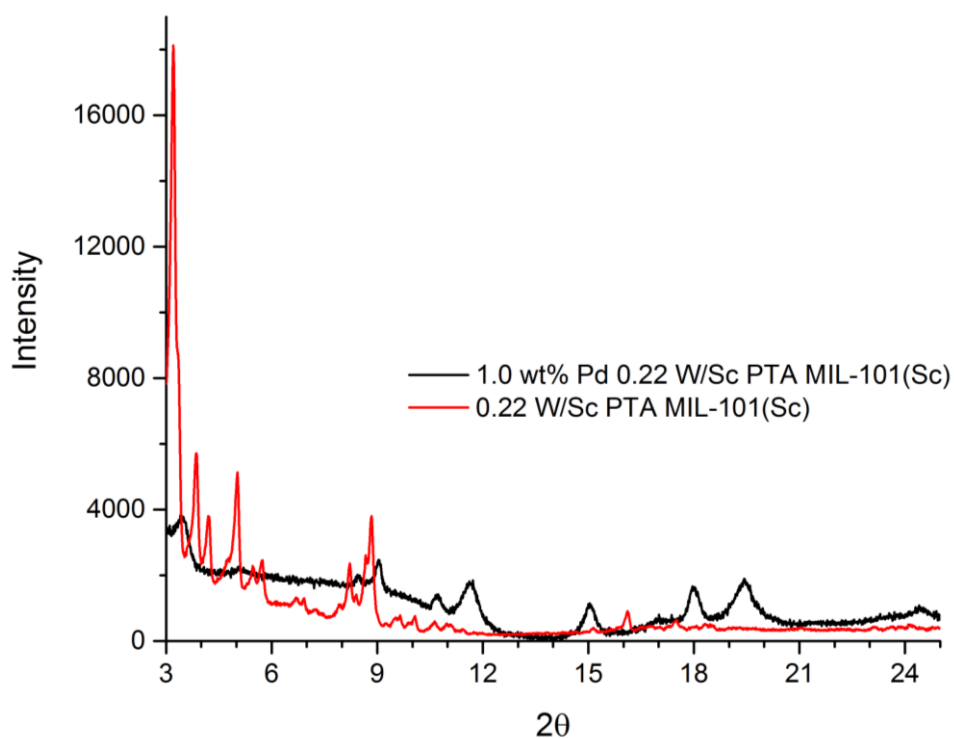


Figure 4.38 PXRD patterns comparing the POM/MOF material before and after Pd deposition.

## 4.7 Conclusions and Outlook

In both MIL-101(Cr) and MIL-100(Sc) the MNP deposition enhances the imine formation catalysis. These catalysts were then tested in a reductive amination reaction where both the MOF sites and Pd MNP sites behave as separate active catalysts within the single material. At 50 °C, 1.0 wt% Pd in MIL-101(Cr) and 1.0 wt% Pd in MIL-100(Sc) are selective towards the desired 2° amine product, but the catalyst is not very active, achieving only 65% conversion in 16 hours for the MIL-101(Cr). The 1.0 wt% Pd in MIL-101(Cr) catalyst was shown to behave heterogeneously by a hot filtration test. Pd in MIL-101(Cr) can successfully be reused up to three times while Pd MIL-100(Sc) is not stable under recycling conditions.

Increasing the temperature to 90 °C leads to full conversion but a change in selectivity. The desired 2° amine undergoes a hydrogenolysis reaction to produce an undesired primary amine and toluene. For this reason, the ratios of Pd MNP active site to MOF active site were varied in an attempt to tune the selectivity. Four loadings of Pd were deposited within the MIL-101(Cr) material and the selectivity to the desired 2° amine was tuned from 9% to 90% by changing the ratio of Pd sites to Lewis acid sites. This

demonstrates that while many methods for selective catalysis have been researched for MNP in MOF catalysts, a simple balancing of the number of active sites is a good alternative. A MATLAB model was created to determine how the change in Pd to Lewis acid site ratio changed the activity of each step in the tandem reaction. The 0.4 wt% Pd MIL-101(Cr) was shown to be the best catalyst for maximisation of 2° amine while also maximising activity. Following the MATLAB model, the maximum 2° amine was produced with the 0.4 wt% Pd MIL-101(Cr) catalyst between 6 to 12 hours. Next, the 1.0 wt% Pd in MIL-101(Cr) catalyst was subjected to a hot filtration test and recycling was performed. However, while the 1.0 wt% Pd in MIL-101(Cr) catalyst proved to still catalyse heterogeneously at the higher reaction temperature, the recyclability tests proved more difficult and modifications into a better experimental design should be tested.

Two alternative reactions were examined using the Pd in MIL-101(Cr) catalyst. First the tandem citronellal to menthol reaction was investigated. It was proven to be challenging to balance the ratio of highly active Pd MNPs to MOF Lewis acid sites, and alternate reductive reaction pathways gave undesirable products. Other MOF systems were tested in the hope to find more active catalysts for the isopulegol formation, but the selectivity to the desired isopulegol decreased in the cases with an increased cyclisation rate. If the full tandem reaction were to be tuned further, experiments into lowering the H<sub>2</sub> reaction pressure and changing the Pd MNP to Lewis acid active sites should be examined.

The selective reduction of chloronitrobenzene to chloroaniline was performed using 1.0 wt% Pd in MIL-101(Cr) as a catalyst. Initially, the Pd MNPs are very active which leads to dehalogenation catalysis occurring. It was determined that strategic oxidation of the Pd catalyst led to a significantly more selective catalyst towards the desired chloroaniline. This topic would be interesting to examine with bimetallic PdAu MNPs, for instance, which may show the high selectivity without the need for oxidation. Additionally, adding some tandem catalysis application for the MOF acid sites could be an interesting way to test the full bimetallic and multifunctional PdAu MOF catalyst.

Finally, polyoxometalates were added to MIL-101(Cr) and MIL-101(Sc) to help stabilise and add additional acid sites within the MOF structure in order to increase catalytic activity. It was determined that 0.22 W/Sc PTA was necessary to maintain stability within the MIL-101(Sc) during imine formation catalysis and this catalyst performed better than the MIL-101(Cr) catalyst. STA was also added to the MIL-101(Sc) synthesis, but the quantity of POM added to the system did not necessarily correlate to the actual loading in the final material. For MIL-101(Cr) with PTA catalysts, the addition of PTA caused a decrease in conversion, thus leading to a less active catalyst in the imine formation reaction. Pd MNPs were not successfully deposited in 0.22 W/Sc MIL-101(Sc) materials using the double solvent deposition method. In this case, the MOF did not remain the same crystalline phase during the deposition procedure, and peaks for both MIL-101(Sc) and MIL-88B were seen in PXRD patterns.

Overall, multifunctional materials were created which efficiently catalyse a multi-step tandem reaction. MIL-101(Cr) was the most useful MOF for the immobilisation of nanoparticles due to its stability. A method for tuning the reaction towards the desired product was achieved by changing the metal nanoparticle active site to Lewis acid active site ratio. This simple method of tuning the bifunctional catalysts could possibly be used in many multi-step reactions.

## 4.8 References

1. Cirujano, F. G.; Leyva-Pérez, A.; Corma, A.; Llabrés i Xamena, F. X., MOFs as Multifunctional Catalysts: Synthesis of Secondary Arylamines, Quinolines, Pyrroles, and Arylpyrrolidines over Bifunctional MIL-101. *ChemCatChem* **2013**, *5*, 538-549.
2. Chen, Y.-Z.; Zhou, Y.-X.; Wang, H.; Lu, J.; Uchida, T.; Xu, Q.; Yu, S.-H.; Jiang, H.-L., Multifunctional PdAg@MIL-101 for One-Pot Cascade Reactions: Combination of Host-Guest Cooperation and Bimetallic Synergy in Catalysis. *ACS Catal.* **2015**, *5*, 2062-2069.
3. Mitchell, L.; Gonzalez-Santiago, B.; Mowat, J. P. S.; Gunn, M. E.; Williamson, P.; Acerbi, N.; Clarke, M. L.; Wright, P. A., Remarkable Lewis Acid Catalytic Performance of the Scandium Trimesate Metal Organic Framework MIL-100(Sc) for C-C and C=N Bond-Forming Reactions. *Catal. Sci. Tech.* **2013**, *3*, 606-617.
4. Yap, A. J.; Chan, B.; Yuen, A. K. L.; Ward, A. J.; Masters, A. F.; Maschmeyer, T., A Palladium-Catalyzed Multicascade Reaction: Facile Low-Temperature Hydrogenolysis of Activated Nitriles and Related Functional Groups. *ChemCatChem* **2011**, *3*, 1496-1502.
5. Boeker, E. A., Simple Integrated Rate Equations for Reversible Bimolecular Reactions. *Experientia* **1984**, *40*, 453-456.
6. Climent, M. J.; Corma, A.; Iborra, S., Heterogeneous Catalysts for the One-Pot Synthesis of Chemicals and Fine Chemicals. *Chem. Rev.* **2011**, *111*, 1072-1133.
7. Schäfer, B., Menthol. *Chemie in Unserer Zeit* **2013**, *47*, 174-182.
8. Aggarwal, V. K.; Vennall, G. P.; Davey, P. N.; Newman, C., Scandium Trifluoromethanesulfonate, an Efficient Catalyst for the Intermolecular Carbonyl-Ene Reaction and the Intramolecular Cyclisation of Citronellal. *Tetrahedron Lett.* **1998**, *39*, 1997-2000.
9. Nakatani, Y.; Kawashima, K., A Highly Stereoselective Preparation of L-Isopulegol. *Synthesis* **1978**, 147-148.
10. Fuentes, M.; Magraner, J.; De Las Pozas, C.; Roque-Malherbe, R.; Pérez Pariente, J. Í.; Corma, A., Cyclization of Citronellal to Isopulegol by Zeolite Catalysis. *Appl. Catal.* **1989**, *47*, 367-374.
11. Iosif, F.; Coman, S.; Pârvulescu, V.; Grange, P.; Delsarte, S.; de Vos, D.; Jacobs, P., Ir-Beta Zeolite as a Heterogeneous Catalyst for the One-Pot Transformation of Citronellal to Menthol. *Chem. Commun.* **2004**, 1292-1293.
12. Mertens, P.; Verpoort, F.; Parculescu, A.-N.; de Vos, D., Pt/H-Beta Zeolites as Productive Bifunctional Catalysts for the One-Step Citronellal-to-Menthol Conversion. *J. Catal.* **2006**, *243*, 7-13.
13. Milone, C.; Gangemi, C.; Ingoglia, R.; Neri, G.; Galvagno, S., Role of the Support in the Hydrogenation of Citronellal on Ruthenium Catalysts. *Appl. Catal., A* **1999**, *184*, 89-94.
14. Cirujano, F. G.; Llabrés i Xamena, F. X.; Corma, A., MOFs as Multifunctional Catalysts: One-Pot Synthesis of Menthol from Citronellal over a Bifunctional MIL-101 Catalyst. *Dalton Trans.* **2012**, *41*, 4249-4254.
15. Vermoortele, F.; Vandichel, M.; van de Voorde, B.; Ameloot, R.; Waroquier, M.; van Speybroeck, V.; De Vos, D. E., Electronic Effects of Linker Substitution on Lewis

Acid Catalysis with Metal-Organic Frameworks. *Angewandte Chemie* **2012**, *51*, 4887-4890.

16. Mitchell, L.; Williamson, P.; Ehrlichova, B.; Anderson, A. E.; Seymour, V. R.; Ashbrook, S. E.; Acerbi, N.; Daniels, L. M.; Walton, R. I.; Clarke, M. L.; Wright, P. A., Mixed-Metal MIL-100(Sc,M) (M=Al, Cr, Fe) for Lewis Acid Catalysis and Tandem C-C Bond Formation and Alcohol Oxidation. *Chem. Eur. J.* **2014**, *20*, 17185-17197.

17. Cárdenas-Lizana, F.; Gómez-Quero, S.; Hugon, A.; Delannoy, L.; Louis, C.; Keane, M. A., Pd-Promoted Selective Gas Phase Hydrogenation of P-Chloronitrobenzene over Alumina Supported Au. *J. Catal.* **2009**, *262*, 235-243.

18. Augustine, R. L., *Heterogeneous Catalysis for the Synthetic Chemist*. Marcel Dekker, Inc.: 1996.

19. Cárdenas-Lizana, F.; Gómez-Quero, S.; Keane, M. A., Clean Production of Chloroanilines by Selective Gas Phase Hydrogenation over Supported Ni Catalysts. *Appl. Catal., A* **2008**, *334*, 199-206.

20. Dabiri, M.; Bashiribod, S., Phosphotungstic Acid: An Efficient, Cost-Effective and Recyclable Catalyst for the Synthesis of Polysubstituted Quinolines. *Molecules* **2009**, *14*, 1126-1144.

21. Firouzabadi, H.; Jafari, A. A., Heteropoly Acids, Their Salts and Polyoxometalates as Heterogeneous, Efficient and Eco-Friendly Catalysts in Organic Reactions: Some Recent Advances. *J. Iran. Chem. Soc.* **2005**, *2*, 85-114.

22. González Santiago, B. *Synthesis and Properties of Scandium Carboxylate Metal-Organic Frameworks*. University of St Andrews, 2014.

23. Misono, M., Recent Progress in the Practical Applications of Heteropolyacid and Perovskite Catalysts: Catalytic Technology for the Sustainable Society. *Catal. Today* **2009**, *144*, 285-291.

24. Bromberg, L.; Diao, Y.; Wu, H.; Speakman, S. A.; Hatton, T. A., Chromium(III) Terephthalate Metal Organic Framework (MIL-101): HF-Free Synthesis, Structure, Polyoxometalate Composites, and Catalytic Properties. *Chem. Mater.* **2012**, *24*, 1664-1675.

# Chapter 5

---

Bottom-Up Catalyst Synthesis:

MOF Growth on Pd SiO<sub>2</sub> Spheres

## 5.1 Introduction

Following the realisation of multifunctional MNP in MOF materials, progress into methods to combine these species into controlled metal nanoparticle placement within a MOF has been a challenge of recent research.<sup>1</sup> Obtaining a material which fully immobilises the MNPs within the MOF is of use in catalysis for size selectivity, tuning diffusion rates to the MNP site and enhancing stability and durability of the metal nanoparticle catalyst. Additionally, by using MOFs which contain catalytic active sites within their framework, multifunctional catalysis can take place.

Methods which discuss core-shell morphologies, which can better control the MNP placement within the MOF support, have been mostly focused on zeolitic imidazolate framework (ZIF) materials. These materials have relatively high thermal and chemical stability due to a wide choice of metal nodes and imidazolate linkers. No acid sites are present in ZIF materials with ideal structure due to full coordination of the tetrahedral metal node, however defects have shown to exist and act as acid sites. They are microporous and rarely extend above a 1 nm pore size. This has been utilised in catalysis for size selectivity when MNPs are immobilised within the ZIF. Zhang *et al.* demonstrated a procedure in which Pd MNPs-containing mesoporous silica spheres were coated with ZIF-8.<sup>2</sup> These materials were tested in the hydrogenation of cyclohexene and 1-hexene. 1-Hexene was easily able to diffuse through the ZIF-8 shell and was readily reduced on the Pd MNPs. However, cyclohexene was too bulky to easily fit through the ZIF-8 pores, and was reduced at a significantly slower rate. This shows that the core-shell materials can display size selective catalysis. In contrast, when the Pd in mesoporous silica was tested as a catalyst, large amount of leaching of Pd MNPs was observed. This indicates that the core-shell material not only allows for size selective catalysis, but also aides in the immobilisation of the MNPs.

Ke *et al.* synthesised  $\text{Fe}_3\text{O}_4@\text{MIL-100}(\text{Fe})$  catalysts which were active in a Claisen-Schmidt condensation reaction to form chalcones.<sup>3</sup> In this procedure, mercaptoacetic acid was coated on  $\text{Fe}_3\text{O}_4$  spheres and subsequently MIL-100(Fe) layers were grown in a multi-cycle method by exchanging the spheres between  $\text{FeCl}_3$  solutions and benzenetricarboxylic acid (BTC) solutions. Due to the presence of the  $\text{Fe}_3\text{O}_4$  core, these

catalysts could be easily separated from the catalytic reaction mixture via magnetic decantation. Moreover, the catalyst could be reused in up to 5 catalytic cycles with negligible loss in MIL-100(Fe) crystallinity. However, the combined effect of the core and shell on the activity was not thoroughly investigated. The control experiment in order to test the activity of the Fe<sub>3</sub>O<sub>4</sub> core alone in the Claisen-Schmidt condensation reaction was not performed, so possibly both core and MOF shell active sites partake in the catalytic reaction.

In order to obtain more control over the metal nanoparticle distribution within the MOF supports, core-shell materials have been designed. In the approach discussed in this chapter, Pd MNP precursors were deposited on silica spheres and subsequently a MOF layer was grown around the Pd SiO<sub>2</sub> spheres. The synthesis, characterization and further functionalization of the silica spheres is outlined in section 5.3. Methods into depositing Pd nanoparticles on the silica are discussed in section 5.4. Section 5.5 discusses the multi-cycle MOF growth in order to achieve core-shell materials, as well as attempts to provide more homogeneous materials through modifications of the MOF growth. Other methodologies were attempted on SiO<sub>2</sub> to attempt to produce more homogeneous core-shell materials, as shown in section 5.6. Finally, MOF catalysis was attempted by similar materials with forethought into optimising reaction conditions for the MIL-100(Fe)@Pd SiO<sub>2</sub> materials in section 5.7.

## 5.2 Experimental

Chemicals used were used as received unless otherwise specified.

XPS was performed by Dr. Steve Francis on a Scienta ESCA-300 with an Al X-Ray source at 1486.7 eV. The XP spectra were deconvoluted using CasaXPS with a Shirley background and a 70:30 Gaussian-Lorentzian shape for each emission.

TEM was performed on a Jeol JEM 2011 TEM with an accelerating voltage of 200 kV. The samples were prepared by grinding the sample with acetone and depositing on a holey carbon coated Cu grid.

SEM and EDX was performed on a Jeol JSM-5600 SEM.

FTIR was performed using a Perkin Elmer Spectrum GX IR spectrometer. DRIFTS was performed by Dr. Federico Grillo using a Digilab FTS 7000 series spectrometer with a Specac DRIFTS cell. The samples were mixed with KBr and scanned using 512 scans with a sensitivity of 16 and a resolution of 4 cm<sup>-1</sup>.

### 5.2.1 Silica Sphere Synthesis and Functionalisation

In a typical Stöber sphere preparation, a molar ratio of 1:1.17:2.5 NH<sub>4</sub>OH (Fisher, 35% w/w): H<sub>2</sub>O: EtOH is stirred vigorously in a beaker for 5 minutes (typically 27.3 ml NH<sub>4</sub>OH, 14.4 ml H<sub>2</sub>O and 100 ml EtOH). Next, 27.8 mmol (6.2 ml) tetraethyl orthosilicate (TEOS, Aldrich, 98%) is quickly added and allowed to stir vigorously for 2 hours at room temperature. The resulting solution is filtered, washed with water, and dried at 80 °C in air. The silica spheres are then loaded into a tube furnace and calcined in air at 400 °C for 4 hours.

Amine functionalisation of silica was performed following a procedure from Najafi *et al.* by adding 2.2 ml aminopropyltriethoxysilane (APTES, Aldrich, 98%) to 2 g silica spheres in 100 ml toluene.<sup>4</sup> This solution was stirred and refluxed for 2 hours before filtering and drying. This material was then loaded into a Soxhlet thimble and a Soxhlet extraction was performed for 24 hours in EtOH. Upon drying this material, the amine functionalisation was completed.

### 5.2.2 Metal Nanoparticle Deposition

Initially, Pd MNP deposition was performed using a modified method published by Burton *et al.*<sup>5</sup> 12.3 mg palladium acetate (Aldrich, ≥99.9%) was dissolved in 16 ml MeOH using sonication. This solution was mixed with 250 mg of silica spheres in a round bottom flask and placed on a rotary evaporator until dry.

Alternatively, Pd MNP deposition was performed using electrostatic adsorption. 140 mg SiO<sub>2</sub>-NH<sub>2</sub> spheres were placed in 5 ml pH 2 solution (using HCl to achieve desired pH). 4.8 mg PdCl<sub>2</sub> was added to the solution and stirred for 3 hours, periodically checking pH and adjusting to maintain pH 2. The resulting solution was filtered, washed with water and dried at 80 °C overnight.

### 5.2.3 MOF Growth Methods

Following a method published by Ke *et al.*<sup>6</sup> MIL-100(Fe) was grown on the silica spheres in a step-wise fashion. Initially, 10 mg Stöber spheres were added to a 4 ml 2 mM FeCl<sub>3</sub> solution in EtOH. The solution was heated to 70 °C and allowed to react without stirring for 15 minutes. The solution was centrifuged, decanted and washed with ethanol. Next, the Stöber spheres were placed in a 4 ml 2 mM benzenetricarboxylic acid (BTC) solution in EtOH at 70 °C for 30 minutes. The solution was then centrifuged, decanted and washed with ethanol. After this, one cycle has been completed. The cycles were repeated until the desired MOF thickness was achieved.

Modifications into this methodology were also investigated, and are discussed within the chapter.

### 5.2.4 Catalysis

MIL-100(Fe) was synthesised by a microwave procedure reported by Márquez *et al.* using a 1,3,5-tricarboxylic acid (Alfa Aesar, 98%): iron chloride hexahydrate (Sigma Aldrich, 97%): water ratio of 1:1.5:417.<sup>7</sup> The reaction was then heated to 130°C and kept at this temperature for 5.5 minutes. The mixture was cooled then centrifuged. The resulting solid was washed three times with ethanol before being dried at 70°C overnight in air.

Pd in MIL-101(Cr) was synthesised as discussed in Chapter 3.

A chalcone formation reaction was used to test the MOF catalyst. In this reaction 2.8 mol% MIL-100(Fe) catalyst, calculated using the full molecular MOF weight, was combined with benzaldehyde and acetophenone (1:1 molar ratio) in dry toluene under N<sub>2</sub> atmosphere. The reaction vial was heated to the desired temperature and stirred for 24 hours. The reaction solution was cooled and centrifuged and the liquid decanted. The conversion was found using GC analysis with a Thermo Trace GC ultra. The following GC conditions were used: a Restek RTX-1 (30 m x 0.25 mm x 0.25 µm) column, 50 °C, ramp 8 °C min<sup>-1</sup> to 70 °C, hold 2 min. Ramp 20 °C min<sup>-1</sup> to 300 °C, hold 1 min.

The activity and selectivity of the Pd MNPs were then tested with a chalcone hydrogenation reaction. In this setup 3.5 mol% 1.0 wt% Pd MIL-101(Cr) catalyst, calculated using the MOF molecular weight compared to trans-chalcone, was combined with 0.1 mmol trans-chalcone and dry toluene. The vial was placed into a stainless-steel autoclave and pressurised to 5 bar H<sub>2</sub>. The reaction was heated to the desired temperature and stirred for 16 hours. The reaction was quenched by placing the autoclave in a water bath and allowed to cool to room temperature. The autoclave was slowly depressurised and the reaction vial removed. The reaction solution was centrifuged and the liquid decanted. The conversions and selectivities were determined by GC analysis with a Thermo Trace GC ultra. The following GC conditions were used: a Restek RTX-1 (30 m x 0.25 mm x 0.25 µm) column, 50 °C, ramp 8 °C min<sup>-1</sup> to 70 °C, hold 2 min. Ramp 20 °C min<sup>-1</sup> to 300 °C, hold 1 min.

### 5.3 Silica Sphere Characterisation

Silica spheres were prepared using a modified Stöber sphere method.<sup>8</sup> The Stöber growth in this work occurs by the hydrolysis and condensation of TEOS in a mixture of an alcohol and ammonia. The silica sphere size can be modified by changing the solvent from ethanol to methanol, shown in Figure 5.1. The average sphere size with the ethanol preparation is around 530 nm and the average size when methanol is utilized is around 340 nm. After the synthesis, the spheres were filtered from the reaction solution, washed with water, dried and then calcined at 400 °C for 4 hours to remove the carbon residues from the silica surface.

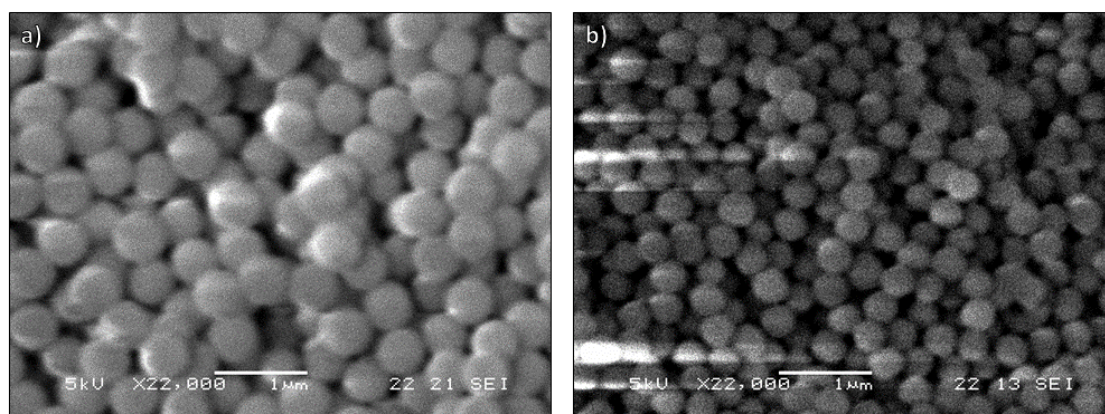


Figure 5.1 Stöber spheres synthesised with (a) ethanol and (b) methanol.

Functionalisation of the surface of the Stöber spheres was accomplished by reaction with silanes.<sup>4</sup> For instance, amine functionality could be introduced by reaction with aminopropyltriethoxysilane (APTES). Infrared spectroscopy (IR) and X-ray photoelectron spectroscopy (XPS) were performed to determine the change in spectra upon adding functionality.

Infrared spectroscopy was performed in two ways: Fourier transfer infrared spectroscopy (FTIR) and diffuse reflectance infrared Fourier transform spectroscopy (DRIFTS). Initially FTIR was used, shown in Figure 5.2.

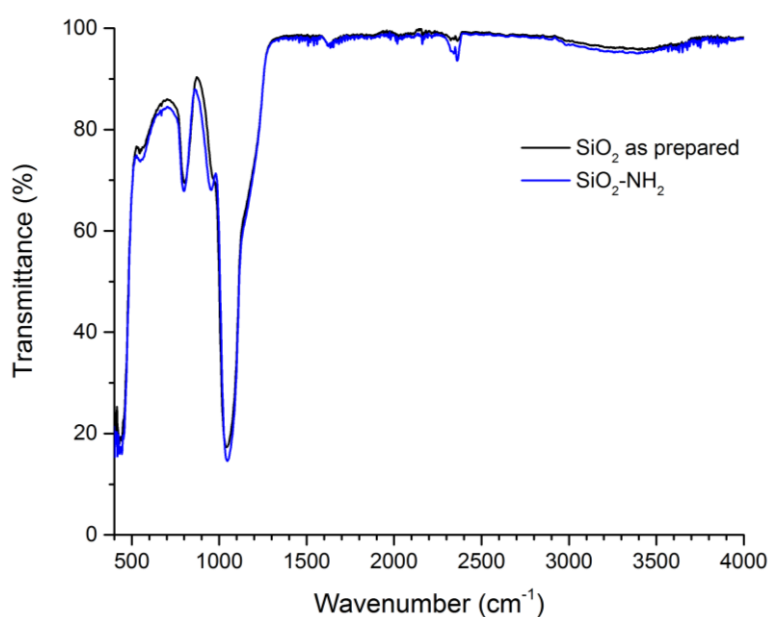


Figure 5.2 FTIR spectra of SiO<sub>2</sub> as prepared and after the amine functionalisation.

No significant change in peaks could be observed although there is a slight peak increase between 3300 and 3500 cm<sup>-1</sup>, which could indicate amine functionality. The overall lack of change in the spectra may be because the surface concentration is small compared to the bulk concentration. This would mean that the amine concentration at the surface is very small compared to the SiO<sub>2</sub> signal from the entire sphere. Because of this, DRIFTS was used, shown in Figure 5.3.

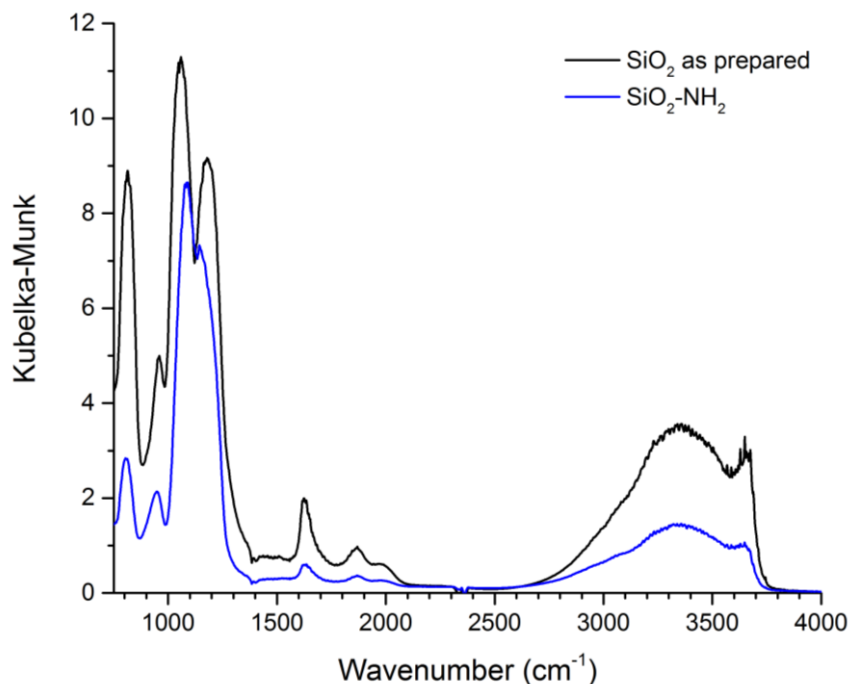


Figure 5.3 DRIFT spectra of the as prepared Stöber spheres and after amine functionalisation.

A significant decrease in the peaks is observed after functionalisation. This may be due to the diminishing silanol bonds on the surface after the APTES is added. Additionally, the shape and intensity of the broad peak around 3300 cm<sup>-1</sup> is changed after functionalisation. This may be due to the decrease in -OH functionality on the surface and an increase of amine. It is interesting, however, that there is not a large enhancement in this region due to the addition of amine. To determine if amine was actually present on the sphere surface, XPS was performed on the material.

XPS, seen in Figure 5.4, shows nitrogen is present on the surface after the amination procedure, indicating the successful addition of nitrogen species to the surface. The presence of two species of nitrogen, which allows for the best deconvolution of the experimentally obtained peak, is not well-understood at this time. Further application of the amine functionalized silica spheres is discussed in section 5.4.

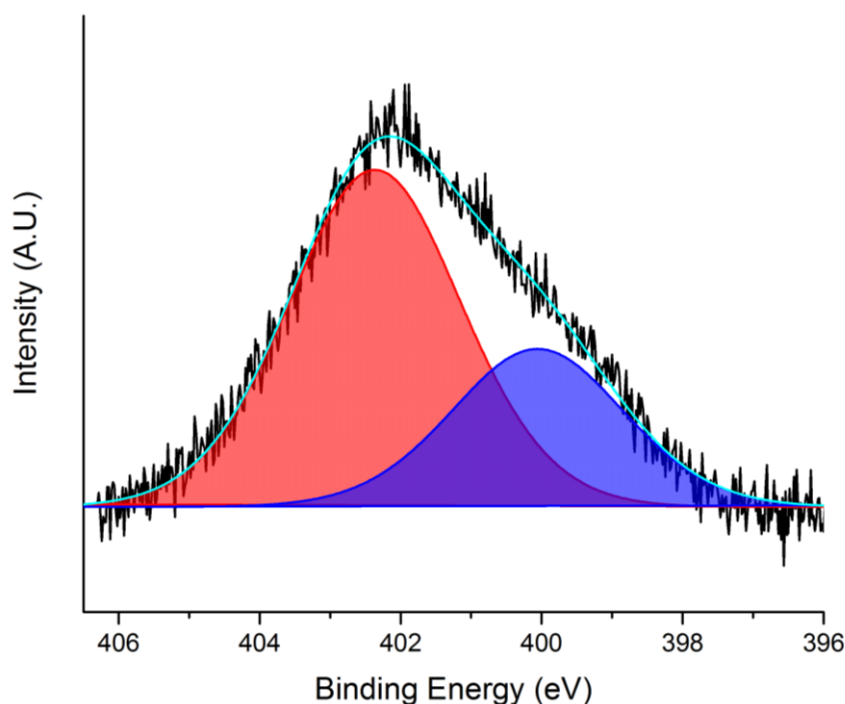


Figure 5.4 N 1s XP spectra and deconvolution showing the successful introduction of a nitrogen moiety on the silica spheres.

## 5.4 Metal Nanoparticle Deposition

Initially a method by Burton *et al.* was investigated in order to attempt the deposition of Pd MNPs on the SiO<sub>2</sub> spheres.<sup>5</sup> In this work it was determined that the room temperature reduction of Pd(OAc)<sub>2</sub> in methanol on carbon produced a well dispersed Pd MNP/C material. This method was attempted for the deposition of Pd on SiO<sub>2</sub> spheres. This approach did produce a Pd MNP on SiO<sub>2</sub> material, shown in Figure 5.5. As seen, however, the metal nanoparticles appear to be agglomerated on the SiO<sub>2</sub> surface. The nanoparticles are neither well dispersed over the SiO<sub>2</sub> support nor are uniform in size. For this reason, this method for nanoparticle deposition was not pursued further.

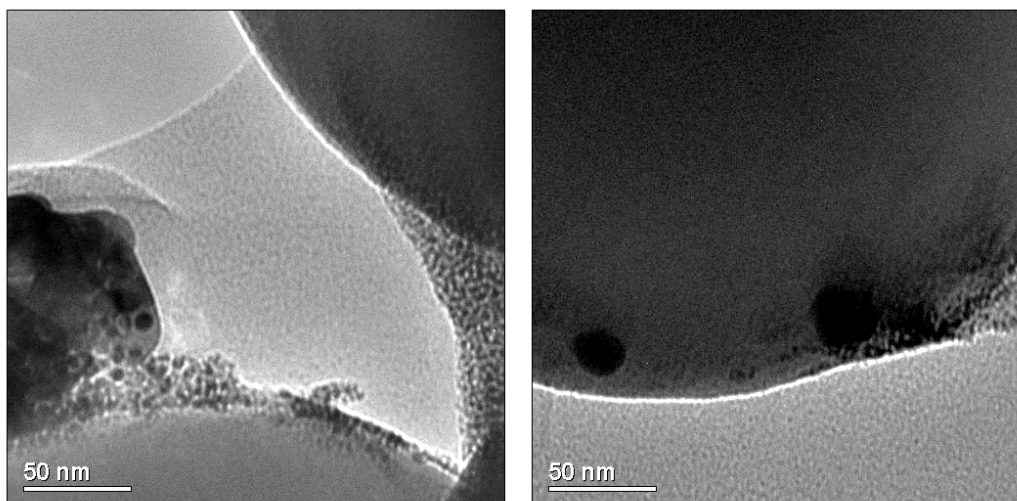


Figure 5.5 TEM image of Burton *et al.* method for Pd MNP on SiO<sub>2</sub> spheres.

An electrostatic adsorption deposition technique was alternatively used for the preparation of Pd on SiO<sub>2</sub> materials. In this method, the pH is kept constant throughout the deposition procedure to allow for a favourable interaction between the support surface and metal salt, which would be H<sub>2</sub>PdCl<sub>4</sub> in acidic solution. The point of zero charge of SiO<sub>2</sub> is at a pH of 4.2,<sup>9</sup> which means the deposition of palladium chloride would need to take place in acidic conditions to allow for good electrostatic adsorption between the -OH terminated silica surface and PdCl<sub>4</sub><sup>2-</sup>. Often for SiO<sub>2</sub> samples, metal amines are used for strong electrostatic adsorption under basic conditions.<sup>9</sup> Because pH 4 is already acidic, this does not give much variance for alteration of pH when using PdCl<sub>2</sub> for the metal nanoparticle precursor to allow for a large difference between zero point charge and pH of solution. Due to this, the -OH groups of the SiO<sub>2</sub> were functionalised with APTES to create a different surface charge environment. This leads to the point of zero charge being a pH of 8.7,<sup>10</sup> which would mean a large available range of acidic environments for deposition of PdCl<sub>2</sub> are possible. This allows for the positively charged surface to best interact with the negatively charged PdCl<sub>4</sub><sup>2-</sup>. Initially, the deposition was attempted at a pH of 2 and 4. The pH of the slurry of SiO<sub>2</sub>-NH<sub>2</sub> in water was modulated down to the desired pH using HCl, and maintained at this pH throughout the deposition procedure. Next, the PdCl<sub>2</sub> was added to the slurry and allowed to stir for 3 hours. The solid was filtered and washed with water, then left to dry. Finally, to determine which pH leads to the better

MNP deposition, the material was reduced under H<sub>2</sub>/N<sub>2</sub> in a tube furnace at 200 °C. Figure 5.6 shows the Pd deposition on SiO<sub>2</sub>-NH<sub>2</sub> at pH 2 and 4.

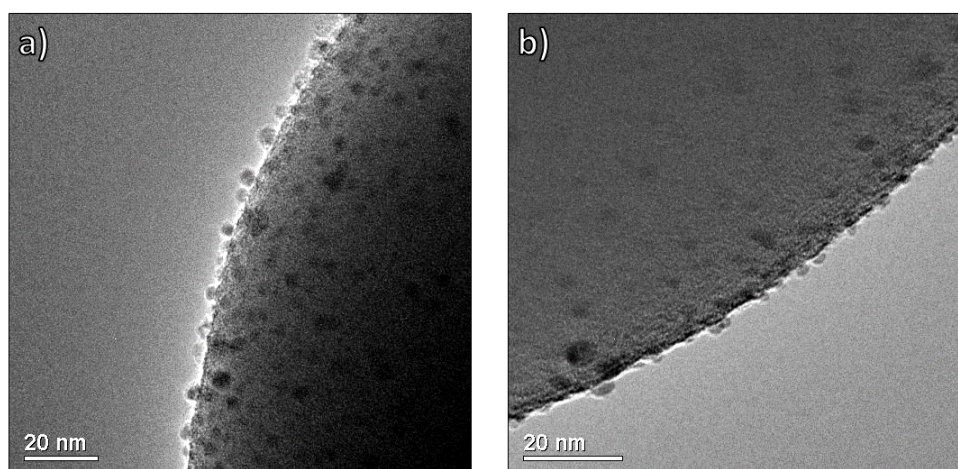


Figure 5.6 Electrostatic adsorption deposition for Pd MNPs on SiO<sub>2</sub>-NH<sub>2</sub> for (a) pH of 2 and (b) pH of 4.

For the deposition which occurs at pH 2 the final metal nanoparticle loading appears higher. This indicates that the adsorption of Pd to the SiO<sub>2</sub>-NH<sub>2</sub> was more favourable under more acidic conditions. The pH 2 deposition leads to nanoparticles around 4 nm in diameter and they appear well-dispersed over the SiO<sub>2</sub>-NH<sub>2</sub> surface. Subsequent experiments for MOF growth use the deposition of precursors for Pd MNPs at pH 2.

## 5.5 Multi-cycle MOF growth

The precursors FeCl<sub>3</sub> and BTC were used to grow the MOF MIL-100(Fe) on the SiO<sub>2</sub> spheres in a similar method to Ke *et al.* which used Fe<sub>3</sub>O<sub>4</sub> spheres<sup>3</sup>. In this work, the precursors were dissolved in separate ethanol solutions of 2 mM. Next, the SiO<sub>2</sub> spheres were placed in the solution and left for either 15 minutes for FeCl<sub>3</sub> or 30 minutes for BTC. The solid is then centrifuged, washed and placed into the other solution. After the solid has been in both the FeCl<sub>3</sub> and the BTC solution, one cycle had been completed. The cycles were repeated until the desired MOF thickness was achieved.

Using this procedure on the as-prepared silica spheres, no MOF growth was achieved after 10 cycles, seen in Figure 5.7a. The -OH moieties on the surface apparently do not act as a good nucleation point for MOF growth. The MOF growth was also attempted on the SiO<sub>2</sub>-NH<sub>2</sub> spheres with no success, seen in Figure 5.7b. This indicates that

the  $\text{-NH}_2$  group also does not act as a good functionality for MOF nucleation and growth.

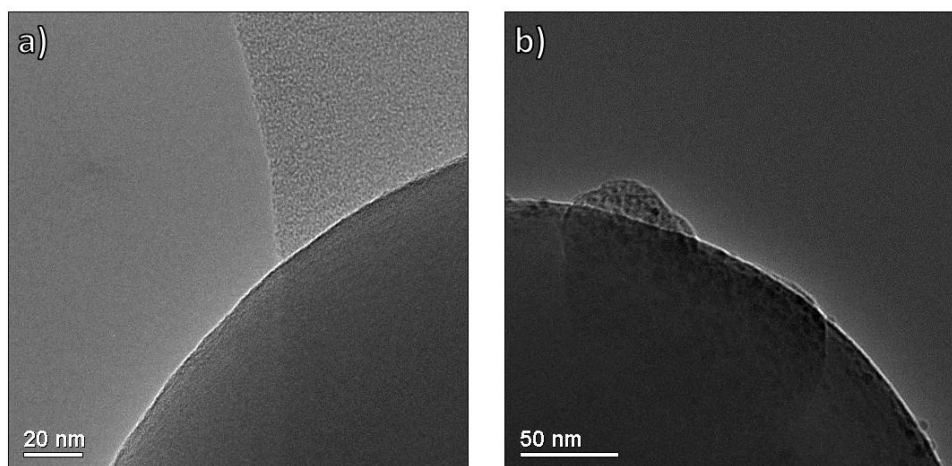


Figure 5.7 Multi-cycle MIL-100(Fe) growth with (a) 10 cycles on  $\text{SiO}_2$  spheres and (b) 25 cycles on  $\text{SiO}_2\text{-NH}_2$ .

Using this MOF growth method on reduced Pd on  $\text{SiO}_2\text{-NH}_2$ , no MOF was observed after 6 cycles, seen in Figure 5.8. This is probably because the amine moieties decompose under the reduction conditions, most likely leading to the elimination of ammonia with carbon residues and alcohol functionalities remaining on surface of the silica material. This means that the overall surface charge is likely not homogeneous and is not favourable for MOF growth. It is seen, however, that the Pd MNPs sinter throughout the MOF growth cycles, which is due to no immobilisation along with the smooth silica sphere surface and thus allowing for easy Ostwald ripening to occur.

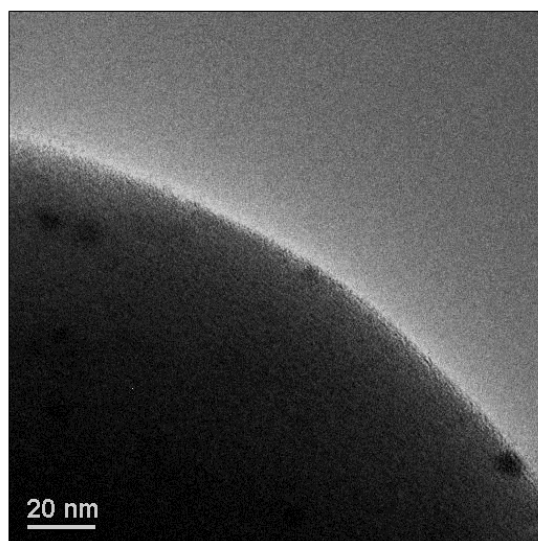


Figure 5.8 MIL-100(Fe) multi-cycle growth on Pd<sup>0</sup>-SiO<sub>2</sub>-NH<sub>2</sub>.

When using this procedure on the freshly deposited Pd on SiO<sub>2</sub>-NH<sub>2</sub> the MOF growth was successful. Figure 5.9 shows (a.) 6 cycles and (b.) 25 cycles. As expected, the MOF thickness becomes larger as more growth cycles are completed, and grows from around 10 nm at 6 layers to around 50 nm at 25 layers.

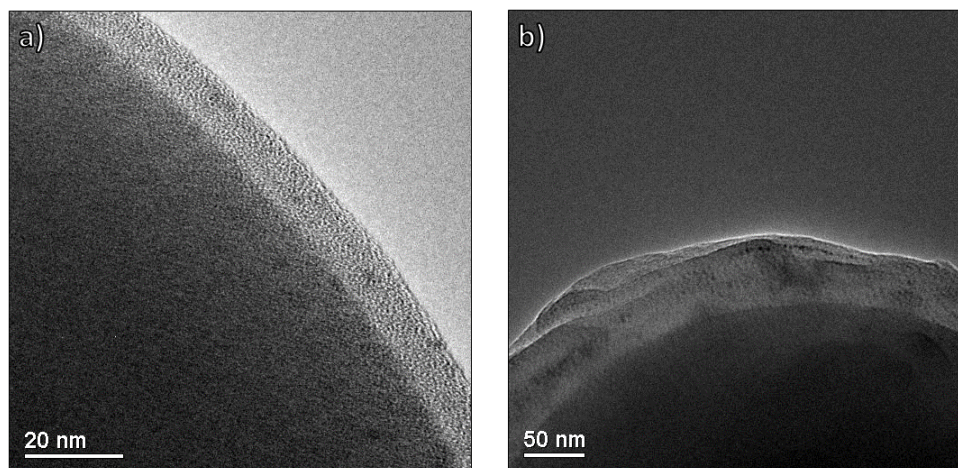


Figure 5.9 MIL-100(Fe) multi-cycle growth on freshly deposited Pd on SiO<sub>2</sub>-NH<sub>2</sub> with (a) 6 cycles and (b) 25 cycles.

These core shell materials were then characterised with XRD, XPS and SEM. The XRD of the 25 cycle MIL-100(Fe) on Pd-SiO<sub>2</sub>-NH<sub>2</sub>, seen in Figure 5.10, shows characteristic MOF peaks at 4° and 10-12°. The broad peak at 23° corresponds to the amorphous

silica sphere. The MOF signal is not very strong because it is only a thin layer compared to the large SiO<sub>2</sub> signal.

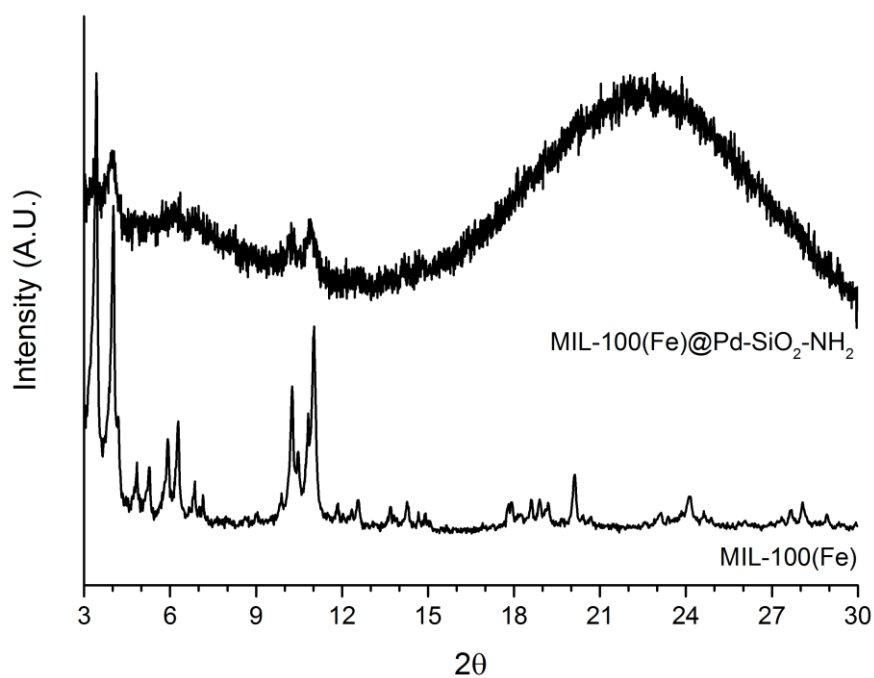


Figure 5.10 PXRD pattern of 25 cycles of MIL-100(Fe) on Pd SiO<sub>2</sub>-NH<sub>2</sub>.

XPS shows the MOF components as well as Pd and SiO<sub>2</sub>. Figure 5.11 shows the survey scans for each step towards the final 10 cycle MIL-100(Fe) Pd-SiO<sub>2</sub>-NH<sub>2</sub> material. All the signals remain apparent in the MOF@Pd SiO<sub>2</sub>-NH<sub>2</sub> material. The identification of each elemental component from the XPS is summarised in Table 5.1.

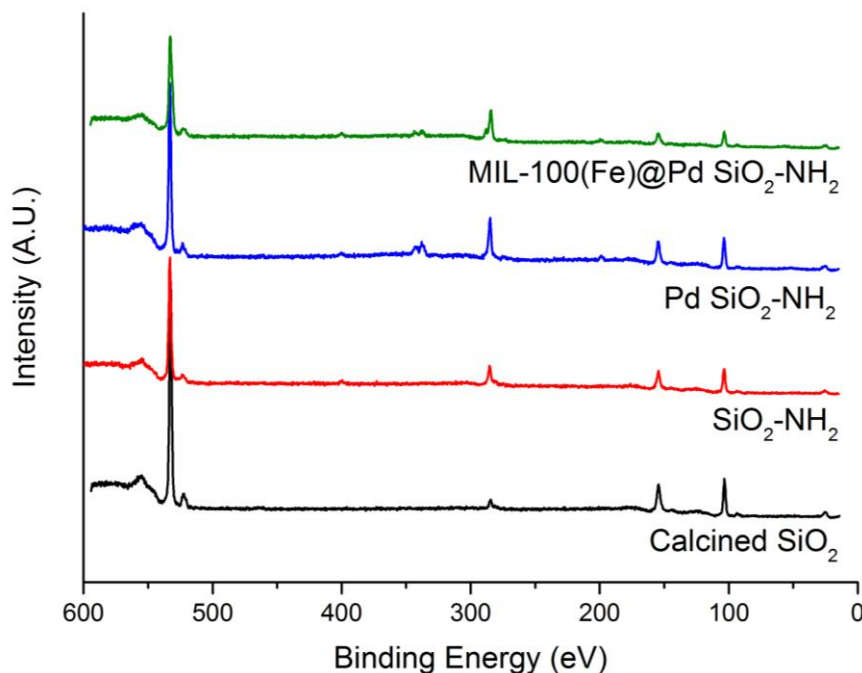


Figure 5.11 Survey XPS spectra of each step of the MIL-100(Fe)@Pd SiO<sub>2</sub>-NH<sub>2</sub> material synthesis.

Table 5.1 Summary of elemental identification from XPS survey scans. (\*) Si 2p has been used as calibration.

Component	Approx. Binding Energy (eV)
O 1s	530
N 1s	400
Pd 3d	340
C 1s	285
Cl 2p	200
Si 2p	103.7 (*)

By taking longer scans over a shorter energy range, each elemental region can be observed in detail and the overall signal can be deconvoluted with a series of smaller peaks. For instance, in the C 1s spectra, seen in Figure 5.12, the carbon within the aminopropyltriethoxysilane can be found at the highest binding energy, which matches with literature values.<sup>11</sup> Alternatively, this feature could be attributed to a satellite feature from the phenyl rings within the BTC linker.<sup>12</sup> The carbon associated with the carboxylate within the MOF linker can be seen at 288.1 eV, and the phenyl ring of the BTC can be defined as the peak at 284.2 eV, matching with reported values by

Wepasnick *et al.*<sup>13</sup>. The ethanol, used when growing the MOF, can be assigned to the peak at 285.9 eV, again matching values reported by Wepasnick *et al.*<sup>13</sup>. An additional peak at lower binding energy, shown in green in Figure 5.12, is matched to best represent the collected data but remains undefined at this time.

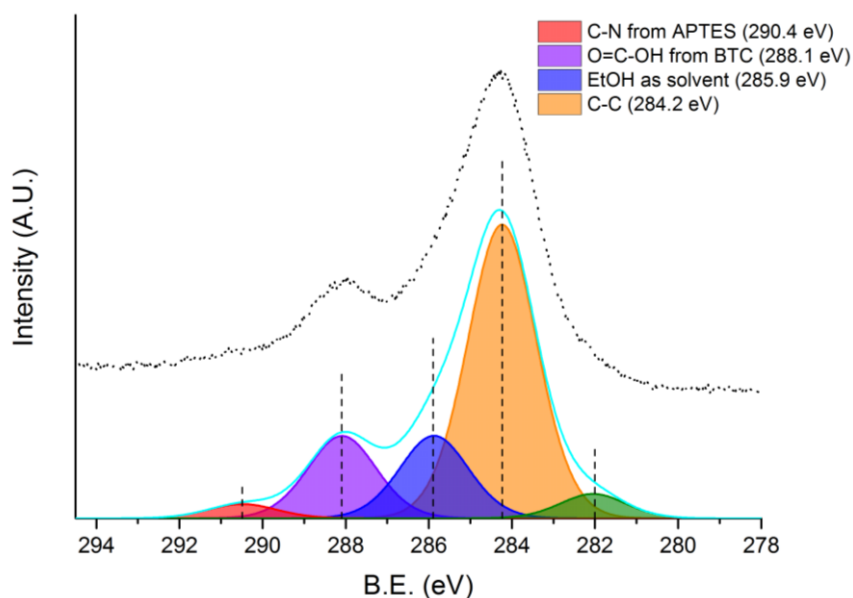


Figure 5.12 C 1s XP spectra of 10 cycle MIL-100(Fe)@Pd SiO<sub>2</sub>-NH<sub>2</sub>.

Similarly, the O 1s spectra can be deconvoluted and assigned in a similar fashion. Figure 5.13 shows the O 1s spectra, which is fitted with three peaks. The largest is the oxygen coming from the carboxylate of the BTC linker in the MOF at 533.2 eV which matches with literature values of carboxylates.<sup>14</sup> This is in line with expectations as it is closest to the surface, thus many of the ejected photoelectrons will be able to escape and reach the detector. The next largest peak could either be assigned to the oxygen in the SiO<sub>2</sub> sphere, or to the -OH species within the BTC linker.<sup>14</sup> The smallest peak at highest binding energy can be assigned to the oxygen from the ethanol used as a solvent during the MOF growth cycles.<sup>15</sup>

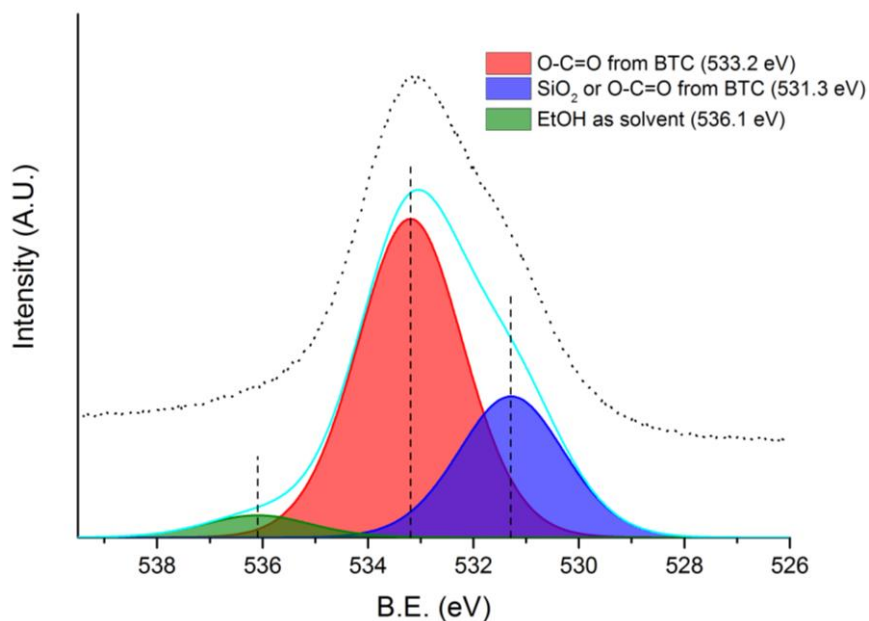


Figure 5.13 O 1s XP spectra from the 10 cycle MIL-100(Fe)@Pd SiO<sub>2</sub>-NH<sub>2</sub> material.

Figure 5.14 shows the Si 2p peaks for each step in the MOF@Pd SiO<sub>2</sub>-NH<sub>2</sub> synthesis. It can be clearly seen that the Si 2p peak diminishes with each step, for example as the surface is functionalised with amines, Pd is deposited on the surface, and the MOF is grown. This agrees with the TEM because the Si 2p signal should get smaller due to the reduction of the number of photoelectrons able to escape when they are ejected from deeper within the core of the material.

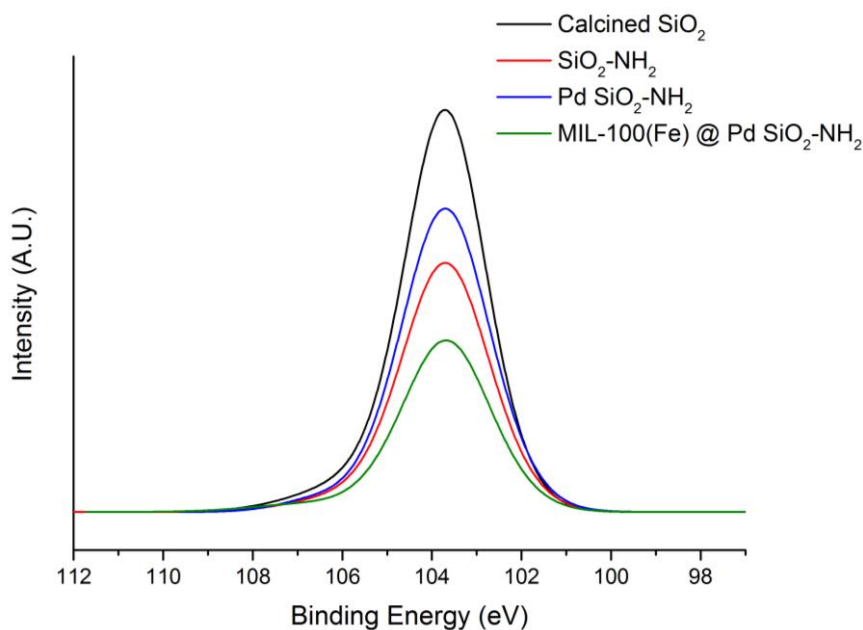


Figure 5.14 Si 2p XP spectra showing the decay in intensity of Si 2p signal as more material is added to the surface of the silica spheres.

Comparing the Pd 3d peaks before and after MOF growth, a 43% decrease in signal is observed. Figure 5.15 shows the decay in Pd 3d before and after 10 cycles of MIL-100(Fe) growth. The peak deconvolution within each spectra does not appear to shift, indicating the Pd oxidation state is unaltered during the MOF growth procedure. The peak at lower binding energy, shown in purple, can be assigned to the Pd<sup>0</sup> oxidation state, while the higher binding energy peak, shown in orange, is assigned to Pd<sup>2+</sup>. Additionally, the ratio of Pd<sup>0</sup>:Pd<sup>2+</sup> remains the same at approximately 60:40.

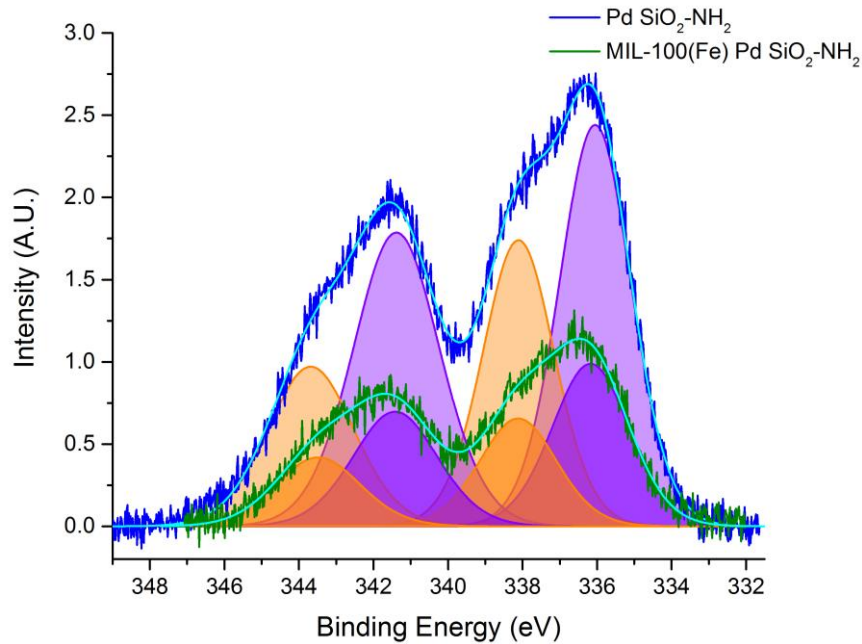


Figure 5.15 XP spectra of Pd 3d before and after MIL-100(Fe) growth cycles.

Using a simplified model, shown in Figure 5.16, the average thickness of MOF using equation 5.1 can be calculated. Knowing the density of the MOF material and the molecular weight, the calculated inelastic mean free path (using equations by Tanuma *et al.*<sup>16</sup>) is 58 Å. When using this simple model the calculated average MOF shell is 4.9 nm. Therefore, if the average Pd particle is 4 nm, then the overall shell depth is around 9 nm after 10 growth cycles. This assumes a homogeneous shell on each silica sphere.

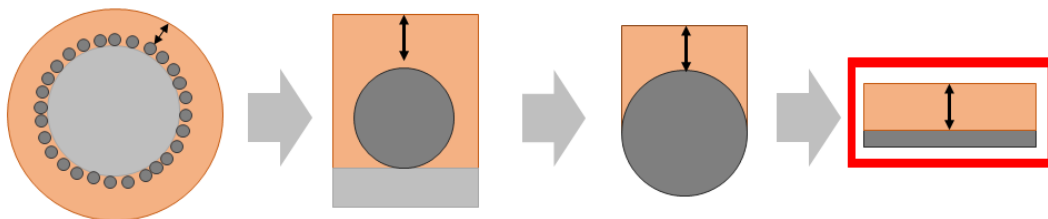


Figure 5.16 The model used (boxed in red) for calculating the MOF shell thickness and how it relates back to the real material. Light grey: silica, dark grey: Pd MNP, orange: MOF.

$$\frac{I}{I_0} = e^{-\frac{d}{\lambda}} \quad 5.1$$

From Figure 5.15 it is seen that no change in oxidation state is observed, indicating that the MOF growth procedure does not reduce the palladium chloride into metal

nanoparticles. The aim was to have Pd metal nanoparticles within the MOF shell, so then reduction of the metal salt was attempted after the MOF formation. (The MOF only forms when the surface conditions are such that there is a large negative charge on the surface. With the materials tried, the only surface that appears to have enough negative charge to allow MOF shell growth is when the PdCl<sub>2</sub> is on the aminated silica material.) The core-shell material with 25 cycles of MIL-100(Fe) was reduced under H<sub>2</sub> at 200 °C, followed by characterization using XPS to observe the change in Pd species upon reduction, depicted in Figure 5.17.

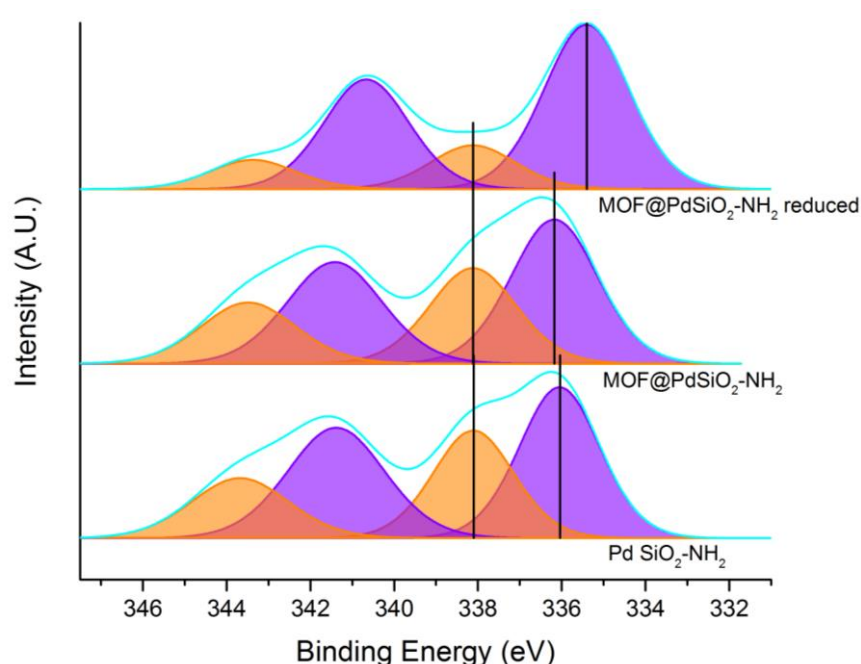


Figure 5.17 Normalised envelope and deconvolution of XP spectra showing the shift in Pd 3d peak upon reduction after MOF multi-cycle growth. Purple peaks correspond to Pd<sup>0</sup> while orange peaks correspond to Pd<sup>2+</sup>.

It can be seen that upon the reduction procedure the peak corresponding to Pd<sup>0</sup> shifts from 336.1 eV to 335.4 eV. This indicates that the species of Pd is changing upon the reduction procedure and becoming more similar to bulk Pd. This may be due to formation of Pd MNPs upon reduction. Additionally, the ratio of Pd<sup>0</sup>:Pd<sup>2+</sup> shifts to 80:20, showing that the oxide species or chloride species is less abundant after reduction. TEM was attempted on this sample after reduction, however no MNPs were visible through the thick MOF shell. This shows that utilising the PdCl<sub>2</sub> on the aminated

silica surface is beneficial for MOF growth and upon reduction Pd<sup>0</sup> becomes more apparent, which may indicate the formation of Pd MNPs.

However, while the multi-cycle growth appears to lead to a layer of MOF on the silica sphere, after the procedure a significant portion of spheres were either left uncovered or covered with a thinner MOF shell. This indicates that the MOF growth procedure is not homogeneous and the development of an optimised method was attempted. Figure 5.18 shows a representative SEM image of the 25 cycle MIL-100(Fe)@Pd SiO<sub>2</sub>-NH<sub>2</sub> material. Small crystals of MIL-100(Fe) are observable around the spheres. Further investigation into washing procedures or synthesis modifications needs to be completed to achieve a homogeneous material. Additionally, due to the time it takes to create silica spheres covered in MOF, the scale-up to quantities of material large enough to perform and optimise catalysis is not practical at this point.

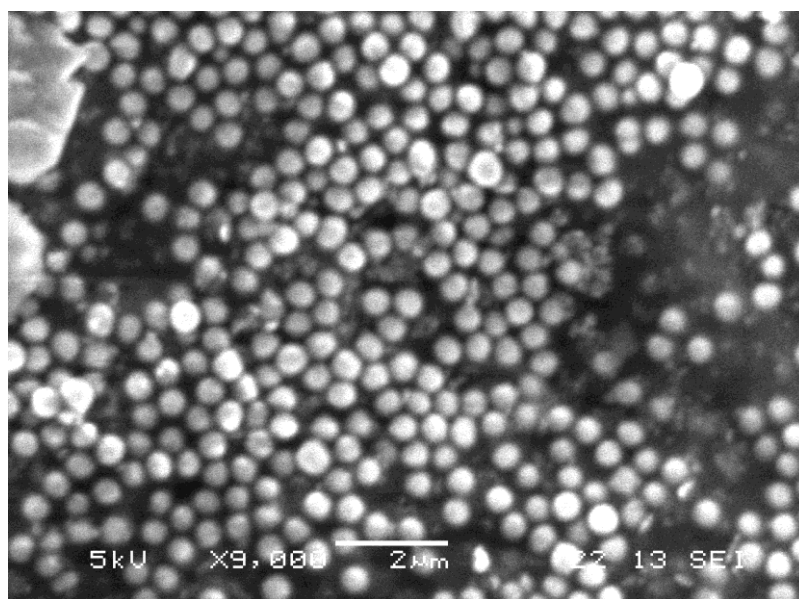


Figure 5.18 SEM of 25 cycles MIL-100(Fe)@PdSiO<sub>2</sub>-NH<sub>2</sub>.

Modifications of the MOF synthesis procedure were attempted to scale up and provide more homogeneity within the samples. A rotary synthesis was tried to allow for the MOF precursor solutions to interact with all of the silica material. Initially, an all-in-one preparation was attempted on Pd SiO<sub>2</sub>-NH<sub>2</sub>, with no MOF formed after 8 hours of rotation at 70 °C. Figure 5.19 shows the result of the rotary all-in-one procedure in which large agglomerations of material are dispersed over the surface.

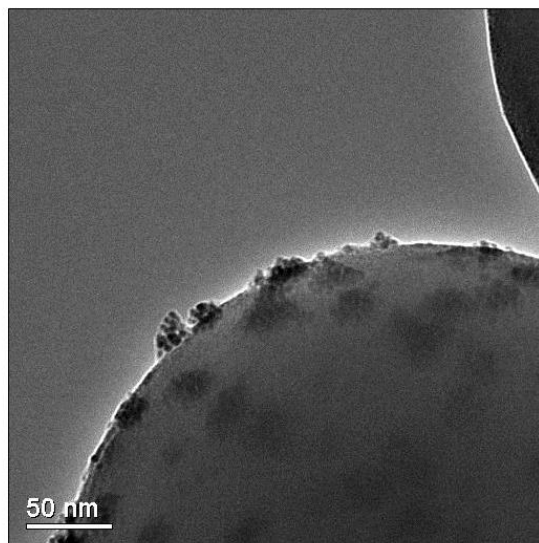


Figure 5.19 All-in-one rotary synthesis of MIL-100(Fe) on Pd SiO<sub>2</sub>-NH<sub>2</sub>.

Next, the solutions were changed in a multi-cycle procedure as before, but were rotated rather than left stagnant. The rotation speed played a large role in the final morphology of the sample. At high rotation the MOF did not grow on the silica, but at low rotation speed (20 rpm) MOF did form. Additionally, the step of centrifugation vs just decanting appears to play a large role. When using the multi-cycle rotary synthesis and only decanting between cycles, it appears that the MOF dissolves and recrystallizes on the silica surface, leading to large crystals rather than a shell, seen in Figure 5.20a. When the multi-cycle rotary synthesis with centrifugation between each step is employed, a material with a more core-shell like morphology is formed, seen in Figure 5.20b. However, the homogeneity in both the decantation and the centrifugation materials was not satisfactory and both samples had many coated and uncoated spheres, seen in Figure 5.20c and d, respectively.

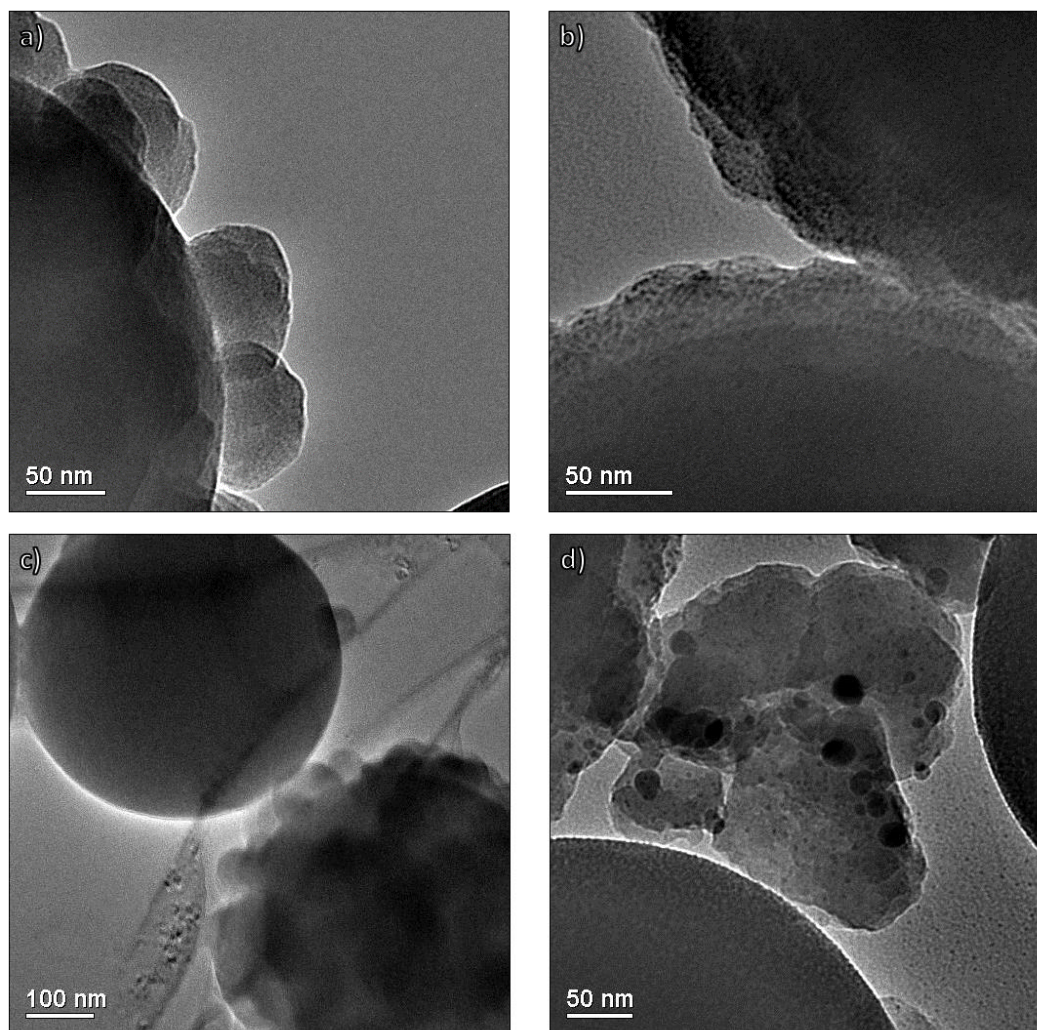


Figure 5.20 MIL-100(Fe) on Pd SiO<sub>2</sub>-NH<sub>2</sub> using a multi-cycle rotary synthesis method with decantation (a, c) and with centrifugation (b, d) between each cycle.

## 5.6 Modifying Surface Charge

As discussed, the MOF is only able to grow on the silica spheres when a large negative charge is present on the surface. Even the freshly calcined SiO<sub>2</sub>, which has -OH groups on the surface does not provide enough negative charge to attract the MOF metal ions to the surface. Only when there is chlorine present, from the PdCl<sub>2</sub> deposition, does the MOF grow. This indicates that the surface charge plays a large role in the MOF synthesis. Alternative surfaces which may allow for the MOF growth to occur have been explored, but more work needs to be accomplished to confirm the surface reaction species necessary for the growth to occur.

Carboxylic acid groups on silica would act as a good coordination point for MOF metal ions, which could lead to better homogeneity of the MOF shell.<sup>17</sup> However, amine groups proved to be a good functionality for Pd deposition with PdCl<sub>2</sub>, so a balance of these two groups may be best. A material could be envisaged where the silica is initially aminated to allow for Pd deposition, then the carboxylate moiety is put on the surface after the metal nanoparticle deposition procedure. This should be investigated.

## 5.7 MIL-100(Fe) catalysis

In parallel with the formation and optimisation attempts of the core-shell materials, MIL-100(Fe) was synthesised in bulk to investigate possible catalytic reactions. A full reaction which would be suitable to probe the multifunctionality of the MIL-100(Fe)@Pd SiO<sub>2</sub> materials is a tandem chalcone formation and selective hydrogenation, seen in Figure 5.21. The MIL-100(Fe) sites catalyse the Claisen-Schmidt condensation reaction to form the chalcone. After this step, the Pd MNPs can potentially reduce the chalcone into five different final products. Chalcone and similar molecules are interesting targets for pharmaceutical applications such as anti-inflammatory effects<sup>18</sup> and antitumor agents<sup>19</sup>.

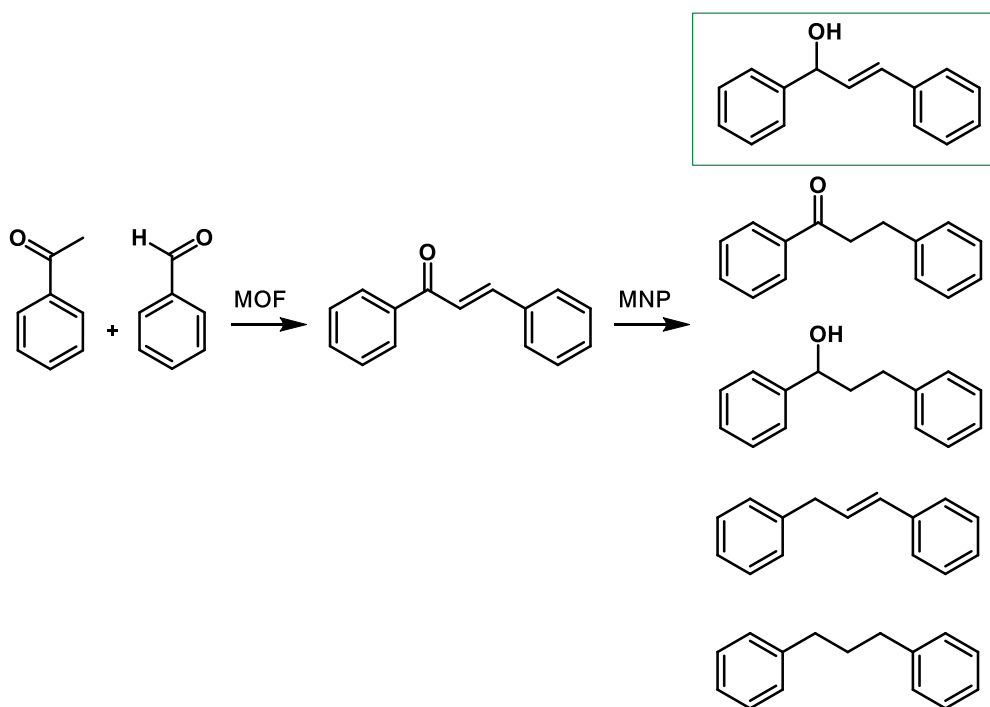


Figure 5.21 Chalcone synthesis and tandem reduction.

The first step of the chalcone synthesis was performed with bulk MIL-100(Fe) in attempts to optimise conditions. Following similar conditions as published by Dhakshinamoorthy *et al.* the chalcone synthesis was performed at 110 °C for 24 hours.<sup>20</sup> After this time no chalcone formation was observed by GC analysis. It was expected that the reaction should occur at toluene reflux conditions, as the solvent boiling point is 110 °C, which is the commonly used temperature during the reaction discussed in Dhakshinamoorthy *et al.* The reaction could be tried again under harsher conditions in a pressurised vessel, to allow the reaction solution to maintain liquid phase during the catalysis. More experiments must be performed to optimise the chalcone formation reaction on MIL-100(Fe).

The selective hydrogenation of chalcone was tested with Pd MNPs in MIL-101(Cr) to identify reaction products. GC analysis determined at the reaction conditions of 110 °C the main product is the complete removal of the ketone and reduction of the C=C bond. The Pd MNPs are very active at this high temperature, and the full removal of a functionality is not desired. Lowering the reaction temperature to 50 °C leads to full conversion after 3 hours and >99% selective to the reduced ketone bond. After 16 hours the selectivity decreases to 93% for this product due to the subsequent reduction of the C=C bond over this time. The Pd SiO<sub>2</sub> material was also tried as a catalyst at the lower reaction temperature with similar results to the Pd in MIL-101(Cr) catalyst. This indicates at the temperatures likely necessary for the chalcone formation make the MNPs very active and thus reduce or remove both the ketone and C=C functionality. More optimisation needs to be performed to find conditions where the chalcone is formed and allows for selective reduction, or the reaction could be performed in a two-step procedure. After the optimum conditions are elucidated, the MIL-100(Fe)@Pd SiO<sub>2</sub>-NH<sub>2</sub> catalyst synthesis needs to be optimised and scaled-up before potential tandem catalysis can occur with the core-shell materials.

## 5.8 Conclusion and Outlook

Pd nanoparticles deposited on SiO<sub>2</sub> were successfully coated with the mesoporous MOF MIL-100(Fe). Not reducing the Pd into nanoparticles appears to be an important step towards the formation of MOF on the Pd SiO<sub>2</sub> spheres. However, the

methodology for creating MIL-100(Fe) using a multi-cycle approach is time intensive and produces inhomogeneous shells on the silica spheres. Modified approaches into the multi-cycle MOF growth were attempted, but a quick and facile approach into MOF layer formation on SiO<sub>2</sub> was not achieved. Further experiments are necessary to speed up and scale up the process.

A Claisen-Schmidt condensation reaction to form a chalcone from benzaldehyde and acetophenone using MIL-100(Fe) was investigated. It was found that no conversion was achieved after 24 hours at 110 °C, and harsher conditions may be necessary for chalcone formation. To achieve higher reaction temperatures, the reaction should take place in a pressurised reaction vessel. The reduction of the chalcone with either Pd in MIL-101(Cr) or Pd SiO<sub>2</sub> spheres at 110 °C was not selective towards either the ketone or C=C functionality. Lowering the temperature led to selective reduction of the ketone bond. However, to eventually perform the chalcone formation and selective reduction in tandem, one set of reaction conditions needs to be optimised. Alternatively, a two-step procedure may be feasible, where the initial chalcone formation takes place under high temperature inert atmosphere, then is cooled, vented and pressurised with hydrogen for the selective reduction.

When the difficulties of optimising and scaling up the MIL-100(Fe)@Pd SiO<sub>2</sub>-NH<sub>2</sub> can be overcome, changing the MOF type, core type, or metal species might be possible, potentially leading to a highly modular approach towards multifunctional materials. For instance, using TiO<sub>2</sub> spheres rather than SiO<sub>2</sub> spheres could induce the MNPs to strong metal-support interactions, which may be interesting for enhanced activity and selectivity of the MNP catalysis. Additionally, changing the MOF type could allow for different porosity and therefore a possibility of size selectivity in catalysis.

## 5.9 References

1. Hu, P.; Morabito, J. V.; Tsung, C.-K., Core-Shell Catalysts of Metal Nanoparticle Core and Metal-Organic Framework Shell. *ACS Catal.* **2014**, *4*, 4409-4419.
2. Zhang, T.; Li, B.; Zhang, X.; Qiu, J.; Han, W.; Yeung, K. L., Pd Nanoparticles Immobilized in a Microporous/Mesoporous Composite ZIF-8/MSS: A Multifunctional Catalyst for the Hydrogenation of Alkenes. *Micropor. Mesopor. Mater.* **2014**, *197*, 324-330.
3. Ke, F.; Qiu, L. G.; Zhu, J., Fe<sub>3</sub>O<sub>4</sub>@MOF Core-Shell Magnetic Microspheres as Excellent Catalysts for the Claisen-Schmidt Condensation Reaction. *Nanoscale* **2014**, *6*, 1596-1601.
4. Najafi, M.; Yousefi, Y.; Rafati, A. A., Synthesis, Characterization and Adsorption Studies of Several Heavy Metal Ions on Amino-Functionalized Silica Nano Hollow Sphere and Silica Gel. *Sep. Purif. Technol.* **2012**, *85*, 193-205.
5. Burton, P. D.; Boyle, T. J.; Datye, A. K., Facile, Surfactant-Free Synthesis of Pd Nanoparticles for Heterogeneous Catalysts. *J. Catal.* **2011**, *280*, 145-149.
6. Ke, F.; Qiu, L.-G.; Yuan, Y.-P.; Jiang, X.; Zhu, J.-F., Fe<sub>3</sub>O<sub>4</sub>@MOF Core-Shell Magnetic Microspheres with a Designable Metal-Organic Framework Shell. *J. Mater. Chem.* **2012**, *22*, 9497.
7. García Márquez, A.; Demessence, A.; Platero-Prats, A. E.; Heurtaux, D.; Horcajada, P.; Serre, C.; Chang, J.-S.; Férey, G.; de la Peña-O'Shea, V. A.; Boissière, C.; Grosso, D.; Sanchez, C., Green Microwave Synthesis of MIL-100(Al, Cr, Fe) Nanoparticles for Thin-Film Elaboration. *Eur. J. Inorg. Chem.* **2012**, *2012*, 5165-5174.
8. Stoeber, W.; Fink, A., Controlled Growth of Monodisperse Silica Spheres in the Micron Size Range. *J. Colloid Interface Sci.* **1968**, *26*, 62-69.
9. Jiao, L.; Regalbuto, J. R., The Synthesis of Highly Dispersed Noble and Base Metals on Silica via Strong Electrostatic Adsorption: I. Amorphous Silica. *J. Catal.* **2008**, *260*, 329-341.
10. Wu, Z.; Xiang, H.; Kim, T.; Chun, M. S.; Lee, K., Surface Properties of Submicrometer Silica Spheres Modified with Aminopropyltriethoxysilane and Phenyltriethoxysilane. *J. Colloid Interface Sci.* **2006**, *304*, 119-124.
11. Bui, L. N.; Thompson, M.; McKeown, N. B.; Romaschin, A. D.; Kalman, P. G., Surface Modification of the Biomedical Polymer Poly(Ethylene Terephthalate). *Analyst* **1993**, *118*, 463-474.
12. Beamson, G.; Briggs, D., *High Resolution XPS of Organic Polymers: The Scienta Esca300 Database*. John Wiley & Sons Ltd: England, 1992.
13. Wepasnick, K. A.; Smith, B. A.; Bitter, J. L.; Fairbrother, D. H., Chemical and Structural Characterization of Carbon Nanotube Surfaces. *Anal. Bioanal. Chem.* **2010**, *396*, 1003-1014.
14. Chi, Y.; Zhao, L.; Yuan, Q.; Yan, X.; Li, Y.; Li, N.; Li, X., In Situ Auto-Reduction of Silver Nanoparticles in Mesoporous Carbon with Multifunctionalized Surfaces. *J. Mater. Chem.* **2012**, *22*, 13571-13577.
15. Gardner, S. D.; Singamsetty, C. S. K.; Booth, G. L.; He, G.-R.; Pittman, C. U., Surface Characterization of Carbon Fibers Using Angle-Resolved XPS and ISS. *Carbon* **1995**, *33*, 587-595.

16. Tanuma, S.; Powell, C. J.; Penn, D. R., Calculations of Electron Inelastic Mean Free Paths. V. Data for 1 Organic Compounds over the 50-2000 eV Range. *Surf. Interface Anal.* **1994**, *21*, 165-176.
17. Jo, C.; Lee, H. J.; Oh, M., One-Pot Synthesis of Silica@Coordination Polymer Core-Shell Microspheres with Controlled Shell Thickness. *Adv. Mater.* **2011**, *23*, 1716-1719.
18. Hsieh, H.-K.; Tsao, L.-T.; Wang, J.-P.; Lin, C.-N., Synthesis and Anti-Inflammatory Effect of Chalcones. *J. Pharm. Pharmacol.* **2000**, *52*, 163-171.
19. Xia, Y.; Yang, Z.-Y.; Xia, P.; Bastow, K. F.; Nakanishi, Y.; Lee, K.-H., Antitumor Agents. Part 202. Novel 2'-Amino Chalcones: Design, Synthesis and Biological Evaluation. *Bioorg. Med. Chem. Lett.* **2000**, *10*, 699-701.
20. Dhakshinamoorthy, A.; Alvaro, M.; Garcia, H., Claisen-Schmidt Condensation Catalyzed by Metal-Organic Frameworks. *Adv. Synth. Catal.* **2010**, *352*, 711-717.

# Chapter 6

---

Well-Defined Catalysts:

Core-Shell Synthesis of MNP@MOF Materials

## 6.1 Introduction

Core-shell structures can be used in MOF catalysis to immobilise active materials and create a porous entry to the active sites. These types of core-shell structures often contain a metal nanoparticle (MNP) as the core with a shell of porous material surrounding it. These structures encapsulate the MNP within the porous material, allowing for reactants to diffuse in, but not for the MNP to diffuse out. Incorporating the shell around the MNP material can help to stabilise the MNP, as well as can offer opportunities to tune the selectivity and activity during catalysis. For instance, depending on the pore size of the shell, size selectivity can be achieved. Additionally, the activity can be modified with the pore size of the shell because diffusion rate through the porous medium can be tuned. Core-shell MNP@MOF materials offer many opportunities due to the near-limitless combination of metal and linker components available to build MOFs. Using the core-shell strategy to immobilise MNPs within MOF supports can lead to a multifunctional catalyst.

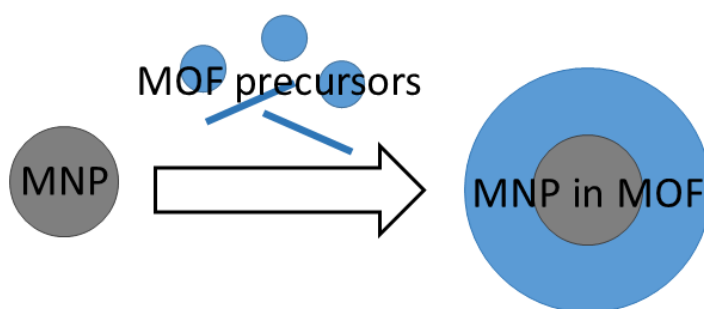


Figure 6.1 Approach to core-shell MNP@MOF materials by mixing colloidal MNPs with MOF precursors.

Combining MOF precursors with a colloidal solution of MNPs can lead to the synthesis of the desired core-shell structures, shown schematically in Figure 6.1. The size and shape of the MNP can be precisely tuned in order to give control over the catalytic performance of the material in final applications. However, the synthetic conditions for the encapsulation of the nanoparticle within the MOF need to be optimised and the interactions between the MOF and nanoparticle have to be taken into account.<sup>1</sup> Colloidal nanoparticles are often capped with a stabilising molecule to retain the MNP

shape and size. The interaction between the capping agent and the MOF precursors is thought to be an important part of achieving desired core-shell structures.<sup>1</sup>

Zeolitic imidazolate frameworks (ZIFs) have been used for obtaining microporous core-shell structures with accessible encapsulated nanoparticles. ZIF-8, obtained from Zn and 2-methylimidazole as building blocks, has been used to immobilise MNPs within well-defined microporous crystals. ZIF-8 has the benefit of being chemically and thermally stable and can be readily synthesised at room temperature.<sup>2</sup> Lu *et al.* grew ZIF-8 around PVP capped nanoparticles to achieve core-shell materials with remarkable spatial distribution and well-defined microporous access.<sup>2</sup> They were able to strategically introduce PVP-capped NPs during the room temperature ZIF-8 synthesis to allow for specific areas of nanoparticles within the final material depending on the time in which the nanoparticles were added during the synthesis. There was good spatial specificity in the final materials, and multiple types of nanoparticles could be added at separate times to allow for interesting multi-NP species@ZIF-8 structures. These materials were shown to be active in CO oxidation catalysis and also showed interesting optical and magnetic behaviour depending on the type of PVP-capped NP used. This study showed the proof of concept to incorporate multiple nanoparticles within a ZIF shell which controls the spatial distribution of the capped nanoparticles. These materials show great promise for the application of core-shell structures as multifunctional materials.

The application of core-shell materials as multifunctional catalysts in tandem reactions has not been thoroughly investigated. Recently, Zhao *et al.* immobilised Pd MNPs within an amino-functionalised IRMOF-3 which is a MOF made with  $\text{Zn}(\text{NO}_3)_2$  and 2-aminoterephthalic acid. The resulting material was used as a catalyst for a two-step reaction consisting of a Knoevenagel condensation followed by a selective hydrogenation step.<sup>3</sup> It was shown that the core-shell catalyst was much more selective in the reduction step when compared to the Pd MNPs on their own or when deposited onto the functionalised IRMOF-3. This shows that the morphology of the catalysts can play a large role in the outcome of the reaction, even when comparing near-identical active sites.

While this avenue is only beginning to be explored, there are many options towards designing MNP@MOF catalysts for multifunctional tandem catalysis. This chapter will discuss the MNP synthesis and characterisation (section 6.3) which will be used in the optimisation of two different MOF types to create core-shell structures (section 6.4). These materials were investigated as catalysts in tandem reductive amination reactions (section 6.5).

## 6.2 Experimental

Chemicals were used as received unless otherwise specified.

XPS was performed by Dr. Steve Francis on a Scienta ESCA-300 with an Al k-alpha X-Ray source at 1486.7 eV. The XP spectra were deconvoluted using CasaXPS with a Shirley background and a 70:30 Gaussian-Lorentzian shape for each emission.

TEM was performed on a Jeol JEM 2011 TEM with an accelerating voltage of 200 kV. The samples were prepared by grinding the sample with acetone and depositing on a holey carbon coated Cu grid.

SEM and EDX was performed on a Jeol JSM-5600 SEM.

### 6.2.1 MNP shape synthesis

Following a procedure by Song *et al.*<sup>4</sup>, MNP shapes were synthesised. 2.5 mL of ethylene glycol (EG) and 0.5 mL AgNO<sub>3</sub> was refluxed for 5 minutes. The concentration of AgNO<sub>3</sub> used depends on the nanoshape desired.

Desired Shape	AgNO <sub>3</sub> Concentration
Cubes	2 mM
Cuboctahedra	20 mM
Octahedra	60 mM

Next, a 1/32 aliquot of 3 mL 0.375 M PVP in EG and a 1/32 aliquot of 1.5 mL 0.0625 M H<sub>2</sub>PtCl<sub>6</sub>·6H<sub>2</sub>O in EG is added to the refluxing EG every 30 seconds for 16 minutes. The resulting mixture is refluxed further for 5 minutes. The solution is cooled and then centrifuged at 5000 rpm for 15 minutes. The supernatant is separated and combined with acetone. This solution is centrifuged at 3000 rpm for 5 minutes. The supernatant

is discarded and the solid is re-suspended in ethanol with sonication. The solution is combined with hexane, which helps to break the colloidal suspension, and is centrifuged at 3000 rpm for 5 minutes. After this, the supernatant is discarded and the solid is re-suspended in DMF with sonication. The amount of DMF used is such that the Pt concentration is  $1 \text{ mg mL}^{-1}$  assuming no loss in Pt throughout the procedure. The colloids appeared to be stable in DMF for months and had no noticeable precipitate formation.

### **6.2.2 Optimised MNP@UiO-66 Synthesis**

Following a modified procedure by Na *et al.*<sup>5</sup> 167 mg  $\text{ZrCl}_4$  and 87 mg terephthalic acid were dissolved into 3.5 mL acetic acid and 50 mL DMF within a Teflon-lined stainless steel autoclave. Next, 4.5 mL MNP shape colloid was added to the autoclave, while stirring. The resulting solution was stirred for 10 minutes. The stirrer bar was removed and the autoclave was sealed and placed into a  $120 \text{ }^\circ\text{C}$  oven for 24 hours. Upon removing the autoclave and allowing to cool, the resulting solution was centrifuged at 6000 rpm for 10 minutes. The solid was washed three times with DMF using a sonicator to re-disperse the particles and centrifugation to separate the core-shell materials from the supernatant. After washing, the prepared materials were immersed in methanol for 72 hours with a centrifugation and methanol refresh every 24 hours.

### **6.2.3 Optimised MNP@MIL-100(Sc) Synthesis**

The procedure for the best performing catalyst of MNP@MIL-100(Sc) was prepared by mixing 0.055 mL 1.5 M  $\text{ScCl}_3$  aqueous solution with 13 mg trimesic acid in 4.5 mL DMF. Upon the trimesic acid dissolving, 0.4 mL MNP colloid was added and allowed to stir for 10 minutes. The stir bar was removed and the autoclave was sealed. The autoclave was placed into a  $160 \text{ }^\circ\text{C}$  oven for 72 hours. Upon removing the autoclave and allowing to cool, the resulting solution was centrifuged at 6000 rpm for 10 minutes. The solid was washed three times with DMF using a sonicator to re-disperse the particles and centrifugation to separate the core-shell materials from the supernatant. After washing, the prepared materials were immersed in methanol for 72 hours with a centrifugation and methanol refresh every 24 hours.

### 6.2.4 Catalysis conditions

In a typical reductive amination catalysis run, 5 mol% MOF catalyst, calculated using the MOF molecular weight with the amount of 4'-fluoroacetophenone added to the reaction, (activated at 150 °C for 4 hours under vacuum) was combined with dry hexane under a nitrogen atmosphere. 4'-Fluoroacetophenone and benzylamine were added to the mixture in a 1:2 molar ratio. Typically, using the MNP@MIL-100(Sc) materials, 3.3 mg catalyst was combined with 13.6  $\mu\text{l}$  4'-fluoroacetophenone and 24.5  $\mu\text{l}$  benzylamine in 2 ml dry hexane. The vials were sealed, pierced with needles then loaded into a stainless steel autoclave and pressurised with  $\text{H}_2$  to 10 bar. The autoclave was then placed into a heated oil bath and kept at the desired temperature for the duration of the reaction. The reaction was stopped by placing the autoclave in a water bath to cool quickly, then depressurised. Upon cooling and depressurising the autoclave was opened and the vials were centrifuged to separate the catalyst from the reaction mixture. Conversions and selectivities were determined using  $^{19}\text{F}$  NMR on a Bruker AV 400 machine.

In a typical styrene hydrogenation reaction, 3 mol% MOF catalyst, using the full MOF molecular weight to calculate the catalyst amount, was added to styrene in ethanol. Typically, 10 mg MNP@UiO-66 was combined with 22.4  $\mu\text{l}$  styrene in 2.5 ml ethanol. The vial was sealed and pierced with needles, then loaded into a stainless steel autoclave and pressurised with  $\text{H}_2$  to 5 bar. The autoclave was then placed into a heated oil bath and kept at the desired temperature for the duration of the reaction. The reaction was stopped by placing the autoclave in a water bath to cool quickly, then depressurised. Upon cooling and depressurising, the autoclave was opened and the vials were centrifuged to separate the catalyst from the reaction mixture. Conversions and selectivities were determined on a Thermo Trace GC ultra with Restek RTX-1 (30 m x 0.25 mm x 0.25  $\mu\text{m}$ ) column. The analysis programme used: 50 °C start, ramp 8 °C  $\text{min}^{-1}$  to 70 °C, hold 2 min. Ramp 20 °C  $\text{min}^{-1}$  to 300 °C, hold 1 min.

### 6.3 MNP Shape and Characterisation

In order to gain more control over nanoparticle morphology and size compared to the top-down growth of nanoparticles described in Chapter 3 and 5, three Pt MNP shapes were synthesised while maintaining an overall nanoparticle size of approximately 10 nm. The cubes, cuboctahedra and octahedra nanoparticles were capped with polyvinylpyrrolidone (PVP) which both reduced and stabilised the MNPs and allowed for colloidal suspensions in various solvents due to the amphiphilic functionalities within the polymer.<sup>6</sup> The Pt MNPs can be seen in Figure 6.2. The cubes consist of 8 {100} surfaces, the cuboctahedra consist of 6 {100} and 8 {111} surfaces and the octahedra consist of 8 {111} surfaces.<sup>4</sup>

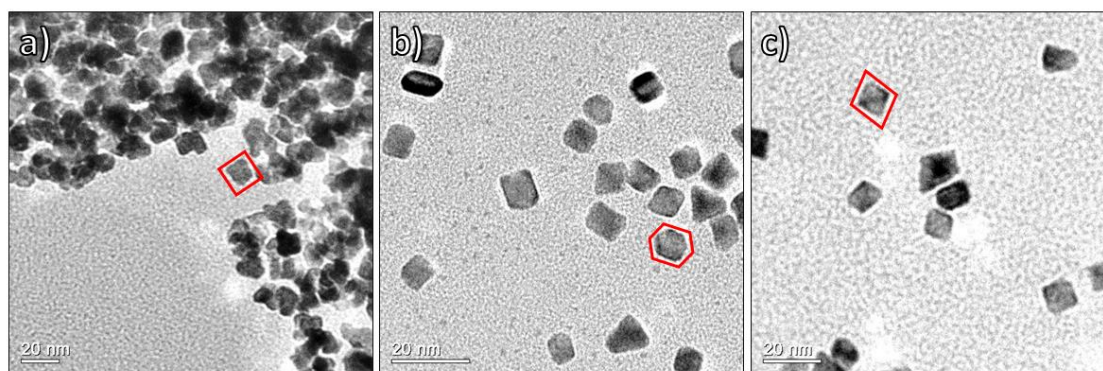


Figure 6.2 PVP capped Pt colloids as (a) cubes, (b) cuboctahedra and (c) octahedra.

Shape control was achieved by adding varying amounts of  $\text{AgNO}_3$  during the synthetic protocol which is based on a report by Song *et al.*<sup>4</sup> Adding the lowest ratio of  $\text{AgNO}_3$  led to the formation of cubes, while adding the largest amount of  $\text{AgNO}_3$  gave octahedra. Song *et al.* discussed a possible growth mechanism, monitored by UV-Vis absorption, which suggests the silver species preferentially adsorbs on {100} surfaces during the initial reaction. As the Pt precursor ( $\text{H}_2\text{PtCl}_6$ ) is continuously added during the nanoparticle synthesis, the Pt salt immediately reduces and the Ag species oxidises, which in turn enhances the growth rate along the {100} direction with the dissolution of AgCl into the solvent. Leong *et al.* further discuss the growth mechanism and elucidated that the Ag is indeed the directing agent rather than  $\text{AgNO}_3$  at the conditions used for Pt MNP synthesis.<sup>7</sup> However, the dissolution of AgCl into the solvent is not discussed. Instead, they developed a growth model for the Pt MNP

shape-direction in which the Ag atoms bind on the {111} faces which blocks the growth along this direction. This model fit well with the experimental results, however this suggests that Ag is on the surface, which was initially not observed by Song *et al.* Instead they describe the possibility that the AgNO<sub>3</sub> is washed out of the final MNPs, leading to negligible amounts of Ag in the colloids when using EDX for metal concentrations.

However, even upon significant washing and exchange of solvents when following the procedure discussed by Song *et al.*, Ag amounts similar to the initial synthesis conditions were found in all colloidal shapes. Comparing the Ag concentrations determined by both EDX and XPS, it was determined that Ag is present within the MNPs and that the surface concentration and bulk concentration of the MNPs is comparable, seen in Table 6.1. This indicates that the shape growth mechanism may not be due to the Ag retardation on a Pt surface while the MNP is growing. The MNPs were deposited on SiO<sub>2</sub> to allow for calibration in the XPS to the Si 2p peak and for ease of handling.

Table 6.1 Pt and Ag concentrations in the MNP shapes. MNPs were deposited on SiO<sub>2</sub> before EDX and XPS analysis. The theoretical concentration is the amount of Ag and Pt added to the synthesis, assuming 100% usage of both species.

Sample	Synthesis		XPS		EDX	
	Ag	Pt	Ag	Pt	Ag	Pt
Cubes	1.1	98.9	1.9	98.1	1.8	98.2
Cuboctahedra	9.6	90.4	14.4	85.6	14.3	85.7
Octahedra	24.2	75.8	25.5	74.5	27	73

Three years after the initial report by Song *et al.*, Grass *et al.* from the same research group discusses removal of silver by selective etching of the Ag-modified Pt nanoparticles.<sup>8</sup> They determined that indeed large amounts of Ag remained in the Pt nanoparticles and were found to be a poison to the Pt nanoparticles when applied as catalysts in ethylene hydrogenation. Washing with nitric acid appears to selectively remove some of the Ag. However, some agglomeration of the nanoparticles was observed due to the degradation of PVP during the washing procedure. In the work

discussed below, no further MNP modification was performed, and a different Pt shape growth method should be used to obtain pure Pt MNP samples in future.

Looking closer at the XPS data collected from the three MNP shapes on SiO<sub>2</sub>, it is observed that the Pt peaks do not significantly shift, while the Ag peaks shift to lower binding energy as more AgNO<sub>3</sub> is added to the synthesis. Figure 6.3 shows the Pt 4f and Ag 3d XP spectra. The Ag within the cubes is the most similar to Ag metal. As the Ag concentration increases the Ag peak position shifts 0.6 eV and 0.8 eV lower. This may be due to an interplay of Pt and Ag, which has been previously shown in literature by Yousaf *et al.*<sup>9</sup>

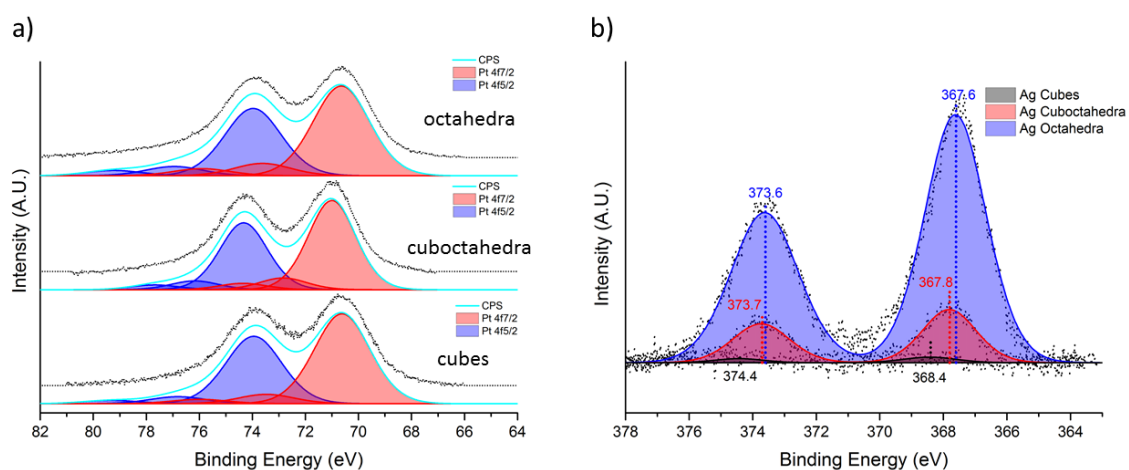


Figure 6.3 comparison of XP spectra of the PtAg MNP shapes on SiO<sub>2</sub>. (a) Pt 4f and (b) Ag 3d spectra.

Cuboctahedral MNPs deposited on SiO<sub>2</sub> were also examined by XRD. However, the signal to noise ratio was not sufficient to determine separate Ag and Pt peaks, shown in Figure 6.4. The broad peak between 39 and 41° 2 $\theta$  could be attributed to Pt (111), Ag(111) or the combination of both components. Significantly longer acquisition times should be attempted in order to achieve better signal to noise ratio. Alternatively, the bimetallic nanoparticles could be investigated using EXAFS to determine the atomic position of Ag in relation to Pt. This could give information on if the Pt and Ag are alloyed, and the extent of this alloying.

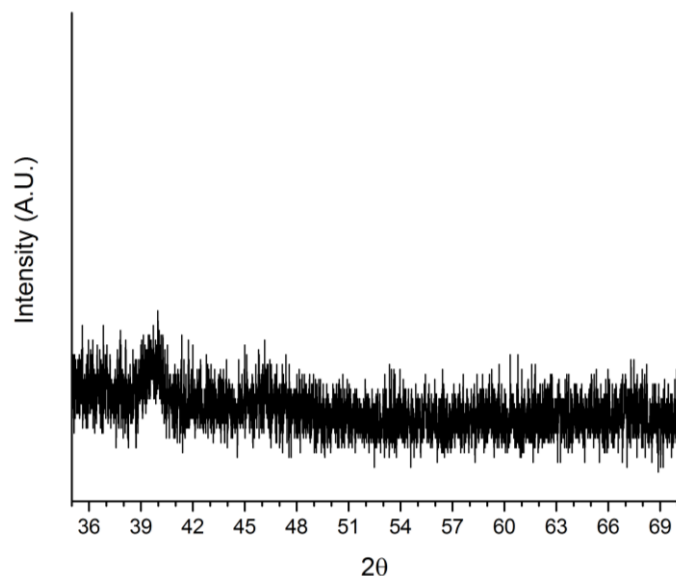


Figure 6.4 PXRD of Pt cuboctahedra deposited on SiO<sub>2</sub>.

Overall, this implies that the catalytic results when using these MNP shapes will not correspond simply to the surface selectivity of the Pt. For instance, it has been observed that Pt{100} is more active for complete phenyl ring reduction when compared to Pt{111}.<sup>10</sup> However, when comparing to the Pt{100} surface in this work, the Ag within the surface may aid or hinder the phenyl ring reduction. Thus, the activity of the catalysts will likely correspond to the concentration of both metals as well as the morphology of the MNPs.

## 6.4 MOF Growth: Optimising Synthesis Concentrations to Achieve Core-Shell Materials

### 6.4.1 UiO-66

Initially, UiO-66 precursors were added to MNP colloids in the concentrations as described in Na *et al.*<sup>5</sup>, however no core-shell materials were found. In this publication, the Pt colloidal nanoparticles were around 2 nm, significantly smaller than the 10 nm particles made in this work. Most likely, the previously published concentrations did not work due to the large difference in MNP size. Jiang *et al.* describes the apparent influences to synthesising core-shell materials in a Pd@ZIF-8 combination.<sup>11</sup> In this work it was determined that the Pd:Zn ratio and the Zn:2-methylimidazole linker ratio were important to achieve Pd encapsulation. Using this body of work, a similar

approach was used to optimise the MNP cubes@UiO-66 materials with the 10 nm particles. Initially, the Pt:Zr ratio was increased, until Pt cube MNPs could easily be observed in the final material. This suggests that the UiO-66 must be interacting with the Pt particles to form agglomerates of sufficient size to withstand the centrifugation work-up process. However, at the Zr:BDC ratio that was used, no core-shell materials were observed. The ratio of Zr:BDC was then lowered from this initial point which appeared to only create extremely small crystals. The idea behind this was to slow the crystallisation process by lowering the concentration of linker. This could allow the Zr ions to interact with the PVP which caps the MNPs before starting the nucleation process to form UiO-66. The ratios and subsequent material outcome are shown in Figure 6.5.

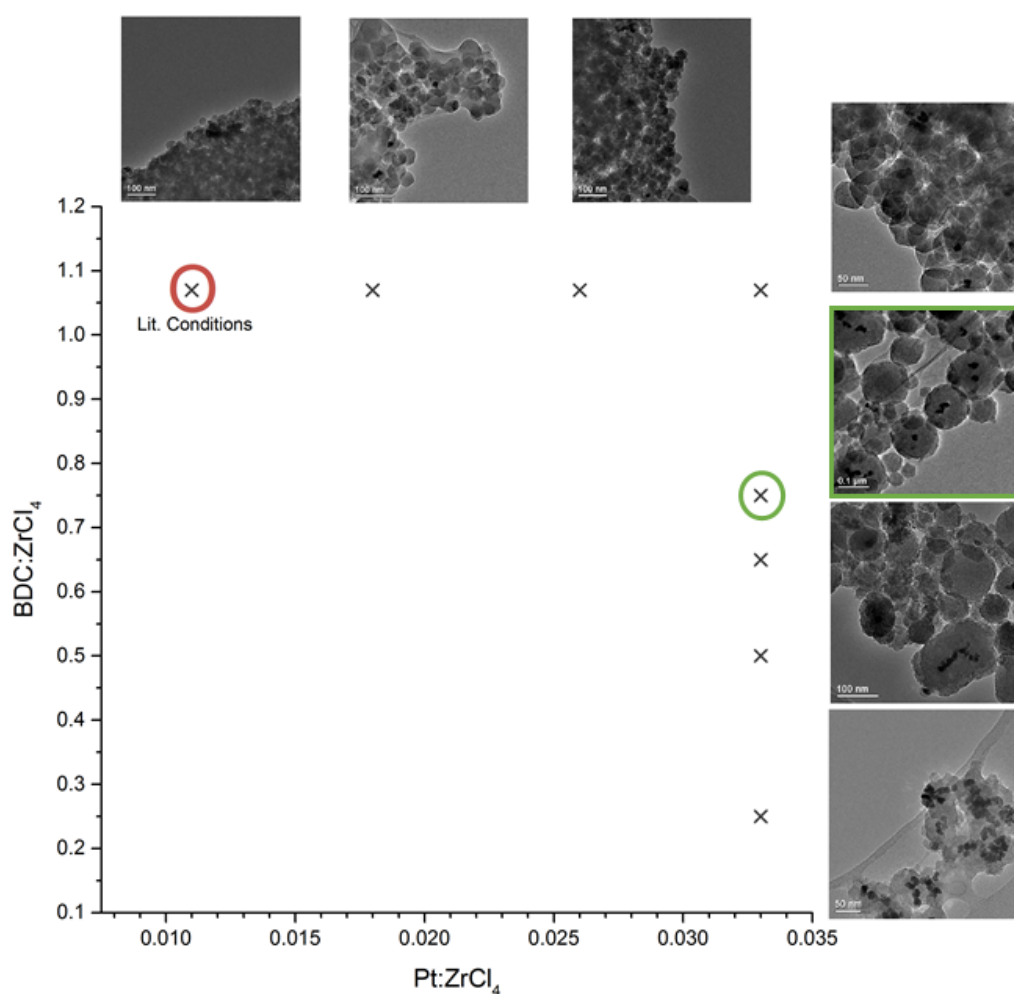


Figure 6.5 Synthesis conditions for optimising UiO-66 core-shell morphologies with MNP cubes and their subsequent outcome. A TEM image is not shown for BDC:Zr 0.25 and Pt:Zr 0.033.

At Pt:Zr of 0.033 and Zr:BDC of 0.75 the desired core-shell materials were obtained, seen in Figure 6.5 with green outlines. The core-shell materials are spherical and around 150 nm in diameter, depending on the number of MNPs within the core. Deviating from these ratios led to less well-formed core-shells. Using the same conditions which were optimised with MNP cubes, UiO-66 was also successfully grown around MNP cuboctahedra and MNP octahedra, seen in Figure 6.6. Interestingly, the syntheses with cuboctahedra colloids formed the most well-defined core-shell, with only one or two MNPs surrounded by UiO-66. This could be due to a variety of reasons. For one, the exact concentration of the colloids is assumed from the synthesis, neglecting any losses which occur during the work-up procedure. This means that there are likely differences in metal nanoparticle colloidal concentration between the different shapes. The exact concentration of the cuboctahedra colloid could be such that a very well-defined core-shell material is made. Another reason could be due to the less agglomeration apparent in the cuboctahedra MNP sample compared to the cubes, seen in the TEM images of Figure 6.2.

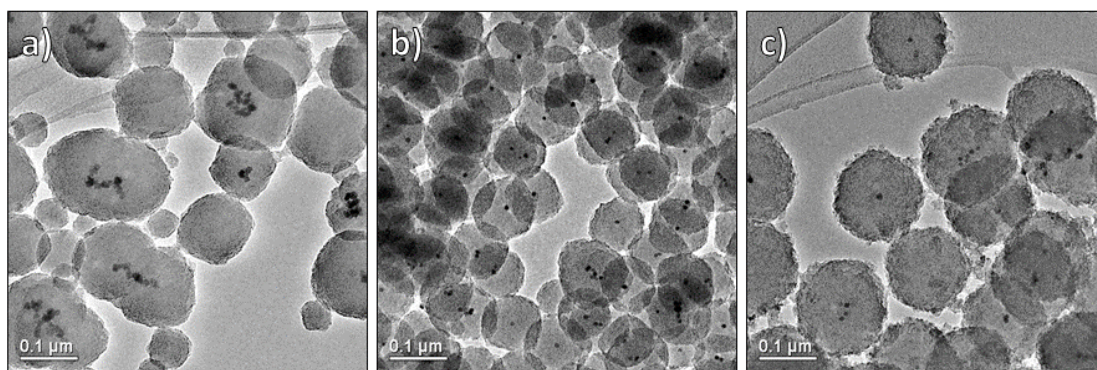


Figure 6.6 TEM images showing the core shell materials with UiO-66 and (a) MNP cubes, (b) MNP cuboctahedra and (c) MNP octahedra.

In each optimisation case, only around 30 mg of material was made to determine if the morphology is core-shell. After the initial optimisation, scale-up procedures were attempted in order to make around 150 mg of core-shell material. With this amount, a thorough characterisation of the material could be performed. A representative  $N_2$  adsorption isotherm from MNP cuboctahedra@UiO-66 can be seen in Figure 6.7. The surface area of this material is around  $848 \text{ m}^2 \text{ g}^{-1}$  and the pore volume is  $0.37 \text{ cm}^3 \text{ g}^{-1}$ .

The large increase in the isotherm greater than 0.9  $P/P_0$  is due to the spherical shape of the core-shell particles. The void spaces created during the packing of the spherical materials creates macropores which can be seen at high relative pressures.

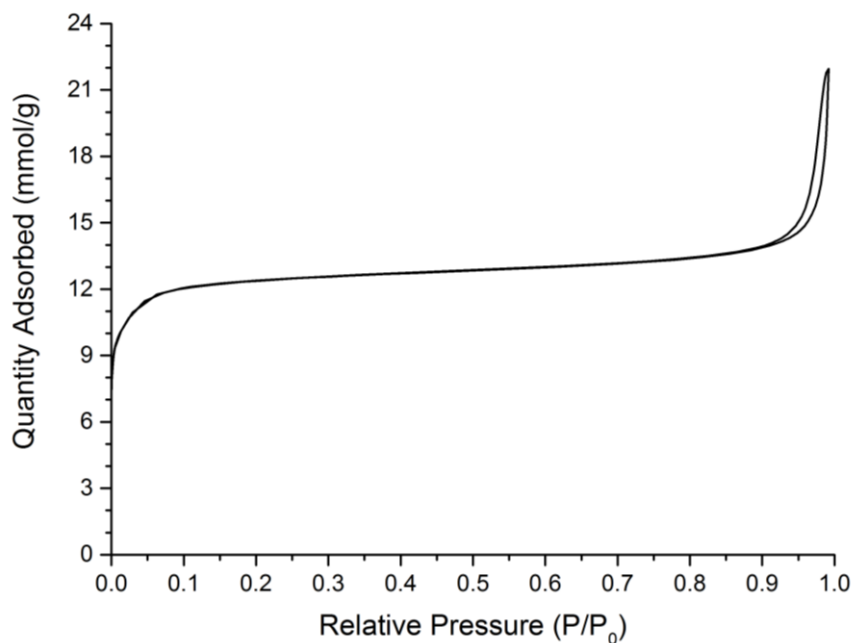


Figure 6.7 N<sub>2</sub> adsorption isotherm at 77 K of MNP cuboctahedra@UiO-66.

Powder XRD was performed showing that the correct MOF was synthesised. Figure 6.8 shows the peaks indicating the UiO-66 structure. No signal of MNP was viewable at high angles, probably due to the broadness of the peaks being hidden within the baseline. However, combining these results with the TEM images, it is obvious MNPs are encapsulated within the UiO-66 material.

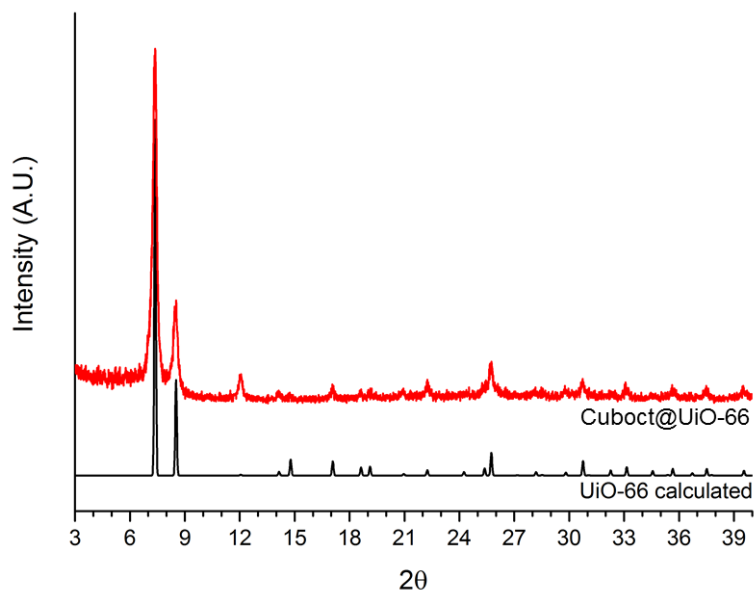


Figure 6.8 Powder XRD of MNP cuboctahedra@UiO-66.

Additionally, XPS was performed on this material. No signal of Pt or Ag was observed, even at long acquisition times. However, the MOF components were easily viewable, indicating that the MNPs are not deposited on the surface of the UiO-66 material. Figure 6.9 shows the XP spectra of the MOF components in the MNP cuboctahedra@UiO-66 material.

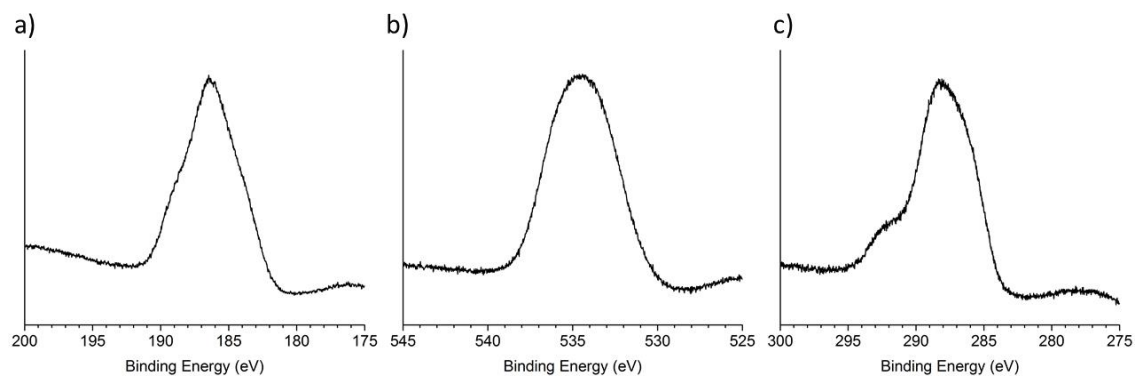


Figure 6.9 XP spectra of MNP cuboctahedra@UiO-66. Pt and Ag are not apparent, but the MOF components are easily viewable. (a) Zr 3d, (b) O 1s and (c) C 1s.

#### 6.4.1.1 Increasing Acidity in MNP@UiO-66 Materials

Due to its high connectivity, UiO-66 is able to remain stable with large defects in its structure. Wu *et al.* showed that these missing-linker defects changed the adsorption capabilities of the MOF.<sup>12</sup> The linker vacancies could be tuned by replacing the terephthalic acid linker with a monocarboxylic acid during the MOF synthesis. In that

work, acetic acid was used as the modulator, which enabled them to tune the number of defects to nearly 10% while maintaining UiO-66 crystallinity stability. This in turn increased the pore volume by 150% and the surface area by 60%, leading to interesting gas adsorption behaviour for CO<sub>2</sub> adsorption. Vermoortele *et al.* has used synthesis modulation to increase the catalytic activity of UiO-66.<sup>13</sup> For that work various monocarboxylic acids were tested as the modulator. Each modulated MOF was activated at 320 °C under vacuum to ensure the full removal of the modulator before catalysis. The influence of the modulation was significant with trifluoroacetic acid (TFA), increasing a citronellal to isopulegol conversion by 41% after 10 hours. It was determined that TFA was the best modulator to influence the catalytic activity, however acetic acid also increased the conversion of citronellal to isopulegol by 11% after 10 hours.

Increasing the catalytic activity of the MOF shell could in turn lead to a better core-shell catalyst. Modulating the MOF crystallinity by varying amounts of acetic acid and/or trifluoroacetic acid while forming the core-shell materials was therefore investigated. Ideally, a core-shell material could be synthesised with additional Lewis acid sites due to the replacement of terephthalic acid with a monocarboxylic acid in the MOF synthesis. Initially, the effect of varying the concentration of acetic acid was investigated. The original Na *et al.* synthesis of the core-shell materials used a ratio of 1 to 85 Zr to acetic acid. Based on this, Zr to acetic acid ratios of 1 to 0, 146, 219, 280 and 341 were tried in the core-shell synthesis with MNP cubes. It can be seen in Figure 6.10 that acetic acid is instrumental to the formation of core-shell morphology.

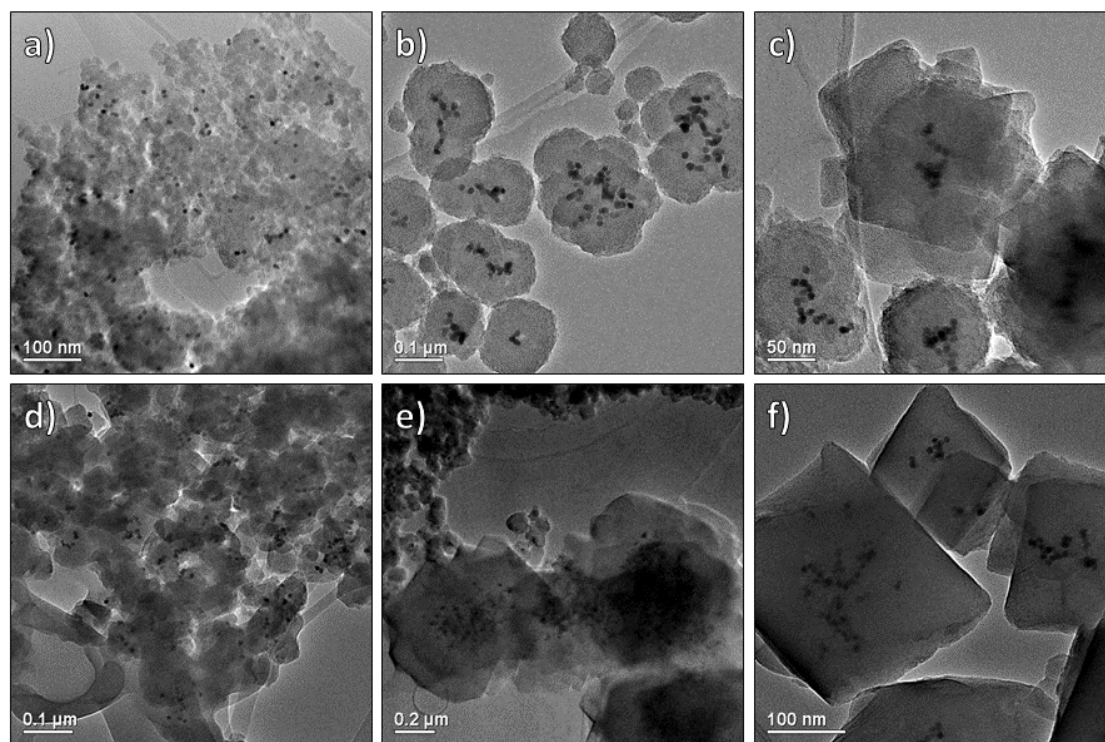


Figure 6.10 TEM images showing the influence acetic acid plays in core-shell morphology formation. Zr to acetic acid ratios of 1 to (a) 0, (b) 85, (c) 146, (d) 219, (e) 280 and (f) 341.

In the case no acetic acid is added, no core-shell morphology is observed (Figure 6.10a). This may indicate acetic acid is necessary to slow the growth of the MOF, which could allow for more MOF forming around a MNP rather than any other nucleation site. Increasing the acetic acid ratio to 146 acetic acid to 1 Zr led to core-shell morphologies formed, however the overall shape of the core-shell material has changed (Figure 6.10c). Many of the core-shell structures have many large well-defined crystal edges which make up the shell. Interestingly, increasing to 219 and 280 appear to be at incorrect concentrations for homogeneous core-shell formation (Figure 6.10d-e). However, increasing the ratio to 341 provides well-defined crystals of UiO-66 to be formed around the MNP cubes (Figure 6.10f). This series of acetic acid variation shows that acetic acid is an important component for the desired core-shell morphology when growing UiO-66 around MNPs. By changing the amount of acetic acid in the synthesis, morphologies ranging from spherical shells to well-defined crystal shells can be made.

Next, the influence of adding TFA during the core-shell synthesis was investigated. Knowing that acetic acid plays a large role in the morphology of the materials, TFA was tried as an addition to the normal synthesis conditions and also on its own as a modulator as a 0.9 mmol addition. Figure 6.11 shows both preparations.

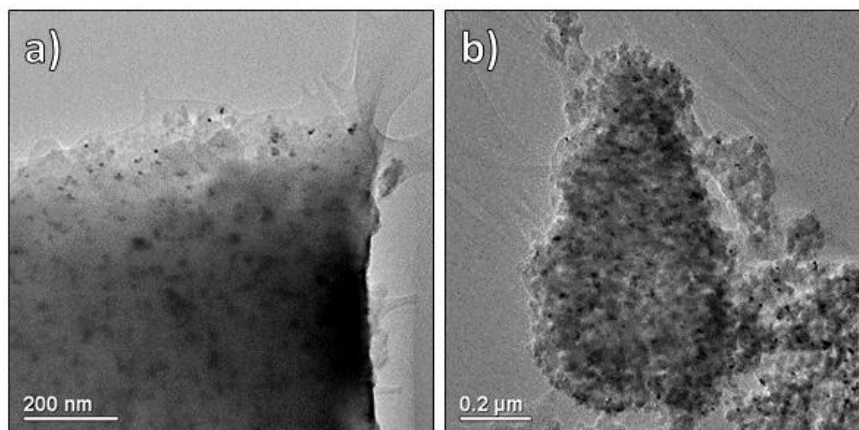


Figure 6.11 TEM images of TFA-modulated UiO-66. (a.) The addition of TFA included in the normal synthesis of core-shell materials with acetic acid and (b.) preparation of UiO-66 with only TFA added as modulator.

In both cases the desired core-shell morphology was not obtained. Further experimentation into varying the TFA and/or acetic acid concentrations should be tried in order to determine if TFA can be an effective modulator in the preparation of increased Lewis acidic UiO-66 shells.

#### 6.4.2 MIL-100(Sc)

MIL-100(Sc) was also tried for shell growth over the PtAg MNP shapes. The synthesis of MIL-100(Sc) based core-shell materials using an autoclave procedure was investigated. Again, a series of synthesis conditions were investigated, altering the Pt:Sc ratio and the BTC:Sc ratio, shown in Table 6.2.

Table 6.2 Synthesis ratios for autoclave synthesis of MNP@MIL-100(Sc) core-shell materials.

Pt:Sc	BTC:Sc
0.009	0.62
0.009	0.75
0.009	0.88
0.009	1
0.02	0.75
0.025	0.75
0.03	0.75
0.033	0.75
0.033	1.5
0.33	0.75
0.33	1.5

Comparing the materials with BTC:Sc ratios of 0.75 in which MNPs could easily be seen, a significant difference in MNP amount is observed. Figure 6.12 shows the TEM images of these materials. MIL-100(Sc) appears to have a wide range of conditions where core-shell morphology is observed and the amount of metal within the shells can be tuned by altering the Pt:Sc ratio.

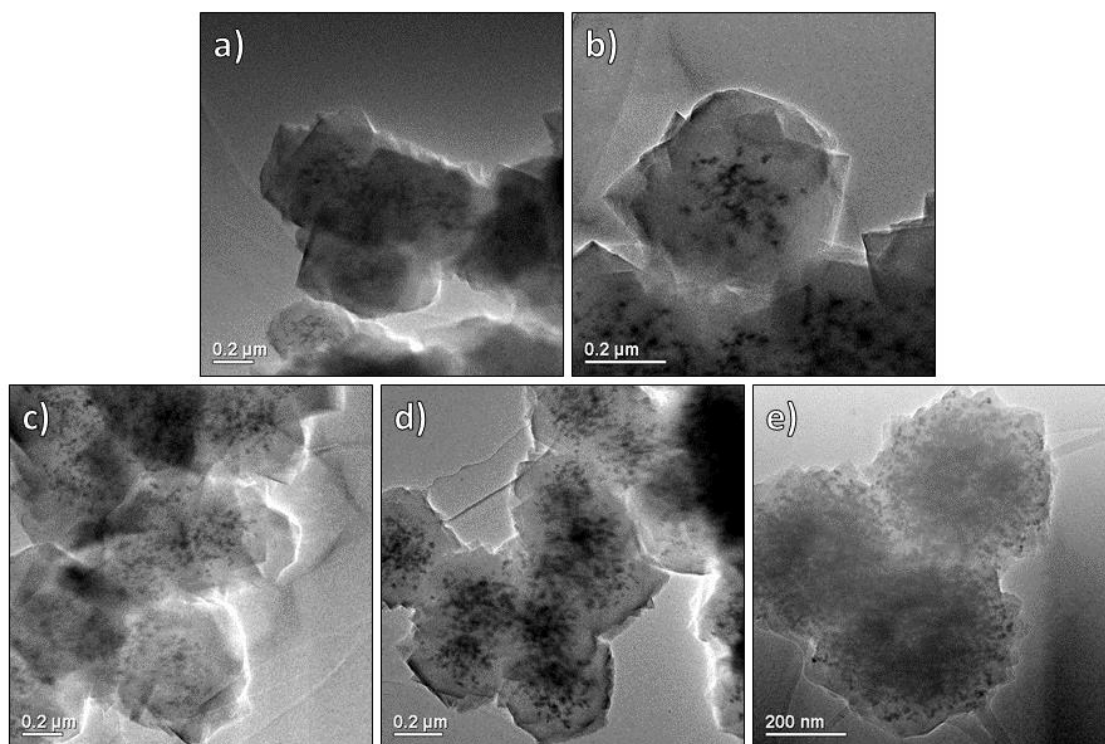


Figure 6.12 TEM images of MNP@MIL-100(Sc) with Pt:Sc ratios of (a) 0.02, (b) 0.025, (c) 0.03, (d) 0.033 and (e) 0.33.

Although the core-shell materials made with MIL-100(Sc) are not as well-defined and homogeneous as those prepared with UiO-66, the concept of altering the synthesis conditions to obtain the desired morphology is shown to be applicable to multiple MOF types. The formation of the desired MIL-100(Sc) material was confirmed using powder XRD, seen in Figure 6.13. To determine the extent of MNPs on the surface of the material compared to the core, XPS and EDX were both performed. EDX showed around 3 wt% MNP within the Pt:Sc 0.025 sample. Using the same sample for XPS, no Pt or Ag was observed, even at long acquisition times. However, the elements which make up MIL-100(Sc) were readily viewable, seen in Figure 6.14. This indicates that the MNPs are within the MIL-100(Sc) structure rather than on the surface of the MOF.

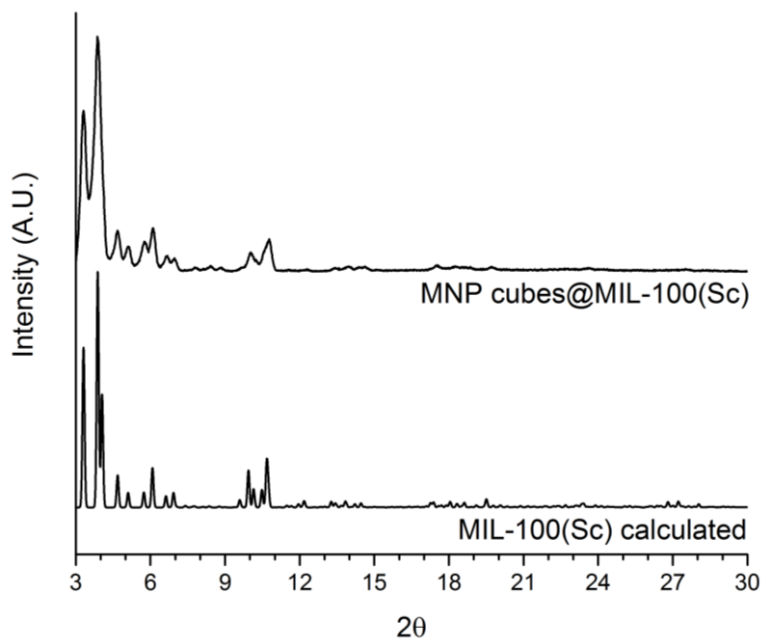


Figure 6.13 Powder XRD of MNP cubes@MIL-100(Sc). XRD corresponds to the Pt:Sc ratio of 0.025.

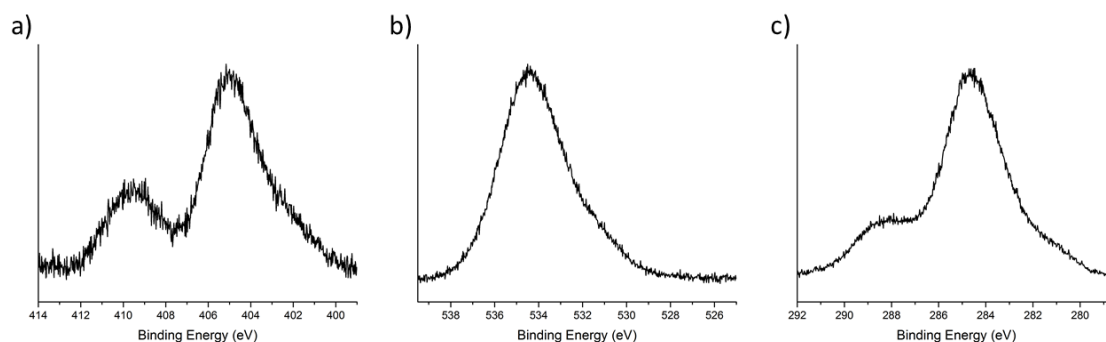


Figure 6.14 XP spectra of MNP cubes@MIL-100(Sc). The Pt and Ag signals are not apparent but the MOF components are easily viewable. (a) Sc 2p, (b) O 1s and (c) C 1s.

## 6.5 Catalysis

The prepared core-shell materials were tested for their catalytic activity. Ideally, tandem reactions could occur within this material, with the MNP and the Lewis acid sites catalysing subsequent steps independently.

### 6.5.1 UiO-66

Initially, MNP cuboctahedra@UiO-66 was tested in the reductive amination reaction shown in Figure 6.15. As thoroughly discussed in Chapter 4, the Lewis acid sites within the MOF catalyse the 4'-fluoroacetophenone and benzylamine into an imine, which

can then be reduced into a secondary amine on the MNP. The reaction can proceed further on the MNPs and the secondary amine can undergo hydrogenolysis to form a primary amine and toluene. The desired product is the secondary amine. The intermediate product is the imine and the undesired product is the fluorinated primary amine.

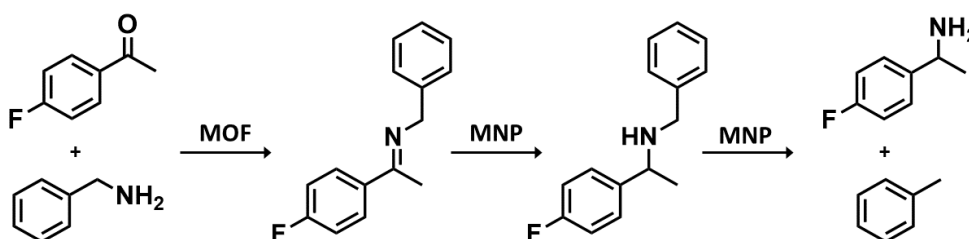


Figure 6.15 Reductive amination reaction using a multifunctional Lewis acid and nanoparticle catalyst.

After 16 hours at 50 °C and 10 bar H<sub>2</sub> the MNP cuboctahedra@UiO-66 converted 17% of the 4'-fluoroacetophenone to the intermediate imine. However, no reduction was observed at this time. This indicates either the MNPs are inactive or the MOF has pores too small for the imine to diffuse through. Because UiO-66 has a pore sizes of around 6 Å<sup>14</sup>, it is likely that the large imine molecule cannot diffuse through the pores and the conversion observed is due to surface reactions on the UiO-66 material.

However, to rule out the possibility of inactive MNPs, an alternative reaction using the MNPs@UiO-66 was performed. Styrene reduction, seen in Figure 6.16, was used as a probe reaction to test the activity of the MNPs within the core-shell materials. This small molecule easily fits within the pore dimensions of UiO-66, and should be able to be reduced on the MNP if there are active sites available for reaction.

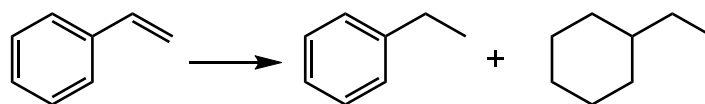


Figure 6.16 Styrene reduction on MNP shapes. The major product in the styrene reduction is ethylbenzene. The minor product is assumed to be ethylcyclohexane, but full phenyl ring reduction may not occur.

All of the MNP shapes used for formation of MNP@UiO-66 were active in the styrene reduction reaction. In all cases, the MNP shapes@UiO-66 reached full conversion after

5 hours at reaction conditions, shown in Table 6.3. This indicates that the lack of reduction in the reductive amination reaction is not due to the inactivity of the MNPs. Therefore, the 17% conversion within the MNP cuboctahedra@UiO-66 material must be due to surface reaction on the MOF shell. The lack of full conversion in the catalyst which has the MNP cuboctahedra on SiO<sub>2</sub> could be due to a discrepancy of total metal loading, which was based on the loading during material synthesis rather than by EDX of the prepared catalyst. However, it could also be due to an enhanced activity of the MNP within the core-shell material, which has been seen in literature for similar Pt@UiO-66 catalysts by Na *et al.*<sup>5</sup>

Table 6.3 Styrene reduction reaction performed by MNP shapes. Reaction conditions: 3 mol% MOF catalyst, 50 °C, 5 bar H<sub>2</sub> in EtOH for 5 hours.

Sample	Conversion (%)
MNP cuboctahedra on SiO <sub>2</sub>	91
MNP cubes@UiO-66	100
MNP cuboctahedra@UiO-66	100
MNP octahedra@UiO-66	100

Interestingly, in the styrene reduction, an alternative product was found in small amounts for all of the reactions performed with MNP@UiO-66 catalysts. Literature has suggested with highly active MNP catalysts, reduction of the phenyl ring is also possible during styrene reduction giving ethylcyclohexane as the final, fully reduced product.<sup>15</sup> Although it remains undetermined of the extent in which the phenyl ring is reduced, this product is made in small amounts, shown in Figure 6.17.

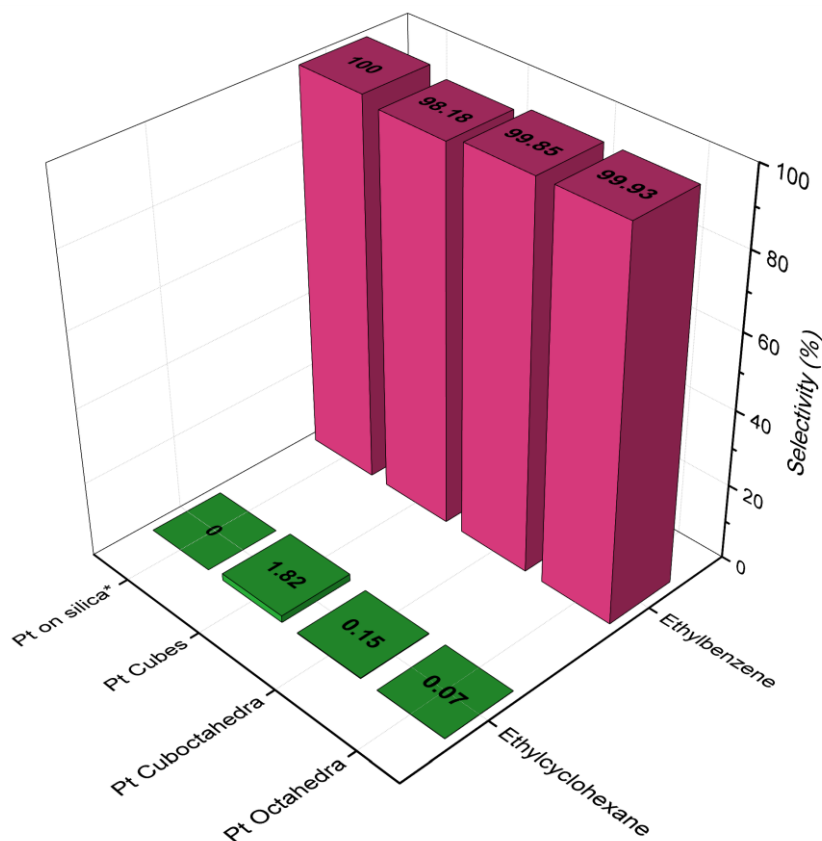


Figure 6.17 Styrene reduction selectivity with MNP shapes. Ethylcyclohexane is the suggested product, however full phenyl ring reduction may not occur. \*cuboctahedra

The MNP cubes give the most of this secondary product as 1.82% selectivity, and the MNP octahedra give the least, at only 0.07% selectivity. The MNP cubes have {100} planes on all sides, which has been shown to fully reduce phenyl rings more effectively than {111} planes (octahedral particles).<sup>10</sup> This change in selectivity could alternatively be due to the relative activity of each shape. If, for instance, the cubes were to reduce the styrene significantly more quickly, then more ethylbenzene would be available for further reduction. Whereas if the octahedra reduced the styrene slowly, just reaching 100% at 5 hours, for instance, there may not be as much opportunity for the ethylbenzene to be further reduced. Another alternative, and possibly the most likely, is that the MNP cubes have the least amount of Ag on the surface. As Ag is an inhibitor, the shapes with the least Ag would be the most active in reductions.<sup>8</sup> The MNP octahedra have the most Ag on the surface, with over a quarter of the surface containing Ag. This could effectively inhibit phenyl ring reduction.

Catalysis runs which progress with less time, such as 1 hour, need to be completed to determine if a difference of activity is present between the shapes. With all MNP@UiO-66 catalysts achieving full conversion after 5 hours, it is not possible to determine the extent the crystal face or Pt and Ag amounts play in the activity of the styrene reduction catalysis.

The MNP cuboctahedra@UiO-66 was observed before and after styrene catalysis in the TEM. Figure 6.18 shows the before and after images. The core-shell morphology remains after the 5 hour reaction, and even the nanoparticle shape appears to be immobilised in the MOF support after the reaction.

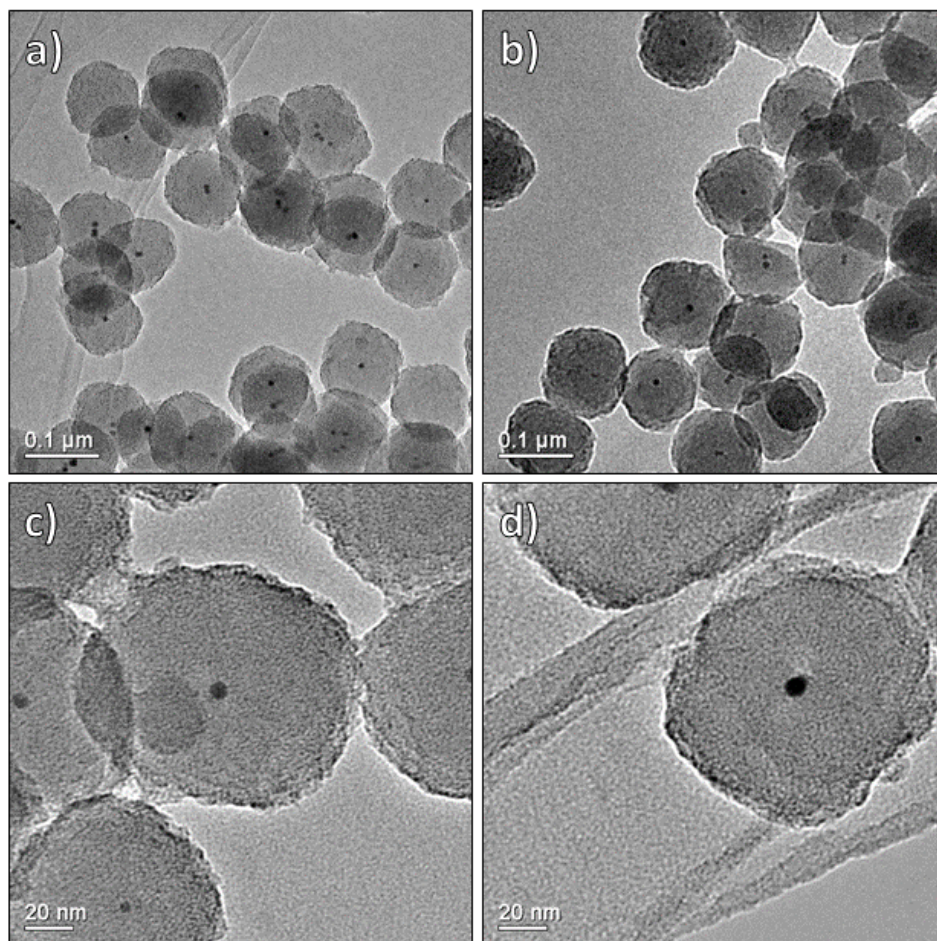


Figure 6.18 MNP@UiO-66 TEM images showing (a, c) before and (b, d) after styrene reduction catalysis. Reaction conditions: 3 mol% MOF catalyst, 5 hours, 50 °C and 5 bar H<sub>2</sub> in EtOH.

### 6.5.2 MIL-100(Sc)

MIL-100(Sc) is a mesoporous caged MOF which has windows in the microporous region. However, the diffusion limitation that was present through the UiO-66 should not be an issue in MIL-100(Sc). The MNP@MIL-100(Sc) materials shown in Figure 6.12a-d were tested as catalysts in the reductive amination reaction, shown in Figure 6.15. The difference between these catalysts is the Pt:Sc ratio, discussed previously in section 6.4.2. The results of the reductive amination catalysis are shown in Table 6.4.

Table 6.4 Reductive amination results from PtAg MNP cubes@MIL-100(Sc) catalysis. Reaction conditions: 5 mol% MOF catalyst, 50 °C, 10 bar H<sub>2</sub> in dry hexane for 16 hours.

Pt:Sc	Conversion (%)	Selectivity (%)		
		Imine	2° Amine	1° Amine
0.02	80	24	76	0
0.025	89	11	89	0
0.03	62	58	42	0
0.033	68	95	5	0

Compared to the UiO-66 core shell material, a significant enhancement of activity and selectivity is seen in all catalysts. This is likely because of the increased Lewis acidity within the MIL-100(Sc). This is due to the comparative structures, where UiO-66 mainly gets the Lewis acid sites from defects within the structure and MIL-100(Sc) has structural water which upon removal acts as a coordinatively unsaturated Lewis acid site. Additionally, when using the UiO-66 material as a catalyst the imine formation reaction is likely to be occurring on defect sites on the crystalline surface. This means that there is a much smaller number of acid sites available for reaction when compared to the MIL-100(Sc).

Comparing the four MNP cubes@MIL-100(Sc) catalysts, a significant difference was observed. The catalyst with a Pt:Sc ratio of 0.025 gave the best performance. Approximately the same amount of MIL-100(Sc) is present in each reaction, and the amount of MNP differs in each case. When there is less MNP, at a Pt:Sc ratio of 0.02, the overall conversion of the 4'-fluoroacetophenone is lower as well as the selectivity

to the desired secondary amine product. Unexpectedly, increasing the Pt:Sc ratio above 0.025:1 appears to cause a significant decrease in reduction to the desired amine. It appears that there are textural features of the MOF/MNP composites that are playing a dominant role. These should be investigated further. The MNPs are capped with polymers and this may lead to a close pack agglomeration in the centre of the core-shell material at high MNP loading, and therefore the imine struggles to diffuse through the high density of polymeric capping agent towards the active sites on the MNP surface. This could be why upon increasing the Pt:Sc amount from 0.025 to 0.03 to 0.033 the activity of the reduction drastically declines.

Comparing to the Pd in MIL-101(Cr) system discussed in Chapter 4, the best performing Pt@MIL-100(Sc) is a better catalyst. At 50 °C the Pd in MIL-101(Cr) catalyst achieves 65% conversion and 91% selectivity after 16 hours, where the Pt@MIL-100(Sc) catalyst achieves 89% conversion while maintaining similar selectivity. This corresponds to 0.019 mol 4'-fluoroacetophenone g<sup>-1</sup> catalyst for Pd in MIL-101(Cr) and 0.03 mol 4'-fluoroacetophenone g<sup>-1</sup> catalyst for Pt@MIL-100(Sc).

With the promising results from the reductive amination reaction with MNP@MIL-100(Sc), the preparation of this catalyst should be scaled up and tested for recyclability stability and activity. If the core-shell material is active for multiple runs, this can be a good alternative method to use MIL-100(Sc) as a Lewis acidic MOF support for MNPs.

## 6.6 Conclusions and Outlook

Colloidal PVP-capped MNP nanoshapes consisting of Ag and Pt were successfully synthesised. Characterisation of these particles showed that the Ag and Pt surface concentration were similar to the bulk particle concentration, determined by comparing EDX and XPS results. This indicates that Ag is not acting as a surface modifier but is incorporating itself into the MNPs. However, the well-defined shapes and the larger particle size, compared to the nanoparticles synthesised in previous chapters, allowed for ease of identification for core-shell formation.

Synthesis procedures were optimised to create core-shell materials. The Pt:MOF metal and MOF linker:MOF metal ratios were altered in order to achieve the desired core-

shell structure. It was found the optimum for MNP@UiO-66 was Pt:Zr of 0.033 and BDC:Zr of 0.75. The optimum synthesis conditions for MNP@MIL-100(Sc) was found to be Pt:Sc between 0.02 and 0.033 and BTC:Sc of 0.75. Interestingly, both systems have a MOF linker to MOF metal ratio of 0.75, even though the final MOF forms do not have structures with this ratio. MIL-100(Sc) formed much larger core-shell materials, with many MNPs inside a single shell. Further optimisation may be possible to achieve more well-defined single MNP in MIL-100(Sc).

Catalysis was performed with MNP@UiO-66 and MNP@MIL-100(Sc). The reductive amination with MNP@UiO-66 only achieved 17% conversion after 16 hours. Additionally, no reduction of the intermediate imine was accomplished. This indicates that the pore size of UiO-66 may hinder the diffusion towards the MNP active sites. The conversion that was achieved can be attributed to surface reactions on the UiO-66 shell. To investigate this, the MNP@UiO-66 materials were used as catalysts in a styrene hydrogenation reaction. In this case, all MNP shapes@UiO-66 were active and all core-shell catalysts gave full conversion after 5 hours. There was some secondary product from the styrene reduction, thought to be due to the reduction of the phenyl ring on the MNP surface. The MNP cubes converted the highest concentration of this product, which is attributed to containing the smallest amount of Ag within the PtAg MNPs.

MNP@MIL-100(Sc) was also used as a catalyst for the reductive amination reaction. In this case, four core-shell materials with varying Pt:Sc ratios were compared for their activity and selectivity to the desired secondary amine. The best performing MNP@MIL-100(Sc) catalyst had a Pt:Sc ratio of 0.025 and achieved 89% conversion with 89% selectivity after the 16 hour reaction. This catalyst should be further investigated for its recyclability and activity.

Showing that modifying the synthesis ratios can optimise the core-shell morphology for both UiO-66 and MIL-100(Sc), more MOF types should be tried. An initial trial of a modified UiO-66 material synthesised with 2-nitroterephthalic acid was attempted, shown in Figure 6.19. It is likely that with slight modification of BDC-NO<sub>2</sub>:Zr ratio the core-shell morphology could be the dominant feature. This MOF could have good

catalysis results in a reaction such as the citronellal to menthol reaction discussed in Chapter 4.

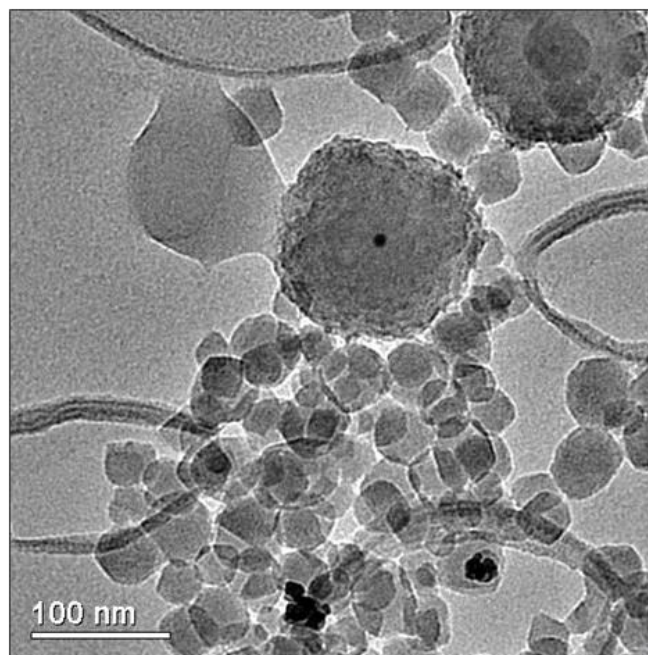


Figure 6.19 TEM image of MNP cubes@UiO-66-NO<sub>2</sub>.

Changing the MNP species and the capping agent should also be investigated. A method to synthesising Pt nanoshapes without the Ag added should be tried and tested in catalysis. Alayoglu *et al.* showed Pt nanoshapes behaving interestingly in methylcyclopentane hydrogenative conversions.<sup>16</sup> Na *et al.* initially grew UiO-66 around small Pt NPs which were also used in methylcyclopentane hydrogenative conversions.<sup>5</sup> If UiO-66 could be grown round Pt nanoshapes these materials might have a significant enhancement in activity and selectivity for reactions such as methylcyclopentane hydrogenative conversions.

Changing the MNP species and capping agent was also tried with CoO NPs capped with oleylamine. These materials, provided by Dr. Juan María González Carballo, were suspended in toluene and used in place of the PtAg MNPs in the optimised synthesis of the UiO-66 core-shell materials. Figure 6.20 shows the morphology of this sample. It is apparent that while core-shell materials are prepared, many UiO-66 crystals are made without any CoO NPs within them. With some more optimisation it may be possible to tune the synthesis to create exclusively core-shell materials.

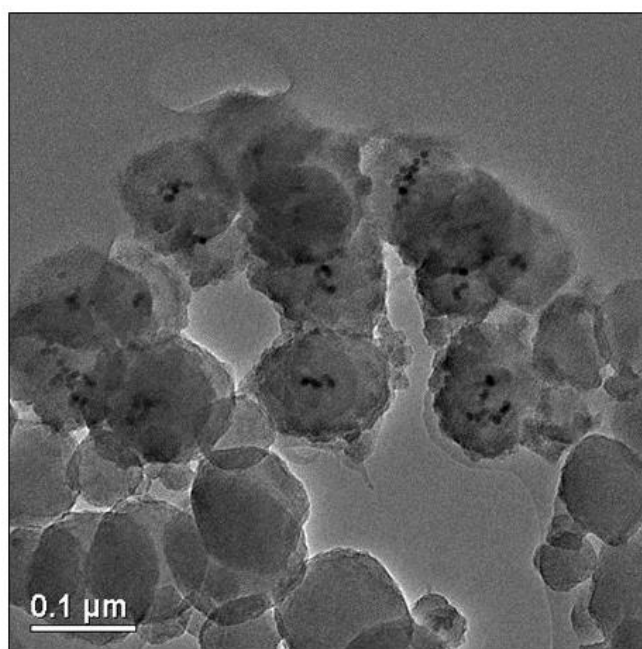


Figure 6.20 TEM image of CoO@UiO-66.

The idea of tuning MOF growth to form the desired morphological features is one that has many applications and core-shell NP@MOF materials are one of many possibilities. Using the optimisation process described here, a range of other NP/MOF systems are open to investigation.

## 6.7 References

1. Hu, P.; Morabito, J. V.; Tsung, C.-K., Core-Shell Catalysts of Metal Nanoparticle Core and Metal-Organic Framework Shell. *ACS Catal.* **2014**, *4*, 4409-4419.
2. Lu, G.; Li, S.; Guo, Z.; Farha, O. K.; Hauser, B. G.; Qi, X.; Wang, Y.; Wang, X.; Han, S.; Liu, X.; DuChene, J. S.; Zang, H.; Zhang, Q.; Chen, X.; Ma, J.; Loo, S. C. J.; Wei, W. D.; Yang, Y.; Hupp, J. T.; Huo, F., Imparting Functionality to a Metal-Organic Framework Material by Controlled Nanoparticle Encapsulation. *Nat. Chem.* **2012**, *4*, 310-316.
3. Zhao, M.; Deng, K.; He, L.; Liu, Y.; Li, G.; Zhao, H.; Tang, Z., Core-Shell Palladium Nanoparticle@Metal-Organic Frameworks as Multifunctional Catalysts for Cascade Reactions. *J. Am. Chem. Soc.* **2014**, *136*, 1738-1741.
4. Song, H.; Kim, F.; Connor, S.; Somorjai, G. A.; Yang, P., Pt Nanocrystals: Shape Control and Langmuir-Blodgett Monolayer Formation. *J. Phys. Chem. B* **2005**, *109*, 188-193.
5. Na, K.; Choi, K. M.; Yaghi, O. M.; Somorjai, G. A., Metal Nanocrystals Embedded in Single Nanocrystals of MOFs Give Unusual Selectivity as Heterogeneous Catalysts. *Nano Lett.* **2014**, *14*, 5979-5983.
6. Koczkur, K. M.; Mourdikoudis, S.; Polavarapu, L.; Skrabalak, S. E., Polyvinylpyrrolidone (PVP) in Nanoparticle Synthesis. *Dalton Trans.* **2015**, *44*, 17883-17905.
7. Leong, G. J.; Ebnonnasir, A.; Schulze, M. C.; Strand, M. B.; Ngo, C.; Maloney, D.; Frisco, S. L.; Dinh, H. N.; Pivovar, B.; Gilmer, G. H.; Kodambaka, S.; Ciobanu, C. V.; Richards, R. M., Shape-Directional Growth of Pt and Pd Nanoparticles. *Nanoscale* **2014**, *6*, 11364-11371.
8. Grass, M. E.; Yue, Y.; Habas, S. E.; Rioux, R. M.; Teall, C. I.; Yang, P.; Somorjai, G. A., Silver Ion Mediated Shape Control of Platinum Nanoparticles: Removal of Silver by Selective Etching Leads to Increased Catalytic Activity. *J. Phys. Chem. C* **2008**, *112*, 4797-4804.
9. Yousaf, A. B.; Imran, M.; Zeb, A.; Wen, T.; Xie, X.; Jiang, Y.-F.; Yuan, C.-Z.; Xu, A.-W., Single Phase PtAg Bimetallic Alloy Nanoparticles Highly Dispersed on Reduced Graphene Oxide for Electrocatalytic Application of Methanol Oxidation Reaction. *Electrochim. Acta* **2016**, *197*, 117-125.
10. Bratlie, K. M.; Lee, H.; Komvopoulos, K.; Yang, P.; Somorjai, G. A., Platinum Nanoparticle Shape Effects of Benzene Hydrogenation Selectivity. *Nano Lett.* **2007**, *7*, 3097-3101.
11. Jiang, H.; Yan, Q.; Chen, R.; Xing, W., Synthesis of Pd@ZIF-8 via an Assembly Method: Influence of the Molar Ratios of Pd/Zn<sup>2+</sup> and 2-Methylimidazole/Zn<sup>2+</sup>. *Micropor. Mesopor. Mater.* **2016**, *225*, 33-40.
12. Wu, H.; Chua, Y. S.; Krungleviciute, V.; Tyagi, M.; Chen, P.; Yildirim, T.; Zhou, W., Unusual and Highly Tunable Missing-Linker Defects in Zirconium Metal-Organic Framework UiO-66 and Their Important Effects on Gas Adsorption. *J. Am. Chem. Soc.* **2013**, *135*, 10525-10532.
13. Vermoortele, F.; Bueken, B.; Le Bars, G.; Van de Voorde, B.; Vandichel, M.; Houthoofd, K.; Vimont, A.; Daturi, M.; Waroquier, M.; Van Speybroeck, V.; Kirschhock, C.; De Vos, D. E., Synthesis Modulation as a Tool to Increase the Catalytic Activity of

Metal–Organic Frameworks: The Unique Case of UiO-66(Zr). *J. Am. Chem. Soc.* **2013**, *135*, 11465-11468.

14. Cavka, J. H.; Jakobsen, S.; Olsbye, U.; Guillou, N.; Lamberti, C.; Bordiga, S.; Lillerud, K. P., A New Zirconium Inorganic Building Brick Forming Metal Organic Frameworks with Exceptional Stability *J. Am. Chem. Soc.* **2008**, *130*, 13850-13851.

15. Jacinto, M. J.; Landers, R.; Rossi, L. M., Preparation of Supported Pt(0) Nanoparticles as Efficient Recyclable Catalysts for Hydrogenation of Alkenes and Ketones. *Chem. Commun.* **2009**, *10*, 1971-1974.

16. Alayoglu, S.; Aliaga, C.; Sprung, C.; Somorjai, G. A., Size and Shape Dependence on Pt Nanoparticles for the Methylcyclopentane/Hydrogen Ring Opening/Ring Enlargement Reaction. *Catal. Lett.* **2011**, *141*, 914-924.



# Chapter 7

---

Metallosupramolecular Assembly by Dissociation of Metal  
Carbonyls on Au(111)

This chapter has been published in an adapted form. See reference <sup>1</sup>.

## 7.1 Introduction

Metallosupramolecular assembly on surfaces has recently gained attention with regards to the bottom-up approach to well-defined and stable surface structures. These metal-organic coordination networks (MOCNs) on surfaces have many applications such as nanoelectronics<sup>2</sup>, templating<sup>3-6</sup>, and catalysis<sup>7-9</sup> due to the combined interactions between surface, metal and linker molecules. Additionally, these surface structures can act as model MOF systems and by probing the characteristics of MOCNs during synthesis, functionalization or metal deposition it may lead to insight of how to improve a “bulk” MOF system. MOCNs, similarly to MOFs, can show a variety of structures on surfaces depending on factors such as functionality of the linker molecules, surface coverage of each species and the electronic properties of the metal used.

*p*-Terphenyldinitrile (*p*-TPN) has been used extensively for investigation into unusual coordination symmetry in MOCNs. This molecule acts as a bridging ligand due to its large and rigid shape. Most notably, when depositing Co and *p*-TPN on a passive Ag(111) metal surface it can form large hexagonal shaped pores with an inner diameter around 3.4 nm.<sup>10</sup> This honeycomb structure has been further investigated by increasing the number of phenyl rings in the linker molecule, and have reached pore sizes larger than 6 nm with six phenyl rings as the dicarbonitrile-oligophenyl linker.<sup>11</sup> When using *p*-TPN linker and changing the metal from Co to a lanthanide metal a different MOCN self-assembly was observed.<sup>12</sup> In this case the CN-Ce orientation caused 5-fold symmetry around the metal atom, leading to an Archimedean tessellation structure. Figure 7.1 shows the honeycomb structure made with *p*-TPN and Co (a.) and the Archimedean tessellation structure made with *p*-TPN and Ce (b.).

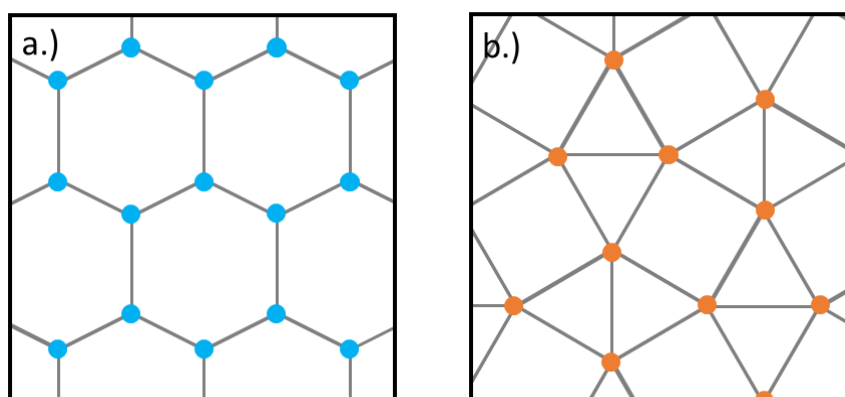


Figure 7.1 (a.) The MOCN structure made with *p*-TPN and  $\text{Co}^{10}$  and (b.) the MOCN structure made with *p*-TPN and  $\text{Ce}^{12}$ .

Metal carbonyls have been investigated for applications in heterogeneous catalysis for over 50 years. Their carbonyl dissociation and decompositions are well known.<sup>13-15</sup> However, with regards to their use as metal sources in coordination chemistry on surfaces, their properties have only begun to be utilized. In general, metals are commonly introduced to form MOCNs by evaporation from solid metal chips, rods or wire by heating. In this chapter chromium hexacarbonyl, a volatile solid, is used as the metal source to create a metal organic coordination network on a surface by depositing vapor onto a Au(111) surface. Chromium hexacarbonyl decomposition and desorption on surfaces has been investigated on Cu(100)<sup>16</sup>, Pd(100)<sup>17</sup>, and Ni(100)<sup>14</sup>. Dosing  $\text{Cr}(\text{CO})_6$  on both Pd(100) and Ni(100) at temperatures below  $-170\text{ }^\circ\text{C}$  led to decomposition of the metal carbonyl and subsequent adsorption of CO on the surface. In the case of Ni(100) thin chromium metal films could be formed, however C and O contaminants were present within the film. In general, Au(111) surfaces are inactive towards CO chemisorption, unlike Ni(100) and Pd(100), and pre-treatments to the gold surface are necessary in order to allow any significant interaction with CO.<sup>18</sup> This means that CO contaminants from the decomposition of  $\text{Cr}(\text{CO})_6$  on the Au(111) surface are extremely unlikely and will likely result in immediate CO desorption from the surface upon decomposition of the metal carbonyl.

This chapter will discuss the experiments and results that show a new type of MOCN formed from the dissociation of chromium hexacarbonyl on a Au(111) surface previously deposited with *p*-TPN. A novel  $\pi$ -bond for surface bound metal organic

coordination networks was found to connect the metal to bridging ligand, creating one dimensional MOCN chains across the gold surface. By using metal carbonyls with labile CO moieties, a novel method for forming MOCNs with chromium nodes was discovered. The interesting coordination chemistry required to obtain the unusual CN-Cr bond configuration within the network, along with the use of metal carbonyls for metal sources, has potential to be further used in other MOCN formations.

## 7.2 Experimental

[*p*-Terphenyl]-4,4''-dicyanitrile (*p*-TPN) was synthesised using a modified procedure presented by Mandali and Chand.<sup>19</sup> A 2 mM palladium nanoparticle solution in methanol and acetonitrile was prepared and left to stir for 3 hours. 0.75 mmol 1,4-benzenediboronic acid (Aldrich, ≥95%) and 1.6 mmol 1,4-bromobenzonitrile (Aldrich, 99%) were added to the nanoparticle solution. The coupling reaction was monitored by TLC and filtered upon the consumption of the boronic acid. The product was filtered then extracted with chloroform. The chloroform layer was evaporated to obtain the desired product as a white powder. Yield: 0.1 g (48%). <sup>1</sup>H NMR (CDCl<sub>3</sub>): δ= 7.89 (s, 4H), 7.94-7.96 (m, 8H).

STM experiments were performed at room temperature using an Omicron variable temperature STM under ultra-high vacuum (UHV). Base pressure was below 1 x 10<sup>-10</sup> mbar. STM measurements were performed in constant current mode using an electrochemically etched W tip.

Reflection absorption infrared spectroscopy (RAIRS) can be carried out on the same machine by moving the sample to another chamber while maintaining UHV conditions. The RAIRS chamber consists of two KBr viewport flanges to allow for the incoming and outgoing IR beam and an external liquid nitrogen cooled mercury-cadmium telluride (MCT) detector which is calibrated before use.

A Au(111) crystal was cleaned by cycles of ion sputtering (Ar<sup>+</sup>, 0.8 kV) and annealing (600 °C) until the characteristic herringbone reconstruction was observed and large terraces were formed.

*p*-TPN was sublimed at 190 °C onto the room temperature Au(111) crystal using a homemade quartz crucible using molecular beam epitaxy. Cr(CO)<sub>6</sub> was loaded into a glass vial and dosed by sublimation at room temperature through a precision leak valve. Cr(CO)<sub>6</sub> exposures were measured using an ion gauge pressure reading in the dosing chamber and exposures ranged from 0.9 to 9400 L (1 L is equivalent to a 1 s exposure at 10<sup>-6</sup> torr).

High resolution electron energy loss spectroscopy (HREELS) measurements were performed with assistance by Dr. Federico Grillo. The measurements were carried out in a UHV chamber with base pressure below 1 x 10<sup>-10</sup> mbar. A VSW HIB 1000 double pass spectrometer was used in the specular geometry with a primary energy beam of 5 eV. Cr(CO)<sub>6</sub> and *p*-TPN were dosed and the surface was annealed in a separate UHV chamber, which could be isolated with a gate valve such that the HREEL chamber remains clean. This allows for fast sample exchange between chambers while maintaining UHV conditions.

Poisson statistics were used on the raw HREEL spectra to recover spectra from instrumental broadening.<sup>20-21</sup> This led to an overall resolution of the elastic peak of approximately 50 cm<sup>-1</sup> FWHM, seen in Figure 7.2.

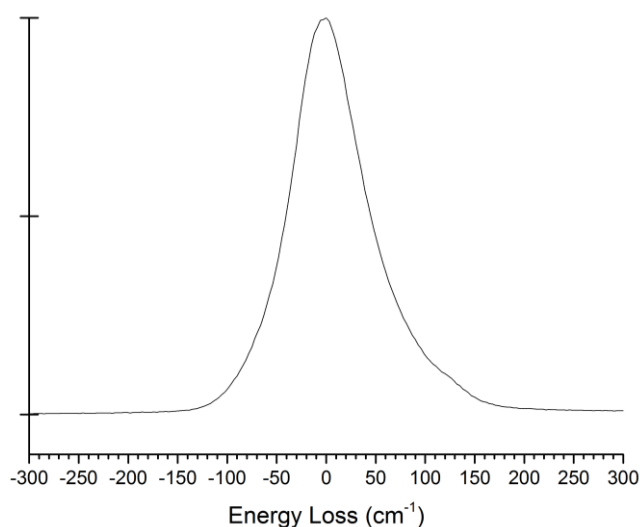


Figure 7.2 A characteristic elastic peak from HREELS experiment showing the FWHM at approximately 50 cm<sup>-1</sup>.

Density functional theory (DFT) calculations were carried out by Dr. Herbert Früchtl using the VASP plane-wave code.<sup>22-23</sup> The PBE functional<sup>24</sup> with Grimme's 3-centre van

der Waals correction with Beke-Johnson damping<sup>25-26</sup> was employed. The plane-wave basis set cutoff was 400 eV. The model system consisted of 3 gold layers, with the bottom two layers frozen at the optimised bulk geometry. Geometry optimisations were carried out on the experimentally determined unit cell of  $(2\sqrt{3} \times 2\sqrt{3})R30^\circ$  with 3 K-points in each of the surface directions. Results were then re-optimised on a rectangular  $(6 \times 2\sqrt{3})$  unit cell which is equivalent to two of the original experimentally determined unit cells. In this case only 1 K-point was necessary in the long direction and 3 in the short direction.

The adsorption energies were calculated using Equation 7.1 where  $E_{\text{Au+Cr+p-TPN}}$  is the energy of the complete system,  $E_{\text{Au+Cr}}$  is the energy of the gold surface with the Cr atoms optimised in the FCC hollow site, and  $E_{\text{p-TPN}}$  is the organic molecule optimised in the gas phase. All adsorption energies are normalised to one unit cell.

$$E_{\text{ads}} = E_{\text{Au+Cr+p-TPN}} - E_{\text{Au+Cr}} - E_{\text{p-TPN}} \quad 7.1$$

## 7.3 Results and Discussion

### 7.3.1 Scanning Tunnelling Microscopy

Upon dosing *p*-TPN on Au(111) at room temperature, the highly mobile molecules diffuse rapidly across the surface, which precludes the imaging of molecular features in room temperature STM, seen in Figure 7.3. This high mobility of the molecules agrees with previously reported results from Schlickum *et al.*<sup>27</sup>.

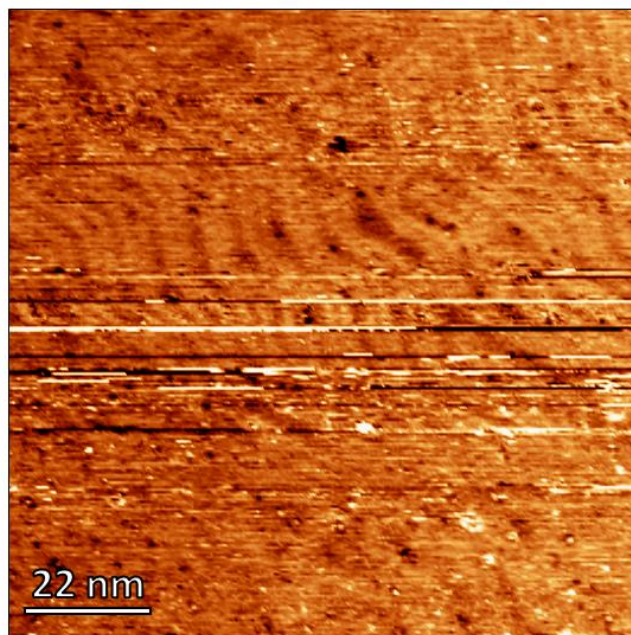


Figure 7.3 *p*-TPN dosed at 190 °C on Au(111) at room temperature. The Au(111) herringbone reconstruction is visible underneath the mobile *p*-TPN molecules. (1 V, 0.4 nA)

Dosing chromium hexacarbonyl, a volatile solid, onto Au(111) after the surface has been exposed to *p*-TPN results in the formation of an ordered arrangement of molecular features, seen in Figure 7.4. The Au(111) (22 × √3) herringbone reconstruction remains visible underneath the organometallic network indicating a weak interaction of the molecular layer with the Au surface such that the reconstruction is not lifted.

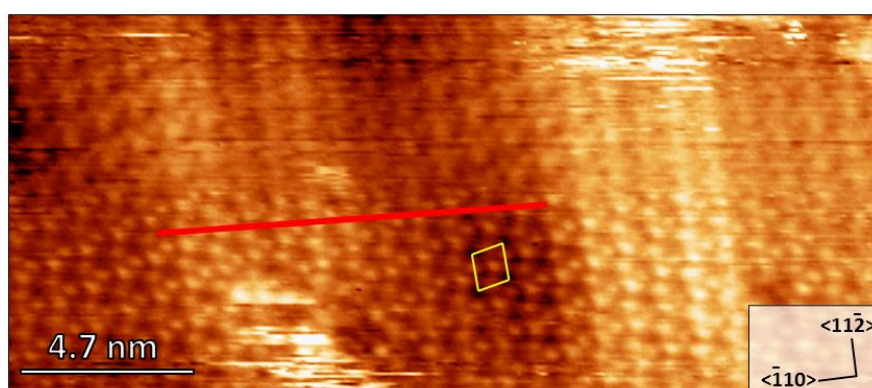


Figure 7.4 MOCN formed after room temperature dosing of  $\text{Cr}(\text{CO})_6$  on the room temperature Au(111) surface that has previously been exposed to *p*-TPN. The sample was then annealed at 50 °C and allowed to cool to room temperature before scanning. The yellow box indicates the unit cell. The red line is the distance between the herringbone reconstruction of 10.5 nm. No drift correction has been applied. (0.8 V, 0.2 nA)

The herringbone reconstruction does not affect the domain structure of the MOCN. The dimensions and directions of the unit cell are consistent with the MOCN of a commensurate structure of  $(2\sqrt{3} \times 2\sqrt{3})R30^\circ$ . This gives an overall coverage of  $1/12$  ML, where 1 ML is one adlayer molecule per surface Au atom. The MOCN forms in all three symmetry equivalent rotational domains as is expected for a surface with 3-fold symmetry, seen in Figure 7.5.

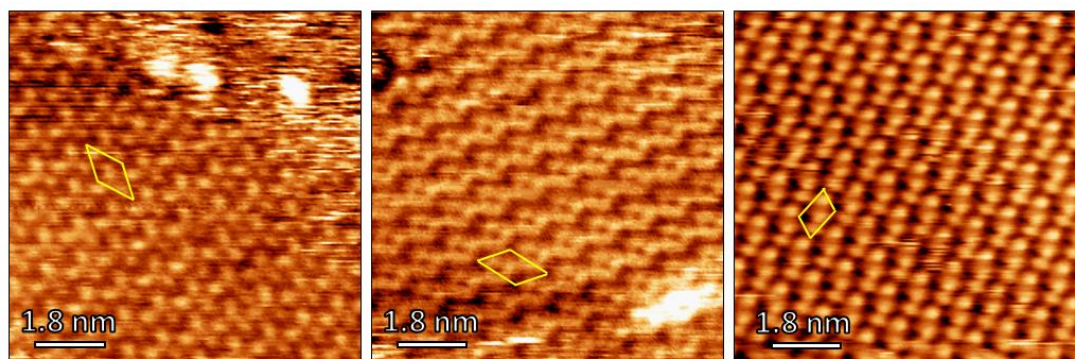


Figure 7.5 The three rotation symmetrical domains of the MOCN. The identical unit cells have been outlined in yellow. No drift correction was performed. (left to right: 0.4 V, 0.08 nA; 0.2 V, 0.08 nA; 0.5 V, 0.15 nA) The sample was flash annealed to 50 °C, 70 °C and 100 °C (left to right) and allowed to cool to room temperature before scanning.

Dosing  $\text{Cr}(\text{CO})_6$  alone on the surface led to no features seen in the STM, even at doses larger than 9400 L. The preferred location for Cr adsorption, if all the CO were removed upon impact, would be the herringbone reconstruction elbows, which are the highest energy sites on the Au(111) surface.<sup>28</sup> However, if only a few of the CO moieties are removed from  $\text{Cr}(\text{CO})_6$  upon deposition, the preferred binding site might be different. In order to probe the surface for any CO, which would indicate  $\text{Cr}(\text{CO})_x$  because CO does not adsorb alone on Au(111), RAIRS experiments were performed, seen in Section 7.3.2.

Comparing the packing density of this network to the packing density previously reported of *p*-TPN alone on the surface there is a significant difference. In the high coverage *p*-TPN packing from Schlickum *et al.*<sup>27</sup> the packing density is calculated at  $5.89 \times 10^{13}$  molecules  $\text{cm}^{-2}$ . The MOCN observed in these experiments has a nearly 97% denser structure at  $1.16 \times 10^{14}$  molecules  $\text{cm}^{-2}$ . In the study by Schlickum *et al.* molecular ordering of the *p*-TPN was only observed at room temperature when the

dosing levels were very high, which was not performed in these experiments. The drastic increase of packing density when the addition of the Cr is added to the system, compared to the previously reported molecule-only structure, indicates the Cr acts as a stabiliser to allow the molecules to adopt a more compact structure. The Cr coverage within the MOCN structure is 0.08 ML, assuming one Cr per *p*-TPN molecule in the unit cell.

The MOCN stability was tested by heating the sample up to the desired annealing temperature, letting it cool back to room temperature and imaging again. The MOCN structure remains stable until temperatures of 150 °C. At this temperature there are smaller areas of order and larger areas of mobile molecules moving across the surface. The images with the best resolution were found after the heating the sample at 100 °C. This may be because the molecules not participating in the MOCN formation had fully desorbed from the Au(111) surface by this point, or it could be the imaging conditions used, which are slightly different than that after other annealing treatments. Figure 7.6 shows the STM scans after annealing at 50 to 150 °C.

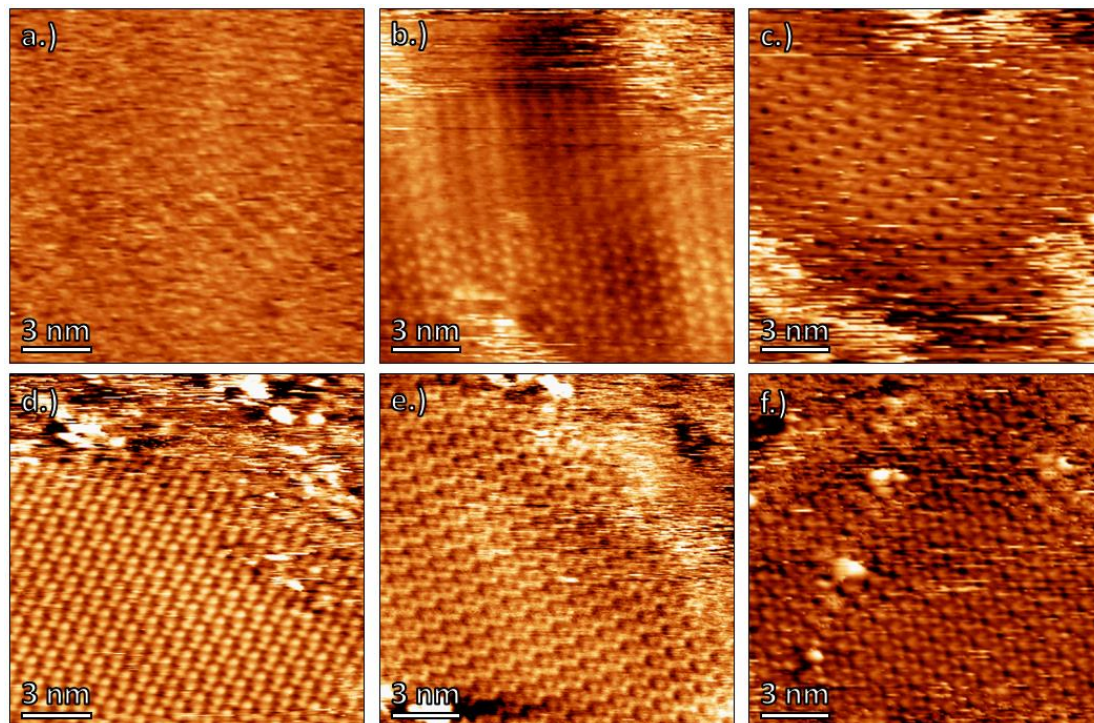


Figure 7.6 STM scans after annealing to (a.) no anneal (0.2 V, 0.25 nA); (b.) 50 °C (0.8 V, 0.2 nA); (c.) 70 °C (0.5 V, 0.2 nA); (d.) 100 °C (0.5 V, 0.15 nA); (e.) 120 °C (0.3 V, 0.08 nA); (f.) 150 °C (0.4 V, 0.2 nA).

### 7.3.2 Reflection Absorption Infrared Spectroscopy

RAIRS experiments were attempted to determine the amount and orientation of the dosed molecules on Au(111). Dosing  $\text{Cr}(\text{CO})_6$  on clean Au(111) shows no CO peaks. The sticking probabilities of metal carbonyls at the dosing temperature of 20 °C have been shown to be very low in the case of similar metal carbonyls like  $\text{Mo}(\text{CO})_6$  on Ni(111)<sup>29</sup> and is likely the case when dosing chromium hexacarbonyl on clean Au(111). Figure 7.7 shows the RAIR spectrum. The CO vibration should come between 1800 to 2100  $\text{cm}^{-1}$ . The large absorption band at 3000-3500  $\text{cm}^{-1}$  is caused by ice adsorption on the MCT detector which is cooled by liquid nitrogen.

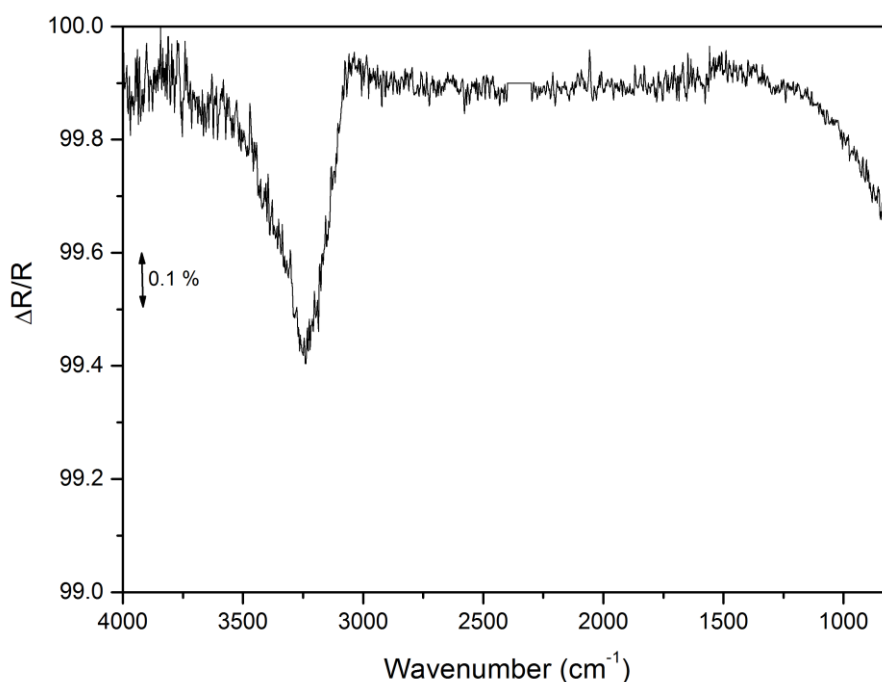


Figure 7.7 RAIR spectrum showing no CO on the surface after dosing  $\text{Cr}(\text{CO})_6$ .

Because the RAIR spectra are not able to confirm the presence of Cr within the system because no CO was detected, it was decided to try HREELS experiments, which can detect vibrational modes at much lower wavenumbers. This makes it possible to observe ligand to metal bonds in some cases.

### 7.3.3 High Resolution Electron Energy Loss Spectroscopy

Figure 7.8 shows the HREEL spectra difference between only the molecular dosing of *p*-TPN on the Au(111) surface and the dosing of the MOCN, by first dosing *p*-TPN then Cr(CO)<sub>6</sub>, on the surface.

When *p*-TPN is dosed alone on the room temperature surface, a broad peak is seen around 850 cm<sup>-1</sup> indicating multiple C-H wagging modes of the phenyl rings. The broadness of the peak likely indicates a range of molecular orientations on the surface because if the molecule is randomly oriented on the surface many vibrational modes would be apparent. The variety in dihedral angle of the phenyl rings on the surface along with the non-equivalent C-H environments lead to the different vibrations, and because they are all in a similar region it is observed as an overall broadening in the spectrum with two distinct maxima around 820 and 910 cm<sup>-1</sup>. This double feature remains throughout the annealing of the *p*-TPN, however the overall intensity of the two peaks switch after annealing to 150 °C. This likely indicates an overall change in the molecular orientation on the surface around the desorption temperature, as the peaks at the next higher annealing temperature of 180 °C are greatly reduced. An additional experiment with lower coverages of *p*-TPN, determined by dosing time and diminished peak intensities, show similar HREEL spectra, but the features disappear at lower temperatures. This indicates that the desorption of *p*-TPN from Au(111) likely follows zero order kinetics.

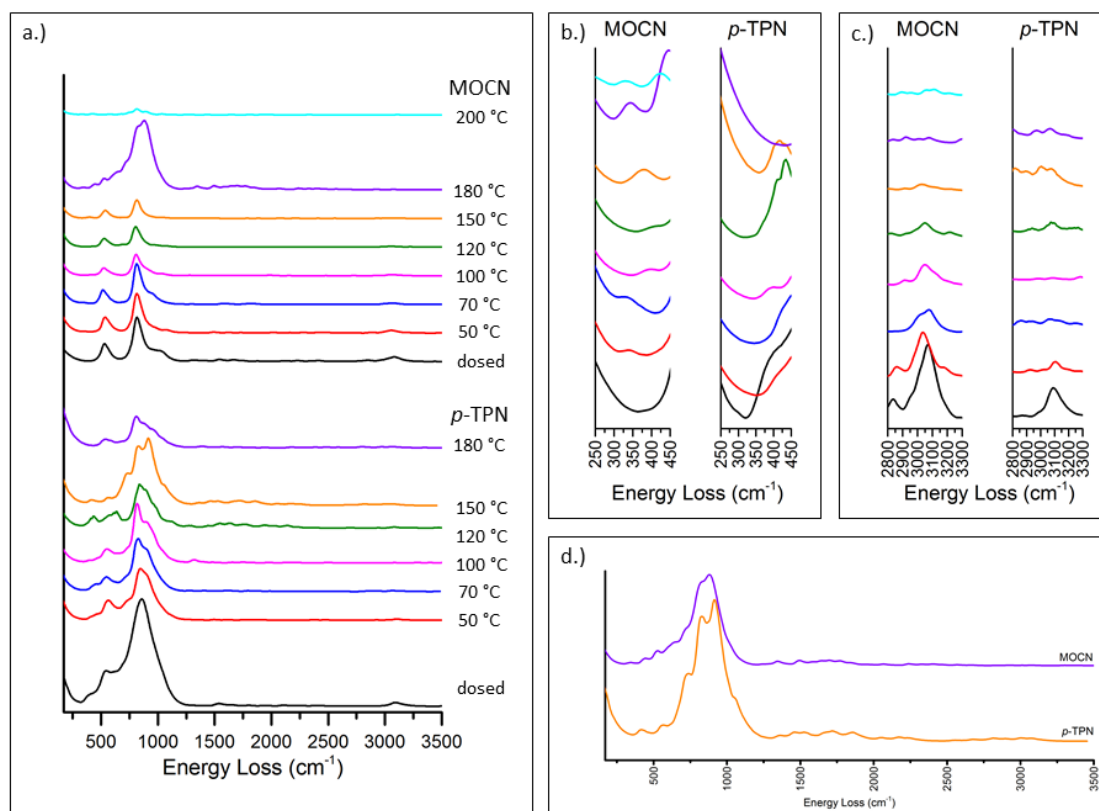


Figure 7.8 HREEL spectra of (a.) dosed *p*-TPN only (bottom) and *p*-TPN and  $\text{Cr}(\text{CO})_6$  (top) and the subsequent dosing treatments. (b.) Enlarged 250  $\text{cm}^{-1}$  to 450  $\text{cm}^{-1}$  range. (c.) Enlarged 2800  $\text{cm}^{-1}$  to 3300  $\text{cm}^{-1}$  range. (d.) Comparison of the two systems before the major desorption event (150 °C for *p*-TPN and 180 °C for MOCN).

The small peak around 3100  $\text{cm}^{-1}$  indicates C-H in-plane stretching, but this peak diminishes upon annealing. Molecules which have dipole moments parallel to the surface do not show up in HREELS due to surface selection rules. For *p*-TPN lying flat on the Au(111) surface, in-plane stretching in the 3100  $\text{cm}^{-1}$  region would be weak. This indicates upon dosing some molecules may be in more upright positions on the surface and upon annealing some molecules desorb and the molecules left on the surface can adopt a flatter orientation.

A significant difference in the spectra is seen when dosing  $\text{Cr}(\text{CO})_6$  after *p*-TPN is on the surface while keeping the Au(111) crystal at room temperature throughout both dosing processes. Two major peaks are observed; one at 540  $\text{cm}^{-1}$  and one at 820  $\text{cm}^{-1}$ . The large peak at 820  $\text{cm}^{-1}$  has a shoulder at higher energy loss. These two peaks are in a similar region to the broad peak seen in the *p*-TPN spectra, but are much more well-defined. This indicates the molecules are likely forced into a single bonding orientation

on the surface due to the coordination with the Cr nodes. The C-H stretching in the  $3100\text{ cm}^{-1}$  region is more pronounced in the MOCN spectra compared to the *p*-TPN only spectra, and does not diminish upon annealing treatments. This suggests the molecules are stable in their initial dosing orientation, which would indicate the MOCN structure is formed and remains the same through annealing treatments, which agrees strongly with the STM experiments. Additionally, there is a small peak observed between  $350$  and  $400\text{ cm}^{-1}$ , seen in Figure 7.8b, which may indicate  $\pi$ -bonding of the nitrile to metal. This bond is likely to be near-parallel to the surface, thus dipole selection rules minimise the intensity of the peak. It is interesting to note the small shift of peak seen in this region occurs after the annealing treatment at  $100\text{ }^{\circ}\text{C}$ , which is similar to the conditions used in the STM to obtain the highest resolution images. This may correlate to a slightly different nitrile bond orientation.

Interestingly, no nitrile stretch vibration is found in any spectrum, which is calculated to be around  $2300\text{ cm}^{-1}$  for *p*-TPN in the gas phase, seen in Figure 7.9. Even when scanning in the off-specular position no nitrile vibrations are detected. This is likely due to the low polarizability of the CN group, the parallel nature of the bond on the surface and the lack of an out of plane dipole moment in both experiments with and without the Cr nodes. These similar features have been previously published elsewhere.<sup>30-31</sup>

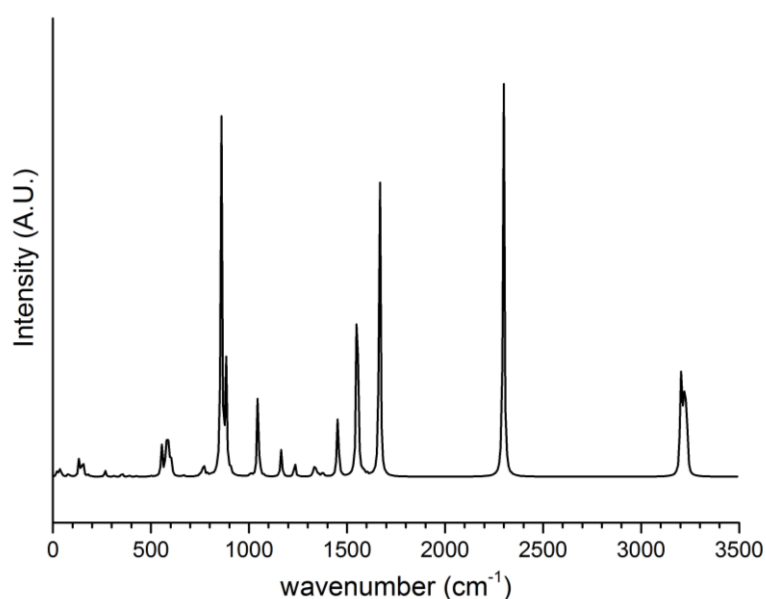


Figure 7.9 Calculated IR spectra of *p*-TPN in the gas phase. Spectra was calculated with Gaussian, using B3LYP with a basis set of 6-31G.

The MOCN HREEL spectrum at 180 °C is very similar to the *p*-TPN HREEL spectrum at 150 °C, seen in Figure 7.8d. There is a large intensity change around 850  $\text{cm}^{-1}$ , indicating a large molecular orientation change before the desorption event occurs. The fact that the two spectra are so similar suggests that some of the nitrile to Cr  $\pi$  bonds are broken during the flash annealing treatment at 180 °C. Additionally, the final annealing treatment at 200 °C shows a large decrease in all peak intensities, indicating a large desorption event occurred on the surface around this temperature. This suggests the desorption event is similar in both cases regardless of the Cr nodes being deposited on the surface.

When repeating the experiment with lower *p*-TPN dosing the nitrile to metal bond region at 350 to 400  $\text{cm}^{-1}$  is significantly more intense, while the peaks at 540 and 820  $\text{cm}^{-1}$  are diminished; a comparison between high and low *p*-TPN dosing is seen in Figure 7.10. Regardless of dosing amounts the MOCN remains on the surface until annealing treatments of 150 °C.

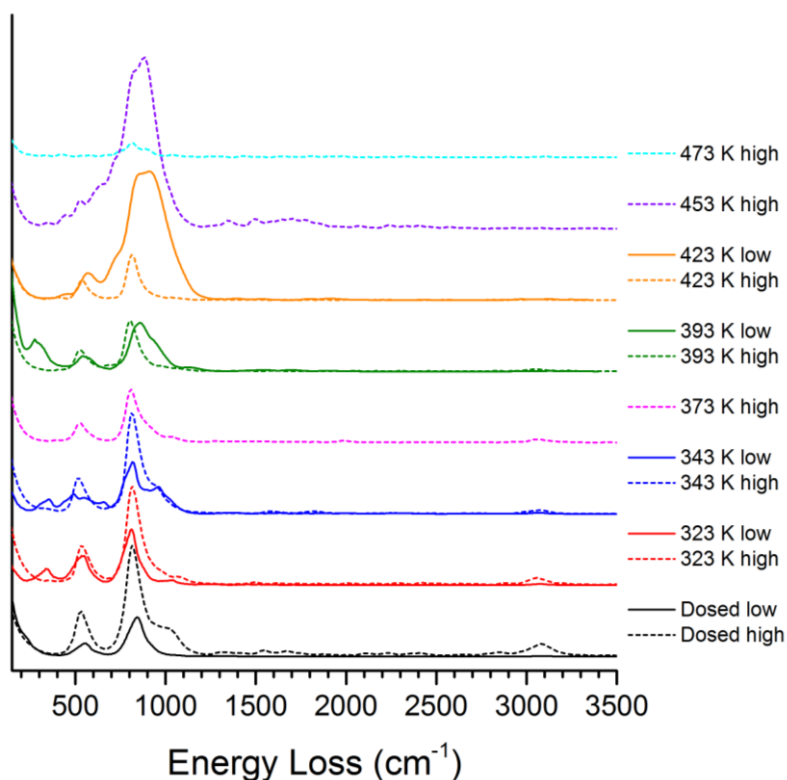


Figure 7.10 A comparison of the MOCN HREELS with a lower dose of *p*-TPN compared to the higher dose seen in Figure 7.8. The metal-nitrile bonding region is more intense with the lower *p*-TPN dose.

When  $\text{Cr}(\text{CO})_6$  is dosed alone on the surface of Au(111) no  $\text{Cr}(\text{CO})_x$  is detected, in agreement with experiments performed in STM and RAIRS. This indicates any chromium that sticks to the clean Au(111) surface undergoes carbonyl dissociation either upon or before hitting the surface. If the Cr atoms were to stick on the surface they would not be easily identifiable by HREELS because the Cr-Au phonon vibration is at low wavenumber and would not be recovered from the large elastic peak. However, combining the results from STM, RAIRS and HREELS it is likely that the sticking probability of  $\text{Cr}(\text{CO})_6$  is so low that even at large doses there is no Cr on the surface. Dosing the *p*-TPN first increases the sticking probability of the Cr when compared to clean Au(111). The network, once created with *p*-TPN and Cr, does not appear to reorder into any other phase, which shows that once the high density structure is formed it is robust throughout annealing treatments. A summary of the peak identification at each annealing treatment is seen in Table 7.1.

Table 7.1 The major vibrations assignments for (a.) *p*-TPN only on Au(111) and (b.) the MOCN on Au(111) after anneal treatments at varying temperatures. The energy loss peak is accurate to  $\pm 25 \text{ cm}^{-1}$ .  $\rho$  = rock,  $\nu$  = stretch,  $\omega$  = wag,  $\delta$  = bend,  $\tau$  = twist,  $\pi$  =  $\pi$ -bond, phen= phenyl rings

Peak ( $\text{cm}^{-1}$ )	20		50		70		100		120		150		180		200		( $^{\circ}\text{C}$ )		
	a	b	a	b	a	b	a	b	a	b	a	b	a	b	a	b	Assignment		
360		X		X		X		X		X		X		X	-	X	$\nu(\text{M-NC})$		
430	X		X		X		X		X		X		X		X	-	X	$\omega(\text{phen})$	
540	X	X	X	X	X	X	X	X	X	X	X	X	X	X	-			$\tau(\text{NC-C})$	
640									X	X				X	-			$\delta_{\text{ip}}(\text{phen})$	
730											X			X	-	X		$\delta_{\text{as}}(\text{C-H})$	
820	X	X	X	X	X	X	X	X	X	X	X	X	X	X	X	-	X		$\omega_{\text{s}}(\text{C-H})$
910			X		X	X	X		X		X		X	X	-			$\omega_{\text{s}}(\text{C-H})$	
1030		X		X				X							-			$\tau(\text{phen})$	
1050											X				-	X		$\omega_{\text{as}}(\text{C-H})$	
1120									X						-			$\delta_{\text{ip}}: \text{C-H}$	
1340							X							X	-			$\nu_{\text{as}}(\text{phen})$	
1520	X													X	-			$\rho_{\text{s}}(\text{phen})$	
3080	X	X	X	X		X		X		X					-			$\nu: \text{C-H}$	

### 7.3.4 Density Functional Theory Calculations

Density functional theory (DFT) calculations, performed by Dr. Herbert Früchtl, were used to determine the molecular network structures concurrently with the experimental data gathered. Starting with the Cr in the hollow site of the Au(111) surface, energy minimization occurs for the *p*-TPN when the nitrile undergoes  $\pi$  bonding with the Cr atom, seen in Figure 7.11. This is a unique bonding configuration, which has not previously been reported on surface structures. However, a small collection of organometallic complexes have been previously reported with this bond type.<sup>32-35</sup> Due to the nature of the close-packing of *p*-TPN on the surface, the position of the nitrile bond could be parallel to the chromium metal orbital available for binding, which could force the  $\pi$ -bonding to occur.<sup>36</sup> The perpendicular orientation of the metal to nitrile bond allows for the maximum overlap of the  $\pi$ -bonds to associate with the metal node.<sup>34</sup> The orientation of the nitrile to metal bond causes some steric hindrance from the three phenyl rings. The rings are at an energy minimum when they orient themselves by twisting in order to allow for the nitrile to Cr bond to be parallel to the surface, seen in the top image of Figure 7.11.

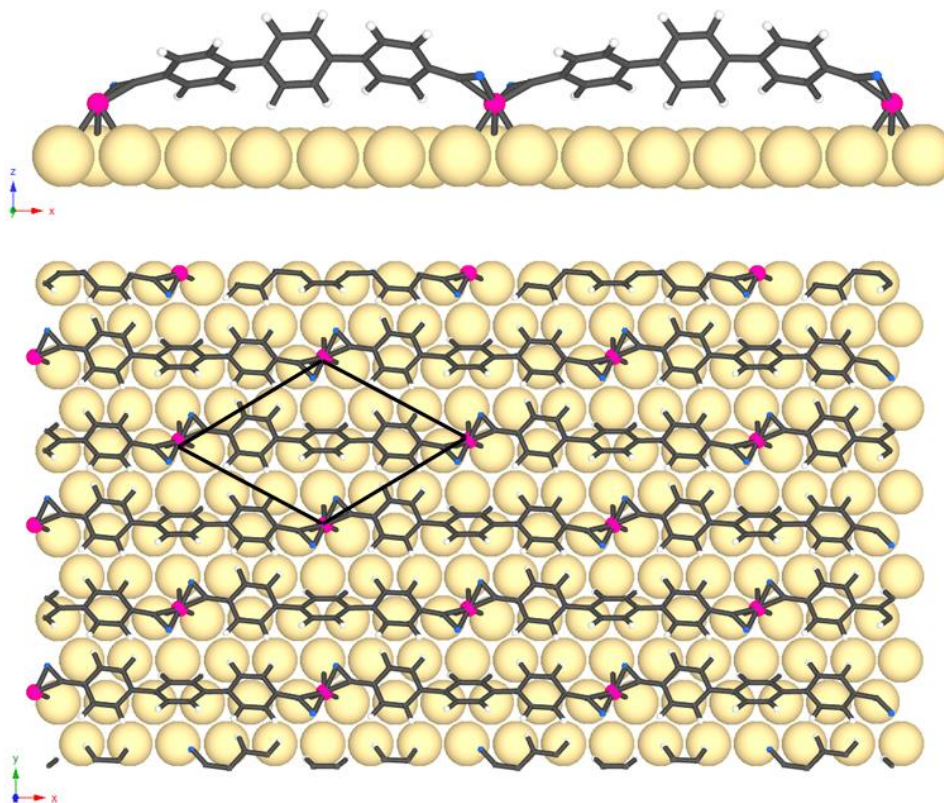


Figure 7.11 Calculated structure of the MOCN. The chromium atom sits in a fcc hollow site, while the *p*-TPN bind through a  $\pi$ -interaction of the nitrile to metal. Cr pink, N blue, C dark gray. The unit cell is outlined in black.

Simulating constant height STM images from the calculated MOCN structure yields a strikingly similar result to the experimental constant current STM images. This indicates the DFT model as a good fit with the experimental data, as seen in Figure 7.12. The colour scheme has been changed to better show the molecular features.

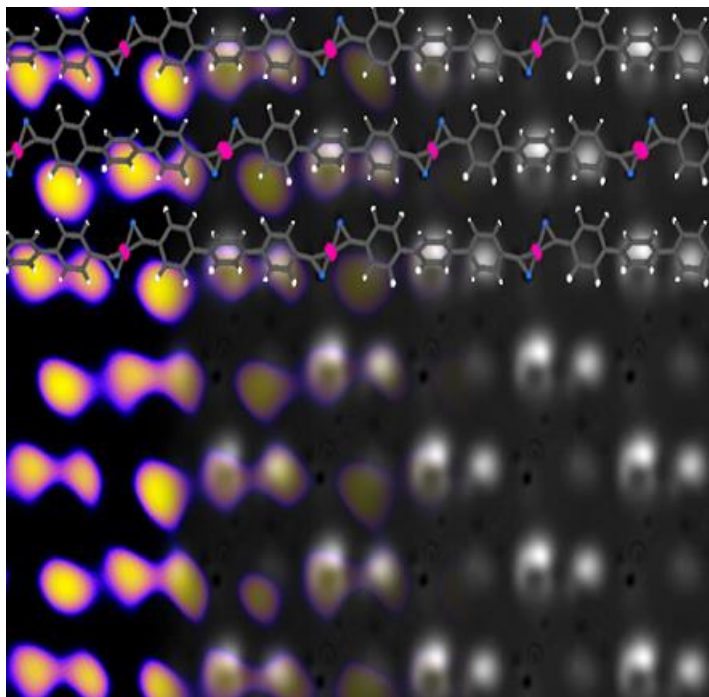


Figure 7.12 Overlaid image of the calculated MOCN structure on a constant height simulated STM image and an experimental constant current STM images. (0.3 V, 0.08 nA)

When the *p*-TPN molecules are placed in the more common CN-Cr end on binding orientation the terphenyl molecules drastically bow when the unit cell is fixed to the experimentally determined size. Chemically and physically the phenyl rings are most energetically favoured when they lie flat on the surface due to the  $\pi$  interactions from the phenyl rings with the surface. It is not likely that the end on nitrile to Cr bond would be preferable for this reason, as seen in the calculation in Figure 7.13a. Additionally, if this end-on configuration were the experimental structure the two phenyl rings with near perpendicular orientation with respect to the surface would show large CH stretches in the HREELS, which do not appear. This end-on configuration is nearly 80 kJ mol<sup>-1</sup> less stable when compared to the more likely  $\pi$ -bonded CN-Cr structure seen in Figure 7.13b.

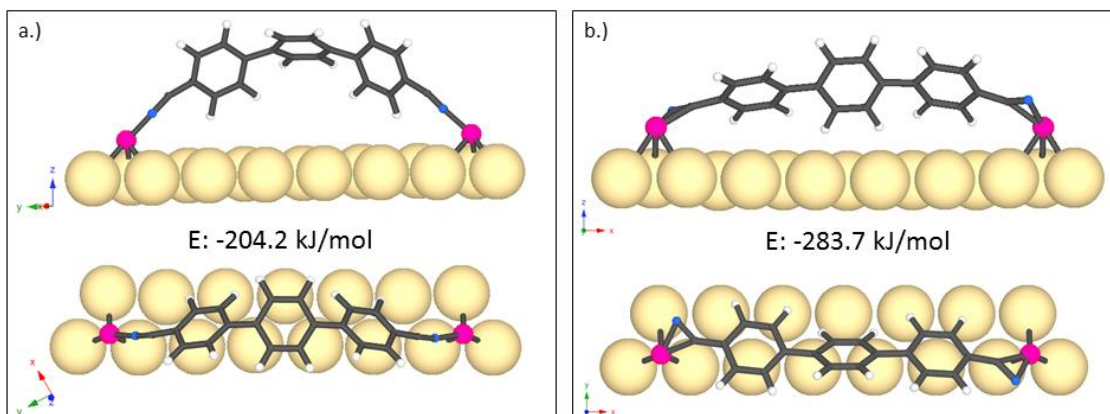


Figure 7.13 Calculated structures of possible MOCNs with experimentally determined unit cell size. (a.) End-on nitrile coordination to Cr and (b.) most reasonable structure with pi-bonded CN-Cr that agrees with experimental STM and HREELS collected.

Placing the *p*-TPN alone on the Au(111) surface led to the structure seen in Figure 7.14. In this structure without Cr the *p*-TPN molecules tilt up as to minimise the interaction with the nitrile functionality on the neighbouring molecule. The STM experimental results saw no organisation of *p*-TPN on Au(111) at room temperature, indicating it is highly mobile on the surface. Additionally, if the structure observed were to be the one without Cr in the system there would be a large C≡N stretch in HREELS because the nitrile dipole moment would have a perpendicular component relative to the surface, thus being observable with respect to the surface selection rules.

Additionally, comparing the stability of the *p*-TPN only structure on Au(111) to the MOCN structure we see a difference of 77 kJ mol<sup>-1</sup>. The Cr on the surface helps to stabilise the structure. This agrees with the HREELS results where the MOCN is able to withstand higher annealing temperatures compared to the *p*-TPN only experiments. A driving force to the formation of this stable MOCN is because the surface is able to accommodate almost twice as many molecules when the Cr is on the surface compared to the previously reported structure<sup>27</sup> with only *p*-TPN.

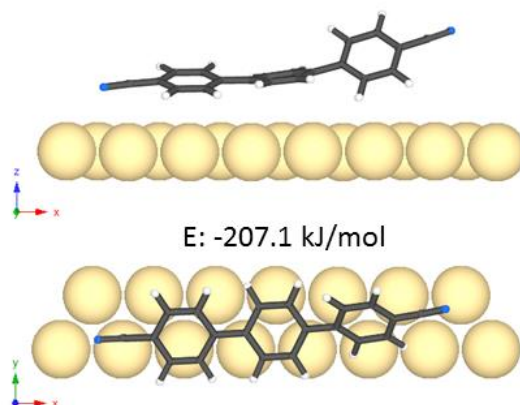


Figure 7.14 DFT calculation of *p*-TPN only on the surface of Au(111) with the experimentally determined unit cell constraint to the calculation.

Depending on imaging conditions, the MOCN can be viewed in two ways from the experimental STM images. Figure 7.15a shows the DFT calculated model overlaid on an STM image where the metal node appears as a dark area, as has been seen in other systems.<sup>27, 37</sup> This is the most commonly seen condition. Where no metal node is seen each phenyl ring appears as a bright feature with a dark feature for the metal node and nitrile coordination. However, in other imaging conditions the end phenyl rings appear as large bright features and the metal to nitrile coordination appears as a small bright feature, seen in Figure 7.15b. The packing density and the overall MOCN structure are identical in these two cases. The difference lies in the STM tip probing different orbitals.

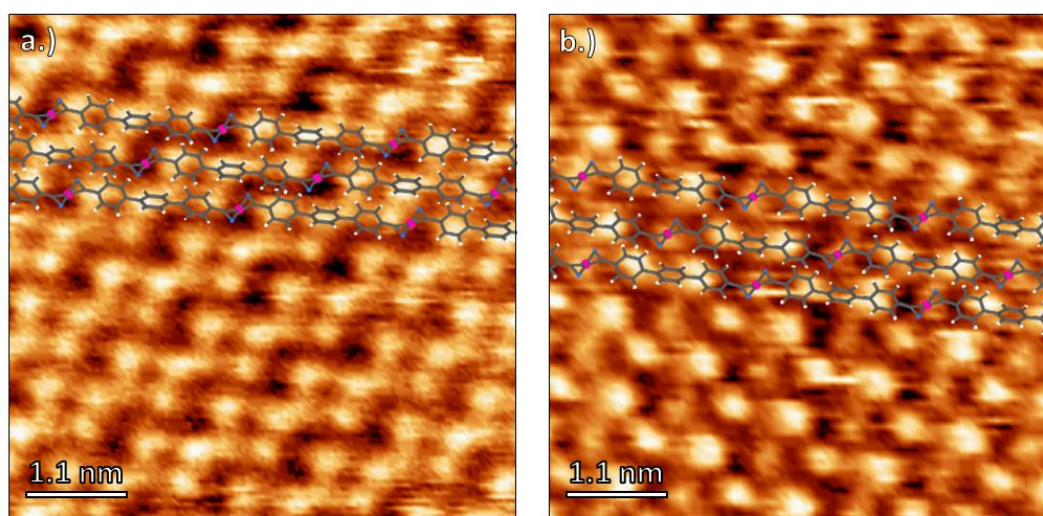


Figure 7.15 DFT model on top of STM images. a.) The most common imaging condition where the three phenyl rings show as bright features, and the dark feature corresponds to the metal and nitrile bonding

(0.3 V, 0.08 nA). Image taken after allowing to cool to room temperature after flash annealing at 100 °C and b.) the end phenyl rings show as large bright features with a smaller bright feature corresponding to the metal to nitrile bonding (0.1 V, 0.08 nA). Image taken after allowing to cool to room temperature after flash annealing at 120 °C. For the overlaid DFT model: Cr pink, N blue, C dark grey and H light grey.

## 7.4 Conclusions and Outlook

A novel MOCN was synthesised using *p*-TPN and Cr by using a metal carbonyl as the metal source. The *p*-TPN deposition on the Au(111) surface increases the Cr sticking probability, which comes from the dissociation of carbonyls from Cr(CO)<sub>6</sub>. The 1D MOCN chains made by the nitrile to Cr bond have a unique  $\pi$ -bonding interaction, which has not previously been observed on a surface. The bonding type has been confirmed using HREELS and DFT. The MOCN decomposes and/or desorbs from the surface at temperatures between 150 °C to 180 °C. This route to incorporate high boiling point metals by sublimation of volatile organometallics has potential to be used in a variety of systems.

Although a porous MOCN was not achieved in this work, an interesting bonding configuration and proof that metal can be dosed and used this way in MOCN creation was achieved. To further this project, a porous MOCN may be possible with more modification of linker and metal dosings. At a specific concentration of metal and/or *p*-TPN there may form a porous network.

An alternative extension of this project could come by functionalising the *p*-TPN molecule. This may lead towards different MOCN formations, and could also be of interest to elucidate if another functional group could form a better bond with the metal carbonyl metal. For instance, functionalising the middle phenyl ring with amine groups or nitro groups could be a good start to changing the functionality and possibly coordination of the MOCN.

## 7.5 References

1. Anderson, A. E.; Grillo, F.; Larrea, C. R.; Seljamäe-Green, R. T.; Früchtl, H. A.; Baddeley, C. J., Metallosupramolecular Assembly of Cr and p-Terphenyldinitrile by Dissociation of Metal Carbonyls on Au(111). *J. Phys. Chem. C* **2016**, *120*, 1049-1055.
2. Mas-Ballesté, R.; Gómez-Herrero, J.; Zamora, F., One-Dimensional Coordination Polymers on Surfaces: Towards Single Molecule Devices. *Chem. Soc. Rev.* **2010**, *39*, 4220-4233.
3. Decker, R.; Schlickum, U.; Klappenberger, F.; Zoppellaro, G.; Klyatskaya, S.; Ruben, M.; Barth, J. V.; Brune, H., Using Metal-Organic Templates to Steer the Growth of Fe and Co Nanoclusters. *Appl. Phys. Lett.* **2008**, *93*, 243102.
4. Tait, S. L.; Wang, Y.; Costantini, G.; Lin, N.; Baraldi, A.; Esch, F.; Petaccia, L.; Lizzit, S.; Kern, K., Metal-Organic Coordination Interaction in Fe-Terephthalic Acid Networks on Cu(100). *J. Am. Chem. Soc.* **2008**, *130*, 2108-2113.
5. Shi, Z.; Lin, N., Structural and Chemical Control in Assembly of Multicomponent Metal-Organic Coordination Networks on a Surface. *J. Am. Chem. Soc.* **2010**, *132*, 10756-10761.
6. Stepanow, S.; Lingenfelder, M.; Dmitriev, A.; Spillmann, H.; Delvigne, E.; Lin, N.; Deng, X.; Cai, C.; Barth, J. V.; Kern, K., Steering Molecular Organization and Host-Guest Interactions Using Two-Dimensional Nanoporous Coordination Systems. *Nature materials* **2004**, *3*, 229-233.
7. Trant, A. G.; Jones, T. E.; Noakes, T. C. Q.; Bailey, P.; Baddeley, C. J., Adsorption of (S)-Glutamic Acid Induces Segregation of Ni at Bimetallic Au/Ni Surfaces. *Surf. Sci.* **2010**, *604*, 300-307.
8. Wilson, K. E.; Baddeley, C. J., Chiral Assemblies of Nickel Lysinate via the Corrosive Adsorption of (S)-Lysine on Ni/Au{111}. *Surf. Sci.* **2014**, *629*, 102-107.
9. Grumelli, D.; Wurster, B.; Stepanow, S.; Kern, K., Bio-Inspired Nanocatalysts for the Oxygen Reduction Reaction. *Nat. Commun.* **2013**, *4*, 2904.
10. Schlickum, U.; Decker, R.; Klappenberger, F.; Zopellaro, G.; Klyatskaya, S.; Ruben, M.; Silanes, I.; Arnau, A.; Kern, K.; Brune, H.; Barth, J. V., Metal-Organic Honeycomb Nanomeshes with Tunable Cavity Size. *Nano Lett.* **2007**, *7*, 3813-3817.
11. Kühne, D.; Klappenberger, F.; Decker, R.; Schlickum, U.; Brune, H.; Klyatskaya, S.; Ruben, M.; Barth, J. V., High-Quality 2d Metal-Organic Coordination Network Providing Giant Cavities within Mesoscale Domains. *J. Chem. Soc., Chem. Commun.* **2009**, *131*, 3881-3883.
12. Ćija, D.; Urgel, J. I.; Papageorgiou, A. C.; Joshi, S.; Auwärter, W.; Seitsonen, A. P.; Klyatskaya, S.; Ruben, M.; Fischer, S.; Vijayaraghavan, S.; Reichert, J.; Barth, J. V., Five-Vertex Archimedean Surface Tessellation by Lanthanide-Directed Molecular Self-Assembly. *PNAS* **2013**, *110*, 6678-6681.
13. Phillips, J.; Dumesic, J. A., Production of Supported Metal Catalysts by the Decomposition of Metal Carbonyls (Review). *Appl. Catal.* **1984**, 1-30.
14. Xu, M.; Zaera, F., Mechanistic Studies of the Thermal Decomposition of Metal Carbonyls on Ni(100) Surfaces in Connection with Chemical Vapor Deposition Processes. *J. Vac. Sci. Technol. A* **1996**, *14*, 415.

15. Fillman, L. M.; Tang, S. C., Thermal Decomposition of Metal Carbonyls: A Thermogravimetry-Mass Spectrometry Study. *Thermochim. Acta* **1984**, *75*, 71-84.
16. Cook, J. C.; McCash, E. M., Physisorption of Metal Carbonyls on Cu(100). *Surf. Sci.* **1996**, *364*, L605-L611.
17. Clowes, S. K.; Seddon, E. A.; McCash, E. M., The Adsorption and Decomposition of Chromium Hexacarbonyl on Pd(100). *Surf. Sci.* **2000**, *464*, L667-L672.
18. Paszti, Z.; Hakkel, O.; Keszthelyi, T.; Berko, A.; Balazs, N.; Bako, I.; Gucci, L., Interaction of Carbon Monoxide with Au(111) Modified by Ion Bombardment: A Surface Spectroscopy Study under Elevated Pressure. *Langmuir : the ACS journal of surfaces and colloids* **2010**, *26*, 16312-16324.
19. Mandali, P. K.; Chand, D. K., Palladium Nanoparticles Catalyzed Suzuki Cross-Coupling Reactions in Ambient Conditions. *Chem. Commun.* **2013**, *31*, 16-20.
20. Frederick, B. G.; Jones, T. S.; Pudney, P. D. A.; Richardson, N. V., HREELS and RAIRS a Complete Vibrational Study of the Surface Benzoate Species Adsorbed on Copper. *J. Electron. Spectrosc. Relat. Phenom.* **1993**, *64-65*, 115-122.
21. Frederick, B. G.; Richardson, N. V., Comment on "Ultrahigh Resolution Electron Energy Loss Spectroscopy". *Phys. Rev. Lett.* **1994**, *73*, 772-772.
22. Kresse, G.; Hafner, J., Ab Initio Molecular Dynamics for Liquid Metals. *Phys. Rev. B* **1993**, *47*, 558-561.
23. Kresse, G.; Furthmüller, J., Efficiency of Ab-Initio Total Energy Calculations for Metals and Semiconductors Using a Plane-Wave Basis Set. *Comput. Mater. Sci.* **1996**, *6*, 15-50.
24. Perdew, J. P.; Burke, K.; Ernzerhof, M., Generalized Gradient Approximation Made Simple. *Phys. Rev. Lett.* **1996**, *77*, 3865-3868.
25. Grimme, S.; Antony, J.; Ehrlich, S.; Krieg, H., A Consistent and Accurate Ab Initio Parametrization of Density Functional Dispersion Correction (Dft-D) for the 94 Elements H-Pu. *J. Chem. Phys.* **2010**, *132*, 154104-1-154104-19.
26. Grimme, S.; Ehrlich, S.; Goerigk, L., Effect of the Damping Function in Dispersion Corrected Density Functional Theory. *J. Comp. Chem.* **2011**, *32*, 1456-1465.
27. Schlickum, U.; Klappenberger, F.; Decker, R.; Zopellaro, G.; Klyatskaya, S.; Ruben, M.; Kern, K.; Brune, H.; Barth, J. V., Surface-Confined Metal-Organic Nanostructures from Co-Directed Assembly of Linear Terphenyl-Dicarbonitrile Linkers on Ag(111). *J. Phys. Chem. C* **2010**, *114*, 15602-15606.
28. Rai, A.; Nayak, J.; Barman, S. R., Chromium Nano-Islands on Au(111). *e-J. Surf. Sci. Nanotech.* **2014**, *12*, 49-52.
29. Jones, T. E.; Noakes, T. C. Q.; Bailey, P.; Baddeley, C. J., Structural and Compositional Analysis of Two Ordered near-Surface Alloys Produced by Adsorption and Thermal Decomposition of Mo(CO)<sub>6</sub> on Ni{111}. *Surf. Sci.* **2002**, *523*, 12-20.
30. Politano, A.; Chiarello, G.; Benedek, G.; Chulkov, E. V.; Echenique, P. M., Vibrational Spectroscopy and Theory of Alkali Metal Adsorption and Co-Adsorption on Single-Crystal Surfaces. *Surf. Sci. Rep.* **2013**, *68*, 305-389.
31. Dubey, G.; Rosei, F.; Lopinski, G. P., Highly Sensitive Electrical Detection of TCNE on Chemically Passivated Silicon-on-Insulator. *Chem. Commun.* **2011**, *47*, 10593-10595.

32. Thomas, S.; Tiekink, E. R. T.; Young, C. G., Synthesis, Structures, and Reactivity of Four-Electron-Donor  $\eta^2$ -Organonitrile, Carbonyl Oxo, and Carbonyl Thio Complexes of Tungsten. *Organometallics* **1996**, *15*, 2428-2430.
33. Storhoff, B.; Infante, A. J., Rhenium(I) Complexes of (O-Cyanophenyl)Diphenylphosphine. *Inorg. Chem.* **1974**, *13*, 3043-3045.
34. Kiplinger, J. L.; Arif, A. M.; Richmond, T. G., Synthesis and Reactivity of Tungsten(II) Carbonyl  $\eta^2$ -Nitrile Complexes: Crystal Structure of Tetrafluoroterephthalonitrile as a Four-Electron Donor Ligand. *Chem. Commun.* **1996**, 1691-1692.
35. Cho, H.-G.; Andrews, L., Infrared Spectra and Density Functional Calculations of the  $M \leftarrow NCCCH_3$ ,  $\eta^2-M(Nc)-CH_3$ ,  $CH_3-MNC$ ,  $CH_2=M(H)NC$ , and  $CH \equiv M(H)_2NC$  Complexes Produced by Reactions of Group 6 Metal Atoms with Acetonitrile. *J. Organomet. Chem.* **2012**, *703*, 25-33.
36. Sutton, J. E.; Zink, J. I., Spectroscopic Studies of Perpendicular Nitrile-Metal Interactions. *Inorg. Chem.* **1976**, *15*, 675-678.
37. Seljamäe-Green, R. T.; Simpson, G. J.; Grillo, F.; Greenwood, J.; Francis, S. M.; Schaub, R.; Gano, J. E.; Früchtl, H. A.; Lacovig, P.; Baddeley, C. J., Formation of Bioinorganic Complexes by the Corrosive Adsorption of (S)-Proline on Ni/Au(111). *Langmuir : the ACS journal of surfaces and colloids* **2015**, *31*, 262-271.

# Chapter 8

---

## Conclusions and Outlook

## 8.1 Conclusions

Immobilising metal nanoparticles within metal-organic frameworks for applications in tandem catalysis was accomplished in this thesis in three methodologies. First, metal nanoparticle precursors were strategically deposited in the porous frameworks and then reduced to form small nanoparticles. The double solvents deposition technique provided nanoparticles around 2.7 nm in MIL-101(Cr) materials. Attempts to extend the technique to other MOF types was not successful. This was shown to be due to the lack of stability against water and heat needed to maintain the crystalline structure of the MOF throughout the deposition procedure. While most efforts were placed into Pd in MIL-101(Cr), Pt, Au and Ru were also shown to be good candidates for this deposition technique within this MOF.

Pd in MIL-101(Cr) was investigated as a multifunctional catalyst for a tandem reductive amination reaction. In this reaction at 50 °C, 1.0 wt% Pd in MIL-101(Cr) was shown to be a moderately active catalyst achieving 65% conversion after 16 hours. This catalyst achieved a selectivity of 90% to the desired secondary amine product. Upon increasing the temperature to 90 °C in order to achieve full conversion, the same catalyst demonstrated a dramatic change in selectivity. After 16 hours, the 1.0 wt% Pd in MIL-101(Cr) catalyst achieved full conversion but the selectivity was 91% to an undesired primary amine product. However, by altering the ratio of metal nanoparticle active sites to metal-organic framework active sites, the selectivity could be tuned. After optimisation of the ratio, 100% conversion and 90% selectivity to the desired secondary amine was achieved at an elevated temperature of 90 °C. Next, the series of various Pd loaded MIL-101(Cr) materials were investigated in time trials to obtain kinetic information. Using a MATLAB model with a series of ordinary differential rate equations, the experimental data was fit with kinetic parameters. It was seen that the 0.4 wt% Pd in MIL-101(Cr) was the best catalyst for the maximisation of secondary amine while also maximising activity.

Another method to forming immobilised MNP in MOF materials was by cyclically growing MOF on previously deposited Pd on SiO<sub>2</sub> spheres. The Pd deposition could be accomplished by functionalising the SiO<sub>2</sub> spheres with amine groups beforehand. At a

pH of 2 the Pd was well-dispersed on the silica. Subsequently, MIL-100(Fe) was grown on the spheres. The surface charge appeared to be the largest factor in determining MOF growth. The surface needed a large negative charge, provided by the PdCl<sub>2</sub>. When the Cl was removed during reduction and nanoparticles were formed, the MOF did not grow. Additionally, the cyclical MOF growth procedure was not possible on either the as prepared SiO<sub>2</sub> spheres or on just the functionalised SiO<sub>2</sub>-NH<sub>2</sub> spheres. However, even upon successful MOF growth, the sphere coverage remained inhomogeneous. Overall, a different route or further modification of the cyclical growth methodology should be investigated in order to achieve well-formed MOF on Pd SiO<sub>2</sub>.

The third methodology investigated to achieve immobilised MNP in MOFs was a core-shell method using colloidal nanoparticles. In this method, PVP-capped PtAg nanoparticles were synthesised in three shapes: cubes, cuboctahedra and octahedra. Next, the MOF growth conditions were optimised around the MNP by altering the concentrations of Pt to MOF metal and MOF metal to MOF linker. Successful conditions to obtain core-shell materials were found for both UiO-66 and MIL-100(Sc). The core-shell materials were tested in a catalytic tandem reductive amination. The MNP cuboctahedra@UiO-66 catalyst only achieved a conversion of 17% and a selectivity of 0% to the desired secondary amine after 16 hours. This was shown to likely be due to the diffusion limitations present in the microporous UiO-66 material. This indicates that the conversion was achieved on the surface of the core-shell material and was not able to diffuse through to react on the metal nanoparticle. The core-shell MIL-100(Sc) materials performed much more favourably. The best core-shell MIL-100(Sc) catalyst achieved 89% conversion and 89% selectivity to the desired secondary amine after 16 hours.

These methodologies towards immobilised MNP in MOFs create opportunities for selective and active catalysis. The area of multifunctional catalytic materials has been under heavy research in order to find optimum materials to perform the catalytic transformations that are needed in the modern world.

In addition to the immobilisation techniques, a metallosupramolecular assembly was elucidated on Au(111). In this work Cr and *p*-terphenyldinitrile were deposited on a

Au(111) single crystal and annealed to form one-dimensional metallosupramolecular chains under UHV conditions. The characterisation of the assembly was performed with a combination of HREELS, STM and DFT calculations. The Cr was provided for the assembly by dosing  $\text{Cr}(\text{CO})_6$ , a volatile solid. This application of dosing metal complexes with labile ligands to achieve assembly with another molecule has not previously been widely studied.

## 8.2 Outlook

The work presented shows a wide range techniques to achieve immobilised MNPs within metal-organic frameworks. More MOF types should be tried using the double solvent deposition method. For instance, MOF-808(Hf) did not work possibly because of the lack of stability towards water. However, MOF-808(Zr) was not tried, and it may be more stable. Additionally, polyoxometalates proved not to be useful for stabilisation in either the MIL-100(Sc) or the MIL-101(Cr) but may help in stabilising and adding extra acid sites within another MOF type. This may allow other MOFs to be useable in the double solvent deposition method.

The cyclical growth of MIL-100(Fe) was somewhat effective in covering Pd on  $\text{SiO}_2$  spheres. This should be investigated further to improve the coating procedure. After optimisation, many multifunctional materials could be envisaged and readily obtainable. For instance, changing the silica for other oxide materials could change the activity of the metal nanoparticles. Also, changing the metal nanoparticle type or changing the MOF type could be tried as well.

The core-shell synthesis from colloidal nanoparticles has many further projects that could be completed. As discussed, the Pt nanoshapes contained Ag after the workup procedures. Looking at the structure of the PtAg on the surface could give interesting insight into the activity of the bimetallic particles and information on the effect of Ag within the particle for shape formation. Also, methodologies into making pure Pt nanoshapes could be investigated. Using pure Pt nanoshapes in the core-shell synthesis could provide interesting shape selective catalysis when combined with the surrounding acidity provided by the MOF shell.

It was shown that two MOF types, UiO-66 and MIL-100(Sc) were optimised for core-shell formation. Extending this optimisation method to other MOF types could prove to give very stable materials with interesting MOF active sites. For instance, the highly acidic MOF-808 materials could be investigated for core-shell morphology optimisation. This MOF was shown not to be stable enough to withstand water during the double solvents deposition. However, water is not needed for the core-shell formation, and thus might provide interesting catalytic materials.



# Abbreviations

APTES	aminopropyltriethoxysilane
BDC	Terephthalic acid
BET	Brunauer, Emmett and Teller
BTC	Trimesic acid
CSD	Cambridge Structural Database
DFT	Density functional theory
DMF	N,N-Dimethylformamide
DRIFTS	Diffuse reflectance infrared Fourier transform
EDX	Energy dispersive X-ray spectroscopy
EtOH	Ethanol
FTIR	Fourier transform infrared
HREELS	High resolution electron energy loss spectroscopy
ICDD	International Centre for Diffraction Data
IR	Infrared
IUPAC	International Union of Pure and Applied Chemistry
L	Langmuir (1 second exposure at $10^{-6}$ torr)
MeOH	Methanol
MNP	Metal nanoparticle
MOCN	Metal organic coordination network
MOF	Metal organic framework
NMR	Nuclear magnetic resonance
POM	Polyoxometalate
PSS	Poly(sodium styrene sulfonate)
PTA	Phosphotungstic acid
<i>p</i> -TPN	<i>p</i> -Terphenyldinitrile
PVP	Polyvinylpyrrolidone
RAIRS	Reflection absorption infrared spectroscopy
rpm	Rotations per minute
SEM	Scanning electron microscopy
STA	Silicotungstic acid
STM	Scanning tunneling microscopy
TEM	Transmission electron microscopy
TEOS	tetraethylorthosilicate

## Abbreviations

---

TFA	Trifluoroacetic acid
UHV	Ultra-high vacuum
XPS	X-Ray photoelectron spectroscopy
XRD	X-Ray diffraction
ZIF	Zeolitic imidazolate framework
$\delta$	Bend (IR)
$\delta$	Twist (IR)
$\nu$	Stretch (IR)
$\rho$	Rock (IR)
$\omega$	Wag (IR)